Étude du rayonnement cosmique de haute énergie: contribution à sa mesure et à la recherche de son origine.

Giovanni Lamanna

Laboratoire d'Annecy-le-Vieux de Physique des Particules

Mémoire d'Habilitation à Diriger des Recherches

Etude du rayonnement cosmique de haute énergie: contribution à sa mesure et à la recherche de son origine.

Présenté a l'Université de Savoie par

Giovanni Lamanna

Soutenue le 25 novembre 2009 devant la commission d'examen:

Pascal	COYLE	Rapporteur
Alain	FALVARD	Rapporteur
Yannis	KARYOTAKIS	
Martin	POHL	Rapporteur
Sylvie	ROSIER-LEES	
Pierre	SALATI	

Remerciements

Je tiens à remercier très sincèrement Pascal Coyle, Alain Falvard, Yannis Karyotakis, Martin Pohl, Sylvie Rosier-Lees et Pierre Salati d'avoir accepté d'évaluer mon travail et de participer au jury de soutenance de mon habilitation au LAPP.

Ce document met en avant ma contribution pour les différentes activités de recherche auxquelles j'ai eu la chance de participer durant ces neuf dernières années. Les résultats significatifs obtenus sont le fruit d'une bonne collaboration au sein des différents groupes de recherches dans lesquels j'ai eu la chance d'être accueilli mais également au sein des coopérations sur le plan international.
Je remercie également tous les gens que j'ai pu rencontrer lors de mon parcours de recherche et qui l'ont rendu possible.

Je tiens à remercier Roberto Battiston, Agnieszka Jacholkowska, Martin Pohl et tous les membres du « working group gamma d'AMS» pour avoir rendu possible et soutenu le développement de la gamma-astronomie dans AMS. Je remercie Bruna Bertucci, Bill Burger et toute la collaboration Si-Tracker de l'Université de Perugia et de l'Université de Genève pour m'avoir dévoilé les secrets du trajectographe et pour l'ambiance amicale de travail. Un merci particulier à John Carr pour son estime et pour l'accueil au sein de la collaboration ANTARES. Merci à Elie Aslanides, Charlin Tao, Jose Busto, Vincent Bertin, Pascal Coyle, Greg Hallewel et tous mes collègues du CPPM pour les merveilleux moments passés à Marseille et pour l'exceptionnelle ambiance de travail. Je garderai un important souvenir de mon expérience dans ANTARES.
Je tiens à remercier Marie-Noelle Minard et Jacques Colas pour leur accueil aux LAPP. Merci à Yannis Karyotakis pour ses conseils, pour son soutien et pour son amitié.
Un grand merci à Jean Pierre Vialle, Guy Coignet, Sylvie Rosier-Lees, Roman Kossakowski et mes collègues du groupe HESS LAPP pour l'ambiance de travail, leurs précieux conseils, leur aide et d'avoir partagé avec passion les défis de recherche des ces dernières années. Merci à Nadine Neyroud pour son soutien et pour son amitié. Je tiens aussi à remercier mes collègues du service électronique, informatique et mécanique pour la qualité et la professionnalité de leur travail, et d'avoir accepté de démarrer avec moi de nouvelles activités de recherche (CTA et POLAR).
Je voudrais également remercier les étudiants que j'ai eu le plaisir de rencontrer lors de mon parcours et d'encadrer durant ces années et tout particulièrement Florent Dubois pour la qualité de son travail de thèse dans HESS.
Finalement, merci à mon épouse Stéphanie pour m'avoir accompagné dans cette aventure, et encore pour mille plus deux* raisons (*Adriano et Livia).

Table des matières

INTRODUCTION

Dans ce document, présenté en vue d'obtenir l'habilitation à diriger des recherches, j'ai pris inspiration des sujets de recherche auxquels je me suis intéressé et des activités que j'ai menées tout au long de mon parcours de chercheur, pour un voyage à travers la thématique de l'origine et la nature du rayonnement cosmique de haute énergie. Les mots clefs à retenir dans la lecture de ce dossier sont: 1) la gamma astronomie ; 2) les phénomènes violents de l'univers ; 3) la matière noire ; 4) la détection du rayonnement du cosmos.

Mon travail de thèse a porté sur l'étude des premières mesures de précision en dehors de l'atmosphère terrestre, avec l'expérience spatiale *Alpha Magnetic Spectrometer* (AMS), des populations des protons cosmiques de haute énergie et ses isotopes, qui caractérisent l'environnement spatial à proximité de notre planète. Le flux de protons cosmiques mesuré avec une grande précision statistique et une incertitude systématique limitée à moins de 5%, ont permis de confirmer la compatibilité des théories de confinement galactique de particules primaires, mais surtout de corriger les assomptions de flux à énergies de 1-200 GeV, utiles par exemple, aux calculs de flux secondaires de neutrinos atmosphériques. Les protons sont les éléments les plus abondants dans le flux des rayons cosmiques qui arrivent sur notre planète et leur intensité en fonction de l'énergie nous permet de déduire indirectement les spectres au niveau des sources astrophysiques où ils sont accélérés.
Les isotopes plus abondants des ^{1}H sont les deutérons, environ 2% des protons. Comme d'autres noyaux, les moins lourds : ^{3}He, Li, Be, B sont produits des collisions de désintégration des ions primaires plus lourds contre la matière interstellaire. La détection de spectres de deutérons est une des mesures les plus originales et importantes acquises par AMS. C'est aussi un sujet fondamental de ma thèse, en raison de sa statistique élevée, en vertu du domaine d'énergie exploré et à la possibilité de pouvoir la comparer aux mesures simultanées des spectres de particules primaires (protons and He) du même spectromètre. En fait, puisque la longueur de parcours moyen des deutérons est plus importante que la longueur moyenne de parcours de confinement galactique, ils sont considérés comme étant des messagers importants et presque uniques. Le rapport des deutérons avec les rayons primaires comme l'^{4}He sont des indicateurs importants de la composition et de la densité de la matière interstellaire, et aussi de la dynamique de confinement des rayons cosmiques. Ces mesures ont permis de déduire le paramètre d'accélération du «Local Interstellar Spectrum » et un indice de puissance du parcours moyen de confinement qui se révèlent parfaitement compatibles avec l'indice spectral de protons cosmiques également mesuré avec AMS. Les mesures de deutérons ont permis de fixer indirectement une limite supérieure à la densité de matière interstellaire (7-8 gr/cm2). Mon analyse a en effet permis

d'exclure une bonne partie des modèles théoriques plus exotiques, et de poser des contraintes extrêmement rigides sur la dynamique de confinement.

Après ma thèse j'ai continué à travailler au CERN dans le groupe d'analyse de la collaboration internationale AMS avec une bourse post doctorale de la « *Fondazione A. Della Riccia* », *« Postdoc Felllowship for first class young Italian scientists abroad »,* puis avec un contrat de *« Maitre Assistant »* au Département de Physique Nucléaire et Corpusculaire de l'Université de Genève, pour enfin obtenir une bourse *« Fellowship »* en Physique du CERN de 2001 au 2003.
Je dois à cette longue et intense expérience au CERN dans la collaboration AMS, mon intérêt de recherche vers les questions de la physique des astroparticules et leur caractère d'interdisciplinarité entre la physique des particules, l'astrophysique, la géophysique, la physique fondamentale et la cosmologie qui m'ont aussi stimulé et conditionné dans mes choix professionnels dans les années qui ont suivi.

J'ai tout d'abord désiré continuer à m'impliquer dans l'analyse de données de la mission spatiale d'AMS de 1998: le rayonnement cosmique spatial à proximité de la terre est affecté par la modulation solaire et la modulation géomagnétique. Les deux effets ont également fait l'objet d'une étude approfondie. Le niveau quantitative de modulation solaire correspondant à la période de vol d'AMS a été mesuré et confirmé avec deux mesures indépendantes (flux des protons et flux de deutérons) ; cela m'a également permis de valider la méthode de son estimation, déjà dans ma thèse. En ce qui concerne la modulation géomagnétique, la mesure du rayonnement à toutes les longitudes et à différentes latitudes géomagnétiques a donné la possibilité d'une investigation précise des spectres de rayons cosmiques en dessous de la coupure géomagnétique de rigidité. Grâce aux résolutions angulaire et énergétique optimales du détecteur SiTracker, les études originales et de précision de la cinématique de ces particules pris au piège dans le champ géomagnétique ont été enfin possibles. Cela a représenté une méthode directe de caractérisation phénoménologique du champ magnétique terrestre. Les travaux d'interprétation des spectres de rayons cosmiques pris au piège dans le champ géomagnétique et mesurés par le détecteur AMS01 lors du vol de 1998, déjà débutés dans le contexte de la thèse de doctorat, ont été poursuivis en collaboration avec l'équipe AMS de l'Université de Perugia. Les particules cosmiques secondaires de retour de l'atmosphère et remises en orbite en dehors de l'atmosphère sous l'influence des lignes de champ géomagnétique donnent lieu à des "ceintures de radiations" jamais observées avant AMS. Ces travaux ont donné lieu à des études interdisciplinaires entre la physique des astroparticules et la géophysique, et débouchés sur la publication de deux articles dans des revues internationales de géophysique.

Au CERN j'ai aussi désiré élargir ma contribution à la collaboration dans la préparation de la phase 2 d'AMS dans sa configuration finale et pour une mission de longue durée à bord de la Station Spatiale Internationale ISS. Avant tout j'ai voulu me familiariser avec des aspects plus techniques du métier de chercheur en contribuant aux études de calibrage et monitorage des paramètres globaux et de performances du détecteur SiTracker (en terme de résolution énergétique, spatiale, multiplicité de « strips » de lecture, niveau de bruit, canaux inactifs et alignement de plans), pendant la mission spatiale du 1998. Ces études sont devenues importantes pour le développement de la thématique de recherche dans laquelle je me suis ensuite impliqué: l'étude de tous les aspects concernant la faisabilité et les attentes en physique de la détection de rayons gamma de haute énergie (5 - 300 GeV) avec le spectromètre AMS-02, alors que ceci est fondamentalement conçu pour la détection des rayons cosmiques chargés. Les motivations expérimentales de cet objectif sont basées sur la possibilité offerte en terme de résolution angulaire (et la « significativité de détection » conséquente) par le détecteur des traces au silicium (SiTracker) à travers la reconstruction des trajectoires léptoniques issues du canal de conversion $\gamma \rightarrow e^+e^-$. Les performances de détection envisagées, très compétitives même quand elles sont comparées aux télescopes spatiaux conçus avec l'objectif de cette mesure (e.g. GLAST), ont déterminé un intérêt scientifique important dans la collaboration internationale AMS. J'ai personnellement joué un rôle porteur dans ce contexte et sur divers aspects : développement du logiciel de reconstruction des événements à double traces dans le spectromètre AMS. Ce logiciel tient

compte de l'optimisation des procédures de «pattern recognition » des signaux des senseurs au silicium pour la maximisation d'individuation du nombre des événements à double traces (e^+e^-) limité par la longueur de radiation et conséquente probabilité de conversion de photon en amont du « SiTracker ». Etude de la logique de trigger pour la rejection du fond de rayons cosmiques chargés qui mimeraient les photons donnant lieu à des événements double-traces dans le spectromètre et capable d'être confondu avec les gammas. De plus j'ai désiré me consacrer à un programme d'étude de la sensibilité des objectifs les plus importants pour la physique de rayons gamma. Apres avoir initié cette étape, j'ai animé et coordonné un groupe de travail de physique au sein de la collaboration internationale AMS pour l'exploration de cas scientifiques. C'est dans ce contexte que j'ai coordonné les efforts d'un sous groupe de travail dédié à l'étude potentielle de sources astrophysiques avec les rayons gamma de haute énergie : en particulier les attentes de discrimination de l'effet EBL – fond de lumière diffuse extragalactique – et l'estimation de l'opacité du fond extragalactique (aux énergies de centaines de GeV) à travers l'analyse spectrale des AGN; les études de caractérisation de modèles d'éjection à travers l'analyse spectrale et l'éventuelle coupure spectrale à haute énergies dans les émissions gammas de Pulsars.

Le potentiel de la γ-astronomie est dans son implication multidisciplinaire. Dans ce contexte j'ai accordé une attention particulière pour les études phénoménologiques d'exploration du potentiel d'AMS02 à la détection des anomalies dans les spectres de rayons cosmiques (et des photons en particulier) introduites par les produits de désintégration des particules massives exotiques candidates de la matière sombre (WIMP). En collaboration avec les membres du groupe de travail sur le gamma, afin de prédire le signal gamma, un générateur de spectres a été développé en fonction de la nature du candidat. La modélisation du halo galactique et celle du fond attendu dans le détecteur AMS02 ont été considérées; la possibilité, compte tenu de la sensibilité attendue, de remonter au modèle de nouvelle physique (e.g. SUSY) par ces mesures a été exploré. Les résultats de ces études ont fait l'objet de publications scientifiques originales et m'ont également donné la possibilité de faire partie des groupes de travail et de discussions internationaux sur le sujet de la détection indirecte de matière noire.

En octobre 2003 j'ai obtenu un poste de chargé de recherche de première classe au CNRS. Cela m'a permis d'aborder les mêmes sujets de physique qui m'intéressent particulièrement, mais cette fois à travers un autre messager du cosmos : les neutrinos de très haute énergie (à l'échelle des TeV). J'ai en effet rejoint le groupe ANTARES du CPPM de Marseille.
Pour la préparation à l'analyse des données j'ai conduit une étude de Monte Carlo finalisée principalement à la recherche de signatures indirectes de matière sombre et leur corrélation avec les mesures de rayons gamma de très haute énergie. En particulier l'estimation du comptage de neutrinos dans ANTARES en modélisant un flux primaire de neutrinos cosmiques sur la base des mesures les plus récentes de l'émission gamma de très haute énergie du centre galactique avec le système HESS. Du point de vue phénoménologique les hypothèses de matière sombre dans le contexte Kaluza-Klein ont été explorées en considérant une approche non-originale, basée sur les dernières études théoriques et complétée par la simulation d'efficacité et de sensibilité réelle du détecteur.
Avant la prise de données scientifiques de l'expérience (à l'époque dans sa phase de construction) une phase de réglages et de calibrage s'impose.
Les neutrinos détectés par l'observatoire ANTARES permettront à travers leurs trajectoires de remonter à leurs sources astrophysiques. Pour cela la résolution angulaire du détecteur ANTARES est une figure de mérite fondamentale et aussi un paramètre qui rend cette expérience très compétitive par rapport aux expériences concurrentes. Afin de bien reconstruire l'évolution espace-temps du parcours des neutrinos dans le détecteur, une lecture temporelle rapide et correcte des Modules Optiques de l'expérience est fondamentale. Mes contributions aux activités dans la collaboration ANTARES ont été focalisées sur l'optimisation de cet aspect et sur la réussite de l'acquisition des premières données scientifiques dans le site expérimental au fond de la mer méditerranée. J'ai notamment été responsable du système et des procédures de calibration temporelle des modules optiques de la ligne instrumentale MILOM et de la première des douze lignes de l'expérience. En particulier, en collaboration avec mes collègues du CPPM un banc de tests optiques a été réalisé et la procédure d'analyse pour la calibration temporelle a été finalisée, testée en laboratoire et validée par l'analyse des toutes premières données

d'ANTARES des modules optiques de la ligne MILOM, qui ont fait l'objet d'une publication au nom de toute la collaboration.

A partir de janvier 2006 j'ai rejoint le laboratoire LAPP où j'ai eu la possibilité de travailler sur l'analyse des données de gamma de très haute énergie. Au LAPP je me suis impliqué dans trois activités:
- la responsabilité de diriger les analyses de physique des données d'HESS-I m'a rapidement été confiée : investigation de certaines sources Galactiques étendues (e.g. *SNR – Supernova Remnants et PWN – Pulsar Wind Nebulae*) en étudiant la morphologie et la corrélation spatiale avec d'autres longueurs d'ondes pour tester la dépendance entre densité de champ magnétique et densité de masse. Ces études sont critiques pour contraindre les modèles d'origine du rayonnement gamma dans les deux scénarios possibles: léptonique ou hadronique ; introduction des méthodes d'analyse multi-variable pour les analyses HESS-I et les études de Monte Carlo de HESS-II
- la supervision du développement du logiciel de contrôle et de sécurité de la caméra et du système de débarquement, ce dernier étant d'ailleurs en construction au LAPP, et plus récemment
- la direction des projets en informatique et mécanique pour l'étude de faisabilité du futur réseau de télescopes Tcherenkov CTA. J'ai en particulier assuré la conception, la mise en œuvre et la coordination du projet international « CTACG - CTA Computing Grid » avec pour finalité la production et la gestion des données de simulations Monte Carlo (ces simulations sont fondamentales pour les études des performances instrumentales attendues et pour les calibrations et la compréhension des données à venir) à travers la gestion de ressources de calcul distribuées au niveau international et leur exploitation à travers la grille de calcul. CTACG est aussi un projet plus vaste qui se développera dans les prochaines années et qui a pour objectifs: l'étude de faisabilité de la gestion des données du futur observatoire CTA à travers les technologies de grille et la proposition d'une plateforme intégrée informatique et de réseaux intercontinentaux de recherche.

Au LAPP j'ai trouvé le bon environnement me permettant de soulever des discussions avec mes collègues du groupe HESS mais également en connexion avec des collègues théoriciens du LAPTH, sur le rôle de la mesure de polarisation du rayonnement cosmique électromagnétique, en provenance de sources astrophysiques les plus violentes de l'univers. Dans ce contexte j'ai développé la volonté de rejoindre un groupe de recherche international pour la réalisation d'un mini satellite spatiale POLAR. Grâce au soutien du laboratoire et de l'Université de Savoie, et á l'expertise précieuse du service électronique du LAPP, je participe á la conception d'un circuit électronique intégré pour la mesure précise de signaux du polarimètre POLAR.

En résumé, mon parcours professionnel tout d'abord au CERN dans l'expérience CMS mais surtout dans AMS, puis ensuite au CNRS dans les expériences ANTARES et HESS, m'a permis de maitriser différentes compétences riches pour leur complémentarité en : recherche et développement de détecteurs de particules et d'électronique nucléaire, analyse de données, étude phénoménologique, en physique des astroparticules, et enfin la gestion de projets de recherche.
Cela m'a permis d'aborder et de contribuer avec mes recherches au domaine de la physique des astroparticules à différentes échelles d'énergie : du X au VHE gamma rays, à travers différents messagers : des rayons cosmiques chargés au gamma-rays et neutrinos, avec différents instruments : du Si-Tracker au Tcherenkov et aux photodétecteurs, et de m'intéresser aux différents aspects du rayonnement cosmique : de la propagation et confinement galactique au rayonnement environnemental géomagnétique ; des sources astrophysiques galactiques à la détection des signaux de matière sombre, de l'origine du rayonnement gamma aux mécanismes d'accélération et éjection des sources astrophysiques, jusqu' à la perspective d'études en cosmologie.

I. MESURES ET METHODES DE DETECTION DU RAYONNEMENT COSMIQUE DE HAUTE ENERGIE

I.1. Introduction

L'étude du rayonnement cosmique et plus en générale de la physique des astroparticules a connu des avancées importantes au cours des derniers 15-20 ans et les perspectives pour les prochaines décennies sont encore plus riches.

Cela a été possible grâce à un fort investissement des chercheurs dans des projets de R&D de nouveaux détecteurs des particules ou plus exactement dans la conception de nouvelles et plus grandes applications de ces technologies à la mesure du rayonnement cosmique. Mon parcours professionnel a été conditionné par ces progrès mais il m'a surtout donné l'occasion d'y participer avec des contributions personnelles dans le contexte des programmes de recherche d'expériences comme : AMS, ANTARES, HESS, CTA et POLAR.

J'ai tout d'abord participé aux études de performance des détecteurs de traces Silicon-Tracker pour la détection de particules chargées en environnement spatial (avec l'expérience AMS) et aux études de l'application de ce détecteur à la mesure des rayons gamma des énergies > GeV. Ensuite, lors de mon implication dans les études de détection des neutrinos d'ultra haute énergie (UHE) (avec l'expérience ANTARES), j'ai étendu ma contribution à la préparation et à la mise en fonction des photodétecteurs en environnement sous-marin. La détection Tcherenkov en atmosphère de rayons cosmiques pour la gamma astronomie est désormais une technologie consolidée. Mes implications dans le contexte instrumental (dans la collaboration HESS puis dans les perspectives du futur observatoire CTA) sont essentiellement orientées vers des réflexions sur les choix mécaniques et de photodétection pour la future génération d'observatoire gamma de très haute énergie (VHE). En parallèle à ce travail j'ai désiré continuer à m'impliquer dans des groupes de travail et de réflexion sur les futures missions spatiales dédiées à l'exploration des phénomènes les plus violents de l'Univers et cela m'a porté à m'intéresser à la mesure de polarisation de rayons X durs des sources astrophysiques est donc à une série d'aspects instrumentaux à optimiser pour la réalisation de cette mesure. En particulier la conception et l'optimisation de l'électronique d'acquisition de photodetecteurs appliqués à cette finalité (avec le polarimètre POLAR). Dans ce chapitre je résumerais ces contributions à travers l'exposition d'une série choisie de considérations sur certains aspects des méthodes de mesure en physiques des astroparticules. L'annexe A présente la liste détaillée des travaux personnels en rapport avec ce chapitre ainsi qu'une note technique interne à la collaboration ANTARES dont j'ai été l'auteur et qui résume les méthodes de synchronisation et de calibrage des mesures en temps des photodetecteurs et leur comparaison avec les toutes premières données de ces derniers en environnement sous-marin.

I.2. Le détecteur de trajectoires du spectromètre AMS

Il ya plus de 20 ans que l'application des détecteurs au silicium a été proposée, pour la première fois, pour des applications dans l'Espace en profitant des avancées et du succès du développement de ces détecteurs par la communauté de la Physique d'Haute Energie (HEP). La possibilité de rallonger la vie moyenne de trajectographe en remplaçant les détecteurs à gaz avec des senseurs de silicium, la possibilité de réduire le temps mort de réponse de la *ms* à la μs, en permettent de mieux investiguer les

sources astrophysiques transitoires et aléatoires, sans oublier la réduction de coûts progressive du silicium, ont permis le projet d'expériences Spatiales avec l'application de grandes surfaces de détecteurs au silicium. L'une de ces expériences est AMS – *Alpha Magnetic Spectrometer.*
Le spectromètre spatial AMS01 (fig. 1.1.a) mis en orbite en Juin 1998 avec la navette spatiale NASA-*Discovery* est équipé d'un détecteur de traces au silicium « *SiTracker* ». Cela a représenté la première application pour la recherche de rayons cosmiques et aussi la première application dans l'espace d'un détecteur au silicium de grande surface (> 5 m^2) [1], conçu pour la physique des particules, dont la technologie avais déjà été appliquée dans les détecteurs de vertex des expériences L3 et ALEPH du LEP (*Large Electron-Positron collider*) au CERN.
Il s'agit d'un détecteur à micro-pistes double faces à six plans. Un plan est constitué de deux groupes d'échelles (*ladders*) disposées tête-bêche. A l'extrémité disjointe d'une échelle se trouve l'électronique de conversion composée de deux circuits appelés *hybrides*, chacun dédié à la lecture de l'une des faces (fig. 1.1.b). Le corps d'une échelle est constitue d'un assemblage en série de plaquettes de silicium double face (les senseurs), entre 7 et 15 par échelle, reliée entre elles par des microsoudures. Chaque plaquette a une épaisseur de 300 μm qui représente un compromis entre la nécessité de réduire les effets de diffusion multiple tout en gardant une amplitude de signal raisonnable. La structure de support mécanique des échelles est en matériaux composites (aluminium et fibre de carbone) assemblée en géométrie souple (nid d'abeilles). Cela assure la stabilité et minimise le matériel: une échelle correspond a 0.65% X_0.

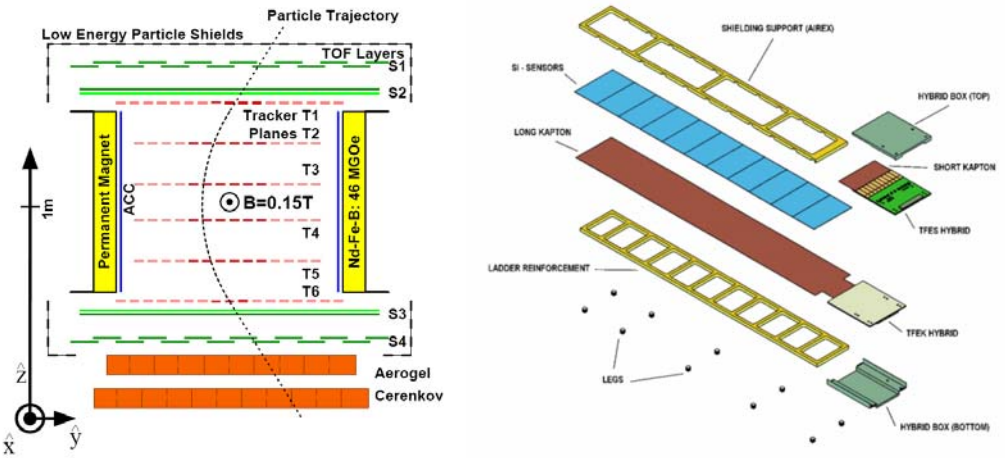

Figure 1.1 : a) Vue schématique du détecteur AMS-01. On note la présence des éléments principaux: l'aimant cylindrique de 1,034 m de diamètre interne et compose de block de Nd-Fe-B (5 x 5 x 2 cm^3). Un total de quatre (S1-S4) plans de scintillateurs pour la mesure des temps de vol et en particulier les six plans du SiTracker (T1,..., T6), séparés par une distance totale de 1 m et dont quatre sont à l'intérieur du cylindre de l'aimant ; b) Vue explosée d'une échelle (« ladder ») de SiTracker.

Le cœur d'une plaquette de silicium double face est une région de silicium dopé *n*, sur l'une des faces se trouvent des implants p^+ qui forment les pistes du coté S (jonction ou p), sur la face opposée (cote K, ohmique ou n) se trouvent des implants n^+ en direction orthogonale par rapport aux pistes du coté S. Sur cette face, des implants p^+ sont disposés entre les pistes et qui sont appelés les *p*-stop, destinés à fortement augmenter la résistance entre deux pistes voisines lorsque la région de déplétion est suffisamment étendue car l'environnement des pistes n^+ est formé de silicium *n* et la résistance est bien moins grande que celle qui prévaut entre deux pistes p^+ sur la face opposée. Le croisement de pistes côté S et côté K permet la détermination des deux coordonnées (x, y) de passage de la particule chargée sur une plaquette. La plaquette de silicium à les dimensions 4.1 x 7.2 cm (qui déterminent les différentes longueurs des pistes sur les deux cotés S x K). La présence des pistes « flottantes » (pas lues par l'électronique) détermine une différence entre les distances d'implantation et celles de lecture entre les pistes parallèles pour chacun des deux côtés, 27.5 μm et 110 μm respectivement pour le côté S et 52 μm et 208 μm pour le côté K. Le nombre de micro-pistes lues du côté S est de 640 et de 192 du cote K. La résolution est donc meilleure du côté S non seulement en raison de l'espace réduit entre

deux micro-pistes mais également parce que la structure du champ électrique est telle que les lignes de champs sont bien plus denses de ce côté-ci de la plaquette.

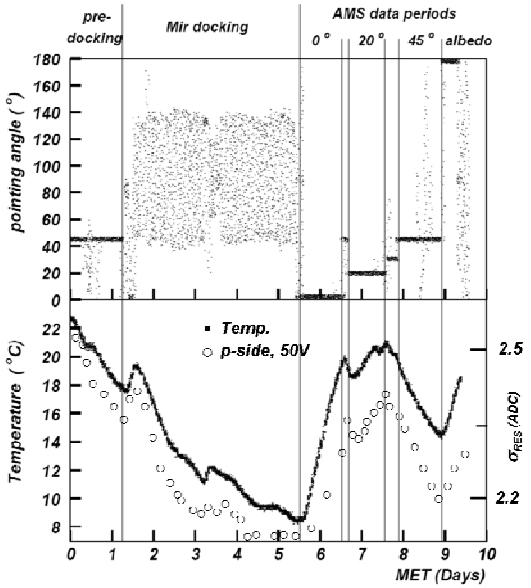

Figure 1.2: L'évolution de l'angle de pointe d'AMS, dûe aux manouvres de vol de la navette spatiale, explique parfaitement les différences de température mesurées à l'intérieur de l'aimant. Les valeurs moyennes des largeurs des piédestaux sont fortement corrélées avec les variations de température [1].

Un bas niveau de bruit, une plage dynamique large et une consommation contenue sont les caractéristiques critiques de l'électronique de lecture. Le signal en provenance des plaquettes est acheminé vers l'électronique de conversion via des capacités (couplage AC) qui permettent de mesurer des grandes valeurs de charge tout en évitant la saturation du préamplificateur [2][3][4]. Après le passage à travers les capacités de découplage le signal est pris en charge par l'hybride ou circuit de conversion dont le cœur est le VA_HDR, un amplificateur de charge de la famille des Viking [5][6]. Après la mise en forme et l'échantillonnage, la sortie du circuit est lue à la fréquence de 5 MHz à travers un multiplexer analogique.
Au passage d'une particule, en moyenne 22'000 paires électrons-trous sont crées ou 117 keV en moyenne pour une particule minimum ionisante (MIP) de charge Z=1 (ou encore 3.5fC). La plage du VA_HDR est étendue à environ 100 MIP, c'est-à-dire qu'elle est appropriée à l'intégration de cent fois le signal déposé par une MIP de charge Z=1, avec une réponse linéaire jusqu'à environ 75 MIP et avec une mesure de dE/dX efficace.
Les signaux analogiques sont ensuite acheminés au niveau supérieur de réduction des données appelé TDR où ils sont digitalisés et compressés. Le TDR est aussi en charge de la calibration du détecteur.
Le calibrage du SiTracker consiste à déterminer les valeurs des piédestaux et leur largeur relative pour chaque canal de lecture ainsi qu'à mesurer les niveaux de bruit commun («common-noise ») des VA pour chaque carte de pré-amplification (qui regroupe 64 canaux des plaquettes pour chaque unité logique).
Les mesures de calibrage en vol pendant la mission STS-91 mais aussi leur ré-estimation offline pendant la phase de production et d'analyse des données scientifiques ont permis de mieux connaître et interpréter le comportement de ce détecteur. Pendant la mission STS-91 de 9 jours, la navette, après décollage, a rejoint la station MIR a laquelle elle s'est arrimée. Après avoir ravitaillé MIR, durant quelques jours, elle a librement évolué dans l'espace pour une prise totale de données pendant toute la mission, soit plus de 100 heures d'acquisition.
Les valeurs moyennes des largeurs des bruit communs («common-noise ») des circuits VA_HDR étaient toujours constantes avec des variations de quelques pour cent, et comparable au niveau attendu

avant la mission en vol. Les largeurs moyennes des piédestaux, σ_{PED} étaient toujours inferieures à 3 (4) coups d'ADC pour le côté S (K) mais surtout en forte corrélation avec les excursions thermiques auxquelles le télescope était soumis pendant le vol de la navette spatiale (voir fig.1.2) et de fait, en fonction de l'orientation de la navette par rapport au soleil.
Le TDR est aussi en charge de la suppression des canaux ayant un comportement non gaussien. Ces canaux ne représentent que 3% (4.5%) de la totalité des canaux côté S (côté K). Le TDR supprime également les canaux ayant un très haut niveau de bruit intrinsèque. Leur contribution est déterminée au moment du monitorage des niveaux d'occupation de micro-strippes et représente un additionnel 9% (12.5%) de la totalité des canaux côté S (cote K) [7].
La présence des pistes « flottantes » introduit un couplage capacitif qui améliore la collection de charge dans l'espace entre les pistes de lecture. Cela influence la relation entre la position de passage de la particule et les dépôts relatifs de charge entre deux pistes [8]. Ce dernier exprime avec le paramètre η:

$$\eta = \frac{S_2}{S_1 + S_2}$$

Dans lequel S_1 et S_2 représentent les signaux (l'amplitude de charge) des deux pistes d'un cluster avec les plus hautes valeurs du rapport signal-sur-bruit et identifiés par leur ordre de lecture. La position de passage de la particule est déterminée à travers le calcul du centre de gravité (*COG*) de un cluster composé au maximum de cinq pistes contigües. La position du *COG*, X_{COG} est déterminée à partir de la position de la première piste X_1, le pas p entre les pistes de lecture et le poids lié à la distribution de charge η:

$$X_{COG} = X_1 + p\eta$$

Dans cette dernière formule on suppose une corrélation linéaire entre la charge relative collectée sur deux pistes et la position de la trajectoire dans le pas entre les pistes de lecture, e.g. une distribution uniforme du paramètre η. En réalité la distribution du paramètre η est non –linéaire et montre une forte dépendance de la position de pistes flottantes. Pour cela ce paramètre est en effet remplacé [9] par l'intégral de la fonction de distribution $f(\eta)$ pour mieux extraire la position de la trajectoire :

$$X_\eta = X_1 + p\int_0^\eta f(\eta')d\eta'$$

La résolution spatiale assurée par le SiTracker et validée par l'analyse de données est de 10 μm dans le plan de déflection du champ magnétique (direction X correspondant aux directions des pistes du côté S) et de 30 μm dans le plan orthogonal (direction Y, cote K). L'amplitude du cluster est une mesure directe et importante pour l'estimation de l'énergie déposée (*dE/dx*) par la particule qui traverse le trajectographe, et qui est donc utile pour la détermination de la valeur absolue de la charge ($|Z|e$) même de cette particule. L'énergie déposée est corrigée par la direction de traverse des échelles de silicium ($cos\theta$) et est fonction de la vitesse (β). Mais la mesure fondamentale pour laquelle le détecteur SiTracker est appliqué est la rigidité $R = pc/|Z|e$ de la particule traversant le spectromètre. La rigidité R est obtenue indirectement à travers la mesure du rayon de courbure ρ de la particule:

$$R = \rho Bc = \frac{((L/2)^2 + d^2)}{2d} Bc$$

Ou L est la distance entre les deux plans plus externes du trajectographe, B est le champ magnétique assumé uniforme en première approximation et d est la *sagitta* qui mesure directement le niveau de déflection subi par la particule chargée par l'effet du champ B de l'aimant. La résolution ($\Delta R/R$) du

trajectographe est limitée par les effets de diffusion multiple pour particules de basse énergie (< 10 GeV), alors qu'à haute énergie se trouvent la résolution spatiale du détecteur et le pouvoir de déflection du champ magnétique qui limitent la MDR (Rigidité Maximale Mesurable – avec un $\Delta R/R = 1$) a ~200 GeV (pour particules Z=1, e.g. les protons).

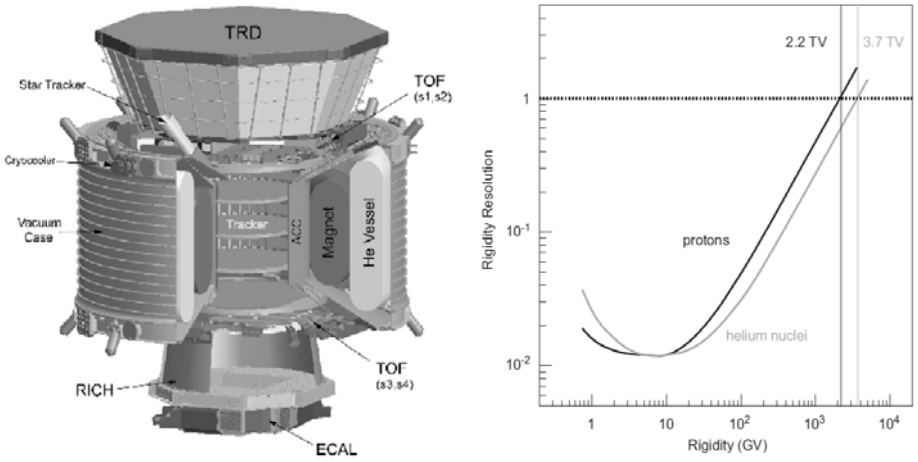

Figure 1.3: a) Le spectromètre de second génération AMS02 consiste en un aimant supraconducteur de 0.8 T, six plans de SiTracker, un Détecteur de Rayonnement de Transition (TRD), un system Temps de Vol (TOF) de scintillateurs plastiques, un détecteur Tcherenkov à image annulaire (RICH), un calorimètre électromagnétique (ECAL) et un système de comptage d'anti-coïncidence (ACC). b) Le nouveau trajectographe SiTracker permet des valeurs de MDR de l'ordre du TV.

Les résultats de physique obtenus suite à la mission de AMS01 sur la navette spatiale sont résumés dans [10]. Mais une série d'autres travaux interdisciplinaires d'analyse ont aussi eu lieu grâce aux performances du SiTracker. En particulier c'est grâce aux résolutions angulaire et énergétique optimales du détecteur SiTracker que des études originales et de précision de la cinématique de particules cosmiques secondaires pris au piège dans le champ géomagnétique ont été enfin possible [11][12][13][14]. Les particules cosmiques secondaires de retour de l'atmosphère et remises en orbite en dehors de l'atmosphère sous l'influence des lignes de champ géomagnétique donnent lieu à des "ceintures de radiations" jamais observées avant AMS. Les "ceintures de radiations de Van Allen" (plus connues) sont étendues de 800 km jusqu' à 60000 km de la Terre et composées essentiellement de protons et d'électrons (de 1 a 100 MeV d'énergie) avec une vie moyenne des quelques années et créés par la désintégration des neutrons provenant de l'atmosphère. Contrairement aux ceintures de Van Allen les ceintures de AMS sont étendues à une altitude de 400 km, sont peuplées d' électrons, de positrons, de protons, de antiprotons, de deutérons et d' ions d' hélium, d'énergie entre 1 GeV et 10 GeV, en provenance directe de l'atmosphère avec une vie moyenne de seulement quelques secondes. Leur vie est fonction de leurs chemins dans ces ceintures et ceci sont conditionnés par les intersections entre les lignes de champ géomagnétique et les trajectoires mêmes des particules. Ces derniers tracés sont reconstruits avec une grande précision grâce au trajectographe d'AMS.
AMS01 est la première expérience d'application dans l'espace d'un détecteur des tracés au silicium. Le succès de la mission spatiale STS-91 et également la réponse parfaite du trajectographe ont démontré que le SiTracker est bien adapté à l'environnement et aux contraintes spatiales [1]. Il y a aussi les leçons apprises, en particulier la nécessité de réduire le bruit des pistes du côté K afin d'améliorer la mesure du dE/dX et la résolution spatiale pour les noyaux lourds. Pour cela, dans la configuration finale du spectromètre (AMS02), les plaquettes de silicium sont redésignées pour augmenter les signaux du côté ohmique tout en réduisant le nombre de pistes du côté K et garantissant une collection de charge plus uniforme [1][9]. Le spectromètre AMS02 (fig. 1.3) sur la Station

Spatiale Internationale (ISS) verra aussi une augmentation du pouvoir de déflection grâce a un aimant supraconducteur de ~ 1 T et une série d'autres sous-détecteurs pour la caractérisation de la nature du rayonnement cosmique. Les performances attendues avec AMS02 (fig. 1.3) ont aussi ouvert des prospectives complémentaires: e.g. la détection de rayons gamma de haute énergie.

I.2.1. Le développement pour la détection des γ de haute énergie

La difficulté d'observer de rayons gamma de l'énergie du GeV sur terre sont très grandes et la détection satellitaire dans l'espace est la seule solution possible, alors que pour des rayons d'énergie plus grande (>100 GeV) les systèmes Tcherenkov au sol permettent d'utiliser de grandes surfaces de détection. L'observation des rayons γ a commencé dans les années '60 et le premier balayage du ciel a énergie > 50 MeV a été accompli par l'instrument EGRET du télescope spatial *Compton Gamma Ray Observatory* [15][16] dans les années '90. Sur les ~300 sources de rayons gamma découvertes par EGRET, 170 n'avaient pas été associées à des objets connus. La compréhension de l'émission gamma diffuse galactique et extragalactique reste encore une question ouverte. Des questions cosmologiques sont invoquées pour expliquer la population des sources extragalactiques et la variation de leurs spectres due à la probable absorption de rayons γ de la part du milieu interstellaire. Ces questions ont déclenché aussi l'étude d'application d'AMS02 et en particulier du SiTracker pour la quête aux rayons gamma de haute énergie en avant première[1].

AMS02 offre deux méthodes complémentaires pour la détection de rayons gamma: la *conversion* a travers la reconstruction dans le trajectographe de paire de particules e+e- issues de l'interaction du γ dans le SiTracker, et la *détection directe* de photons singles (non convertis) et qui rentre dans le champ de vue du calorimètre électromagnétique (ECAL). Ce dernier détecteur permet de reconstruire l'énergie et la direction des événements gammas qui sont observés à travers un système de déclenchement dédié. Par contre l'identification et la reconstruction des événements paire e+e- sont étudiés seulement lorsque la conversion des photons a eu lieu dans le matériel en amont du premier plan (S1) du SiTracker, qui est constitué des deux niveaux de scintillateurs du ToF, des divers niveaux du TRD et aussi des structures de supports mécaniques et des radiateurs thermiques de ceux derniers, pour un total de ~ 0.3 X_0 . Cela signifie que seulement dans 20% des cas les photons qui rentrent dans le volume d'AMS02 seront détectés par conversion. Néanmoins ces photons pourront compter sur une qualité de reconstruction cinématique grâce au SiTracker, et ceci est un aspect critique pour les objectives des scientifiques de l'astronomie gamma.

La logique de déclanchement de premier niveau pour la méthode de conversion (qui correspond à la stratégie de présélection pour l'analyse de Monte Carlo) demande l'absence de signaux dans les trois premiers sous-niveaux du TRD, la présence d'information ToF avec des signaux pour 3 sur 4 niveaux au minimum et que la valeur de la vélocité β (mesurée par le ToF) d'au moins une des deux traces soit compatible avec la valeur 1.
La reconnaissance de traces à travers la combinaison des signaux du SiTracker, compatibles avec des événements à double traces, est à la base du niveau le plus élevé de déclenchement gamma. Pour cela une approche simplifiée consiste à rechercher dans la plan de projection de la déflection des traces (YZ) des doubles dépôts d'énergie (*hits*) pour chaque étage du trajectographe, en se séparant dans des directions opposées en fonction de la profondeur dans le spectromètre: un ajustement avec une courbe polynomiale avec la taille des écarts entre les dépôts d'énergie du même plan en fonction de la direction Z (position de chaque étage) et minimisation du χ^2 conséquent, permet rapidement de sélectionner la totalité des photons convertis. Dans le plan de projection opposé (XZ) un ajustement linéaire des dépôts d'énergie candidats à la reconstruction de deux tracés est appliqué. L'ajustement est appliqué selon la direction d'interpolation entre les positions de passage de particules dans les

[1] Il est en fait important de rappeler qu'avant le retard du programme AMS dû à la suspension de vol de la navette *Shuttle* de la NASA, le calendrier de la mission AMS était de deux-trois ans en avance par rapport a la mission GLAST-FERMI, expérience de référence pour l'astronomie gamma d'énergie > 50 MeV. En conséquence, la perspective de sonder en premier le ciel gamma au GeV avais fournit des motivations davantage pour l'R&D du projet AMS-γ.

scintillateurs des ToF, dans le TRD et aussi selon la direction de développement des gerbes dans ECAL si possible. Le correspondant χ^2 donne une estimation de la qualité de la reconnaissance. L'approche ici résumée est détaillée dans [17] et représente une méthode acceptable pour réduire le nombre des évènements candidats paire et la première estimation de leurs trajectoires.
La reconstruction optimale de traces de paire e+e- et de leur paramètre cinématique est garantie par des procédures d'interpolation avec méthode *path integrals* [18]. Cette dernière est particulièrement efficace dans le cas d'AMS parce que conçue pour des champs magnétiques presque homogènes ou pour lesquels, toutes possibles inhomogénéités ont un effet d'incertitude sur l'estimation de la rigidité d'un ordre de grandeur inferieur à celle introduite par le « multiple scattering ». Ce dernier est pris en compte d' une manière simple à travers l'introduction de dispersions Gaussiennes supplémentaires dans la résolution spatiale du SiTracker qui permettent en suite d'avoir sous contrôle les différentes sources qui affectent la résolution finale en rigidité du trajectographe (voir Fig.1.3).

Facteur géométrique et rejection du fond des rayons cosmiques

Les coupures de sélection dans le cas de la recherche d'événements photons (deux tracés chargés de signes opposés) sont choisies essentiellement avec le propos d'accepter un rapport signal-sur-fond de quelques pourcents. Le fond est représenté par des rayons cosmiques les plus abondants, électrons et protons, qui seraient reconstruits comme des événements vraisemblables a deux traces et qui satisferaient les conditions de présélection: les protons qui subissent des interactions hadroniques peuvent en effet produire des particules secondaires (e.g. avec émission de rayons δ) donc de doubles tracés chargés pouvant être interprétés à tort comme un photon converti. Cela signifie optimiser la sélection des événements pour une rejection de l'ordre entre 10^4 et 10^6.

La réjection plus important du fond passe par une coupure sur :

- les événements vraisemblablement intéressés par des interactions hadroniques : activité dans les compteurs d'anti-coïncidence limitée à un amas, de même que l'activité dans le trajectographe (50 amas), ou dans le TRD avec plusieurs canaux rapprochés simultanément allumés.
- des valeurs trop grandes de la masse invariante reconstruite des deux traces (la sélection prévoit deux coupures possible : Mass Inv. < 0.4 $(GeV/c^2)^2$ ou Mass Inv. < 0.1 $(GeV/c^2)^2$) (fig.1.4).
- la reconstruction du point d'entrée de particules dans le volume fiducielle du spectromètre à travers l'interpolation des lignes de vol des événements candidats sur le bord de la structure du TRD (voir fig.1.6).

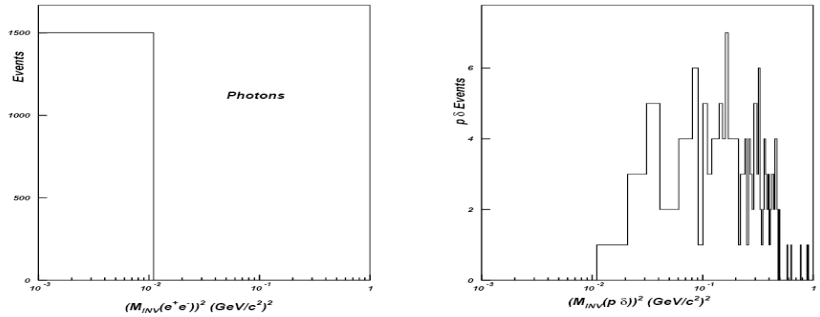

Figure 1.4: Distribution de Mass Invariante pour les événements génuines paire e+e- reconstruits par le trajectographe et les événements du fond du à des protons plus des rayons δ pouvant être interprétés à tort comme un photon converti.

Les sélections exposées conduisent à une réjection de proton de l'ordre de 10^5 et de 10^4 pour les électrons ainsi qu'aux performances montrées dans la figure 1.7 : la partie droite de la figure 1.7

montre l'acceptation différentielle en fonction de l'énergie, la partie gauche la surface efficace équivalente en fonction de l'angle de vue ($\cos\theta$). Le jeu de coupures appliquées permet une rejection du fond nécessaire pour la mesure du fond gamma diffus. Un jeu de coupures plus lâches que dans le cas précédent et finalisé à la détection des photons qui proviennent des sources astrophysiques ponctuelles (a travers une méthode comparative on/off source) permettrais, au prix d'une augmentation du fond cosmique, d'accroître l'acceptation d'un factor 2 environ (les perspectives scientifiques associées à ces performances seront rappelées dans les chapitres suivants et dans l'Annexe B)[20][21][22][23]. Le résultat montre que les mesures d'AMS02 se font au-delà de 10 GeV en raison de la réjection des protons qui est insuffisante en-deçà. La réjection des protons s'améliorant à haute énergie et l'acceptation est en plateau.

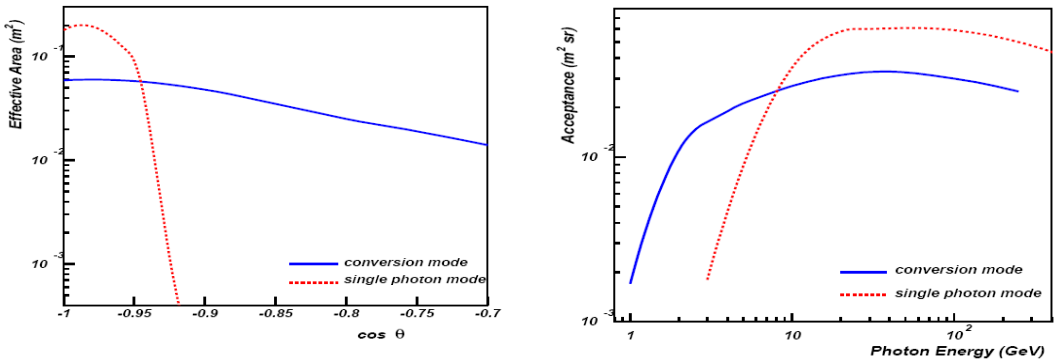

Figure 1.4: La figure de droite montre l' « acceptance » différentielle en fonction de l'énergie (des études plus récente on montré de pouvoir étendre la sensibilité de AMS jusqu'au TeV [19]). La figure de gauche montre la surface efficace en fonction de l'angle de vue ($\cos\theta$), pour un jeu de coupures dures en permettant une rejection du fond nécessaire pour la mesure du fond gamma diffus. Les figures de mérite de détection avec le trajectographe (conversion mode) sont comparées aux homologues obtenus avec ECAL (single photon mode).

AMS02 est solidaire de la station spatiale et il est impossible de pointer l'instrument sur une source. AMS02 est équipé d'une caméra de positionnement stellaire. Il s'agit d'un système de caméras CCD qui observe les étoiles les plus brillantes et compare l'image obtenue du ciel à une carte de référence.

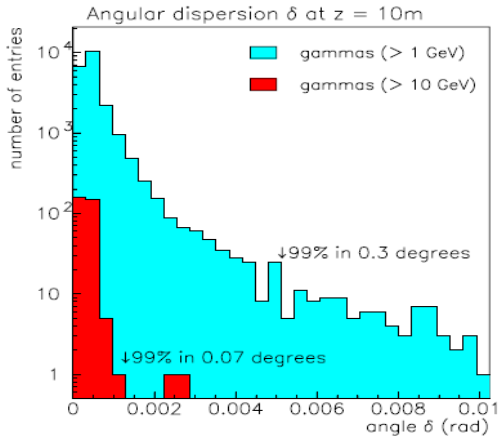

Figure 1.5: Résultats de la simulation de Monte Carlo GEANT de la distribution angulaire relative entre les gammas secondaires et les protons cosmiques primaires qui les ont produites par des collisions avec les structures de panneaux solaires. L'interpolation de direction de vol des gammas jusqu'au point d'impact sur les panneaux permet d'exclure ce source de fond supplémentaire [24].

Cela permet de situer le système de référence du détecteur avec une précision de 3 secondes d'arc. Connaître la position d'AMS est aussi importante pour d'autres considérations :

Les particules secondaires produites par interaction de rayons cosmiques avec la structure voisine de l'ISS pourraient représenter une source supplémentaire de fond dont il faudra tenir compte. A cette effet la NASA met a disposition de la collaboration AMS les projections dans le champ de vue du spectromètre des ombres optiques dans leur forme, taille et évolution temporelle des panneaux solaires de la station (le structures les plus grandes et les sources d'interférence les plus critiques possible). Cela a déclenché l'importance d'une étude préliminaire de simulation Monte Carlo avec le logiciel GEANT pour l'étude des effets d'interaction du rayonnement avec la matière [24].
La production de photons secondaires (E> 10 GeV) par collision de rayons cosmiques avec les panneaux solaires est contenue totalement dans un angle maximum de 0.07 degré avec la direction de vol du primaire. L'interpolation de direction de vol des gammas jusqu'au point d'impact sur les panneaux permet d'exclure cette source de fond supplémentaire sans affecter l'efficacité de reconstruction et la rejection du fond sauf pour la correction du facteur géométrique qui s'imposerait à travers l'exclusion des zones critiques coïncidents avec les ombres des panneaux solaires (fig. 1.8). Si cela est possible grâce aux performances exceptionnelles du trajectographe en termes de résolution directionnelle.

Résolution énergétique et résolution angulaire

Les photons détectés par le trajectographe pourront compter sur une grande qualité de reconstruction cinématique grâce au SiTracker, et ceci est un aspect critique pour les objectives scientifiques de l'astronomie gamma. La résolution angulaire est l'aspect clef pour l'astronomie gamma avec le spectromètre AMS02 et permettra d'obtenir une précision de mesure directionnelle de l'ordre de les 10^{-2} degrés dans la plage d'énergie de plus grande sensibilité (10 GeV- 1 TeV) (fig. 1.6).

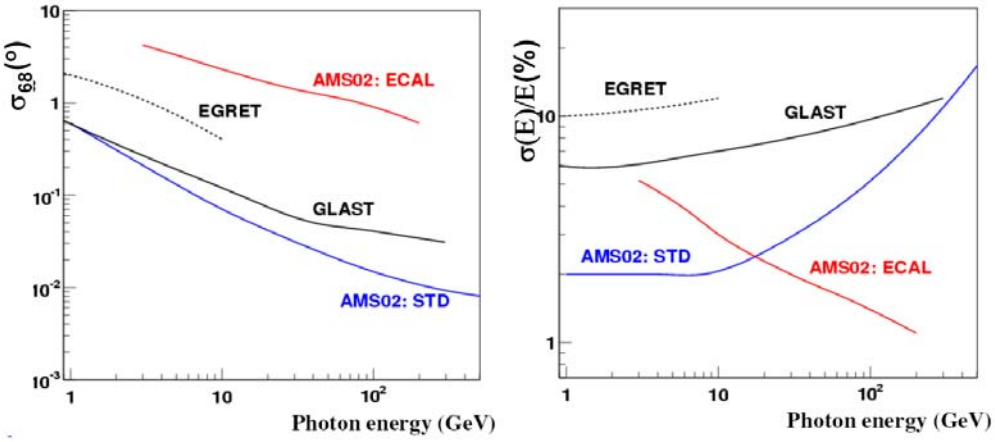

Figure 1.6: La figure de droite montre la résolution énergétique en fonction de l'énergie de gamma, la figure de gauche la résolution angulaire (68%) en fonction de l'énergie des photons. Les résolutions du trajectographe (STD) sont présentées ensemble avec celles obtenues avec ECAL.

En termes de résolution énergétique, grâce à la reconstruction optimale de la rigidité de particules le SiTracker permettra de mesurer l'énergie de photon jusqu'à 0.6-0.7 TeV avec que 30-40% environ d'incertitude. Ceci dit, dans les études de simulation utilisée pour la courbe en figure 1.6 la résolution est calculée à partir de la largeur gaussienne du pic des distributions des différences entre énergie reconstruite et énergie vraie. En effet à cause du rayonnement de freinage de la paire e+e-, une fraction entre 10 et 30 % des événements photons ont une énergie reconstruite considérablement plus bas que

cela attendu (> 5 σ) [17]. Néanmoins une correction pour cet effet physique est envisageable a posteriori.
Au contraire ECAL fait de sa résolution en énergie la figure de mérite la plus importante (fig. 1.6) : e.g. la mesure du fond diffus extra-Galactique par AMS02 pourra s'étendre jusqu'au domaine du TeV. C'est là un résultat très important car aucun autre instrument ne permettra de faire cette mesure. En particulier, le satellite FERMI sera limité à 300 GeV par sa masse de détection (8.5 X0), et les télescopes Tcherenkov au sol ont une ouverture angulaire limitée qui ne permettra pas de mesurer le fond diffus en dehors du plan Galactique.
AMS02 dispose aussi pour cela d'une horloge GPS, offrant une précision meilleure que la microseconde sur le temps absolu. Cela permettra une meilleure sensibilité du détecteur à certains phénomènes astrophysiques qui sont très variables dans le temps (sursauts, pulsars, supernovae).
La détermination de la sensitivité de AMS02 à la localisation et détection de photon en provenance d'une source ponctuelle dépendra du niveau minimal de détection requise en terme de signifiance *S*: le rapport entre nombre de photon signal et la racine carrée du nombre de photons de fond, les deux intégré à partir d'une certaine énergie de seuil E_t [20][25]. Généralement l'hypothèse d'un spectre différentiel de la source $dN/dE = N_0 E^{-\alpha}\ GeV\ cm^{-2}\ s^{-1}$ est assumé pour le signal alors que pour le fond le spectre différentiel du fond diffus gamma *dB/dE* est pris en compte. La valeur de la signifiance attendue dépendra de la formule suivante

$$S(>E_t) \cong \frac{N(>E_t)}{\sqrt{B(>E_t)}} \cong \frac{\int_{E_t}^{\infty} \frac{dN}{dE} A(E) t dE}{\sqrt{\int_{E_t}^{\infty} \frac{dB}{dE} A(E) \Omega(E) t dE}}$$

De la surface efficace *A(E)* et sa dépendance de l'angle de vue θ; de la résolution angulaire en terme d'angle solide $\Omega(E) = \pi\sigma^2_{68}(E)$; du temps d'observation qui dépendra des cartes d'exposition du ciel (AMS02 est solidaire de la station spatiale et il ne peut pas pointer sur une source). La figure 1.7 nous permet d'estimer la comparaison de la sensibilité d'AMS avec celles de son prédécesseur EGRET et de l'expérience de référence GLAST-Fermi. Si dans un côté le facteur géométrique de AMS (un facteur 6 plus petit que Fermi) est la première limite a sa sensibilité, pour des sources plus brillantes, la résolution angulaire du SiTracker permettra un pouvoir de localisation de sources jusqu'aux valeurs inferieur à l'arc-min a plus haute énergie (>10 GeV).

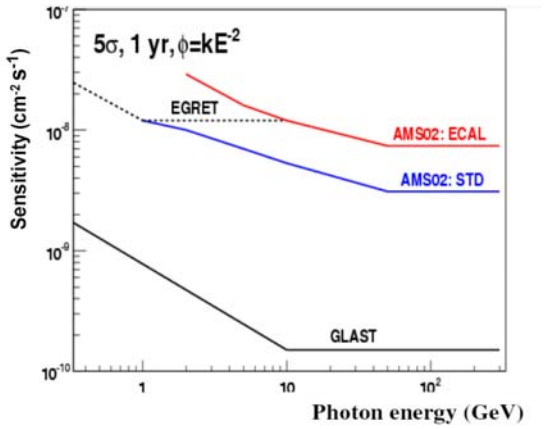

Figure 1.7: Sensibilité de AMS02 en mode conversion (STD) et ECAL (comparé aussi avec EGRET et GLAST),à la détection a 5σ de signifiance âpres 1 ans de fonctionnement et pour un spectre astrophysique de index α=2 [19].

I.3. La synchronisation des photo-détecteurs d'ANTARES

La collaboration ANTARES (*Astronomy with a Neutrino Telescope and Abyss environmental RESearch*) (fig. 1.8(A)) exploite un télescope à neutrinos déployé à 2500 m de profondeur dans la Mer Méditerranée, à environ 40 km au large de Toulon (42°50' latitude Nord, 6°10' longitude Est).

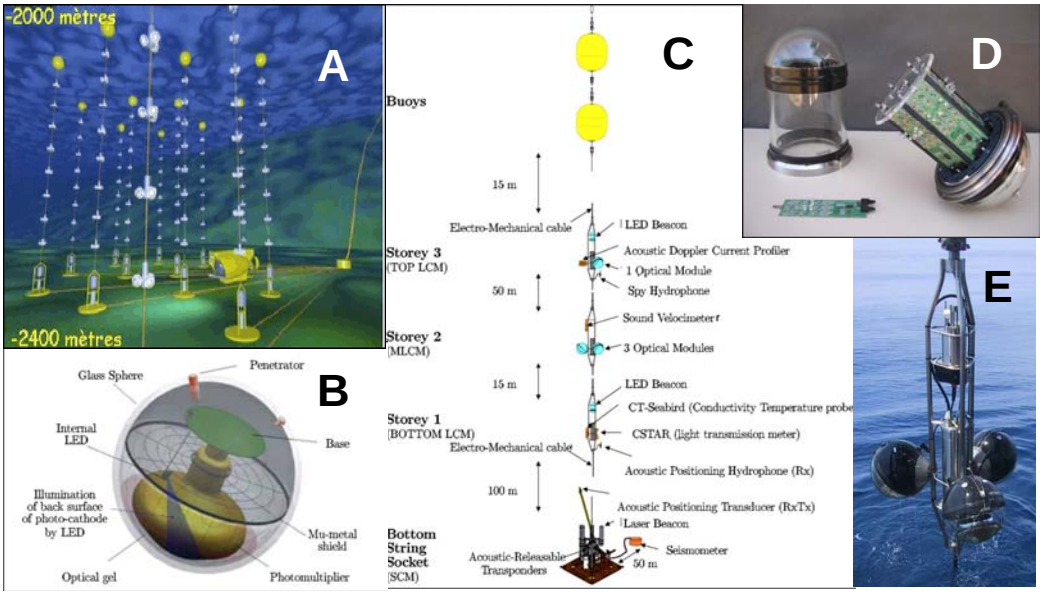

Figure 1.8: A) Vue artistique du télescope ANTARES. B) Schéma du module optique d'ANTARES [26]. C) Schéma de la MILOM [27]. D) Balise LED utilisée dans ANTARES pour l'étalonnage en temps du détecteur [29].E) Photo d'un étage lors de la ligne 1 pendant son déploiement.

La construction du détecteur [28] a été achevée le 30 mai 2008, après de nombreuses années de recherche et développement et d'immersion de prototypes.
La construction du détecteur a démarré en 2001, avec le déploiement d'un câble électro-optique entre le site ANTARES et une station à terre, située a la Seyne-sur-Mer. Un an après, une Boite de Jonction a été installée à son extrémité : cet élément est à la fois le centre de distribution de l'alimentation électrique et des commandes de fonctionnement (envoyées depuis la cote) au détecteur et le point de transmission des données depuis le détecteur vers la station de contrôle.
Entre 2003-2004 le concept du détecteur a été finalisé avec la construction, le déploiement, la connexion à la boîte de jonction et la mise en opération d' une ligne instrumentale prototype, la MILOM (Mini Instrumentation Line with Optical Modules) (fig. 1.8(C)). Enfin, la première des 12 lignes d'ANTARES a été construite, calibrée et déployée en 2005.
L'objective de l'expérience ANTARES est la détection des neutrinos cosmiques de haute énergie (> 1 TeV) comme messager astrophysique ; cela ouvre une nouvelle fenêtre d'observation sur l'Univers. Un télescope à neutrinos utilise la matière terrestre comme bouclier contre toutes les particules, sauf les neutrinos. La détection d'un muon qui monte représente la signature d'une interaction d'un ν dans le détecteur ou dans la matière en dessous. Il est essentiel que le détecteur soit enfoui à grande profondeur pour réduire le flux de muons descendants (beaucoup plus intense que celui des montants) produits par les gerbes de rayons cosmiques dans l'atmosphère.
La lumière Tcherenkov produite par les particules chargées (e.g. les muons), issues de la première interaction d'un neutrino astrophysique avec la terre, est captée par des photomultiplicateurs repartis régulièrement dans un grand volume d'eau. Ces photomultiplicateurs, de diamètre de 37 cm (fig. 1.8(B)), se situent dans des sphères de verre résistant à de fortes pressions (modules optiques - OM)

fixées sur des lignes. Un gel optique assure le contact entre le photomultiplicateur et la sphère, tandis qu'une cage en mu-métal le protège du champ magnétique terrestre et assure une amplification correcte de la charge entre les dynodes. Chacune des 12 lignes d'ANTARES est constituée de 25 « étages » (fig. 1.8(E)), chacun équipé de un triplet de OM orientés vers le bas, a 45° par rapport a la verticale et de l'électronique associé, installé dans des containers en titane, les Local Control Module (LCM), pour un réseau de 900 OM en tout. L'acquisition de données est réalisée au niveau de chaque OM : la sortie analogique de l'anode de chaque photomultiplicateur est lue par deux circuits intégrés, Analogue Ring Sampler (ARS) qui échantillonnent le signal du photomultiplicateur si celui-ci déclenche un trigger : lorsque la tension satisfait a la condition de seuil du trigger L0 (0.3 photoélectron) pendant le temps d'intégration du signal soit 25 ns, le discriminateur de forme compare la forme de l'impulsion en entrée a un gabarit et réalise une intégration de charge qui est directement liée au nombre de photoélectrons incidents : l'ARS fonctionne en mode Single Photo Electron (SPE) [30]. Si cette charge excède un seuil en amplitude le mode *WaveForm* est déclenché. Le signal numérisé est alors envoyé au circuit d'acquisition (DAQ Board). Il y a cinq LCM par secteur, qui contiennent les cartes électroniques de traitement des signaux des OM, de lectures de l'instrument, de la transmission de données, de l'alimentation et pour finir celles du système de positionnement acoustique. L'un d'entre eux, appelé Master LCM (MLCM), contient la carte Ethernet responsable du multiplexage de données de tous les étages. Certains étages sont équipés de hydrophone pour le positionnement acoustique ou par une LED *Optical Beacon* (fig. 1.8(D)) pour le calibrage en temps. L'espace typique séparant deux photomultiplicateurs d'une même ligne est de l'ordre d'une quinzaine de mètres alors que deux lignes sont éloignées de plusieurs dizaines de mètres.
Chaque ligne comporte une ancre nommée Bottom String Socket (BSS). Ce BSS permet, à partir d'un module d'alimentation note String Power Module (SPM) et d'un module de contrôle note String Control Module (SCM), respectivement de fournir l'alimentation et de contrôler les instruments situés sur cet étage c'est-à-dire pour toutes les lignes : le capteur de pression, l'émetteur-récepteur acoustique RxTx et pour les lignes qui en possèdent : le LASER *beacon*, utilisé pour la calibration en temps et qui sera décrit par la suite.
Les données numérisées sont ainsi collectées par des processeurs et envoyées à terre par l'intermédiaire d'un réseau Ethernet (1Gb/s) et d'un système de multiplexage en longueur d'onde qui sera décrit plus en détail par la suite : les lignes sont branchées individuellement à la boîte de jonction alors que cette dernière est connectée à la station de terre par 40 km de câble électro-optique contenant entre autres 48 fibres optiques.

La reconstruction de la trajectoire du muon peut être effectuée à partir des temps d'arrivée et des amplitudes des signaux. Ceci nécessite cependant une grande précision en temps, de l'ordre de la nanoseconde, et en position, de l'ordre de la dizaine de centimètres. Le program de contrôle et la campagne d'optimisation de procédures de calibration [31][32][33] des détecteurs d'ANTARES aussi bien que des sous-systèmes dédiées à l'acquisition et traitement de données ont représenté une phase intense des travaux qui ont abouti au déploiement et au fonctionnement de la MILOM [34] et de la première ligne de détection [35].

I.3.1. Expériences avec la MILOM et la Ligne 1

La MILOM a été un élément clé pour la validation du concept du détecteur. Elle contenait un étage de trois photodétecteurs et les cartes électroniques définitives. Elle était également équipée de balises LED capables d'illuminer le détecteur durant des temps de l'ordre de la nanoseconde, pour vérifier la réponse de l'électronique. La MILOM était donc principalement destinée à mesurer en continu les paramètres de l'environnement marin et la résolution en temps du système électronique.

Distribution du signal d'horloge

La capacité de pointer une source astrophysique est liée à la précision avec laquelle le temps d'arrivée, la position et la charge des photons peuvent être mesurés.

Le traitement de l'information temporelle de signaux de photomultiplicateurs passe avant tout à travers l'application d' un système horloge :

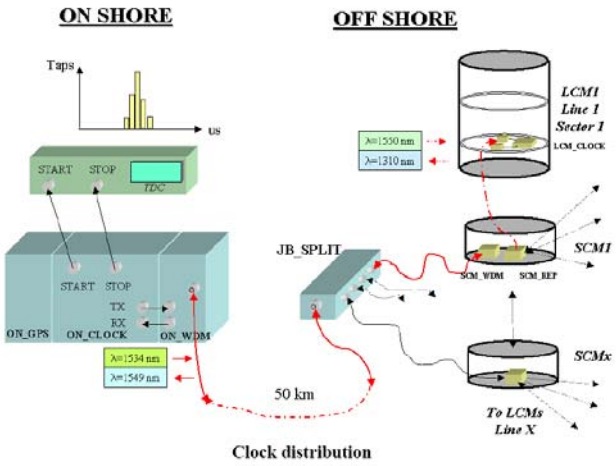

Figure 1.10: Système de distribution du signal horloge.

La génération du signal d'horloge (fig.1.10) de référence est faite à terre grâce à un système dédié qui synchronise une horloge maitresse contrôlée par un ordinateur, dont la fréquence est de 20 MHz, avec un signal de temps GPS dont la précision est de 100 ns. Le signal électrique d'horloge est converti en signal optique et envoyé, via fibre optique, à la Boite de Jonction (BJ). Cette dernière utilise un système de transmission optique bidirectionnelle (à double longueurs d'ondes : e.g. 1534 nm vers la BJ et 1549 nm de retour vers la terre). La BJ est en charge de la multiplication du signal et de la distribution à toutes les lignes. C'est au niveau du SCM de chaque ligne que la reconversion optique/électrique a lieu avant que l'information d'horloge soit adressée à tous les LCM. Les chemins optiques de retour (des LCM de la station à la terre) sont utilises pour mesurer le retard de propagation de l'information aux détecteurs.

La résolution en temps

Apres l'intégration et avant le déploiement d'une ligne, les dispositifs embarqués sont testés de différentes manières. Une fois dans l'eau les lignes sont calibrées régulièrement afin d'assurer le bon fonctionnement des dispositifs et leur stabilité. Pour la calibration en temps tout d'abord, les délais de distribution du signal d'horloge sont bien évidemment à prendre en considération dans l'analyse des données. Ainsi, une calibration des phases d'horloge, spécifiques à chaque LCM, associées à différents chemins optiques (par convention ils sont définis par rapport à la phase du SCM de la ligne 1, qui est considérée comme valeur 0 de référence), est réalisée régulièrement par la mesure de la différence de temps entre l'envoi du signal de calibration et sa réception (à corriger de l'aller-retour : $(T_{SCM->LCMi} + T_{LCMi->SCM})/2$).

Un élément de base du système électronique responsable de la résolution temporelle est constitué par le TVC, le convertisseur temps-tension qui donne un signal analogique proportionnel au temps de déclenchement de niveau 0 dans une période d'horloge. Le timestamp est fourni par une horloge locale de référence (carte clock du LCM) et est basé sur un compteur de périodes d'horloge. En effet, la

tension TVC fournie par un générateur de rampes TVC est proportionnelle au temps écoulé depuis le dernier signal de remise a zéro ou Reset Time Stamp (RTS) et ce, à partir du moment où le seuil de trigger L0 est franchi. La résolution temporelle maximale est alors de : 1/(20MHz x 256) = 0.2 ns avec 20 MHz la fréquence d'horloge, et 256 la gamme dynamique de la rampe TVC. En pratique la gamme s'étend de TVCmin à TVCmax, valeurs spécifiques de chaque ARS qui doivent être mesurées lors de la calibration à terre de façon à être prises en compte lors du décodage des TVC pendant les prises de données. La stabilité des ces mesures avant et après déploiement a déjà été démontrée à l'occasion de l'analyse de données de la MILOM.

La résolution en temps des OM ($\sigma_{OM.}$) est limitée inférieurement par les fluctuations du temps de transit de la charge dans les photomultiplicateurs, conventionnellement appelées TTS pour Transit Time Spread (σ_{TTS}). Les autres éléments de la chaine d'électroniques peuvent également induire des incertitudes sur la mesure du temps ($\sigma_{elec.}$), bien que leur contribution soit plus faible. La contribution due aux systématiques du banc de calibration ($\sigma_{syst\_calib.}$) est également à considérer :

$$\sigma_{OM} = \sqrt{\frac{(\sigma_{TTS}^2 + \sigma_{syst\_calib}^2)}{N_{pe}} + \sigma_{elec}^2}$$

L'ajustement de cette courbe aux valeurs mesurées de σ_{OM} en fonction de l'amplitude des signaux (e.g. N_{pe} , le nombre de photoélectrons), permet de mesurer les différentes contributions.
Les premiers étalonnages des composants des lignes sont effectués en laboratoire lors des phases finales de la construction, où un système d'éclairage utilisant un laser permet de mesurer les retards existant entre les différentes voies de détection [mie note] et en fonction de l'intensité de la lumière (N_{pe}). La figure 1.11 montre un exemple (celui des OM de la MILOM) des résultats de l'ajustement. Les fluctuations TTS conduisent à une indétermination d'environ 1,3 ns à une déviation standard ($\sqrt{\sigma_{TTS}^2 + \sigma_{syst\_calib}^2} \cong$ 1.5 ns) alors que l'incertitude déterminée par l'électronique est plus contenue $\sigma_{elec} \cong$ 0.4 ns. Au final la meilleure résolution en temps obtenue est de l'ordre de 0.4 ns (avec des signaux de grande amplitude). Ce résultat est en très bon accord avec les requêtes de la reconstruction (de l'ordre de la ns).

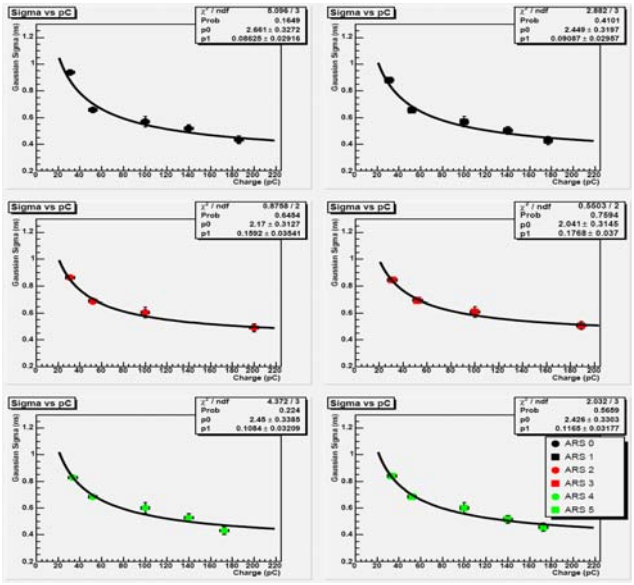

Figure 1.11 : Résolutions en temps en fonction de la charge (pC) des signaux. Les mesures sont relatives aux OM de la MILOM et concernent la campagne d'étalonnage dans la « Dark Room » avec le banc de tests équipé d'un laser avant le déploiement de la ligne.

Apres le déploiement, des mesures sont réalisées in situ, grâce à des balises LED installées sur chacune des lignes, à différentes altitudes, qui peuvent engendrer des impulsions lumineuses éclairant les photomultiplicateurs. L'une de ces balises est montrée dans la figure 1.8(D). Une balise LED éclairant à forte intensité un photomultiplicateur situé sur l'étage en dessus (14,5 m) permet de mesurer les effets induits par l'électronique de lecture et de traitement du signal : en effet, à cette distance les effets de propagation de la lumière dans l'eau sont négligeables, et l'intensité lumineuse reçue étant grande, la contribution de la TTS – qui décroit comme la racine carrée du nombre de photoélectrons – est constante. La figure 1.12 montre la distribution de différence entre les temps d'arrivée de signaux aux OM (T1) et le temps de référence (T0) de l'instant de l'impulsion de la balise LED (la balise est équipée d'un petit photomultiplicateur interne qui permet le monitorage des temps et des amplitudes des signaux émis et de fournir un temps 0 de référence). Les distributions sont centrées à 0 après soustraction des valeurs moyennes caractéristiques de chaque OM, qui avaient été mesurées au moment des étalonnages en laboratoire, et dont les valeurs ont été confirmées par des mesures en situ après déploiement (voir fig.1.13). Enfin les mesures relatives à chaque ARS du triplet de OM de la MILOM confirment la résolution en temps de l'ordre de 0,4 ns déjà mesurée en laboratoire.

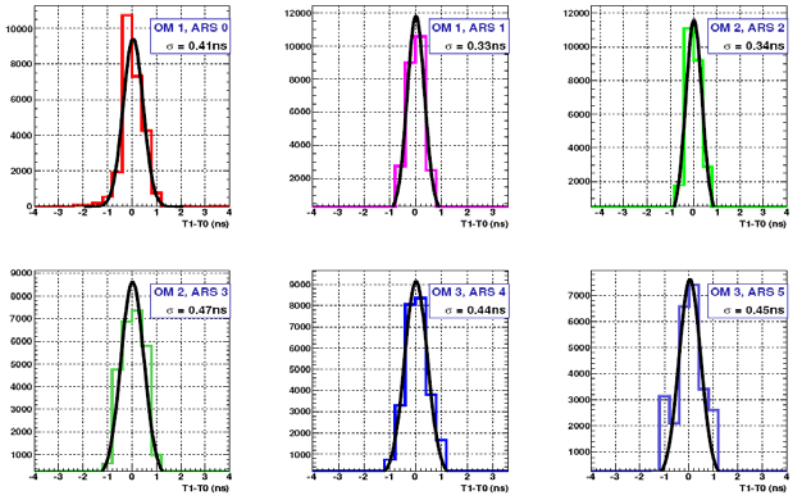

Figure 1.12 : Résolutions en temps pour chaque ARS des OM de la MILOM. Les mesures sont réalisées après déploiement en situ à travers la balise LED.

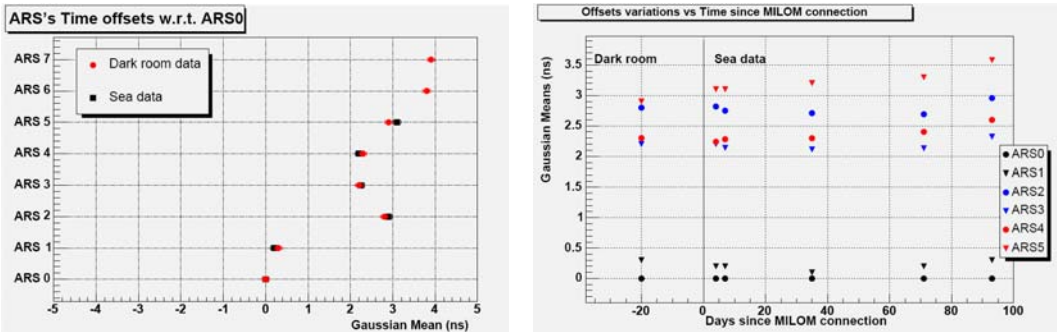

Figure 1.13 : Mesure de valeurs moyennes (figure à gauche) du décalage en temps de la réponse de chaque ARS. Les mesures en « Dark Room » sont confirmées par les mesures dans l'eau après déploiement de la ligne MILOM. La stabilité de ces valeurs avec le temps est aussi confirmée (figure à droite).

En conclusion, les données de la MILOM ont validé les performances des photodétecteurs et des cartes électroniques. Plus de détails sont fournis dans l'Annexe A.
La validation de la résolution en temps à travers les mesures de calibration permet aussi de confirmer les plus importantes figures de mérite attendues et estimées à travers le programme de simulation et de reconstruction d'ANTARES : la résolution angulaire et la superficie efficace équivalente du détecteur (voir figure 1.14).

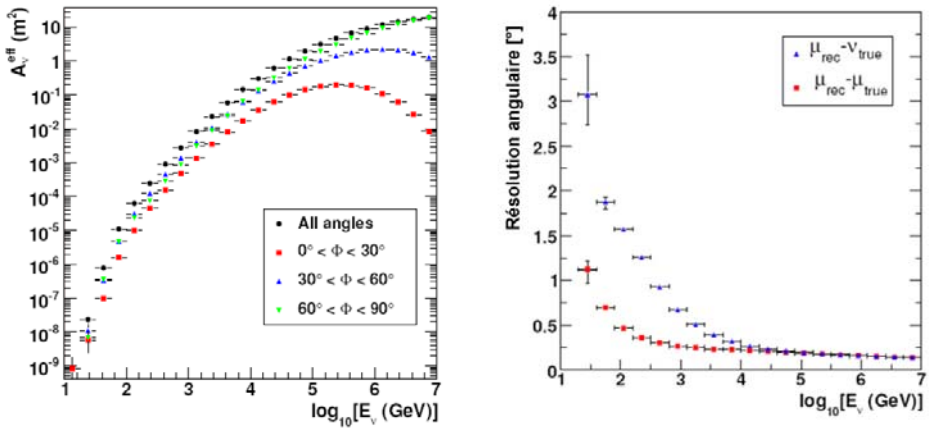

Figure 1.14 : Droite) Surface effective en fonction de l'énergie, calculée pour des neutrinos incidents sous plusieurs intervalles d'angle zénithal. La diminution de surface (du détecteur à 12 lignes) au delà de 100 TeV dans la bande 0°-30° (0° correspond à un neutrino vertical) est un effet de l'opacité de la Terre aux événements les plus énergétiques. Gauche) Distribution de l'écart angulaire entre la trace reconstruite et la vraie direction du muon (en rouge) ou du neutrino (en bleu) .

Peu après la fin des opérations de la MILOM en décembre 2005, la première ligne complète du télescope ANTARES a pu être déployée, après une campagne d'étalonnage identique à celle appliquée à la MILOM, et la prise de données a débutée. Depuis 2008, ANTARES est en prise de données dans sa configuration finale (avec 12 lignes).
Les données de la ligne 1 ont démontré l'importance de la résolution en temps des détecteurs. Dans l'approximation d'une ligne parfaitement verticale qui place tous les modules optiques sur un axe z coïncident avec la ligne, une symétrie de révolution autour de z ne permet pas de mesurer l'angle azimutal ; le temps d'arrivée t_j d'un photon sur un photomultiplicateur placé à l'altitude z_i peut s'exprimer comme :

$$c(t_j - t_d) = (z_j - z_d)\cos\theta + \sqrt{n^2 + 1}\sqrt{d^2 + (z_j - z_d)^2 \sin^2\theta}$$

Où θ est la direction de vol du muon par rapport à l'axe z, t_d et z_d représentent le temps et l'altitude de passage de la trace au point d'approche minimal à la ligne (point définissant la distance d entre la ligne et la trace). L'intensité des muons atmosphériques verticaux reconstruits en ajustant cette équation a été mesurée en fonction de la profondeur. Le flux de muons atmosphériques détectés par ANTARES est en accord avec les résultats d'autres expériences. Dans cette analyse les déplacements aléatoires de la ligne dans l'eau ne sont pas pris en compte. Cela ne permet pas de vérifier le poids de la précision de positionnement du détecteur sur les résultats, néanmoins les incertitudes systématiques correspondantes sont bien prises en compte. Cette mesure a donc permis de démontrer que ce premier segment du détecteur fonctionne correctement, que le bruit du fond optique est bien maitrisé dans la détection des muons, et que la résolution en temps des détecteurs a bien conduit à la précision de reconstruction de traces espérée.

I.4. Les télescopes Tcherenkov au sol

Les flux de γ d''une énergie supérieure à quelques centaines de GeV, qui est la limite supérieure de la fenêtre de sensibilité d'expériences spatiales comme AMS02 (dont les détails ont été présentés dans le paragraphe I.2.1.), sont insuffisants pour être détectés par satellite: les surfaces de collection de quelques mètres carrés qui les caractérisent sont trop faibles.
Une approche expérimentale alternative est la technique de l'imagerie Tcherenkov au sol: une méthode de détection indirecte des γ reposant sur la collection du rayonnement Tcherenkov émis par les gerbes de particules, initiées par les photons incidents et qui se développent dans l'atmosphère. Lors de leur propagation, les particules chargées qui composent la gerbe subissent des diffusions multiples sur les champs coulombiens des noyaux de l'atmosphère, et leur trajectoire est courbée sous l'effet du champ magnétique terrestre. Ces deux effets sont à l'origine du développement latéral des gerbes. Les gerbes électromagnétiques initiées par des gammas entre 100 GeV et 1 TeV atteignent leur maximum de développement à une altitude d'une dizaine de kilomètres. Leur longueur atteint quelques kilomètres pour une extension latérale de quelques dizaines de mètres.
La technique d'imagerie consiste à former l'image de la gerbe de particules en lumière Tcherenkov dans le plan focal d'un grand miroir où l'on place une caméra constituée de plusieurs centaines de photomultiplicateurs. L'analyse des images obtenues permet d'estimer la direction et l'énergie du gamma primaire. Les surfaces efficaces typiques de ces instruments sont de quelques 10^4 m^2, surface de la tâche de lumière Tcherenkov au sol, pour des surfaces de collection des miroirs de l'ordre de 100m2 : seule une fraction de la tâche Tcherenkov au sol est donc collectée par l'imageur. La taille du miroir est liée au seuil en énergie : les gerbes initiées par des γ de plus basses énergies étant moins lumineuses, il est nécessaire de collecter une fraction de lumière plus importante pour les détecter.
H.E.S.S. (High Energy Stereoscopic System) est le premier système de détection d'image Tcherenkov multi-télescopes, sensible à la détection de gammas d'une énergie comprise entre 100 GeV et 100 TeV. L'expérience H.E.S.S. est située en Namibie, à une centaine de kilomètres au sud-ouest de la capitale Windhoek, à une altitude de 1 800 m. Les quatre télescopes de la première phase de H.E.S.S. sont équipés d'un réflecteur d'environ 108 m^2 de superficie à une distance focale de 15 m. Ils sont placés aux sommets d'un carré de 120 m de côté, orienté selon les axes cardinaux. Cet espacement est un compromis entre la nécessité que les photons Tcherenkov issus d'une cascade électromagnétique atteignent plusieurs télescopes et le fait que la vision stéréoscopique est meilleure lorsque la distance entre deux télescopes est plus grande. Il optimise ainsi la surface effective de déclenchement du système d'imageurs.

Figure 1.15 : Photographie du site de H.E.S.S. avec les quatre télescopes.

Les observations multi-télescopes améliorent la précision quant à la position de la source, mais surtout réduisent le déclenchement du aux muons. La réjection du bruit de fond hadronique est aussi améliorée par l'analyse de plusieurs images des cascades. Les images des cascades électromagnétiques

sont caractérisées par une forme allongée avec un axe principal bien défini, alors que les cascades hadroniques peuvent donner des formes diverses, souvent morcelées.

I.4.1. Le développement des méthodes d'analyse de données HESS

La méthode d'analyse la plus simple, dite *standard,* repose sur le calcul de moments géométriques des images des gerbes, projetés sur les caméras, en supposant que l'image est elliptique avec une distribution gaussienne de l'intensité le long des deux axes. Cette méthode a été développée par A.M. Hillas en 1985 [36]. Les différents paramètres calculés sont schématisés dans la figure 1.16 :

- le barycentre de l'image,
- l'écart-type de l'image selon le grand et petit axes de l'image *l* et *w* (*length* et *width*),
- l'amplitude totale de l'image,
- la distance nominale *d* du barycentre de l'image à la position théorique de la source dans le plan focal,
- l'angle α formé par le grand axe de l'ellipse et l'axe reliant le barycentre de l'image à la position de la source dans le plan focal. Il est surtout utilisé en mode mono-télescope,
- l'angle azimuthal φ de l'axe principal de l'image

Les distributions de ces paramètres pour des images de gerbes électromagnétiques et hadroniques sont différentes. Il est donc possible d'effectuer des coupures sur ces paramètres pour rejeter les images hadroniques.

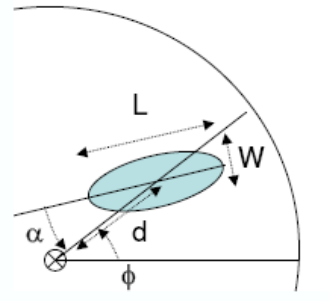

L'analyse standard H.E.S.S. utilise les moments réduits renormalisés. La valeur obtenue pour le *lenght* et *width* de l'image sont renormalisés par la valeur moyenne obtenue par le simulation de Monte Carlo d'un événement gamma de même paramètre d'impact reconstruit (p) et de même amplitude (q), et divisé par les écarts types attendues (σ_l et σ_w) :

$$SW = \frac{w(q,\rho) - \langle w(q,\rho)\rangle}{\sigma_w(q,\rho)} \qquad SL = \frac{l(q,\rho) - \langle l(q,\rho)\rangle}{\sigma_l(q,\rho)}$$

Les variables issues des différentes images obtenues en stéréoscopie sont combinées en deux variables moyennes, *Mean Scaled Width (MSW)* et *Mean Scaled Length (MSL)* :

$$MSW = \frac{\sum_{tels} SW}{\sqrt{ntels}} \qquad MSL = \frac{\sum_{tels} SL}{\sqrt{ntels}}$$

Les distributions de ces variables sont nettement différentes selon la nature des particules. La distribution est centrée pour les rayons γ est très asymétrique pour les hadrons. Une coupure sur ces variables permet de rejeter une grande partie des hadrons tout en conservant une majorité des rayons γ. Deux nouvelles méthodes de reconstruction ont ete introduites plus récemment.

La méthode semi-analytique qui repose sur la comparaison pixel par pixel de l'image de la gerbe, a un gabarit obtenu par un modèle semi-analytique. Un maximum de vraisemblance est obtenu sur l'ensemble des pixels disponibles.
La méthode 3D est une forme de généralisation tridimensionnelle de la méthode Hillas. Cette méthode s'appuie sur l'hypothèse de symétrie de révolution d'une gerbe de rayon γ, modélisée comme une Gaussienne tridimensionnelle. L'observation stéréoscopique (de H.E.S.S.) des gerbes permet d'avoir accès aux paramètres tridimensionnels de la gerbe. La procédure utilisée est identique à celle employée par le modèle semi-analytique : la maximisation de vraisemblance d'un ajustement de simulations sur les images permet d'extraire les paramètres géométriques et physiques de la gerbe.

Analyse multi-variables

Les méthodes multi-variables basées sur l'application d'estimateurs de densité de probabilités (PDE) sont désormais importantes dans l'analyse de données de physique des particules. Le pouvoir de discrimination d'un signal de physique sur le fond à travers ces méthodes est fortement dépendant du niveau de connaissance du processus en examen et de l'instrument de mesure appliqué pour son étude (ainsi que la capacité de les reproduire à travers des méthodes de simulation de Monte Carlo). C'est pour cette motivation que ces méthodes sont plus efficaces quand elles sont introduites au moment où une expérience de physique et les méthodes de mesure qu'elle implique sont enfin bien maitrisées et consolidées. L'expérience H.E.S.S. grâce à la qualité et à la quantité des ces observations et découvertes, a montré la maturité de la discipline de la détection Tcherenkov aussi bien que la maitrise des toutes les systématiques de la mesure de rayon gamma au sol. De plus la possibilité de pouvoir appliquer trois différentes (et indépendantes) méthodes de reconstruction des gerbes atmosphériques, nous a conduit à l'introduction et à l'application d'une analyse multi-variables dans H.E.S.S..
Différentes alternatives de méthodes multi-variables PDE sont apparues au cours de ces dernières années et souvent elles sont comparées à d'autres méthodes multi-variables basées sur l'application de réseaux de neurones ou d'arbres de décision. L'imagerie Tcherenkov de très haute énergie n'a pas d'autre outil de calibrage des mesures que l'approche comparative entre data et Monte Carlo, et la nécessité de tenir sous contrôle la dépendance des variables de reconstruction des conditions de prises de données et des pointés des télescopes nous a amené à un choix analytique (plutôt que des méthodes computationnelles basées sur des processus d'apprentissage). La méthode multi-variables PDE introduite est la Xeff dépendant des fonctions de densité de probabilité des variables de discrimination des trois méthodes de reconstruction (Hillas, semi-analystique et 3D)[37][38].

$$X_{eff}(\{x_i\}) = \frac{\eta H(\{x_i\})}{(1-\eta)G(\{x_i\}) + \eta H(\{x_i\})}$$

Où le H et G sont les PDE pour les hadrons et le gamma respectivement, les x_i sont les variables de discrimination des quelles les PDE dépendent et enfin η est un estimateur de la contamination relative d'hadron dans le lot de données gamma à analyser

$$\eta = \frac{N_{Hadron}}{N_{Hadron} + N_{Gamma}}$$

L'approche Xeff permet d'avoir enfin un seul discriminateur (« hadroness ») pour la rejection du fond (fig. 1.16).
La méthode d'analyse est complétée par un estimateur combinatoire de paramètres physiques (e.g. direction et énergie) des trois reconstructions, qui permet d'optimiser la résolution angulaire et la résolution en énergie sur tout le domaine d'énergie de sensibilité de H.E.S.S..
Les détails du développement et de l'application de Xeff (ainsi que des exemples des résultats compétitifs obtenus) ont fait l'objet d'une publication [37] (voir Annexe A) et sont davantage illustrés dans la Thèses de Florent Dubois [38].

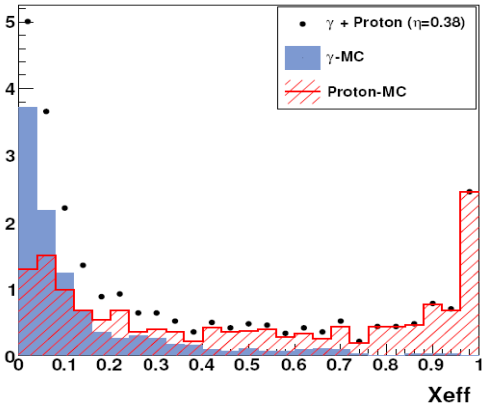

Figure 1.16 : Exemple de distribution de la variable combinée Xeff pour des échantillons MC de proton, gamma et des deux confondus selon une contamination η=0.38.

En bref nous proposons ci dessous comme exemples : la comparaison du facteur de qualité Xeff avec le facteur de qualité obtenu avec une méthode standard Hillas (fig.1.17); les résolutions angulaires et énergétiques de Xeff comparées à celles obtenues avec les trois reconstructions séparément (fig.1.18); et enfin l'exemple d'amélioration de résolution angulaire (en θ^2) pour (le «flare» de) la source AGN PKS 2155-304 (fig.1.19).

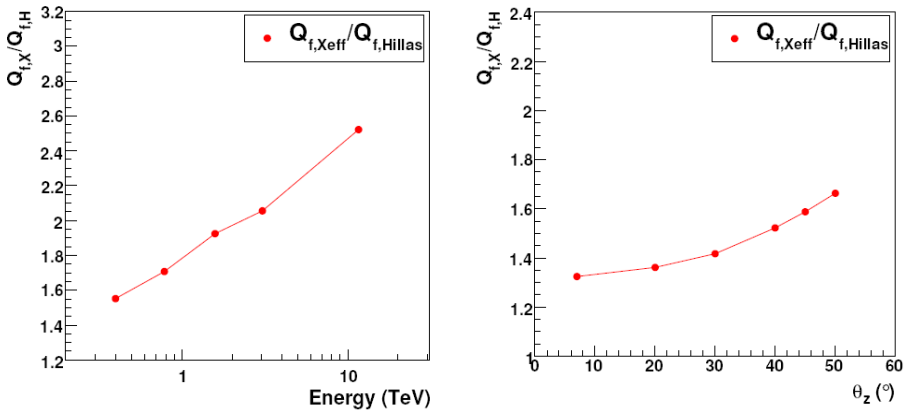

Figure 1.17 : Rapport entre facteur de qualité Xeff et le facteur de qualité Hillas-standard en fonction de l'énergie et en fonction de l'angle de zénith des observations des gamma.

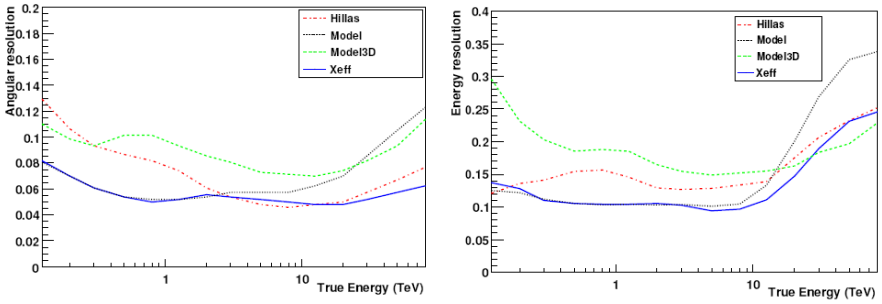

Figure 1.18 : Résolution angulaire et résolution énergétique combinées et appliquées dans la méthode Xeff (en blue) et aussi comparées aux performances des trois reconstructions séparément.

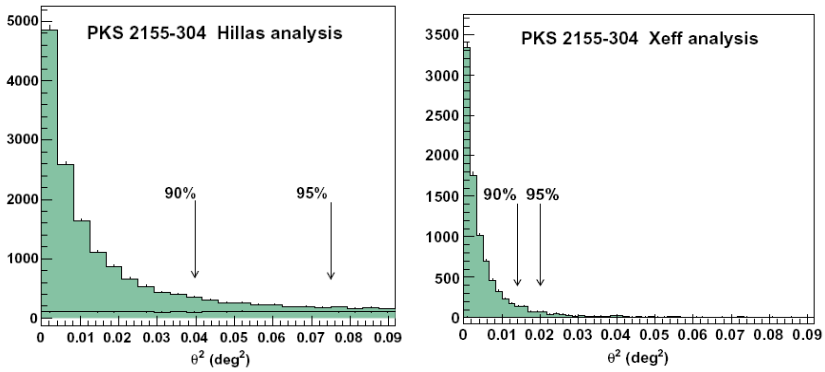

Figure 1.19 : Distribution angulaire en θ^2 des données ON et OFF pour PKS2155-304 avec la reconstruction standard Hillas et avec Xeff.

II. NATURE ET ORIGINE DU RAYONNEMENT COSMIQUE DE HAUTE ENERGIE

II.1. Introduction

La physique des Astroparticules est la discipline du point de rencontre de l'infiniment grand et de l'infiniment petit, ou chercheurs issus de l'astrophysique et de la physique des particules, ont la possibilité d'explorer ensemble l'Univers pour mieux s'interroger sur les questions de physique, de cosmologie et d'astrophysique. Plus particulièrement l'astrophysique à haute énergie, qui a pour objet l'étude des sources extrêmes, celles où se produisent les plus grands transferts d'énergie, est le domaine où l'on examine le rayonnement cosmique plus énergétique en qualité de messagers privilégiés pour mieux comprendre l'histoire et les origines de l'Univers. Cette thématique connaît désormais un développement spectaculaire avec la mise en service d'observatoires spatiaux opérants dans les domaines des rayons X et gamma. L'émergence de l'astronomie gamma à très haute énergie menée à partir du sol encourage l'astronomie des neutrinos de haute énergie et renforce l'intérêt porté à la détection du rayonnement cosmique d'énergie extrême.
Mon parcours de recherche est marqué par des contributions aux études de perspectives, aux analyses de données et aussi à des études phénoménologiques sur des sujets qui sont aussi les principaux objectives scientifiques des expériences dans lesquelles j'ai eu la chance de m'impliquer : AMS, ANTARES, HESS, CTA et POLAR.
Toutes mes contributions sont le résultat d'une activité de recherche cohérente avec deux principaux intérêts scientifiques en physique des astroparticules:

- L'étude du rayonnement de haute énergie pour dévoiler la vraie nature de la matière noire.

- L'étude de l'origine du rayonnement cosmique Galactique pour l'investigation de phénomènes les plus violents de l'Univers.

J'ai tout d'abord approfondi les études des rayons gamma des énergies > GeV a travers la détection spatiale de l'émission de haute énergie de la part de Pulsars et l'effet d'absorption du rayonnement extragalactique provenant des Noyaux Actifs des Galaxies. La recherche indirecte de matière sombre a motivé mes études de perspectives avec AMS et ANTARES sur la possibilité de détection d'un signal d'annihilation de WIMPs (*Weakly Interacting Massive Particles*, composantes possible de la matière sombre) en gamma, neutrino et antimatière (positrons, antiprotons et anti-deutérons). Les mesures spectrales de H.E.S.S. du flux en provenance du centre galactique sont en accord avec une loi de puissance et ne sont pas compatibles avec un signal indirect de matière noire. Les observations actuelles ont aussi démontré l'importance de la compréhension des accélérateurs astrophysiques conventionnels pour mieux étudier le fond diffus galactique et le signal potentiel de matière noire venant du centre galactique. Ces considérations confirment la cohérence des mes implications dans l'analyse de données H.E.S.S. dans les études d'astronomie gamma du TeV a travers l'investigation de certaines sources Galactiques étendues (*SNR – Supernova Remnants et PWN – Pulsar Wind Nebulae*) en étudiant la morphologie et la corrélation spatiale avec d'autres longueurs d'ondes pour tester la dépendance entre densité de champ magnétique et densité de masse. Ces études sont critiques pour contraindre les modèles d'origine du rayonnement gamma dans les deux scénarios possibles: léptonique ou hadronique.
Pour finir, plus récemment, je me suis rapproché davantage de la communauté des astrophysiciens pour partager avec eux des études de réflexion sur l'exploration de phénomènes en jeux dans le Sursaut Gammas et la possibilité d'en percer le secret à travers l'investigation (avec POLAR) de la polarisation du rayonnement X dur émis par ces derniers.

Dans ce chapitre je proposerai l'exposition d'une série choisie de contributions aux études du rayonnement cosmique d'haute énergie en physique des Astroparticules.
L'annexe B présente les travaux personnels concernés par ce chapitre: notamment les perspectives de détection indirecte de matière noire à travers le photon d'énergie du GeV avec AMS [25] et puis une revue (sur invitation) sur l'état de la détection indirecte de la matière noire [39]. Une revue (sur invitation) sur les prospectives de physique des astroparticules avec AMS [40]. Une contribution a une conférence internationales sur l'étude de l'origine de gamma du TeV dans la Galaxie avec H.E.S.S. [41].

II.2. Recherche indirect de matière noire

L'objectif de l'étude de notre Univers en cosmologie est de combiner les mesures observables cosmologiques pour déterminer le jeu de paramètres qui en définit le contenu. Dans le modèle cosmologique standard, l'équation d'état de la constante cosmologique définit les différentes contributions de densité au contenu de l'Univers : $\Omega_{tot} = \Omega_m + \Omega_r + \Omega_\Lambda$.

Parmi les différentes contributions apportées aux densités (Ω_m = densité de matière ; Ω_r = densité de photons et neutrinos ; Ω_Λ = densité de l'énergie du vide) dans l'équation standard cosmologique il est admis que la densité de matière soit la somme des densités de matière baryonique et non-baryonique.
La matière baryonique, les étoiles et ce qui nous constitue, ne représente qu'une faible fraction du contenu en énergie de l'Univers, dont la nécessité d'introduire un type de matière non baryonique non relativiste (dite froide) et non couplée aux photons, nommée matière noire froide (Cold Dark Matter): $\Omega_m = \Omega_b + \Omega_{CDM}$. Le paradigme actuel, issue de la compilation et la mise en commun de tous les résultats expérimentaux, est en faveur actuellement d'un Univers ΛCDM dominé par une constante cosmologique (ou de l'énergie noire) à environ 70% et de la matière noire non baryonique à un niveau de l'ordre de 30%.

L'histoire thermique de notre Univers prévoit qu'il se refroidi à mesure qu'il se dilate, les espèces en présence s'y diluent et les réactions en jeu évoluent. Partant d'un équilibre thermodynamique et faisant baisser la température, les réactions responsables de l'établissement de l'équilibre ralentissent et finissent par s'arrêter. Cet instant pour lequel une espèce s'éloigne de l'équilibre thermique est son découplage (après une espèce stable est dite gelée parce que son taux d'interaction est inferieur au taux d'expansion de l'Univers). Pendant la suite de l'histoire de l'Univers, sa densité co-mobile reste constante et son énergie diminue du fait de l'expansion. Un candidat à la matière noire pourrait être une nouvelle particule stable qui est présente dans le bain primordial. À mesure que l'Univers s'étend, cette particule ne trouve plus de partenaire pour s'annihiler et subit un gel chimique. La densité co-mobile de ces particules reste alors constante et elle peuple l'Univers comme des reliques de cette période jusqu'à nos jours.

Les modèles de matière noire sont contraints en calculant la densité co-mobile de matière noire qu'ils impliquent. Cette valeur est obtenue en multipliant la densité par h^2, e.g. $0.115 < \Omega_{CDM}\, h^2 < 0.120$.

Pour être un bon candidat à la matière noire, une particule doit présenter quelques propriétés évidentes, elle doit en particulier être massive, stable, neutre et non colorée (interagissant faiblement). Elle doit être une WIMP (χ) qui s'annihile avec son antiparticule pour donner des paires particules-antiparticules. En dehors des neutrinos, dont la contribution à la densité critique est très faible ($\Omega_\nu h^2 < 0.0067$), le Model Standard de la Physique de Particules ne fournit pas de candidat a la matière noire qui présenterait les propriétés des WIMPs χ [42].

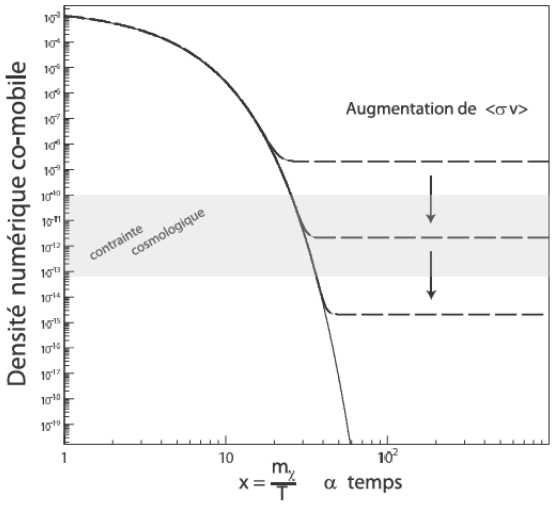

Figure 2.1 : Densité co-mobile de WIMPs en fonction du temps. Les lignes en tiret correspondent aux possibles valeurs d'abondances reliques.

La figure 2.1 montre l'évolution de la densité co-mobile et le gel des WIMPs (qui a lieu à T~m_χ/20). La section efficace d'annihilation, de l'ordre de grandeur (typique des interactions faibles) est $\sigma v \sim 10^{-26}\ cm^3\ s^{-1}$, a un effet sur la variation de la valeur de l'abondance relique à laquelle des contraintes cosmologiques pourraient être aussi appliquées [43]. Les sections efficaces d'annihilation de l'ordre de celles des processus électrofaibles conduisent naturellement à la densité de matière noire actuellement mesurée ($\Omega_\chi h^2 \sim 0.1$). Après le gel des particules de matière noire, les annihilations deviennent extrêmement rares car leur densité par unité de volume co-mobile devient très faible. Longtemps après cette période, la formation des structures dans l'Univers et les puits de potentiels gravitationnels associés permettent aux particules de matière noire d'atteindre, à nouveau, de grandes densités. Les annihilations reprennent alors dans toutes les zones de l'Univers où règne une densité ρ de WIMPs suffisamment grande. La recherche indirecte de matière noire se fait à travers la mesure et l'identification du rayonnement cosmique de nature exotique produit de ces nouvelles annihilations de WIMPS aux échelles galactiques et subgalactiques. Des indices de la présence de matière noire à ces échelles viennent de différentes études:

– La modulation de l'effet de lentilles gravitationnelles autour des galaxies elliptiques, qui montre l'existence de sous-structures d'échelles ~ 10^6 mass solaires.
– L'effet de lentille faible des galaxies distantes par les structures d'avant plan.
– La dispersion de vitesse des galaxies sphéroïdes naines, dont le rapport masse sur luminosité tendent à montrer que la densité de masse y est plus élevée que localement.
– La dispersion de vitesse des satellites de galaxies spirales de la même manière.

Pour faire une prédiction de flux exotique, il est nécessaire de connecter le taux d'annihilation Γ, qui compte le nombre de réactions par unité de volume et de temps, aux particules observées. Ce lien est aussi conditionné par le modèle de nouvelle physique assumée pour caractériser la nature de la WIMP à travers le choix de la section efficace $<\sigma v>$, la masse m_χ de la particule de matière noire et un facteur statistique δ_{stat} lié à sa nature (différent que les WIMPS soient particules de Majorana ou non). Par unité de volume et de temps, le nombre d'annihilations se compte alors comme le nombre de paires de particules qui peuvent être formées, dont l'abondance (la densité ρ) dépendra aussi des caractéristiques des zones de concentration de l'Univers ou nous dirigeons notre recherche de flux exotique.
Pour résumer le taux d'annihilation sera :

$$\Gamma(\vec{x}) = \frac{<\sigma v>}{m_{\chi}^{2}} \frac{\rho^{2}(\vec{x})}{2\delta_{stat}}$$

Dans le cadre conventionnelle de l'astrophysique du rayonnement cosmique, les rayons cosmiques sont de deux types :
– les primaires, pour lesquels il existe des sources, c'est le cas des protons (le plus abondants) et de 90% des électrons et des noyaux plus lourds,
– les secondaires, qui sont créés lors de l'interaction des rayons cosmiques primaires sur le milieu interstellaire. Dans le cadre de la physique conventionnelle, c'est le cas pour une faible fraction des protons, pour les antiprotons, les ions Li, Be, B, les photons, 10 % des électrons, les positons ainsi que les deutérons et antideutérons.
La mise en évidence d'une composante primaire en antiproton, antideuterons et positon pourrait être le signe de nouvelle physique, d'annihilations de matière noire en particulier. Les canaux d'antimatière seront privilégiés pour la recherche indirecte. Il est attendu que la production exotique de rayons cosmiques soit symétrique du point de vue matière/antimatière. Le signal recherché étant rare, le fond conventionnel est bien plus faible dans le cas de l'antimatière, il serait donc plus facile de séparer une composante primaire dans ce cas. Les perspectives de détection de ce signal indirect de matière noire font partie intégrantes des objectifs scientifiques d'AMS02, grâce à sa très haute capacité de discrimination matière/antimatière.

Étant donné la production localisée de particules produites dans la zone où les WIMPs sont concentrés et peuvent s'annihiler, la prédiction des flux de particules issues des processus d'annihilation et de physique standard qui s'en suivent ne se fait pas de la même façon selon que la particule recherchée est neutre ou chargée. En effet, les particules neutres (e.g. γ et ν) se propagent en ligne droite et le flux exotique observé depuis un détecteur sera la somme de toutes les sources présentes sur la ligne de visée. Au contraire, les particules chargées diffusent sur les hétérogénéités des champs magnétiques Galactiques et proviennent d'un volume plus ou moins grand autour de la Terre selon leur espèce. Ainsi, le flux exotique de particules chargées sera la solution d'une équation de diffusion qui tiendra compte de toutes les sources potentiellement présentes dans une sphère dont le rayon est de l'ordre du libre parcours moyen des particules recherchées.

II.2.1. Les messagères neutres : les rayons γ et les neutrinos

La contribution dit "halo" a la structure et masse des galaxies correspond à une masse pas visible et souvent appelée masse sombre que l'on doit ajouter pour expliquer la platitude typique des courbes de rotation observées des galaxies; ce qui indique la présence de masse sur des distances plus grandes que la taille du disque lumineux (dont le rayon est ~ 20 kpc). Le fait que la vitesse de rotation soit quasiment constante implique l'existence d'un halo massif avec une masse M(r)

$$M(r) \;=\; 4\pi \int \rho(r)\, r^2\, dr \quad ,$$

proportionnelle au rayon r de la galaxie et donc un profil en $\rho(r)$ proportionnel a $1/r^2$, ce jusqu'à un rayon d'environ 200 kpc, pour une masse totale de l'ordre de 10^{12} masses solaires.

L'étude de la dynamique des étoiles dans notre propre Galaxie laisse une dégénérescence dans les paramètres permettant de décrire le profil radial de son halo de matière noire. Celui-ci peut être paramétré par la relation

$$\rho(r) = \rho_{\odot} \left[\frac{r_{\odot}}{r}\right]^{\gamma} \left[\frac{1+(r_{\odot}/a)^{\alpha}}{1+(r/a)^{\alpha}}\right]^{\frac{\beta-\gamma}{\alpha}}$$

où

$r_{\odot}$ = la distance supposée nous séparant du centre Galactique ;
$\rho_{\odot}$ = est la densité locale ;
a = le rayon de cœur ;
α,β et γ des paramètres pouvant être déduits des simulations numériques à N corps de formation des halos. Celles-ci tendent à montrer qu'il existerait un profil de halo universel, de même forme quelque soit la masse et l'époque [45].

Les paramétrisations les plus utilisées sont les halos sphériques isothermes [44], de Navarro, Frenk et White (NFW) [45], de Kravtsov [46], et de Moore [47], dont les paramètres sont donnés dans la table 2.1.

	α	β	γ	a (kpc)
Isotherme	2	2	0	4
NFW	1	3	1	20
Kravtsov	2	3	0.4	10
Moore	1.5	3	1.5	28

Tab. 2.1 – Valeurs des paramètres de halo pour quatre types de profils.

Ces paramétrisations diffèrent en particulier dans la description de la densité au centre Galactique. Dans la figure 2.3 sont représentés les trois profils de halos les plus utilisés soit isotherme, NFW et Moore.

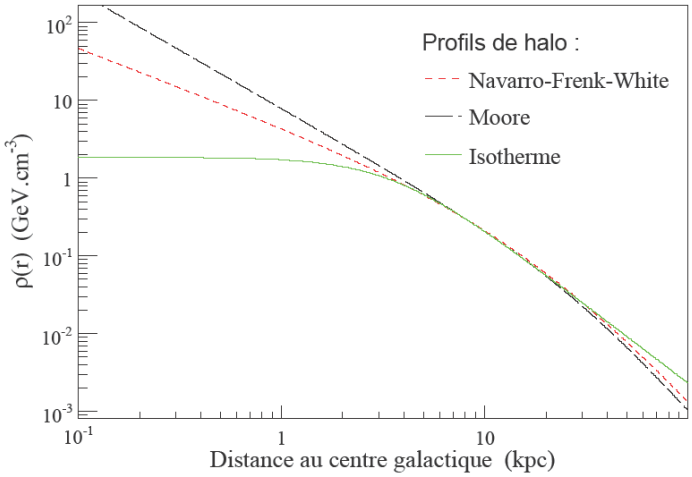

Fig. 2.3 – Profils de densité de matière noire pour trois des jeux de paramètres présentés dans le Tab.2.1, pour $r_\odot$ = 8 kpc.

Ces paramétrisation sont motivés par la conduite de simulations numériques à N-corps, de l'observation du mouvement des étoiles dans la Galaxie, et de l'observation indirecte des halos d'autres galaxies. Les simulations numériques de formation des structures ne sont pas assez précises pour rendre compte de la distribution de matière noire sur des échelles plus petites que le kpc pour un halo de la taille de celui de la Galaxie.

Pour la prédiction du flux de photons ou de neutrinos observés dans une direction donnée, il faut calculer l'intégrale du taux de production de ces particules le long de la ligne de visée. De fait, une ligne de visée est une entité abstraite et dans la réalité il faut également intégrer sur toutes les lignes de visée à l'intérieur d'un angle solide d'observation $\Delta\Omega$. Le flux différentiel exotique de γ ou ν, exprimé en particules par unité d'énergie (GeV) par unité de surface (cm^2) par unité de temps (s^{-1}) et par unité d'angle solide (sr^{-1}) peut s'écrire :

$$\Phi_{\gamma,\nu}(E) \cong \frac{dN_{\gamma,\nu}}{dE\, dS\, dt\, d\Omega} = \frac{1}{4\pi} \frac{<\sigma v>}{m_\chi^2} \frac{dN_{\gamma,\nu}}{dE}(E) \; < J >,$$

où le flux différentiel de photon et/ou neutrino (*dN/dE*) dépendra de la physique exotique et la nature évoquée pour le candidat WIMP et les correspondants canaux d'annihilation qui détermineront la probabilité d'avoir de γ ou de ν dans les états finaux. Le terme $<J>$ représenté est donné par la moyenne du taux de réaction sur les lignes de visée contenues dans l'unité d'angle solide et qu'il faudra intégrer sur la fraction d'angle de vue de l'observateur sur terre :

$$< J > = \int \frac{1}{2\delta_{stst}} \rho^2(\vec{r})\, ds\, d\Omega$$

où *ds* est un élément différentiel courant le long d'une ligne de visée et *r* le vecteur distance entre observateur et source de matière noire, dans le cas ici étudié, le centre de la Galaxie [42].

Le flux de gamma

En générale le modèle de nouvelle physique apparaît dans l'expression du flux de gamma et neutrinos à travers la section efficace $<\sigma v>$, la masse *m* de la particule de matière noire et le facteur δ_{stat} lié à sa nature. Pour faire une prédiction de flux exotique, il est également nécessaire de connecter le taux d'annihilation, qui compte le nombre de réactions par unité de volume et de temps, aux particules observées.

$$\chi\ \chi\ \rightarrow \left| \begin{array}{ll} - & f\bar{f}, \text{ où } f \text{ est un fermion du Modèle Standard :} \\ & b,\, c,\, t,\, d\ ,\, s,\, b,\, \tau,\, \mu,\, e,\, \nu_\tau,\, \nu_\mu,\, \nu_e \\ - & B\bar{B}, \text{ où } B \text{ est un boson du Modèle Standard :} \\ & W,\, Z,\, h^0, \gamma,\, g \\ - & Z\gamma,\, Zh^0 \end{array} \right.$$

Tab. 2.2 – États finals comprenant uniquement des particules du Modèle Standard.

Tous les modèles de matière noire que nous considérerons permettent en principe les canaux d'annihilation de WIMPS ne faisant intervenir que des particules du Modèle Standard comme listées dans le tableau 2.2. Tous ces canaux participeront à la superposition de tous les diagrammes faisant apparaître tous les états finaux possible pour le calcul final de la section efficace d'annihilation.
Des cas particuliers s'ajoutent pour lesquels des états finaux additionnels sont possibles, faisant intervenir de nouvelles particules, dépendant du modèle exotique exploré.
En supersymétrie dans le cadre du MSSM, sont présents des diagrammes contribuant aux annihilations avec dans l'état final $f\bar{f}, Z\bar{Z}, W^+W^-$ mais aussi $\gamma\gamma$ et $Z\gamma$. D'autres états finaux sont possibles dans le MSSM, en raison de la présence dans le spectre de bosons de Higgs supplémentaires dont les masses peuvent être inférieures à celles du neutralino le plus léger.
Dans le modèle mSUGRA, le neutralino est un mélange bino-higgsino, les états finaux attendus pour dominer sont donc $t\bar{t}, b\bar{b}, \tau^+\tau^-$ Lorsque la composante higgsino est importante, la production de bosons de jauge faibles peut également l'être. Pour plus de détails voir [48].

Dans le scénario de brisure AMSB, la LSP (Lightest Supersymmetric Particle - WIMP) est wino, la production de fermions est supprimée et les canaux Z_0Z_0, W^+W^- peuvent être largement dominants. Ce canal est très intéressant, en particulier parce qu'il induit une production efficace de photons de haute énergie importante observable (sur certains hypothèses avec le détecteur AMS02, Fig.2.4).

Une étude approfondie des attentes d'observation d'un signal indirect d'annihilation de WIMP dans le CG à travers l'observation de photon du GeV avec l'expérience AMS02 est détaillé dans [25].
Les étapes de cette étude sont respectivement :

- L'exploration des hypothèses astrophysiques qui concernent le profile de l'« halo » galactique.
- L'exploration des hypothèses de nouvelles physiques SUSY-MSSM, AMS-B, Kaluza Klein (qui seront rappelées ci dessous)
- L'estimation de la sensibilité du détecteur AMS02 compte tenu des performances attendues et étudiées avec les méthodes de simulation de Monte Carlo déjà décrites dans la Partie 1 de ce mémoire.

Les résultats de l'étude en question (dont les détails sont en Annexe B) sont résumés dans la figure 2.4, où la sensibilité d'AMS02-γ est montrée en fonction de la masse du candidat WIMP et pour un large scan de l'espace de paramètres des modèles exotiques de physique des particules (supersymmetrie, AMSB et Kaluza-Klein). En particulier la translation des flux attendus est aussi montrée en fonction de la densité de halo et donc de la modélisation de ce dernier.
Ici nous rappelons brièvement quelques assomptions et caractéristiques de cette étude (voir Annexe B pour plus de détails) :

- Le scenario plus largement exploré est celui de la supersymetrie pour lequel le candidat WIMP est le neutralino (χ_1^0) du Model Standard Minimal Supersymetrique (MSSM), pour lequel χ_1^0 est bien la particule supersymetrique la plus légère et stable en vertu de la conservation de la parité R.
- Les modèles explorés (ainsi que les flux de gamma qui en découlent) correspondent aux différents choix de combinaisons des 5 paramètres fondamentaux dans le contexte de supergravité minimale (mSUGRA).
- En particulier 13 combinaisons « Benchmark » des paramètres mSUGRA ont été examinées car elles avaient déjà été proposées comme étant des scenarios prometteurs pour une découverte SUSY aux futurs accélérateurs des particules (e.g. LHC et Linear Colliders).
- L'expérience Wilkinson Microwave Anisotropy Probe (WMAP) a fourni la mesure la plus détaillée des anisotropies du rayonnement cosmique de fond en microondes (CMB). L'interprétation de cette mesure dans le cadre du modèle standard cosmologique, a permis d'estimer indirectement des limites sur la densité de matière noire froide non-baryonique : $0.095 < \Omega_{CDM} h^2 < 0.129$.

Dans nos études l'exploration de l'espace de paramètres compatibles avec les limites de WMAP mais aussi pour des valeurs de densité inferieures (dans l'hypothèse de production supplémentaire de neutralisons non-thermique) sont prises en examen.

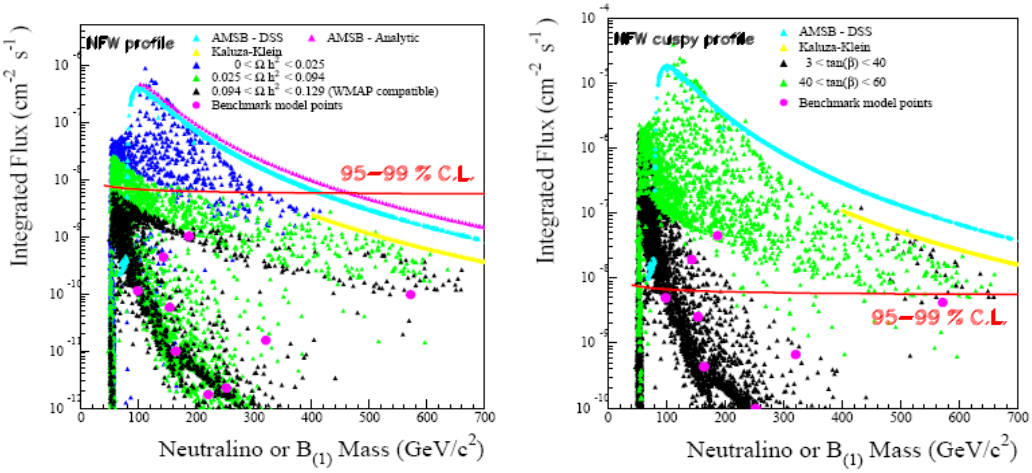

Fig. 2.4 - Les flux gamma intégrales en provenance du Centre Galactique en fonction de la masse du WIMP pour un profile de halo NFW standard (à gauche) et NFW cuspy (à droite). Les modèles MSSM dans le schéma mSUGRA plus AMSB et KK sont considérés. Nous explorons aussi les sélections en terme de densité Ωh^2 (à gauche) et du paramètre tan(β) (à droite) .

Le flux de neutrinos

Les états finaux apparaissant dans les annihilations des particules de Kaluza-Klein dépendent de la classe de modèle considérée. Dans les perspectives de détection gamma et neutrino considérés dans les travaux [25][49][39] nous nous sommes intéressés aux dimensions supplémentaires universelles (UED, dont le candidat matière noire est la LKP), et aux dimensions supplémentaires voilées (wraped, dont le candidat est la LZP).
Dans les modèles UED la particule de matière noire est le premier état excité du boson de jauge faible B(1). L'annihilation en bosons de jauge est supprimée à l'arbre et les états finaux possibles sont $f\bar{f}$ et bosons de Higgs. Les diagrammes correspondant à ces processus sont ici représentés et issus de [50]:

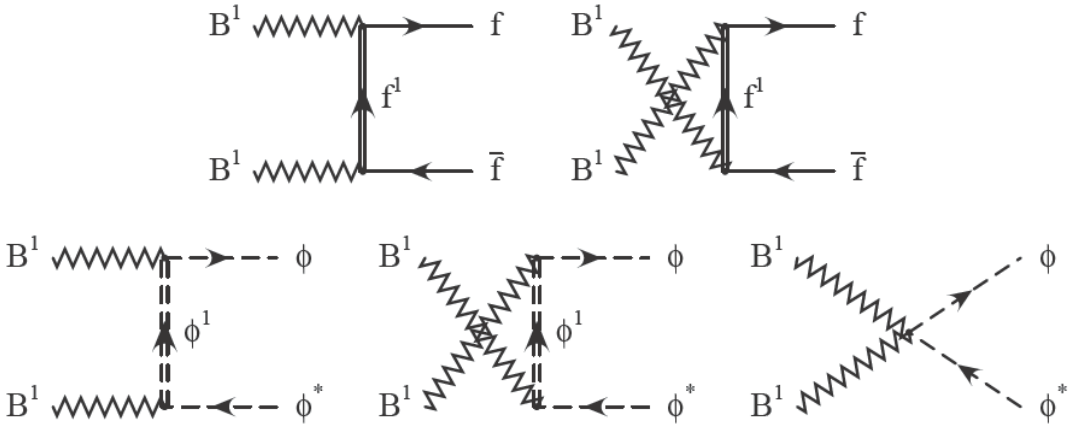

Fig. 2.5 Diagrammes contribuant à l'annihilation d'une particule de Kaluza-Klein LKP en fermions et en Higgs.

Les détails du calcul des sections efficaces peuvent se retrouver en [50] et [49]. Dans ce modèle, le rapport d'embranchement pour un fermion *f* ne dépend que des hypercharges de ses projections chirales (YR et YL) et du nombre de couleurs sous lequel il peut intervenir (Nc = 1 pour un lepton et Nc = 3 pour un quark). La section efficace de l'annihilation en fermions peut s'écrire

$$\sigma(B^{(1)}B^{(1)} \to f\bar{f}) \;=\; \frac{N_c\, g_1^4\, (Y_L^4 + Y_R^4)\, (10(2m^2+s)\; Arctanh(\beta) - 7s\beta)}{72\pi s^2 \beta^2} \quad \text{avec} \quad \beta = \sqrt{1 - \frac{4m^2}{s}} \;\;,$$

Les détecteurs des neutrinos astrophysiques comme ANTARES (, ICECUBE ou le future KM3) peuvent chercher dans le flux de neutrinos la signature indirecte de la présence de matière noire non-baryonique (les candidates KK $B^{(1)}$ en particulier) relique dans le halo galactique. Pour arriver à la détection on assume que des processus d' « amplification » (capture et accumulation) de particules reliques auraient lieu dans des corps célestes comme la Terre ou le Soleil, ce dernier étant favori pour sa masse. Toutes les étapes de ce scénario ont été étudiées, les calculs qui en dérivent ont été finalisés pour arriver en conclusion à une perspective de détection, à travers la simulation de Monte Carlo détaillée, de l'expérience ANTARES à une signature de matière noire KK en provenance du Soleil. Les détails de ce travail original se trouvent en [49] (et une tractation plus approfondie en [51]) dont nous en proposons un résumé.

Le processus se décompose en étapes suivantes :

1- Assomption initiale sur la densité locale et la vélocité qui caractérisent les spectres de particules $B^{(1)}$ dans la Galaxie. Nous avons déjà discuté des possibles parametrizations de halo galactique qui nous permettent de faire des assomptions sur le profil de densité de matière noire et pour chaque profil définir la densité locale (dans le système solaire) et le spectre de vitesse des $B^{(1)}$ (e.g. respectivement 0.3 $GeV\,cm^{-3}$ et 270 $km\,s^{-1}$ dans les études de [49].

2- Capture des $B^{(1)}$ par ralentissement de celles-ci au-travers de diffusions élastiques avec les noyaux de ces corps célestes (e.g. interactions $B^{(1)}$ - noyaux d'hydrogène et hélium dans le Soleil). Accumulation importante par gravité des particules aux alentours du centre des amplificateurs (e.g. le Soleil). Une situation d'équilibre est donc instaurée entre nombre de particules accumulés et l'auto annihilation des ces dernières, dont le taux est donné par l'expression suivante, dépendant de la mass de $B^{(1)}$; les rapports de branchement attendus en fonction des canaux d'annihilation sont dans le tableau 2.3.

$$\Gamma = 1,5075 \times 10^{-6} s^{-1} \left(\frac{1000\,\mathrm{GeV}}{m_{B^{(1)}}}\right)^6 \tanh^2\left(2.4\left(\frac{1000\,\mathrm{GeV}}{m_{B(1)}}\right)^{13/4}\right)$$

processus	rapport de branchement $r_{q_R^1} = 0.14$
$\nu_e\overline{\nu}_e$, $\nu_\mu\overline{\nu}_\mu$, $\nu_\tau\overline{\nu}_\tau$	0.014
e^+e^-, $\mu^+\mu^-$, $\tau^+\tau^-$	0.23
$u\overline{u}$, $c\overline{c}$, $t\overline{t}$	0.077
$d\overline{d}$, $s\overline{s}$, $b\overline{b}$	0.005
$\phi\phi^*$	0.027

Tab. 2.3 – Rapport de branchement pour tous canaux d'annihilation $B^{(1)}$ - $B^{(1)}$.

3- En particulier l'annihilation $B^{(1)}$ - $B^{(1)}$ provocant la production de neutrinos de haute énergie au travers de différents canaux de désintégrations est critique pour nos études. Les canaux de désintégration peuvent être résumés de la manière suivante :

- Neutrinos produits directement par annihilation des $B^{(1)}$, le spectre étant alors mono-énergétique a $E_\nu = m_B$ pour une masse de $B^{(1)}$ donnée.

$$B(1)B(1) \rightarrow \nu\overline{\nu}$$

- Neutrinos dits secondaires provenant de la désintégration des pions charges issus de l'hadronisation de quarks.

$$B(1)B(1) \rightarrow q\overline{q} \rightarrow \pi^{\pm} \rightarrow \mu^{\pm} + \overset{(-)}{\nu}_{\mu} \rightarrow e^{\pm} + \overset{(-)}{\nu}_{e} + \overset{(-)}{\nu}_{\mu} + \overset{(-)}{\nu}_{\mu}$$

- Neutrinos secondaires issus de la désintégration « heavy-quarks » et leptons tau :

4- A partir des flux des neutrinos et antineutrinos calculés nous estimons ensuite leurs interactions avec le soleil pour arriver au flux différentiel final sortant de notre étoile (en $GeV^{-1}\ m^{-2}\ yr^{-1}$) suivant:

$$\frac{dN_\nu}{dE_\nu} = \frac{\Gamma}{4\pi d^2} \sum_{F,f} B^{(F)}_{B^{(1)}f} \frac{dN_{f\nu}}{dE_\nu}$$

ou nous prenons en compte le taux d'annihilation Γ et nous considérons une isotropie du flux de neutrinos au travers du facteur $1/4\pi d^2$ (voir Fig.2.6). Le flux intégré a partir d'une énergie seuil E_ν = 10 GeV nous permet de déduire le nombre de neutrinos et antineutrinos produits et en fonction de la masse de $B^{(1)}$:

$$N_\nu = \int_{10}^{m_{B(1)}} \frac{dN_\nu}{dE_\nu}\ dE_\nu\ .$$

Voir Fig. 2.7 (e.g. pour un masse de 400 GeV, nous obtenons 3000 evt. $m^{-2}\ yr^{-1}$).

5- La dernière étape est la détermination du flux de muons créé par interaction des neutrinos avec le milieu terrestre : tout d'abord le flux arrivant sur Terre devra tenir compte des oscillations des neutrinos dans le vide sur le chemin Soleil-Terre. Nous allons faire l'hypothèse que le flux différentiel nm va donc être à la fois réduit en raison de l'oscillation nu -> nt et augmenté par l'oscillation nt -> nu provenant également du Soleil. Ensuite, le taux de muons détectable par unité de surface et par an peut être déterminé sachant que les neutrinos interagissent principalement avec le milieu terrestre par interaction par courant chargé, dont les sections efficaces sont connues.

6- Enfin la sensibilité finale de l'expérience ANTARES a un signal de neutrino d'origine indirecte d'annihilation de matière noire seras donnée (analytiquement) par la convolution du flux de muons avec la surface efficace A (0.1 km^2 nominale) attendue de ANTARES et le temps d'observation du soleil (le temps d'exposition du détecteur au Soleil est une fraction ~ 0.5 de l'an). Ainsi la possibilité d'appliquer le simulateur de Monte Caro de ANTARES nous permet de valider le calcul analytique à travers une estimation plus précise des efficacités de détection et de dépendance de la surface efficace de l'énergie des muons.

Les résultats de ce travail sont montrés en figure 2.8. Nous obtenons ~ 2 événements par an pour une superficie A = 0.1 Km2 et au 100% d'efficacité et une valeur plus réaliste (compte tenu d' une efficacité de reconstruction de l'ordre de 30%) de ~ 0.25 évènement par an.

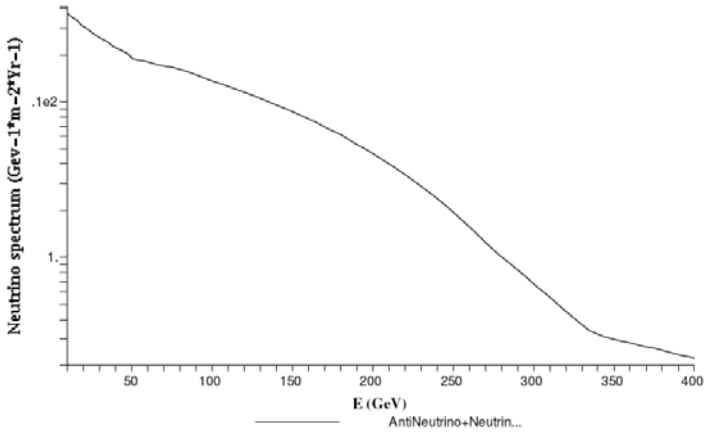

Fig. 2.6 –Flux différentiel de neutrinos de muon déterminé pour une masse de $B^{(1)}$ de 400 GeV et une énergie seuil pour les neutrinos (et antineutrinos) de 10 GeV.

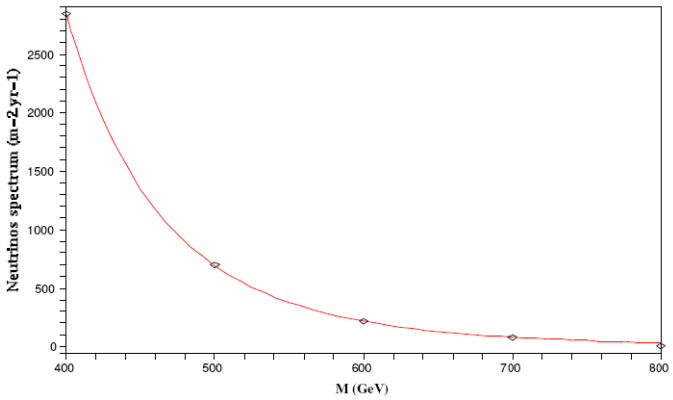

Fig. 2.7 –Comparaison des flux intégrés de neutrinos déterminés pour des masses de $B^{(1)}$ de 400 à 800 GeV.

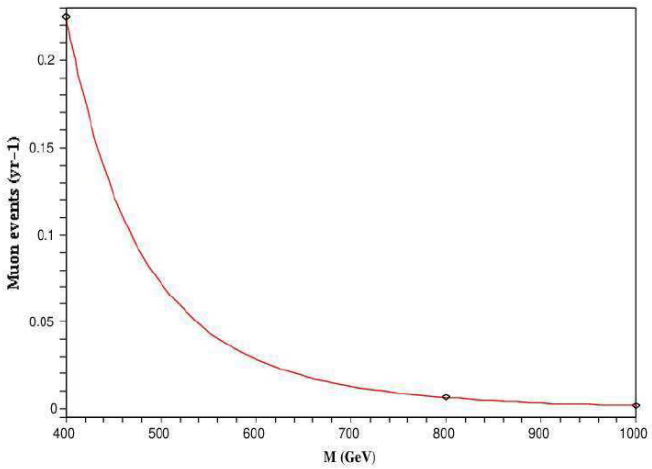

Fig. 2.8 –Muons détectes par ANATRES par an en fonction des masses de $B^{(1)}$ de 400 à 800 GeV.

II.3. La γ-astronomie et l'origine des rayons cosmiques

L'astronomie gamma est l'étude des photons appartenant à la gamme la plus extrême des longueurs d'onde du spectre électromagnétique. Cette gamme en énergie débute aux alentours de quelques centaines de keV jusqu'à des énergies de l'ordre de 10^{20} eV. La gamme en énergie, s'étendant potentiellement sur prés de 14 ordres de grandeur, est subdivisée en plusieurs domaines. En particulier on y reconnait les hautes énergies - HE (de dizaines de MeV jusqu'à la limite de dizaines de GeV voir 100 GeV) et les très hautes énergies - VHE de 100 GeV à des dizaines de TeV. La limite supérieure du domaine HE est celle explorée par les expériences spatiales comme AMS-γ alors que le domaine VHE est propre à des expériences au sol du type H.E.S.S..
Les particules chargées accélérées, suivant leur nature léptonique ou hadronique, peuvent interagir avec le milieu environnant pour produire des photons γ dans la gamme d'énergie du TeV.
Les processus en jeu dans les objets astrophysiques et qui pourraient justifier l'émission gamma de HE et VHE sont fondamentalement la diffusion Compton inverse et la production de pions neutres lors de collisions hadroniques.
L'effet Compton inverse est l'un des processus dominants pour la production de γ en Astrophysique. Ainsi, nous le retrouvons notamment dans les pulsars, les noyaux actifs de galaxies et les vestiges de supernovæ. Les photons du fond diffus cosmologique en micro-ondes sont présents dans tous les objets, auxquels peuvent se rajouter des champs de photons stellaires ou émis par des nuages de poussières. Tout cela rend ce processus très répandu.
Le principe est le suivant : un électron de très haute énergie peut transférer une grande partie de son énergie à un photon mou du rayonnement ambiant et le propulser dans le domaine. Dans le cas d'électrons d'énergie supérieure à quelques dizaines de TeV, le photon produit peut atteindre une énergie supérieure à 1 TeV. Le spectre en énergie des photons produits par la diffusion Compton inverse d'une population d'électrons suivant une distribution en énergie en loi de puissance d'indice spectral α, est en première approximation une loi de puissance d'indice $\Gamma \sim (\alpha+1)/2$ dans la même gamme en énergie que les électrons.

La production de photon gamma par les protons à travers la désintégration de π^0 est le processus qui fournit l'unique voie d'information concernant la composante hadronique des rayons cosmiques. Dans ce processus, des protons et des noyaux relativistes, interagissent avec le milieu ambiant par diffusion inélastique et produisent notamment des pions. À haute énergie, les trois types de pions (π^0 π^+ π^-) sont produits avec la même probabilité.
Le π^0 se désintègre presque instantanément en deux γ. La désintégration des pions chargés produit, quant à elle, des muons à partir des réactions suivantes :

$$\pi^+ \rightarrow \mu^+ + \nu_\mu \quad \text{et} \quad \pi^- \rightarrow \mu^- + \bar{\nu}_\mu$$

Puis, les muons se désintègrent en électrons, positons et neutrinos :

$$\mu^+ \rightarrow e^+ + \nu_e + \bar{\nu}_\mu \quad \text{et} \quad \mu^- \rightarrow e^- + \bar{\nu}_e + \nu_\mu$$

Ces chaînes de réactions créent ainsi des ν_e et des ν_μ qui suivent généralement une distribution spectrale très proche de celle des γ produits par les π^0. Ainsi, grâce à la production de γ et de ν, particules se propageant en ligne droite (car non affectées par les champs magnétiques turbulents ancrés dans le plasma interstellaire de la Galaxie), ce processus nous permet d'avoir une information directe sur les sources de rayons cosmiques. L'astronomie gamma et l'astronomie neutrino en tirent pleinement partie.
Dans la gamme en énergie du GeV ou du TeV, la fraction moyenne de l'énergie du proton emportée par le π^0 est ~0.17. L'énergie moyenne des photons issus de la collision d'un proton d'énergie E est de ce fait de l'ordre d'environ 0.085 E. La section efficace p-p est par ailleurs très peu dépendante de l'énergie du proton dans la gamme du TeV. Cette propriété a pour conséquence que le spectre en énergie des photons émis lors de collisions hadroniques suit une loi de puissance de même indice que celle des protons.

II.3.1. Le rayonnement cosmique Galactique : Pulsars et PWN.

Les pulsars sont des étoiles à neutrons en rotation rapide. En fin de vie, les étoiles les plus massives voient leur cœur s'effondrer en étoile à neutrons lorsque la masse du cœur de fer la constituant dépasse la masse de Chandrasekhar. Cette étoile, de masse d'environ 1,4 masse solaire, est maintenue en équilibre grâce à l'interaction forte des neutrons qui constituent un liquide quantique de fermions.
Les pulsars ont des champs magnétiques atteignant 10^8 T et des périodes de rotation de quelques dizaines de millisecondes, en raison, respectivement, de la conservation du flux magnétique et du moment cinétique lors de l'effondrement de l'étoile massive. Selon certains modèles, l'étoile à neutrons en rotation est entourée d'une magnétosphère remplie par un plasma. L'argument expliquant la présence d'un tel plasma utilise un calcul montrant que le rapport des forces électriques et gravitationnelles vaut, au pôle du pulsar par exemple, 5×10^8 pour un proton et 10^{12} pour un électron. Des charges vont donc être arrachées à la surface de l'étoile pour remplir la magnétosphère et l'extérieur de l'étoile ne peut être vide. Les lignes de champ magnétique qui ne rencontrent pas le cylindre de lumière sont fermées, les autres ouvertes ; les particules s'échappent alors à l'infini en tournant en spirale le long des lignes de champ ouvertes. Cependant, dans cette configuration le champ électrique et le champ magnétique sont perpendiculaires.

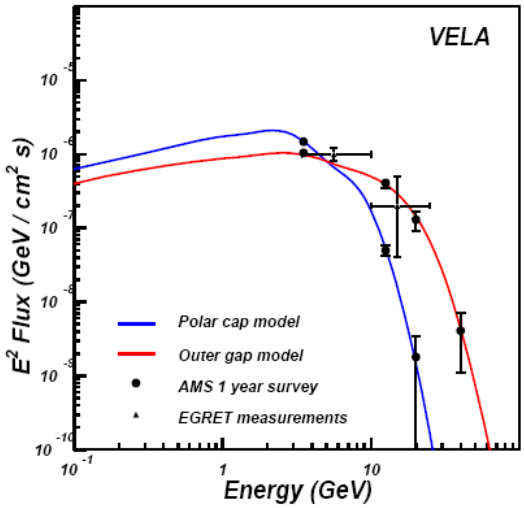

Fig. 2.9 –Flux attendu de gamma de la Pulsar Vela avec le spectromètre AMS02 après un an de prise de données. Les résultats montré sont issu de la simulation détaillé de Monte Carlo de performance de AMS et de condition d'observation sur la ISS.

Ainsi, le champ électrique n'est pas en mesure d'accélérer les particules puisque celles-ci suivent les lignes du champ magnétique (en raison de l'énorme valeur du champ magnétique) [52]. Une solution pour susciter un processus d'accélération est de postuler que des charges s'échappent de la magnétosphère, ce qui provoque l'apparition de vastes régions vides de charges, au sein desquelles les champs ne sont plus perpendiculaires. Ces cavités ne peuvent survivre qu'en des zones bien précises de la magnétosphère : les pôles magnétiques (cavités polaires ou *polar gap*) de l'étoile à neutrons et des régions situées dans la magnétosphère lointaine près du cylindre de lumière (cavités externes ou *outer gap*). Pour de plus amples détails, le lecteur se réfèrera à la référence [53]. Les émissions gamma des pulsars mesuré par EGRET ont montre une atténuation spectrale a dizaine de GeV compatibles avec le deux modèles mais avec de différences dans les niveaux prévus d'atténuation.
Dans le modèle de la calotte polaire nous avons l'émission de photons par les particules primaires arrachées à la surface de l'étoile et par celles secondaires, qui sont des paires e+e- produites précisément a partir des premiers photons. L'absorption des photons par la création de paires e+e- limite ainsi la taille de la cavité accélératrice. Cette absorption pourrais être dominé par interaction des gammas avec le champs magnétiques.
Dans le modèle de la cavité externe l'émission de photons gamma nécessite la création de paires e+e- mais aussi l'émission gamma par ces dernières. L'absorption des gammas est due a un front de création de paires e+e-. A l'opposé du modèle de la calotte polaire, ce modèle fait appel a des processus photon-photon pour produire les paires: par conséquence, une atténuation spectrale vers ~ 10 GeV plus douce est attendue que celle liée au modèle de la calotte polaire et un plus se distingue aussi par la prédiction d'une émission au TeV.
Pour un pulsar gamma, la production de paires e+e- limite donc la page en énergie des γ émis et cette limite s'exprime sous la forme d'une coupure exponentielle à énergie du GeV. Sur la base de cette modélisation le flux gamma attendu montrerait en générale un comportement spectral différent avec l'énergie. Une analyse de Monte Carlo a été conduite pour valider le potentiel de découverte de AMS02-γ. Dans cette étude les performances du détecteur AMS sont issues de l'analyse de Monte Carlo détaillées alors que la sensibilité à l'observation de Pulsars (e.g. Vela) est estimée grâce à une étude de simulation rapide [23] d'observation du ciel galactique sur la Station Spatiale Internationale [21][40] (pour plus de détails voir le Chapitre 1 et l'Annexe B). La Fig. 2.9 résume les résultats de cette étude et montre le potentiel de discrimination de AMS02 entre les deux modèles en discussion pour l'interprétation de l'émission gamma au GeV de la Pulsar Vela.

Quelques pulsars comme ceux du Crabe ou de Vela se trouvent au cœur d'un nébuleux synchrotron, résidu de l'ancienne supernova ayant donné naissance à l'étoile à neutrons. L'intérieur de ces objets, observés en radio, présente un rayonnement synchrotron intense, contrairement aux vestiges de supernovæ en coquilles où l'émission est localisée à la périphérie. Ainsi les désigne-t-on sous le nom de plérions (mot qui vient du Grec et signifie "plein") ou Pulsar Wind Nebulae (PWN). On explique la présence d'électrons de haute énergie dans la nébuleuse par le scénario suivant : le pulsar émet un vent intense de paires e+e- qui crée, dans la nébuleuse elle-même, une onde de choc pouvant accélérer les électrons jusqu'à des énergies très élevées. Il n'est donc pas étonnant que les plérions émettent également un signal non périodique observé jusqu'à de très hautes énergies. Ainsi, le spectre de la nébuleuse du Crabe possède deux larges bosses :
- la première s'étend de la radio jusqu'au domaine du MeV. Elle est généralement attribuée au rayonnement synchrotron des électrons accélérés dans la nébuleuse,
- la deuxième se situe dans le domaine des très hautes énergies ; elle est attribuée généralement à l'effet Compton inverse des photons synchrotron sur les électrons qui leur ont donné naissance : c'est le mécanisme d'auto-comptonisation ("Synchrotron-Self Compton").

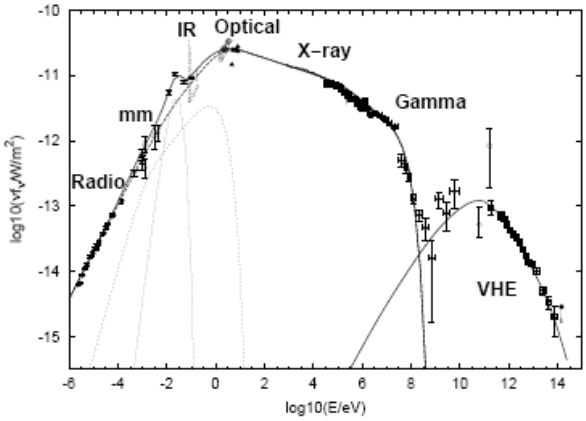

Fig. 2.10 – Modélisation de l'émission provenant de la nébuleuse du Crabe superposée aux données multi longueurs d'onde (IRAM, ISO, Chandra, ROSAT, EGRET et HEGRA).

La figure 2.10, tirée de la référence [54] présente la modélisation du signal du Crabe par une émission synchrotron et une émission synchrotron-self Compton : elle s'adapte très bien aux nombreuses données obtenues sur le Crabe dans les diverses longueurs d'onde. Cette figure illustre bien le fait que des particules sont accélérées jusqu'au PeV dans ces objets : ils sont donc une cible d'étude pour les détecteurs Tcherenkov. Les observations de H.E.S.S. ont démontré que les Pulsar Wind Nebulae sont responsables pour la majorité de l'émission gamma de très haute énergie dans la Galaxie: e.g. la nébuleuse du Crabe, MSH 15-52, G0.9+0.1, HESS J1825-137 et HESS J1616-508 (voir Annexe B pour plus de détails).

L'étude de ces objets astrophysiques est critique pour des études diagnostiques de la distribution spatiale et spectrale des électrons de haute énergie étant considérée comme les premières responsables de l'émission gamma au TeV. L'introduction de la méthode multi-variable Xeff nous permet de contribuer à l'analyse de données H.E.S.S. avec un très fort potentiel surtout sur l'étude morphologique de sources étendues (e.g. le PWN et en particulier Vela X [38][55]) et sur la détection significative de signal gamma des sources moins lumineuses pour lesquelles la méthode Xeff garantie un gain en sensibilité et en précision.

En fig. 2.11 l'exemple d'étude morphologique originale (et préliminaire) de Vela X avec Xeff et en fonction de l'énergie (qui fait l'objet d'une publication en cours de rédaction [56]) est proposé. La comparaison avec la morphologie et l'analyse spectrale aux longueurs d'onde radio et X nous permet aussi de contraindre les modèles d'interprétation des phénomènes qui seraient à l'origine de l'émission gamma. En fait dans l'hypothèse leptonique le rayonnement synchrotron d'électrons d'énergie

supérieure à 1 TeV dans des champs magnétiques astrophysiques de l'ordre de quelques μG conduit à une émission de rayon X. La morphologie de l'émission X est ensuite utile car elle peut être utilisée pour contraindre l'intensité du champ magnétique ou la densité d'électrons accélérés présents dans cette région. L'accord limité entre la carte du ciel X de VelaX et la carte gamma de H.E.S.S. nous ouvre la possibilité d'envisager la présence d'une composante hadronique responsable de l'émission gamma VHE. Ainsi donc d'obtenir une évidence indirecte de sources des rayons cosmiques (hadrons) dans notre Galaxie.

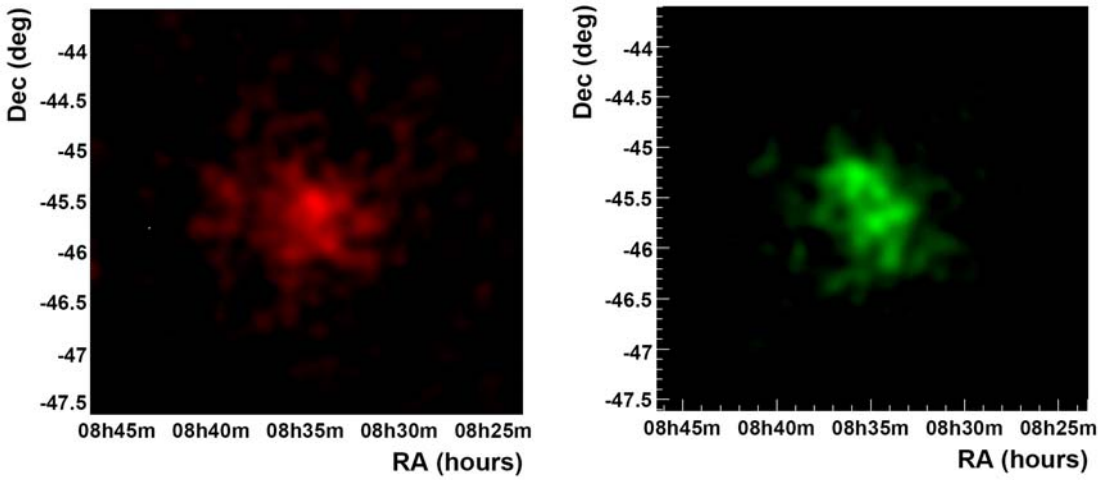

Fig. 2.11 – Deux cartes du ciel préliminaires issues de l'analyse Xeff de données H.E.S.S. de VelaX. La taille de la source est de l'ordre de ~ 2 dégrée de radius et sa morphologie dépend de l'énergie (E<4 TeV à gauche, E> 4 TeV à droite).

Les PWN se sont révélées être des objets de morphologies variées, à la foi liées à l'histoire et aux caractéristiques du pulsar associé, mais aussi aux interactions avec le milieu interstellaire et avec les éjecta de la SNR.

Un nombre non négligeable de pulsars naissent avec des vitesses cinétiques de l'ordre de 500 km s^{-1}. Ces vitesses de déplacement importantes peuvent permettre à certains pulsars de s'échapper de leur position originale et de se propager à travers les éjecta choqués à l'intérieur de la SNR. Pendant le temps écoulé afin que le pulsar parvienne jusqu'au bord de la SNR, sa vitesse augmente significativement jusqu'à ce qu'il devienne supersonique. Des études d'hydrodynamique d'évolution morphologique des PWN dans un milieu inhomogène ont démontré une asymétrie notable dans l'expansion de la nébuleuse, ainsi qu'un décalage de son centre de gravité par rapport au pulsar de l'ordre de grandeur de quelques dizaines de pour cent du rayon de la SNR associée.

Deux conditions sont requises pour un tel phénomène : - le pulsar doit avoir assez de puissance et d'ancienneté pour que la nébuleuse soit large ; - le milieu ambiant doit comporter un gradient de densité de matière de part et d'autre du pulsar. Les pulsars apparentés aux PWN du même type que Vela X ont des âges avancés (10000 ans pour Vela X). La partie diffuse de la nébuleuse X et gamma VHE (voir Fig.2.11 et Annexe B pour plus de détails) est très étendue, et elle montre une asymétrie ainsi qu'une élongation dans le direction perpendiculaire au vecteur vitesse du pulsar. Vela X est donc un candidat important pour les études évolutives de PWN (cet aspect est examiné dans [38] et [56]).

Pendant l'évolution de la nébuleuse les électrons responsable de l'émission gamma perdent peu à peu leur énergie. Dans la morphologie d'une PWN les régions plus éloignées sont remplies par les particules les plus âgées et don moins énergétiques. La rapidité de refroidissement est d'autant plus importante que l'énergie de particules est grande. En conséquence, l'indice spectral dépend, dans ce modèle, de la distance au pulsar (ou a sa position d'origine). C'est effet est nettement observable au TeV pour la source HESS J1825-137 (voir fig. 2.12).

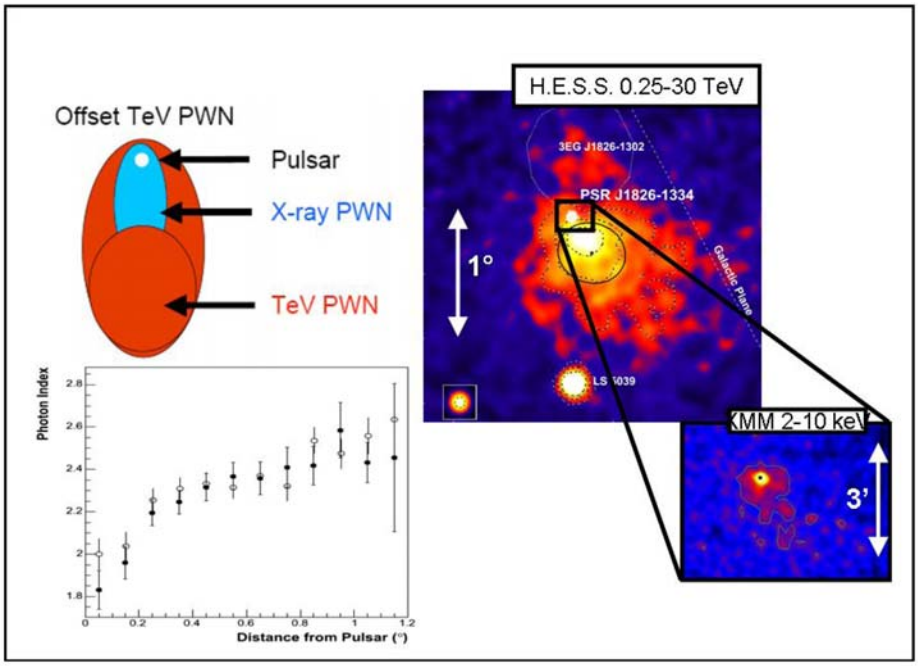

Fig. 2.12 – Dans la morphologie d'une PWN les régions plus éloignées sont remplies par les particules les plus âgées et donc moins énergétiques. L'indice spectral dépend de la distance au pulsar (comme observe pour HESS J1825-137).

Un effet similaire mais moins importante statistiquement a étais observé dans l'analyse multi-variable de Vela X [38] (fig.2.13).

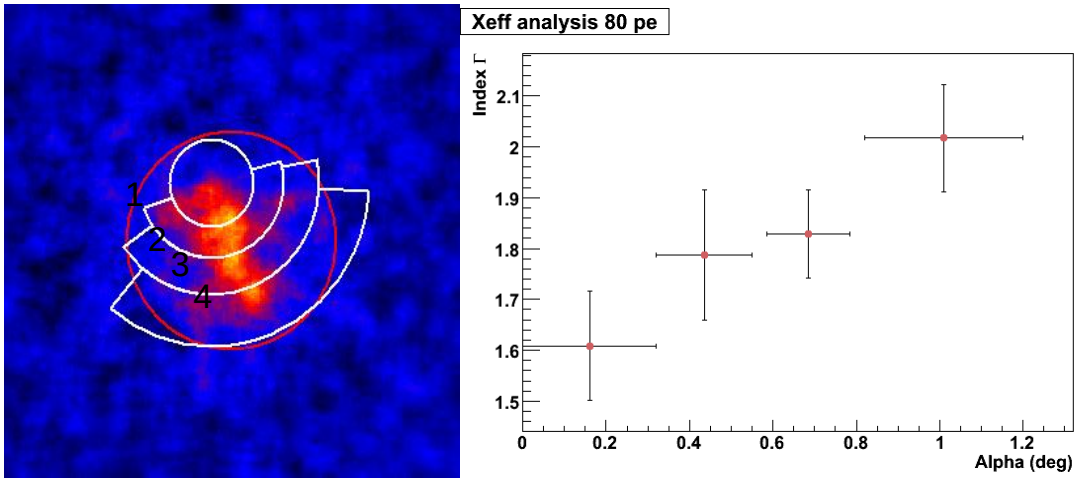

Fig. 2.13 – L'indice spectral du COCOON de Vela X montre une dépendance (dont la significativité préliminaire est limité) de la distance au pulsar.

II.4. Conclusions et perspectives

Mes contributions à l'expérience H.E.S.S. et à la recherche en gamma astronomie de très haute énergie sont aussi reliées aux perspectives futures à court et plus long termes. En particulier la deuxième phase de H.E.S.S. consiste à rajouter un cinquième télescope de plus grand diamètre au centre du système actuel. La plus grande surface de collection augmente la sensibilité du détecteur à des flashes de lumière Tcherenkov plus faibles provoqués par des rayons gamma de plus faible énergie. Le ciel aux énergies de l'ordre de 100 GeV exploré avec des nouveaux observatoires dotés des sensibilités d'ordres de grandeur plus importantes que les actuels télescopes spatiaux (e.g. Fermi et AMS) pourrais enfin permettre de répondre aux questions que j'ai voulu discuter dans ce mémoire et auxquelles je consacre ma recherche : - recherche d'un signal indirecte de matière noire aux énergies (~ 50 GeV) plus compatible avec des masses des WIMP attendues; - l'analyse des coupures spectrales prédîtes par les modèles théoriques pour une bonne partie de sources astrophysiques, permettrais la caractérisation du rayonnement Galactique et la découverte des sites de production et accélération des rayons cosmiques. Par contre réduire le seuil d'investigation aux environs de quelques dizaines de GeV ne seras pas suffisante si nous n'ajoutons pas :

- la capacité d'éliminer le fond dominant de rayons cosmiques hadroniques et d'électrons a ces énergies. Pour cela nous poursuivons l'introduction de technique d'analyse plus performantes et indispensables et nous préparons un approche alternatives à la recherche de signal de matière noire dans le fond diffus proche du centre galactique [57][58] ;
- le gain de précision qui est obtenu grâce à l'approche en mode stéréoscopique. Pour ce dernier le prospectives a plus long termes sont plus encourageant : CTA – Cherenkov Telescope Array.

CTA est le projet européen de grand réseau de télescopes Cherenkov de nouvelle génération en astronomie gamma des très hautes énergies. Son développement s'inscrit dans la suite logique du succès des expériences européennes HESS et MAGIC, qui ont élargi le domaine d'observation du cosmos aux énergies extrêmes. L'observatoire CTA consistera en un réseau de télescopes Cherenkov, qui doit augmenter la sensibilité des détecteurs actuels d'un ordre de magnitude, améliorer les capacités en résolution angulaire et étendre le domaine spectral d'environ 10 GeV jusqu'au delà de 100 TeV (voir fig. 2.14). En particulier mes efforts actuels sont adressés aux études de solutions techniques en mécanique et en électronique pour l'ensemble des télescopes de grand diamètre (24 m) du réseau CTA et qui travailleront en stéréoscopie.

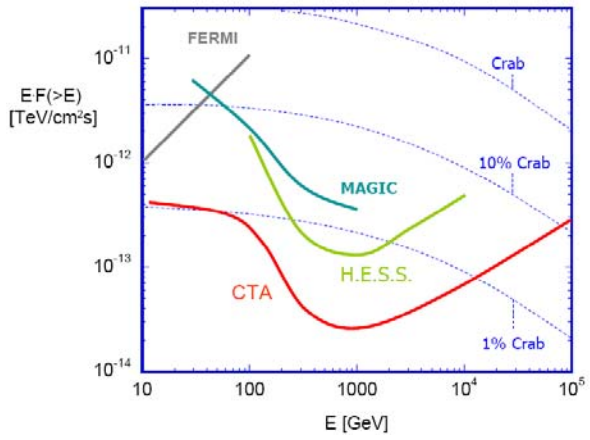

Fig. 2.14 –Sensibilité et domaine spectral globalement visés pour le projet CTA, comparés aux expériences en cours de fonctionnement HESS et MAGIC, et au satellite FERMI (GLAST).

BIBLIOGRAPHIE

[1] J. Alcaraz,..,**G. Lamanna** et al., Il Nuovo Cimento Vol. 112 A, N.11, (1999) 1325.
[2] P. Holl et al., IEEE Trans. Nucl. Sci. 36 (1989) 251
[3] P. Holl et al., Nucl. Instr. Meth. A257 (1987) 587
[4] J.B.A. England et al. , Nucl. Instr. Meth. 185 (1981) 43
[5] E. Nygard et al., Nucl. Instr. Meth. A301 (1991) 506
[6] O. Toker et al., Nucl. Instr. Meth. A340 (1994) 572
[7] M. Ribordy, PhD Thesis, DPNC, Uni. Genève, (2000)
[8] M. Cristinziani, PhD Thesis, DPNC, Uni. Genève (2002)
[9] J. Alcaraz,..,**G. Lamanna** et al. Nucl. Instr. Meth. A593, 376-398 (2008)
[10] M. Aguilar,..,**G. Lamanna** et al., Physics Reports Vol. 366/6 (2002) 331
[11] E. Fiandrini,..,**G. Lamanna** et al., Jour. Geoph. Res. – Space Physics, 107, A6, 10.129, 2002
[12] P. Zuccon,..,**G. Lamanna** et al., Astrop. Physi., Vol 20/2 pp 221-234 (2003)
[13] E. Fiandrini,..,**G. Lamanna** et al., Journ. Geoph. Res.– Vol. 108, No. A11, 1402 10.1029/2003JA
[14] M.Aguilar,..,**G. Lamanna** et al., Nucl.Instr.Meth. B234 (2005) 321-332
[15] D.J. Thompson et al., Astrophys. J. Suppl. 86 (1993) 629
[16] E. do Couto e Silva, Nucl.Instr.Meth. A473 (2001) 107-113
[17] **G. Lamanna** AMS internal note 2003-03-03
[18] J. Alcaraz, Nucl. Instr. Meth. A553, 613-619 (2005)
[19] I. Sevilla Noarbe, PhD Thesis, CIEMAT, Madrid (2006)
[20] **G. Lamanna**, Proc. Suppl. Nuclear Physics B , 113 (2002) 177-185
[21] **G. Lamanna,** ICHEP02,Proc. Suppl. Nuclear Physics B (2002) 119-121
[22] V. Choutko, **G. Lamanna**, A. Malinin, Int. J. Mod. Phys. A17 (2002) 1817
[23] J. Bolmont, **G. Lamanna**, M. Sapinski, I. Sevilla Noarbe,. AMS internal note 2004-02-01
[24] R. Timmer, Stage Master 1, DPNC, Uni. Genève (2001) (**G. Lamanna** maitre de stage)
[25] A. Jacholkowska, **G. Lamanna**, et al., Physical Review D 74,(2006) 023518
[26] ANTARES Collaboration, Technical design report. http://antares.in2p3.fr (2001)
[27] J. A. Aguilar, .., **G. Lamanna** et al. Astropart. Physics 26 (2006) 314-324
[28] ANTARES Collaboration, Nucl. Instr. and Meth. A555 (2005) 132-141
[29] M. Ageron,..,**G. Lamanna** et al. , Nucl. Instr. and Meth. A 578 (2007) 498-509
[30] G. Lelaizant, PhD Thesis, CPPM, Marseille (2008)
[31] G. Hallewell, **G. Lamanna**, Internal Note ANTARES- Note 5-ASS-02-55-A
[32] G. Hallewell, **G. Lamanna**, P. Lamare Internal Note ANTARES-Note 5 ASS 02 58B
[33] **G. Lamanna,** Internal Note ANTARES- Note 5-ASS-02-62-A
[34] **G. Lamanna** et al. , Internal Note ANTARES – Cali/2005-05
[35] **G. Lamanna** et al. , Internal Note ANTARES – Cali/2006-03
[36] A.M. Hillas, Proceedings of 19th ICRC, La Jollan (1985).
[37] F. Dubois, **G. Lamanna** and A. Jacholkowska, Astropart. Phys. 32 (2009) 73-88
[38] F. Dubois, PhD Thesis, LAPP, Annecy (2009) (**G. Lamanna** directeur de thèses)
[39] J. Carr, **G. Lamanna,** J. Lavalle, Rep. Prog. Phys. 69 (2006) 2475-2512
[40] **G. Lamanna,** Modern Physics Letters A, vol.18 (2003) n.28, 1951
[41] **G. Lamanna**, Proc. "SNGHEGE", 2007.
[42] P. Brun, PhD Thesis, LAPP, Annecy (2008)
[43] E.W. Kolb, M.S. Turner, 1990, The Early Universe, Éditions Frontiers in Physics
[44] L. Bergström, P. Ullio, J.H. Buckley, Astropart. Phys., 9 (1998) 137
[45] J.F. Navarro, C.S. Frenk, S.D. White, Astrophys. J., 462 (1996) 563
[46] A.V. Kravstov, A.A. Kyplin, J.S. Bullock, J.R. Primack, Astrophys. J., 502 (1998) 48
[47] B. Moore et al., Mont. Not. Roy. Astron. Soc., 310 (1999) 1147
[48] G. Bertone, D. Hooper, J. Silk, Phys. Rept., 405 (2005) 279

[49] G. Lambard, Stage Master 2, CPPM, Marseille (2005) (**G. Lamanna** maitre de stage)
[50] G. Servant, T. Tait, Nucl. Phys., B, 650 (2003) 391
[51] G. Lambard, PhD Thesis, CPPM, Marseille (2008)
[52] M. Lemoine-Goumard, PhD Thesis, LLR, Paris (2006)
[53] A. Harding, et al., Proc. Conf. Intern. Symp. on High En. γ-Ray Astronomy, Heidelberg (2004).
[54] D. Horns et F. Aharonian, Proc. Conf. 5th Integral Workshop (2004)
[55] F. Dubois, **G. Lamanna** et al. for the H.E.S.S. collaboration. Proc. ICRC, 2009
[56] F. Dubois, **G. Lamanna** et al. for the H.E.S.S. collaboration. (to be submitted)
[57] J. Masbou, **G. Lamanna** et al. for the H.E.S.S. collaboration. Proc. ICRC, 2009
[58] A. Fiasson, **G. Lamanna** et al. (to be submitted)

ANNEXE A

- **G. Lamanna**, Proc. Suppl. Nuclear Physics B , 113 (2002) 177-185
- **G. Lamanna** et al. , Internal Note ANTARES – Cali/2005-05
- **G. Lamanna** et al. , Internal Note ANTARES – Cali/2006-03
- J. A. Aguilar, .., **G. Lamanna** et al. Astropart. Physics 26 (2006) 314-324
- F. Dubois, **G. Lamanna** and A. Jacholkowska, Astropart. Phys. 32 (2009) 73-88

ELSEVIER

Nuclear Physics B (Proc. Suppl.) 113 (2002) 177–185

NUCLEAR PHYSICS B
PROCEEDINGS
SUPPLEMENTS

www.elsevier.com/locate/npe

High-energy gamma-ray detection with the Alpha Magnetic Spectrometer on board the International Space Station

G. Lamanna[a] *

[a]CERN, European Organization for Nuclear Research,
1211 Geneva 23, Switzerland

The Alpha Magnetic Spectrometer (AMS) is a large acceptance, superconducting magnetic spectrometer designed to search for anti-matter and to study, with high accuracy, the origin of dark-matter and the composition of cosmic rays. The results of a Monte Carlo (MC) simulation study of AMS as a high-energy γ-ray detector are presented. AMS will be able to provide accurate measurements of γ-ray spectra over a broad energy range (up to hundreds of GeV) with energy resolution of a few per cent and angular resolution of 0.018-1°. The acceptance of 0.04-0.13 m^2sr has been estimated with maximal opening angle being 20° to 42°. The study of the background events has been done, the irreducible background-to-signal ratio being at the level of a few per cent or below being. The γ-ray sky survey sensitivity of AMS is finally discussed.

1. Introduction

A decade of operation of the Energetic Gamma Ray Experiment Telescope (EGRET) [1], on board the Compton Gamma Ray Observatory (CGRO) [2], has provided the first accurate long-term high-energy (0.1 up to 30 *GeV*) γ-ray sky survey. The EGRET operation has been crucial for the identification of several classes of new gamma sources, such as extragalactic blazars, galactic pulsars, γ-ray bursters, as well as providing a measure of the diffuse emission both of galactic and extragalactic origins. The dynamic universe emerging from these measurements has generated much interest in high energy γ-ray detection: a new generation of space-born γ-ray telescopes AGILE [3] and GLAST [4] are currently under construction. They will extend the survey up to 50 *GeV* and $\sim$ 300 *GeV* respectively.

In this context, it is interesting to analyze the sensitivity for energetic photon detection of the Alpha Magnetic Spectrometer, a large acceptance particle detector which will be operating on the International Space Station for three years, starting in 2005. The AMS experiment has been proposed to search for antimatter in the Universe on the level of less than 10^{-9}, to search for dark matter and to make high statistics measurements of cosmic rays composition over a broad energy range.

A reduced version of the detector was flown and operated successfully during a 10-day shuttle flight in June 1998[2] [5].

2. The AMS-02 detector

The major elements of AMS-02 Detector are shown in Fig.1 and consist of a superconducting magnet, a gaseous transition radiation detector (TRD), a silicon tracker (Tracker), time of flight hodoscopes (ToF), a ring imaging Cerenkov detector (RICH), an electromagnetic calorimeter (ECAL) and anticoincidence Veto counters.

The superconducting magnet has the shape of a cylindrical shell with inner diameter 1.2 m and length 0.8 m and provides a central dipole field of 0.8 Tesla.

The eight layers of double sided silicon tracker are arrayed transverse to the magnet axis. The tracker measures the trajectory of relativistic singly charged particles with an overall accuracy

*This work has been partially supported by INFN & Department of Physics, Perugia University, Italy and by DPNC, Université de Geneve, Switzerland.

[2]NASA mission STS-91

PII S0920-5632(02)01839-X

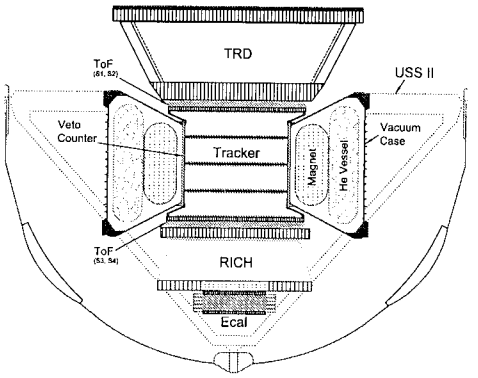

Figure 1. Schematic view of the AMS-02 experiment which will operate on the International Space Station.

of about $10\,\mu$ in the bending coordinate and $30\,\mu$ in the non-bending one, as well as provides measurements of the particle energy loss. The time of flight system has four layers, measures singly charged particle transit times with an accuracy of 140 psec and also yields energy loss and coordinate measurements. The TRD is situated on top of the spectrometer and consists of twenty 12 mm thick foam radiator arrays, interleaved by arrays of 6 mm diameter gas proportional tubes filled with Xe/CO_2 mixture. The TRD provides the e^-/hadron separation better than one hundred up to energy 200 GeV as well as precise charged particle coordinate measurements. The RICH detector is installed below the last ToF plane and consists of a 2 cm thick aerogel radiator with refraction index of 1.05, a reflection mirror and pixel type photo-tubes matrix for the light detection. It assures the measurement of the velocity of the single charged particle with accuracy better than per mil as well as particle flight direction measurement. The ECAL detector is situated at the bottom of AMS. It is a three-dimensional electromagnetic sampling calorimeter with total length of $15X_0$, consisting of 1 mm diameter scintillating fibers sandwiched between grooved lead plates.

3. AMS02-γ Detection Capabilities

3.1. The Monte Carlo Simulation

The AMS-02 Detector geometry and performance were simulated with the dedicated AMS simulation and reconstruction program based on GEANT package.

The simulated performance of the AMS subdetectors was checked against test flight and prototype test beam data and found to be in good agreement with them. In addition, 1 to 2 % of the subdetectors readout channels were assumed dead.

3.2. Signal and Backgrounds

To detect photons in the AMS experiment two complementary methods were explored. The first method or *conversion mode* consisted in the identification and reconstruction of e^+e^- pairs from γ conversions happened somewhere in the material upstream of the first silicon tracker layer, while the second or *single photon mode* was based on the detection of photons in the electromagnetic calorimeter.

The dominant cosmic ray components are the p, following by He and C nuclei and then e^-s, representing the backgrounds to the (tiny) γ signals. Fig. 2 shows the assumed signal and background fluxes for the AMS energy range.

To get a background-to-signal ratio of the order of a few per cent or below an $O(10^4)$ to $O(10^6)$ background rejection level should be obtained.

The simulated events were triggered by either the coincidence of signals in three out of four ToF planes or large energy deposit in the ECAL [6].

Finally, more than 10^9 events containing p, He, $e^{\pm}$ and γ, at different energies, have been fully simulated passing through the detector and then reconstructed.

3.3. The Conversion Mode

The event signature for this mode was two reconstructed tracks in the Tracker coming from a common vertex located somewhere upstream of the first tracker layer[3].

[3]The material in front of the first silicon tracker plane, consisting of the TRD, the first two layers of ToF scintillators, and mechanical supports, represents $\simeq 0.23X_0$ [7].

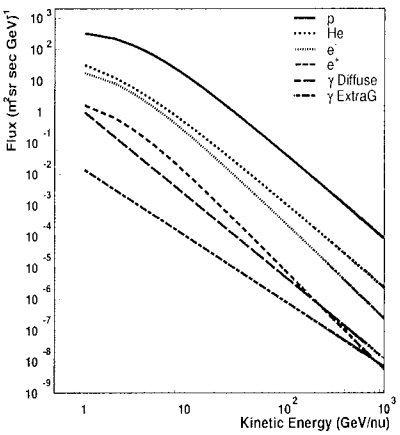

Figure 2. The charged cosmic-ray (*background*) and diffuse γ (*signal*) energy spectra.

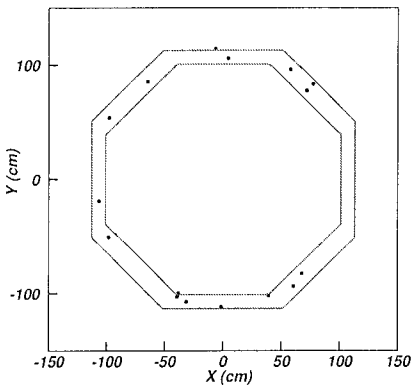

Figure 3. AMS horizontal projection (top view): impact points of a few survived background events by interpolating the reconstructed direction up to the top of the detector. They impinged and entered the detector through the side edges of the TRD octagon mechanical structure producing secondaries. The surface between the two octagons is the exclusion region.

3.3.1. Event Selection and Background Rejection

The main issue of the events selection study concerned the pattern recognition and track finding for double track events originating from a common vertex.

Primary γ-ray energy and incidence direction were determined by adding the fitted momenta vectors of $e^{\pm}$ pair, evaluated at the entrance of the AMS detector.

The main source of background came from p and e^-, which interacted with the AMS materials, producing secondaries, mainly delta rays within the spectrometer and were reconstructed as double-track events, mimicking the e^+e^- from γ conversion. The flux of genuine photon events generated in the vicinity of the AMS, namely in the ISS body and solar panels, was found to be small compare to the cosmic one.

The following criteria were applied to reject background events:

- Identify events with interactions;
- Identify charged particles entering the TRD from the top and lighting all the tubes along its reconstructed trajectory.
- Identify large reconstructed invariant mass events.
- Identify particles entering the fiducial volume of the AMS by passing through the side of the TRD (Fig.3).

Table 1 shows the obtained rejection factors for different cosmic ray species after all cuts [8] have been applied.

Table 1
Rejection factors obtained for p and e^- cosmic-ray particles.

Particles	Rejection Factor
e^-	$> 1. \times 10^4$
p	$> 8. \times 10^5$

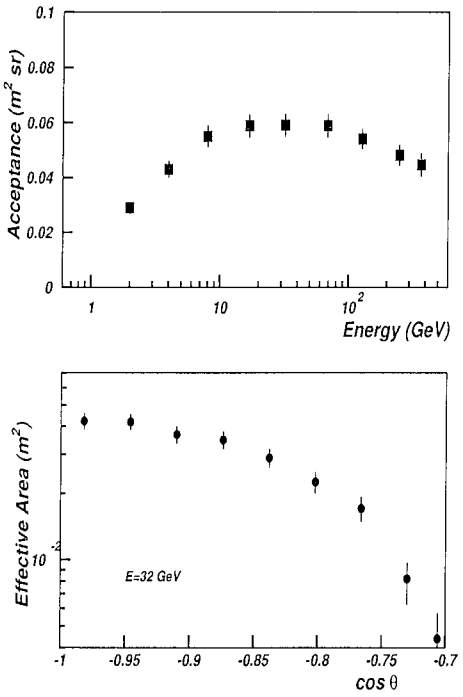

Figure 4. Conversion mode: AMS acceptance as a function of γ-ray energy (top panel). Differential acceptance $A(E,\theta)$ versus zenith angle at 32 GeV (bottom panel).

3.3.2. Results

The AMS-02-γ simulated detection through the *pair conversion method*, yielding the results as shown in Fig.4. The detector acceptance is shown as a function of the γ-ray energy between 1 and 400 GeV. It was a result of three main contributions: the AMS geometrical acceptance, the pair conversion probability, the double-track reconstruction efficiency and event selection efficiency[4].

Above 200 GeV the $e^{\pm}$ pair detection was limited by the double-hit resolution of the Tracker.

[4]Double-track reconstruction and event selection optimization is still pending, therefore the current results have to be considered preliminary.

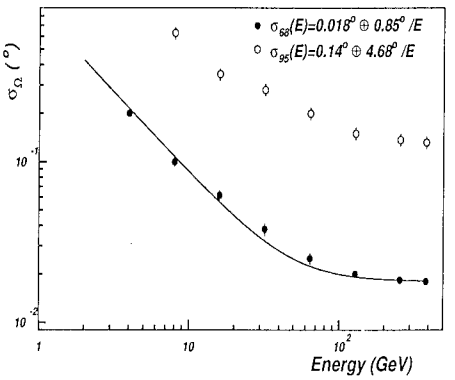

Figure 5. Conversion mode: AMS angular resolution as a function of the photon energy .

Within 7 to 200 GeV the detector acceptance was at the *plateau* value of 0.058 m^2sr. The AMS-02-γ effective area is shown in Fig.4.(bottom). It had a maximal opening angle of about 42°.

For most of the events energy resolution was dominated by multiple scattering and tracker measurement errors and was parametrized as $\frac{\sigma(E)}{E} = 0.03 \oplus 0.5E(TeV)$. Due to the hard bremsstrahlung radiation by e^+e^- pairs in the AMS materials a sizable fraction[5] of the photon events had the reconstructed energy differed from the nominal one by more than 5 standard deviations defined above. Finally the angular resolution (Fig.5) ranged from 0.4^o to 0.018^o, due mainly to the multiple coulomb scattering. The energy dependence of angular resolution was parametrized as $\sigma_{68}(E)=0.018^\circ \oplus \frac{0.85^\circ}{E(GeV)}$.

3.4. The Single Photon Mode

The event signature for this mode was the presence of electromagnetic-type energy deposition in the ECAL, while almost nothing was found in other AMS sub-detectors.

[5]10 to 30 % depending on photon energy

3.4.1. Event Selection and Background Rejection

The identified backgrounds to the genuine γ signal were events with charged particles[6] either passing undetected in the gaps of the AMS active tracking volume or entering the ECAL from the side.

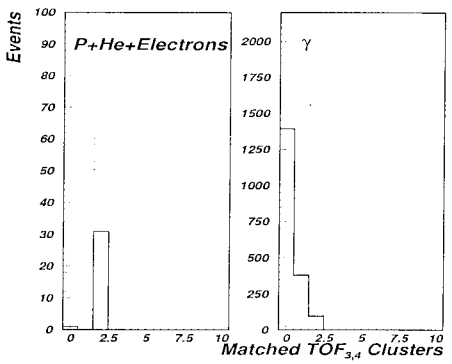

Figure 6. The distribution of the number of the ToF hits found near the reconstructed particle trajectory in the two bottom ToF planes for signal (right panel) and background (left panel) events. The arrows show the value of the cut applied.

The following main criteria were applied to reject background events:

- Identify p, He by analyzing 3-dimensional shower in ECAL;
- Identify charged particles by requiring the trajectory direction of the reconstructed ECAL shower to pass inside AMS sensitive volume and reject events with the signals in various AMS sub-detectors around it. Fig. 6 shows the distribution of the ToF hits found near the reconstructed particle trajectory for the signal and background events.

Table 2 shows the obtained rejection factors for different cosmic ray species after all cuts [9] have been applied.

[6] mostly e^-, p and He nuclei

Table 2
Rejection factors obtained for various cosmic ray particles.

Particles	Rejection Factor
$e^{\pm}$	$> 53 \times 10^3$
p	$(2.5 \pm 1) \times 10^6$
He Nuclei	$> 1.7 \times 10^6$

3.4.2. Results

Fig. 7 shows the obtained average and differential acceptances after all cuts have been applied. The average acceptance is situated around 0.58 m^{2}sr with maximal open angle around 22°. The relative energy resolution was parametrized as $0.03 \oplus \frac{0.13}{\sqrt{\mathrm{E}(GeV)}}$ up to 2 TeV, and angular resolution as $\sigma_{68}(E)$=$0.9° \oplus \frac{8.5°}{\sqrt{\mathrm{E}(GeV)}}$.

3.5. Diffuse Spectra Detection

Combining the above two photon detection methods, we simulated the AMS 3 year measurement of the photon spectra for Galactic and Extragalactic diffuse spectra [1], which is shown in Fig. 9 [9].

3.6. Point Source Sensitivity

A detector's key figure of merit for the identification of some astrophysical point sources of γ-rays as blazars and GRBs, is its *point source sensitivity*. It is defined as the minimum source flux required to achieve a specified level of detection significance. The significance S of a detection is given schematically by:

$$S(> E_t) \sim \frac{N(> E_t)}{\sqrt{B(> E_t)}}, \qquad (1)$$

where $N(> E_t)$ and $B(> E_t)$ are respectively the total number of detected photons from the source and the number of background photons falling within the source area above an energy E_t. E_t is usually the instrument's threshold energy. N and B are a function of the effective detection area $A(E)$ of the instrument, its angular resolution expressed as a solid angle $\Omega(E)$, the viewing time t, and the differential source and background

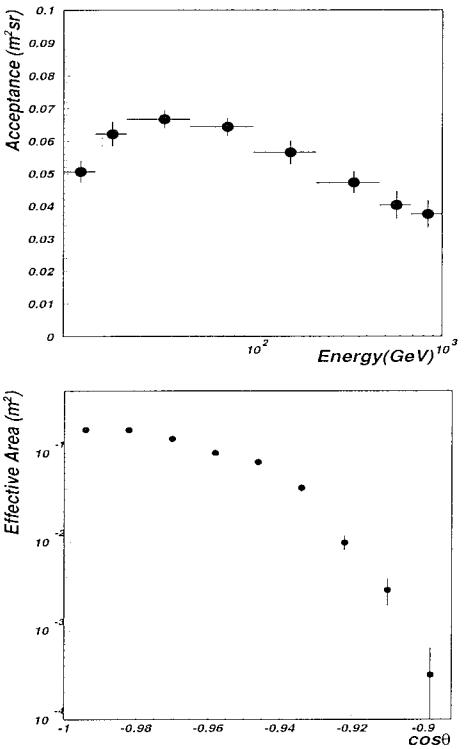

Figure 7. Single Photon Mode: AMS acceptance as a function of energy (top panel). Effective area $A(E,\theta)$ versus zenith angle at 50 GeV (bottom panel).

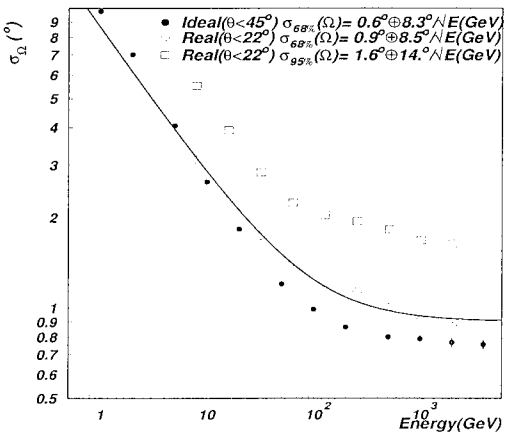

Figure 8. Single photon mode: Angular resolution as a function of the photon energy; *full circle marker*: ideal (γs generated immediately outside the Ecal)(68%) resolution within 45° maximum zenith angular aperture; *empty circle (square) marker*: real 68% (95%) resolution within the effective 22° field of view.

spectra dN/dE and dB/dE,

$$N(>E_t) = \int_{E_t}^{\infty} \frac{dN}{dE} A(E) t dE, \quad (2)$$

and

$$B(>E_t) = \int_{E_t}^{\infty} \frac{dB}{dE} A(E)\Omega(E) t dE. \quad (3)$$

All extragalactic objects (blazars) seen by EGRET are well represented by power law spectra

$$\frac{dN}{dE} = n_0 \left(\frac{E}{1GeV}\right)^{-\alpha} (cm^2 sGeV)^{-1}, \quad (4)$$

where α is the differential spectral index of the source, and n_0 is the differential flux at 1 GeV. We define our point source sensitivity as that value of n_0 which gives a 5σ signal integrated over the period of one year of operation of AMS. It is evident that the point source sensitivity is a function of the source's spectral index; for these calculations we have assumed a source differential spectral index of α=2, which is close to the mean of the source spectral indexes of blazars observed by EGRET [10].

The background flux dB/dE contains components from the isotropic extragalactic γ-ray background radiation and from the galactic diffuse radiation (the latter due to the decay of π^0s produced in collision of cosmic rays with the interstellar medium). The former has been determined by EGRET to be [11]:

$$\frac{dB_{extragal.}}{dE} = \Phi_0 \times \left(\frac{E}{k_0}\right)^{\epsilon} (cm^2 ssrGeV)^{-1}, \quad (5)$$

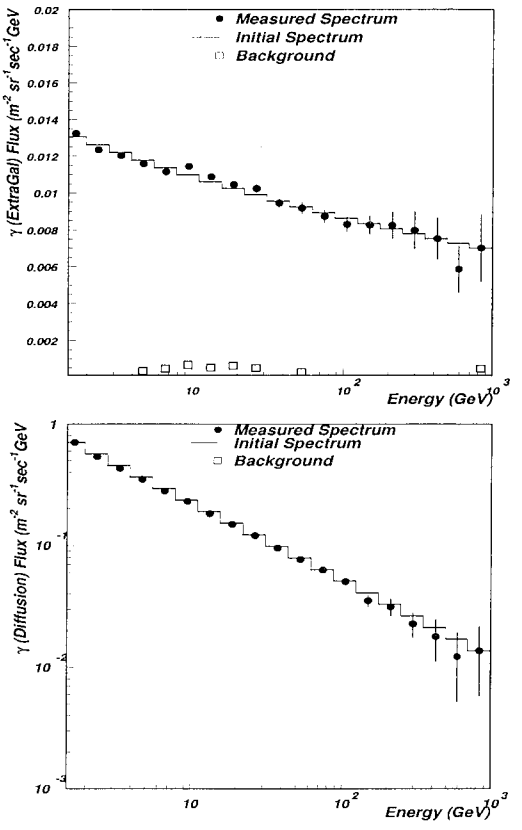

Figure 9. Examples of the AMS three years combined measurement of the cosmic photon spectra: Galactic (bottom panel) and Extragalactic (top panel).

where $\Phi_0=(7.32 \pm 0.34) \times 10^{-6}$ (cm^2 s sr GeV)$^{-1}$, $k_0=0.451$ GeV and $\epsilon=2.10 \pm 0.03$.

The galactic diffuse radiation is a strong function of position in the sky, and been measured and modeled by the EGRET group [12]. We have used here their data[7] to generate background spectra dB/dE over 2^o in galactic latitude b and longitude l. The solid angle $\Omega(E)$ over which the background must be integrated when viewing a source is given by $\Omega(E)=\pi\sigma_{68}^2(E)$, where σ_{68}, following the EGRET's usage, is defined as the angular radius within which 68% of the source photons fall (for the energy dependence parameterizations of the σ_{68} § 3.3.2, § 3.4.2). AMS will be

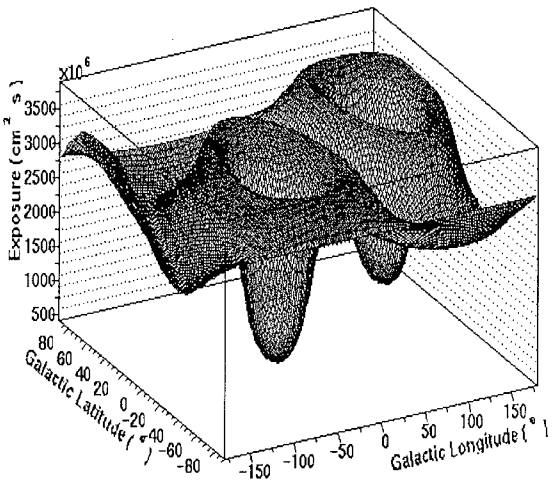

Figure 10. Accumulated effective-area×viewing-time product over one year of AMS operation as a function of galactic coordinates (both Ecal and Tracker contributions have been summed up).

rigidly attached to the ISS which itself will be in 51.6^o inclination orbit, AMS will not spend equal amounts of time viewing all directions in the celestial sphere. Full sky coverage is obtained about 5.3 times per year due to the precession of the orbital plane of the ISS about Earth's pole. Because of this precession, the viewing area × time product over the sky is only a function of E (because the effective area will depend on it) and celestial coordinates. By following the orbit of AMS over one year, the effective area $A(E,\theta)$ × the time spent by the detector viewing a specific zone in the sky within a specific viewing inclination $d\theta$ has been calculated and then integrated over the full viewing θ range (up to 45^o with tracker and 22^o with ECAL). The time intervals when ISS orbits over the SAA region have been subtracted. The resulting *exposure* is shown in Fig. 10.

[7] http://tigre.ucr.edu/halo/repro.html

A preliminary estimation of a 5σ point source sensitivity has been obtained. For any given position in the sky, that computed value of n_0 which gives S=5 starting from a chosen threshold energy E_t is the point source sensitivity for that sky position. Averaging over all longitudes for two latitude ranges, galactic ($|b|<10^o$) and extra galactic ($|b|>10^o$), the AMS-*conversion mode* one year (E_t=1 *GeV*) sensitivities are about 1.5×10^{-8} ph. cm^{-2} s^{-1} and 10^{-9} ph. cm^{-2} s^{-1} respectively (see Fig. 11 for $|b|>10^o$ details). While the AMS-*Ecal single photon mode* one year (E_t=10 *GeV*) sensitivities are 10^{-8} ph. cm^{-2} s^{-1} and 2.5×10^{-9} ph. cm^{-2} s^{-1} respectively.

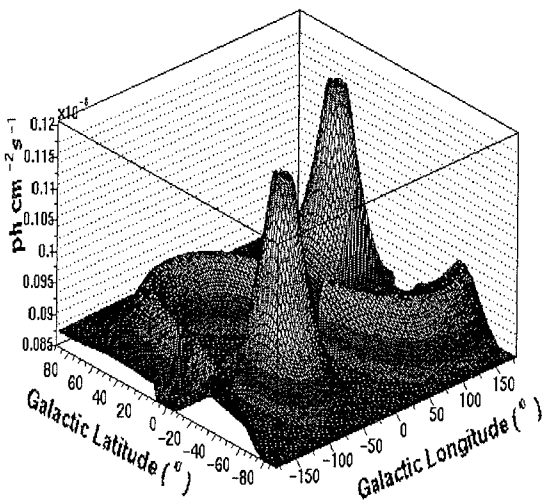

Figure 11. AMS02-*conversion mode* extragalactic point source sensitivity n_0 versus galactic coordinates.

3.6.1. Source counts

EGRET has detected more than 60 blazar AGNs with a mean redshift near z=1 and more than 10 unidentified likely blazar γ-ray sources. AMS will detect about one thousand such objects. In Fig. 12 we have deduced such expectation by

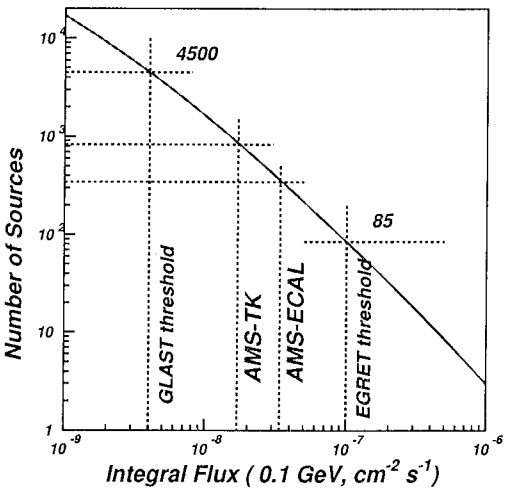

Figure 12. Estimate of the number of AGNs that AMS will detect at high latitude in a 2-year sky survey compared to EGRET's approximate detection limit and GLAST expectation [14].

comparing the AMS sensitivity with the gamma-ray log N - log S relation for AGNs [13]. Note that we have defined our flux sensitivity in terms of the differential flux at 1 GeV (not 0.1 GeV). To place the *equivalent* AMS sensitivity on this figure we have assumed a nominal E^{-2} differential source energy spectrum.

4. Conclusions

The results of the MC simulation study of AMS as a high-energy γ-ray detector have been presented. As inferred from the analysis of the detector's performance, the AMS effective area together with its angular resolution and long exposure time, represent an useful combination for the investigation of the γ-ray sources in the sky.

5. Acknowledgements

I wish to thank my AMS colleagues and in particular the members of the gamma working group

for the fruitful discussions and cooperations.

REFERENCES

1. R.C. Hartman et al., Ap.J. S. 123, p.79, 1999
2. J.D. Kurfess et al., AIP 410, p.509, 1997
3. S. Di Cocco, this Conference Proc.
4. R. Johnson, this Conference Proc.
5. J. Alcaraz et al., Ph. Rep. 366/6, 331, 2002
6. C. Goy, S. Rosier-Lees, *AMS Internal Note* **06-04**,(2001). E. Choumilov *AMS Internal Note* **06-05**,(2001).
7. B. Bertucci, G. Lamanna et al., *Proc. XXVII ICRC* (2001).
8. G.Lamanna http://ams.cern.ch/AMS/Analysis /gamma-pos/lastpre.ps
9. V.Choutko http://ams.cern.ch/AMS/Analysis /hpl3itp1/ams02sg.ps
10. R. Mukherjee et al., Ap.J. 490, p.116, 1997
11. P. Sreekumar et al., Ap.J. 494, p.523, 1998
12. S.D. Hunter et al., Ap.J. 481, p.205, 1997
13. F.W. Stecker, M.H. Salamon, Ap.J. 464, p.600, 1996
14. GLAST Science (http://glast.gsfc.nasa.gov)

ANTARES-Cali/2005-05

Time calibration of the MILOM optical modules.

V. Bertin, J. Busto, P. Coyle, G. Lamanna, M. Melissas

Abstract

In this note we summarize the procedures and results of the optical modules time calibration performed in the CPPM dark room during the MILOM integration. We report also about the validation of the calibration by comparing the results with the analysis of data taken after the MILOM deployment in the ANTARES site.

Introduction

The angular resolution of the ANTARES detector is one of the most relevant and competitive figures of merit of the experiment for the successful detection of astrophysical sources of high-energy neutrinos. The neutrinos direction reconstruction depends on the capability to follow the evolution of the particle path in space and time. For such a purpose a fast read out response of the optical modules is critical, also mandatory is the correction of any time response offset among different OMs. In this note we describe the experimental set-up used for the dark room calibration and the methodology to measure such offsets. The different steps of analysis are also detailed. The resulting offsets between different ARSs in the MILOM will be studied as a function of other critical parameters, i.e. OMs High Voltage and light intensity. We report also about the results of the detector time resolution study in dark room as well as in the sea.

1 Set-up description

The layout of the experimental hall at CPPM, dedicated to the integration, tests and calibrations of the ANTARES detector, is detailed elsewhere [1]. The set-up for the dark room tests of the MILOM is based on an upgrading and optimization of the configuration adopted early for the prototype sector line as described in [2]. Here we remind briefly that after integration the MILOM is moved into the dark room. During tests the dark room is kept closed. The LCMs are cooled during operation.
For the relative time calibration of the ARSs we want to know the time offset between OM's responses to a synchronous signal. Such a signal is provided by a laser equipped with an optical system sitting into the control room. An optical fiber brings the laser light from the control room to the dark room and then distributed simultaneously to the OMs by a 1-to-16 optical splitter also located into the dark room. Sixteen optical fibers are connected at the output of the splitter. These fibers are then used to bring the laser light to all the 4 OMs: 3 OMs connected to the MLCM (hereafter conventionally named OM1, OM2, OM3 of the LCM3) and 1 OM which equips the top storey (OM1 of the LCM4). See fig.1 for the MILOM layout. The end of each fiber is fixed on a cylinder (the *flower pots* as shown in fig.2) which contains the OM. At the bottom of every cylinder, where the fibers are attached, a diffuser allows the spreading of the laser light on the sensitive hemisphere of the OM inside the cylinder and then on the photocatode [2]. The OMs were supplied with High Voltages which allow for the nominal gain of 5×10^7.

2 Laser system

The laser used is similar to the one in the Laser-Beacon: it is the model NG-10120-120 supplied by Nanolase. This laser emits intense (1 μJ), short (FWHM ~ 0.8 ns) light pulses at 532 nm (green light). Its repetition frequency can be set between 1 Hz and 1 kHz (for the tests, 100 Hz frequency was chosen). The light from the laser needs to be attenuated from a nominal value of about 10^{12} p.e. equivalent to a few photoelectrons before being sent to the OMs. For this purpose an optical system for light attenuation tuning has been built ([1]) consisting of the following elements: a 4mm focal distance ocular to diverge the collimated laser beam, a variable aperture (down to 0.2 - 0.3 mm) iris diaphragm to select and transmit only a small fraction of the light spot, three absorptive neutral density filters, of 80%, 50% and 25% nominal transmittance and a Lambertian diffuser. The laser light intensity is tuned by varying the combination of the absorptive filters along the laser optical path. When the intensity variation required for the calibrations is limited to a small fraction, it is sufficient

for the operator to handle the micrometer screw of the laser pedestal which allows introducing a small offset in the laser beam alignment w.r.t. the optical path direction.

The main application of the laser is to inject light into the OMs of each sector line to reproduce in the dark room similar operational conditions to those in the sea. This allows calibration and functionality tests of the active elements of the detector before deployment.

In order to test also the timing response of the detector to the photons arriving from the laser and impinging on the photocathodes, a laser synchronous time reference signal is used. For every light pulse a photo-diode internal to the laser provides such a signal, which is stable in amplitude and with less than five nanoseconds rise time. An independent reference LCM_REF dedicated to the read-out of the photo-diode signal is foreseen for the detector line integration. For the MILOM integration and calibration the SCM (LCM1) and specifically the ARS6 were used as LCM_REF devoted to the readout of the synchronous photo-diode laser reference signal.

3 The SPE time

The arrival time of each pulse (SPE_ITEM) is coded using a 50 ns resolution *timestamp* as provided by the LCM clock and the TVC (Time-to-Voltage Converter) value between 0 and 255 corresponding to the precise time of arrival inside the clock period. To get the exact time of each *spe* some corrections are needed. First of all a uncorrected timestamping is produced due to the misalignment of the starting of the TVC slope with the clock timestamp. This offset correction is generally applied and more details about it can be found in [2].

3.1 TVC calibrations

For each ARS, two TVCs (TVC A and TVC B) are used sequentially, they are needed because the time the electronics takes to come back from the maximum slope value to the minimum is not negligible at the high precision we work [2]. Ideally TVC values of 0 and 255 bits would correspond to 0 and 50 ns respectively with a theoretical resolution of (50 ns / 255 bits) $\times 1/\sqrt{12} \simeq 0.06$ ns. We need to know the real transfer function bit/ns and the dynamic range of every TVC before adding the corresponding TVC value in ns to the *timestamp* of an *spe*. The TVC calibration methodology consists in plotting the TVC values (one histogram for each TVC; two per ARS, i=1,2). For each histogram, the average (*ave*) occupancy over the 256 bins is computed. The lower and upper bounds were defined as the first bin (T_min) the last bin (T_max) in which the number of entries exceeds 10% of *ave*. With the assumption that the real dynamic response of the TVC be still linear[1)], the slope of the transfer function is computed as T_slope (bit/ns) = (T_max - T_min) / 50 ns.

In Fig. 3 an example of TVC histograms for the OM1, OM2, OM3 of the LCM3 (MLCM) is shown. Equivalent distribution for the same run have been studied for the OM1 of the LCM4. The TVC calibrations performed with dark-room data are used to calibrate the sea data taken immediately after deployment. The time stability of the results of the calibrations are also monitored in the sea. The results of the calibrations are reported in Fig. 4 where T_max and T_min are shown for two calibration runs, one in the dark room and one more during data taking in the sea some time after MILOM connection. The comparison of the resulting T_slope (bit/ns) are shown in Fig. 5. In both figures we used the ARS numbering convention from 0 to 5 for the 3 OMs of the MLCM and 6,7 for the single OM of the LCM_TOP[2)].

[1)]The calibration for Differential-Non-Linearity DNL of the TVCs would allow an improvement of the final results of the time calibration. Such a study is still in progress and it will be detailed in a separate note [3]

[2)]The OM1 of the LCM_TOP has not been working since the MILOM deployment , therefore any comparison with

3.2 OMs' Time Offset Calibration

The purpose of the Dark Room OM time calibration is to measure the characteristic time-offset for each OM, which is due to the specific PMT transit time and the front-end electronics. Such time-offsets are then stored in the database and retrieved at the time of sea data taking in order to correct the relative delays between the OMs and realign in time the SPE-time of each OM. The dark room calibration of the relative delays of the OMs is a redundant validating measurement of the same calibration which is expected to be performed after deployment in the sea by mean of the LED beacon system.

The methodology of the calibration consists of the measurement of the time difference between two coincident signals: the reference time of the laser pulse (provided by the laser internal photodiode) and the arrival time of the hit registered by the OM: T_{PD-ref} - T_i. The distribution of the difference between these signals are then analyzed within a time window of few hundreds of nanoseconds. These distributions will follow a Gaussian behavior whose mean value is the time offset of the specific ARS (ARS_T0) and the sigma is an estimation of the time resolution of the system. Before to proceed two basic corrections have to be applied in order to get the best results of the time calibrations: walk effect correction and fiber lengths offsets correction.

3.2.1 Walk effect correction

The walk effect is caused by variations in the amplitude of pulses coming from the PMs and discriminated by the ARSs at a fixed voltage threshold. Coincident signals but with different amplitudes will cross the threshold at different times. The ARSs' walk effect has been already studied and parameterized [4]. The correction to be applied consists in the estimation of such walk by monitoring the response of the ARSs at laser pulses of different intensities. Then the delays introduced by the walk effect are systematically subtracted to all spe-times , as a function of the total integrated charge of the signals by which they are generated.

For every ARS the T_{PD-ref} - T_i distribution is examined as a function of the charge ad then fitting the profile of such correlation with the polynomial function:

$$\frac{p_0 + p_1 Q}{p_2 + Q}, \tag{1}$$

where p_i are the three free parameters of the fit and Q is the charge in pC (see Fig.6 for an example). The transformation AVC counts to pC is performed by applying the transfer function measured during electronics integration tests at IRES [5]. The best fit parameters p_i are then used to correct every spe-time of its own walk-delay. In Fig.15 we show the AVC counts *vs* (T_{PD-ref} - T_i) before correction and Q (to better illustrate the difference the charge Q has been plotted negative) *vs* (T_{PD-ref} - T_i) after correction. Finally in Fig.8 we show an example of the time-difference histogram before and after walk correction.

3.2.2 Fiber lengths correction

The laser light which is distributed to all OMs simultaneously follows different paths along different fibers starting from the 1-to-16 splitter to the diffusers of the OMs' containers. The correction for unequal fiber lengths has been measured by taking data in dark room and swapping the position of the four OMs among the four containers. Such test has allowed to quantify the difference in fiber

pre-deployment dark room tests is impossible.

lengths among the OMs. We choose the OM1 as reference and then we estimate the relative Δt_{12}=0.3 ns, Δt_{13}=0.1 ns and Δt_{14}=-0.3 ns within 0.1 ns uncertainty.

3.2.3 Results

In Fig.9 and Fig.10 the T_{PD-ref} - T_i for each ARS of all OMs are shown for a dark room run with high intensity laser. The distribution have a common offset of about 175 ns due to the difference between the optical path of the laser and the electric path of the PD reference signal. Such an offset has no influence since it is the relative time difference of the distributions which is relevant. The resulting offsets correspond to the relative difference between the mean value of the Gaussian fit of the time distribution of the ARS0 (OM1), which is taken as reference hereafter, and the mean value of the Gaussian fit of other ARSs. The resulting offsets are shown in Fig.11. In this figure dark room results are also compared with sea data after the MILOM connection using a dedicated LED beacon run (run number 11303).

In order to test the validity of the dark room calibration, we have applied the obtained OM offsets corrections to the LED beacon run 11303 in the sea. After correction the distribution of the differences between arrival times of LED optical photons on the OMs are well centered to 0 within 0.3 ns (see Fig.12,13,14). The large tails of the Δt distributions for the run 11303 are probably due to the light scattering and the afterpulses which are triggered with larger delay than the bulk of the hits, as suggested in [3] and [6]. A more detailed analysis is still in progress.

The stability of the timing calibration has been confirmed by monitoring the OMs response in the sea using dedicated LED beacon run (see Fig.15).

3.3 Time resolution

Among the tests foreseen in dark room during MILOM integration, the dependence of the OMs response as a function of HV was monitored. The photomultipliers response has been analyzed by varying the applied high voltage in 60V steps at fixed laser light intensity. These variations affect the electron transit time and the signal charge amplitude due to a larger multiplication. Indirectly this affects the OMs' time offsets making them smaller as HV increases, resulting in a reduction of about 0.8 ns (at +120 Volts) up to 2.2 ns (at +180 Volts).

In order to estimate the time resolution the system can attain, data with different laser light intensity have been taken in dark room. The OM time resolution has three independent contributions: σ_{TTS} due to the spread in the transit time of the photo-electrons laser pulse width, $\sigma_{syst.calib.}$ the resolution due to the calibration system and finally a constant contribution $\sigma_{elec.}$ related to the front-end electronics. This results in:

$$\sigma^2_{t_{OM}} = \frac{\sigma^2_{TTS}}{N_{pe}} + \frac{\sigma^2_{syst.calib.}}{N_{pe}} + \sigma^2_{elec.}, \tag{2}$$

where N_{pe} is the number of photoelectrons.

For each ARS the Gaussian sigmas of the time difference w.r.t. the PD signal, T_{PD-ref} - T_i, have been analyzed as a function of signal amplitude (integrated charge in PC). We have performed the best fit (see Fig.17) of the function

$$\sigma_{t_{OM}} = \sqrt{p0/x + p1} \tag{3}$$

where x corresponds to $N_{pe} \simeq$ charge(pC)/8 ; $p0$ corresponds to $\sigma^2_{TTS} + \sigma^2_{syst.calib.}$ which is actually dominated by the σ_{TTS} due to the transit time spread.; $p1$ corresponds to $\sigma^2_{elec.}$.

For all the ARSs we obtained the best fit parameters corresponding to $\sigma_{elec.} \simeq 0.3$ ns and a $\sqrt{\sigma^2_{syst.calib.} + \sigma^2_{TTS}} \simeq 1.5$ ns. From these results we can deduce that the best time resolution that we expect to attain in the sea for a high amplitude signal is of the order of 0.5 ns or even less. A crosscheck of this important figure of merit with sea data has been obtained with the LED beacon run 11928. From Fig.18 which shows an example of the distribution of difference in time between signals between adjacent optical modules in the MLCM, a time resolution $\sigma = \sigma_G/\sqrt{2} \simeq 0.5$ ns confirms the results obtained in dark room. Fig.18 shows reduced tails in the Δt distribution than those shown in Fig.12,13,14 for the run 11303. In the run 11928 the LED beacon was set-up with about 1/4 of the light intensity than in the run 11303, and only the top LEDs of the beacon are switched on. Finally to remove most of the secondary pulses only those hits with saturated AVC counts and TVC counts synchronous with the LED pulses were considered.

Conclusions

The results of the MILOM time calibrations in the dark room have been detailed and the stability of the calibration results in time *vs* sea data and redundant methodology with the LED beacon system have been illustrated.

References

[1] G. Hallewell, G.Lamanna, ANTARES Note 5-ASS-02-55-A.

[2] S.Karkar, Internal Note ANTARES-Cali/2003-003.

[3] J.A.Aguilar et al., Internal Note ANTARES-Cali/2005-XXX.

[4] J.S.Ricol, PhD thesis, 2002, CPPM.

[5] S.Loucatos, private communication.

[6] J.A.Hernandez Rey, private communication.

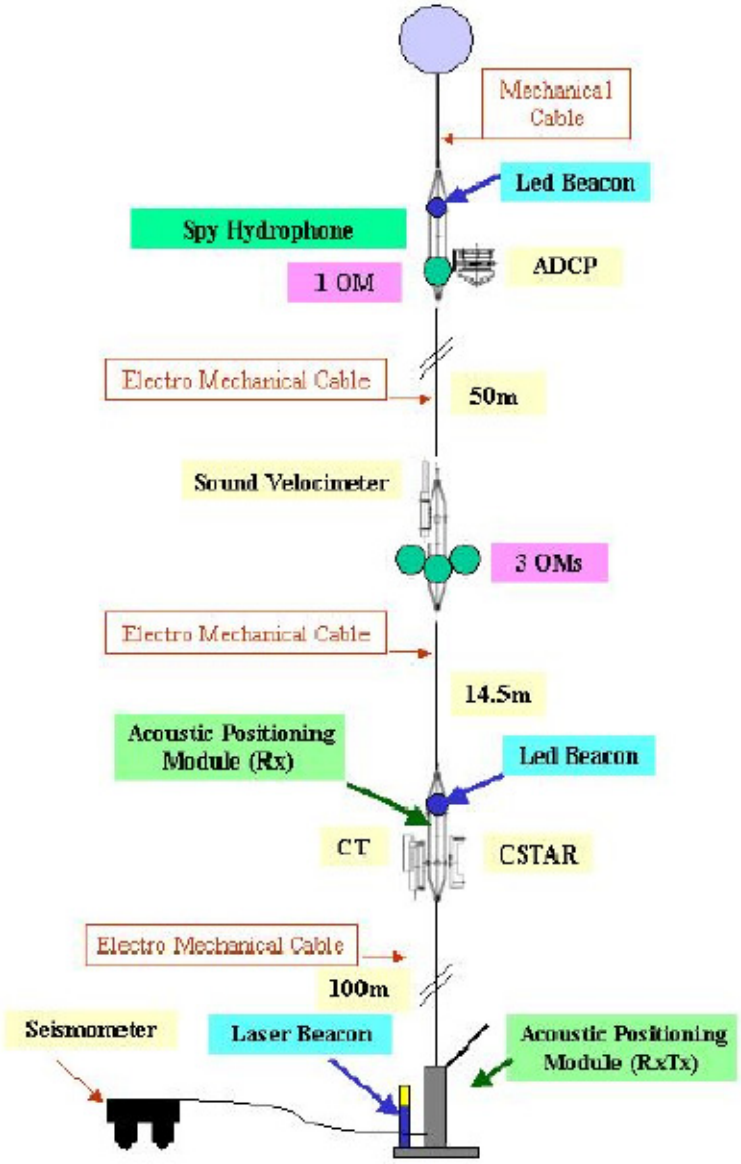

Figure 1: Layout of the instumental line MILOM.

Figure 2: Laser test of OMs in the Dark Room.

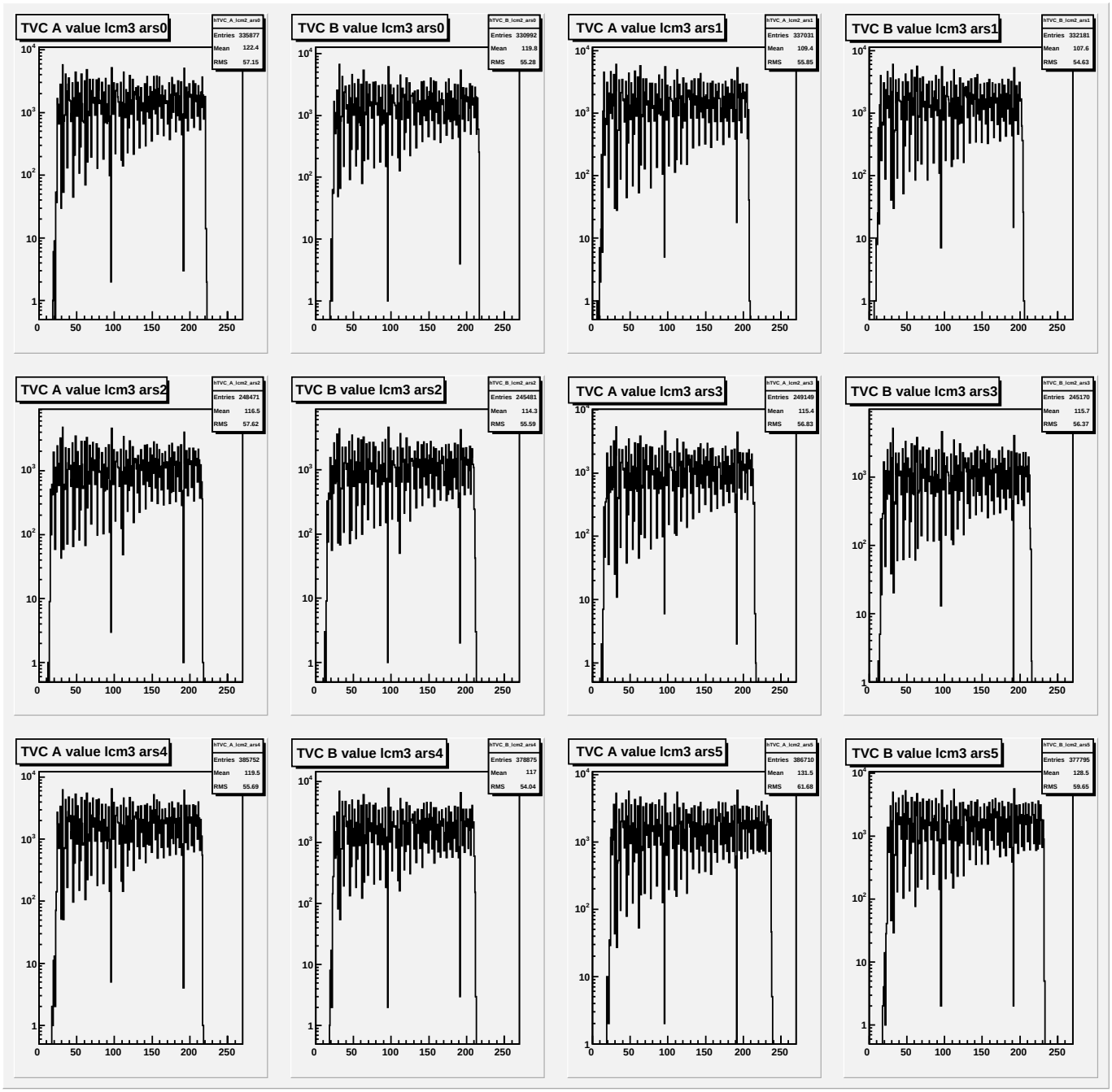

Figure 3: TVC occupancy histograms for the three OMs of the MLCM, during dark room calibrations. From top to bottom: TVCs related to the acquisition of the OM1 (ARS0 and ARS1), OM2 (ARS2 and ARS3) and OM3 (ARS4 and ARS5).

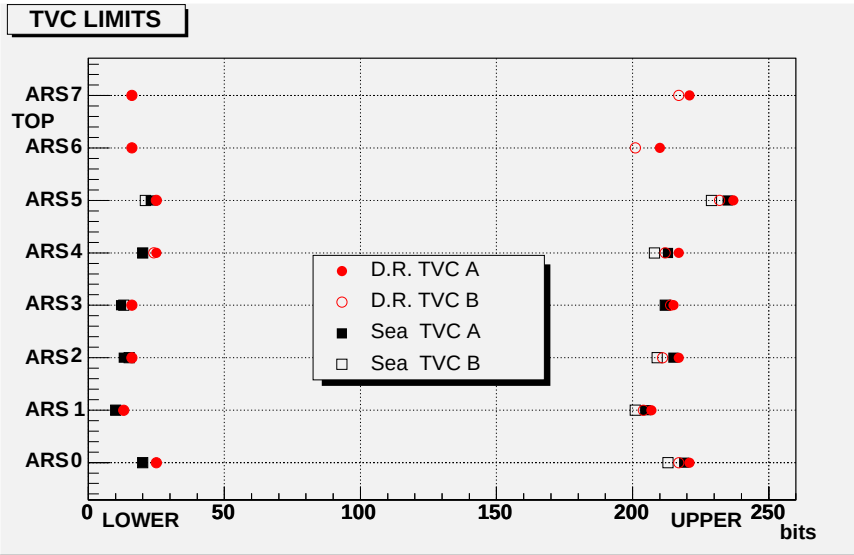

Figure 4: Upper and lower limits of the real dynamic range of the MILOM TVCs. The comparison between dark room and sea calibrations is also shown.

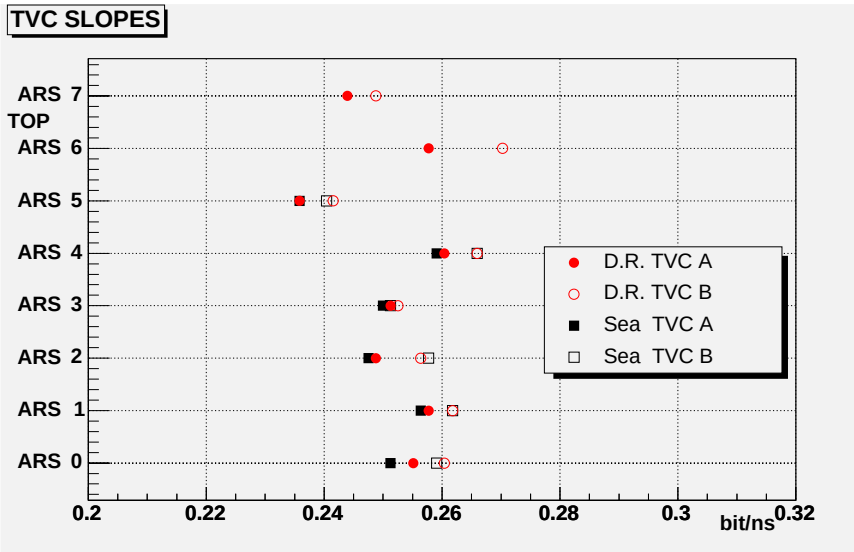

Figure 5: Slopes of the transfer function bit/ns computed for all TVCs of the MILOM. The comparison between dark room and sea calibrations is also shown (no sea data for OM_TOP).

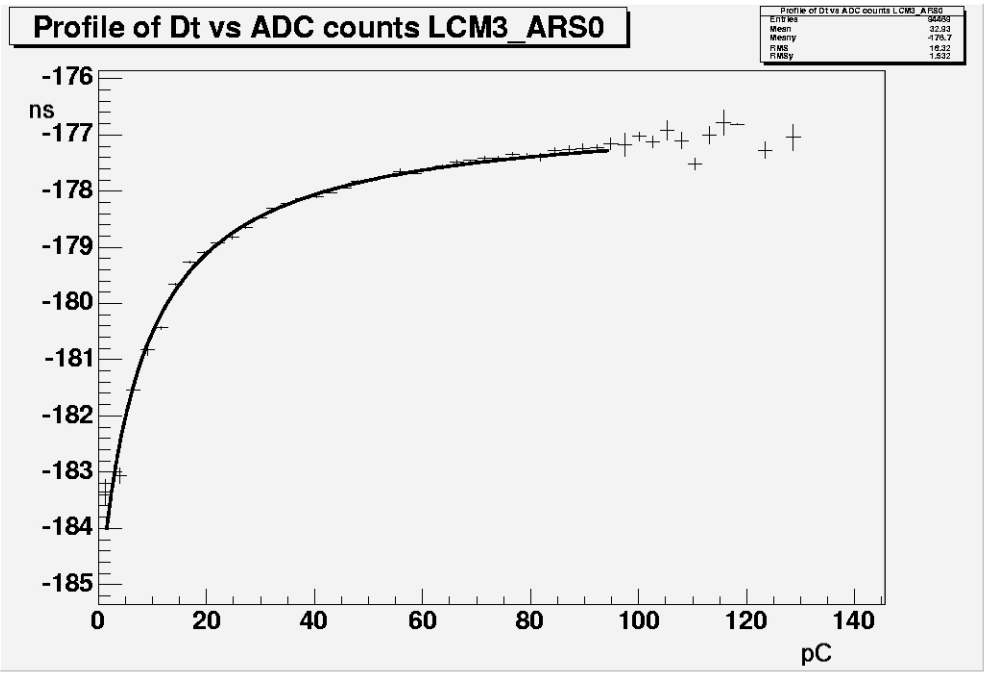

Figure 6: Example of best fit of walk function to the time-charge correlation for the ARS0 of the OM1.

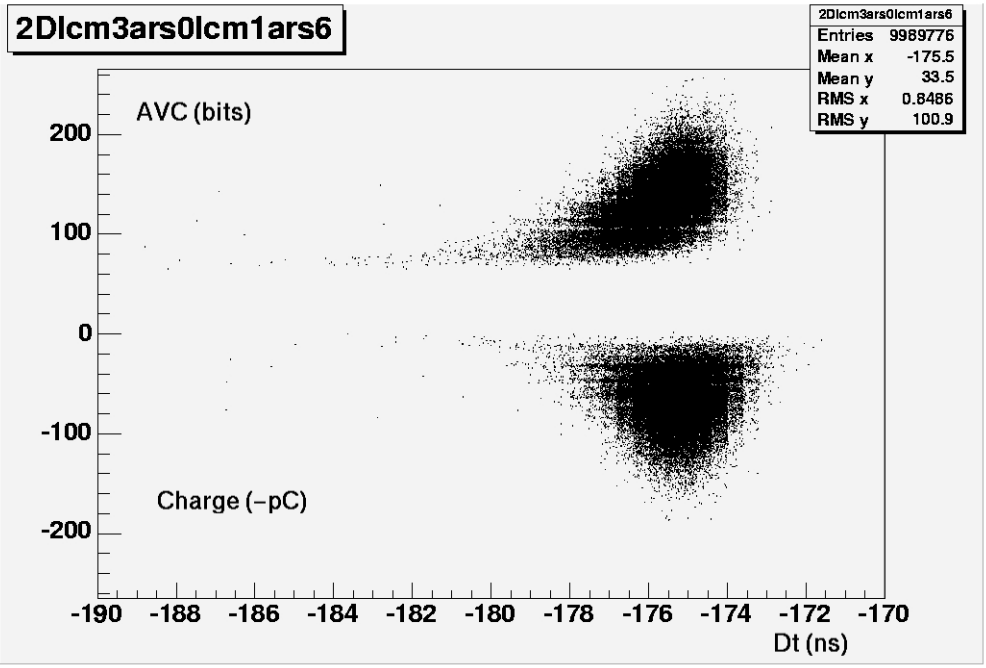

Figure 7: AVC counts-time scatter plot for the ARS0 of the OM1 (upper plot). Charge-time correlation after walk correction (lower plot).

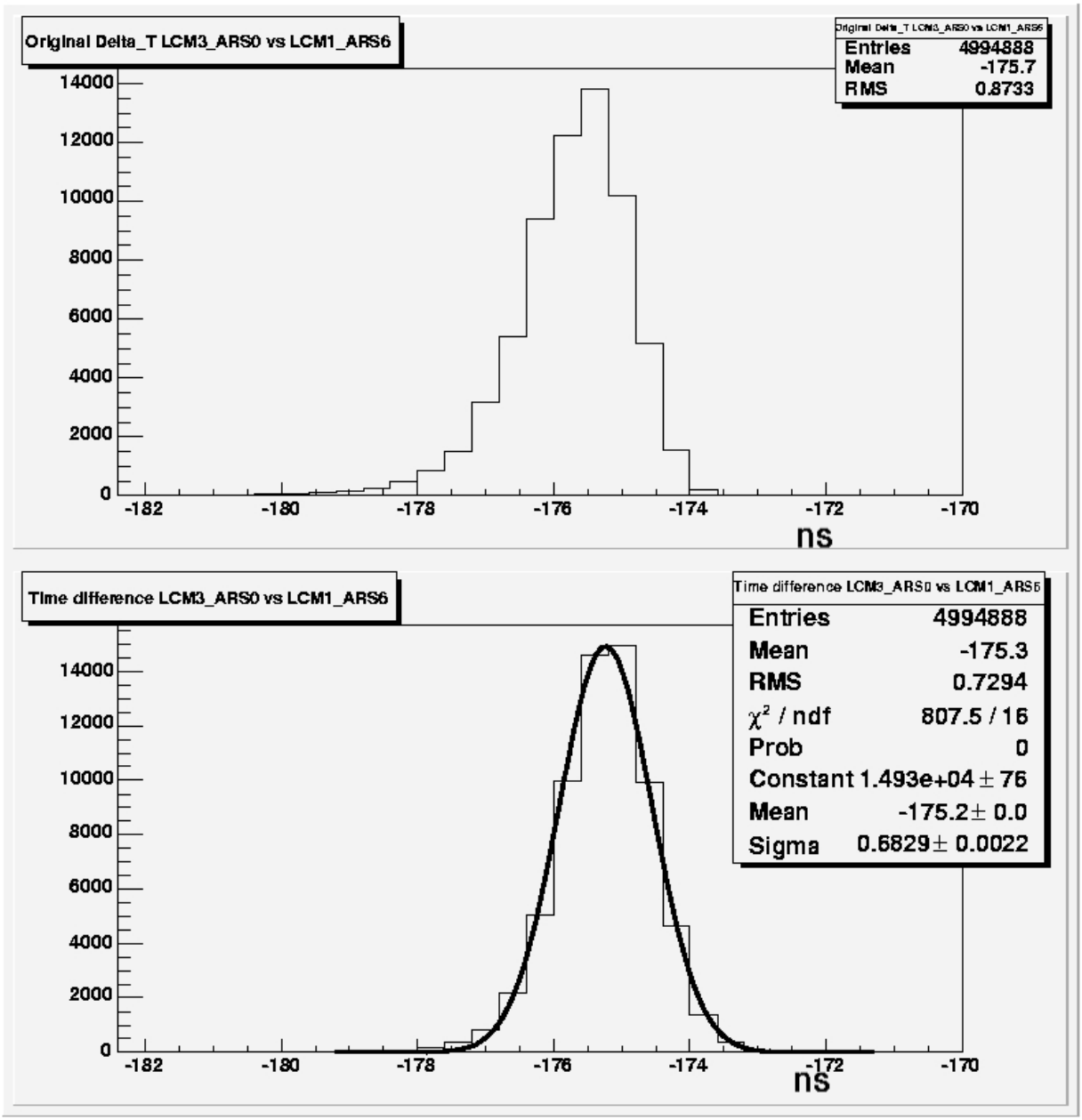

Figure 8: Example of time difference distributions before (top) and after (bottom) corrections for the walk effect.

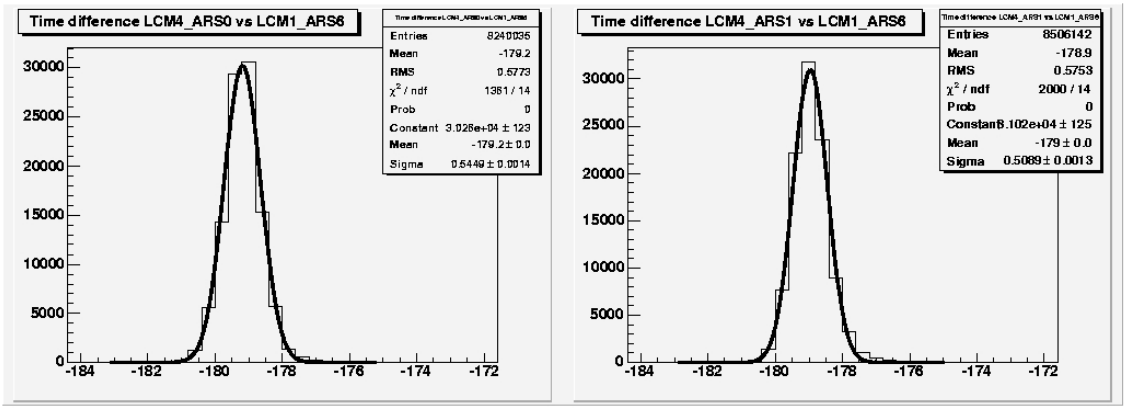

Figure 9: Time difference distributions for the ARSs' of OM1 at the LCM_TOP.

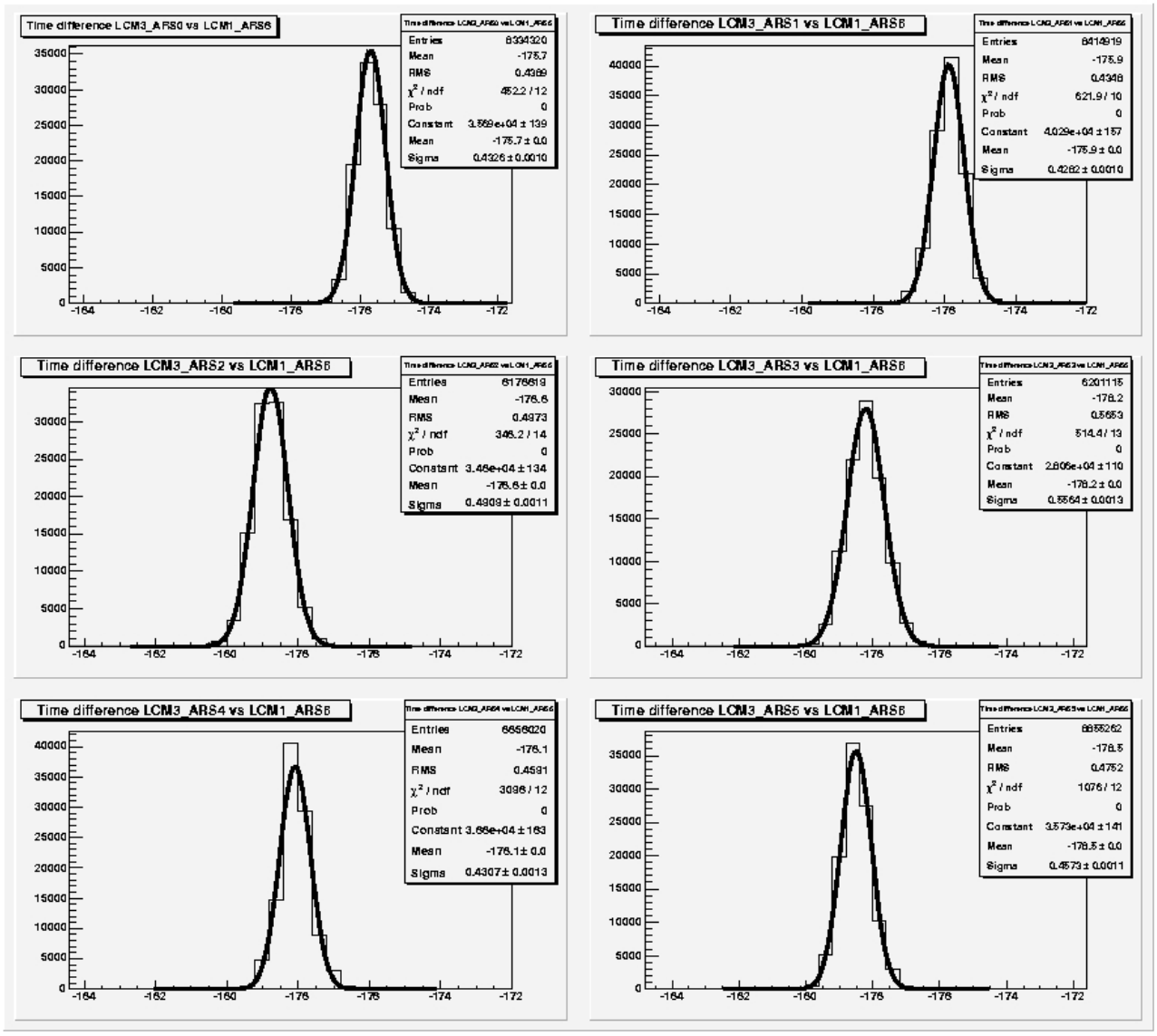

Figure 10: Time difference distributions for the ARSs' of the OM1,2 and 3 at the MLCM.

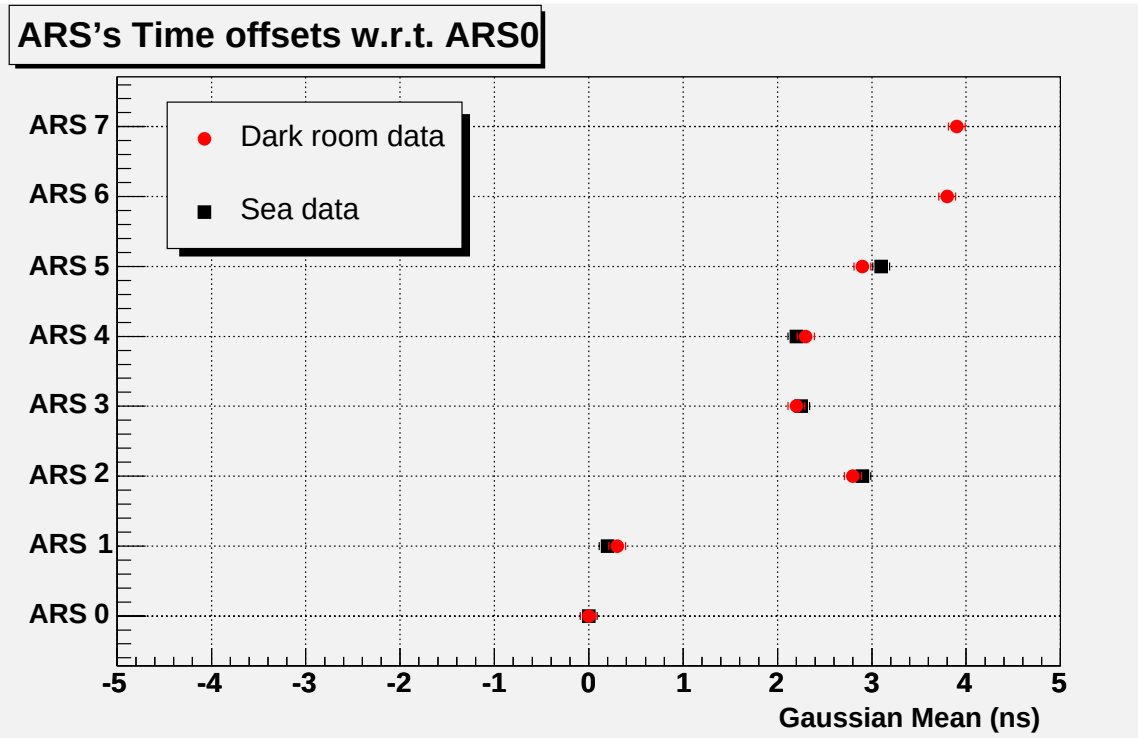

Figure 11: Difference between ARSs and ARS0 mean values of the gaussian fit of the time difference distibution. Dark room results are compared with sea data after MILOM connection.

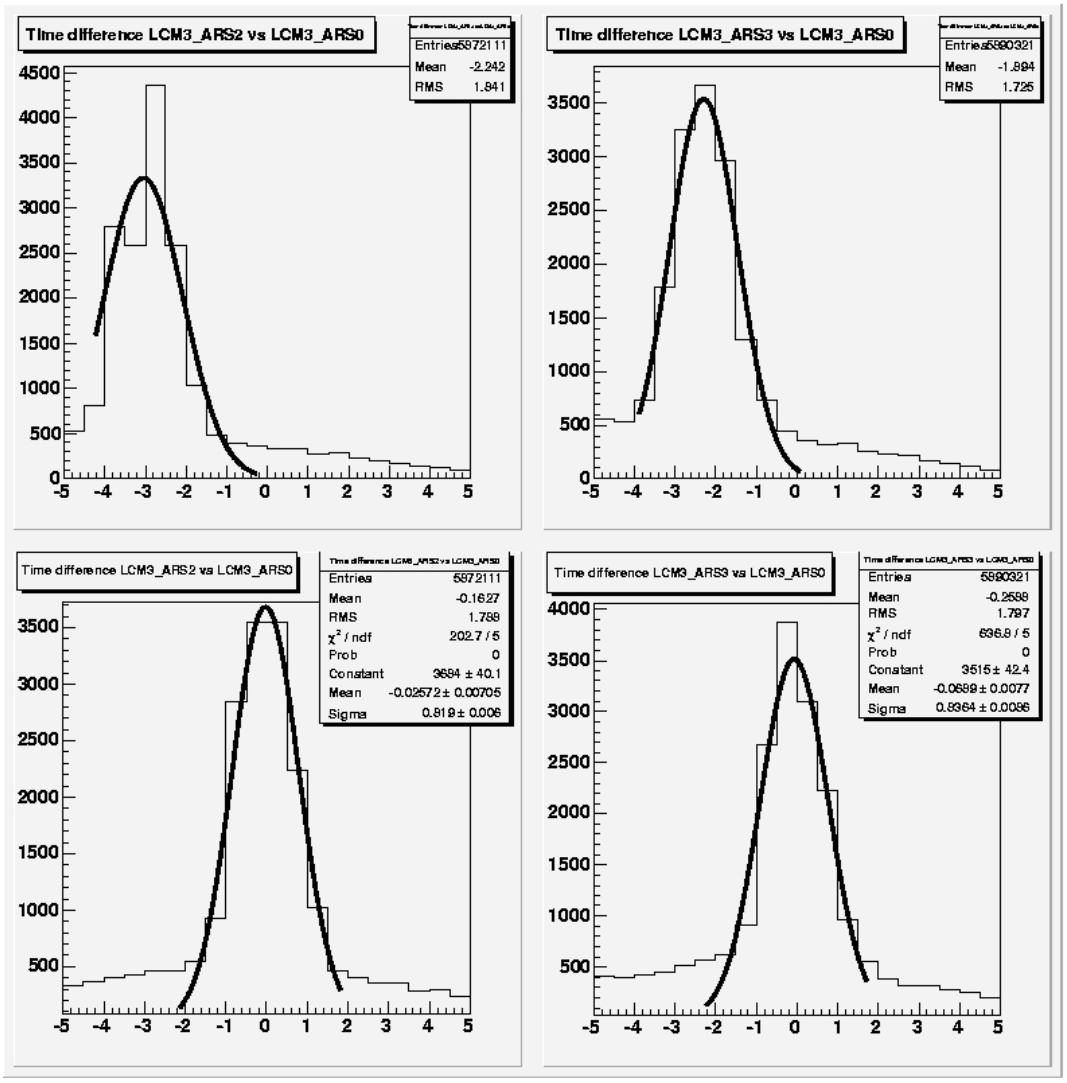

Figure 12: Sea LED beacon run 11303. Time difference distribution between ARS0, OM1 and the two ARSs of OM2, before (top) and after correction for the OMs offset as measured in dark room.

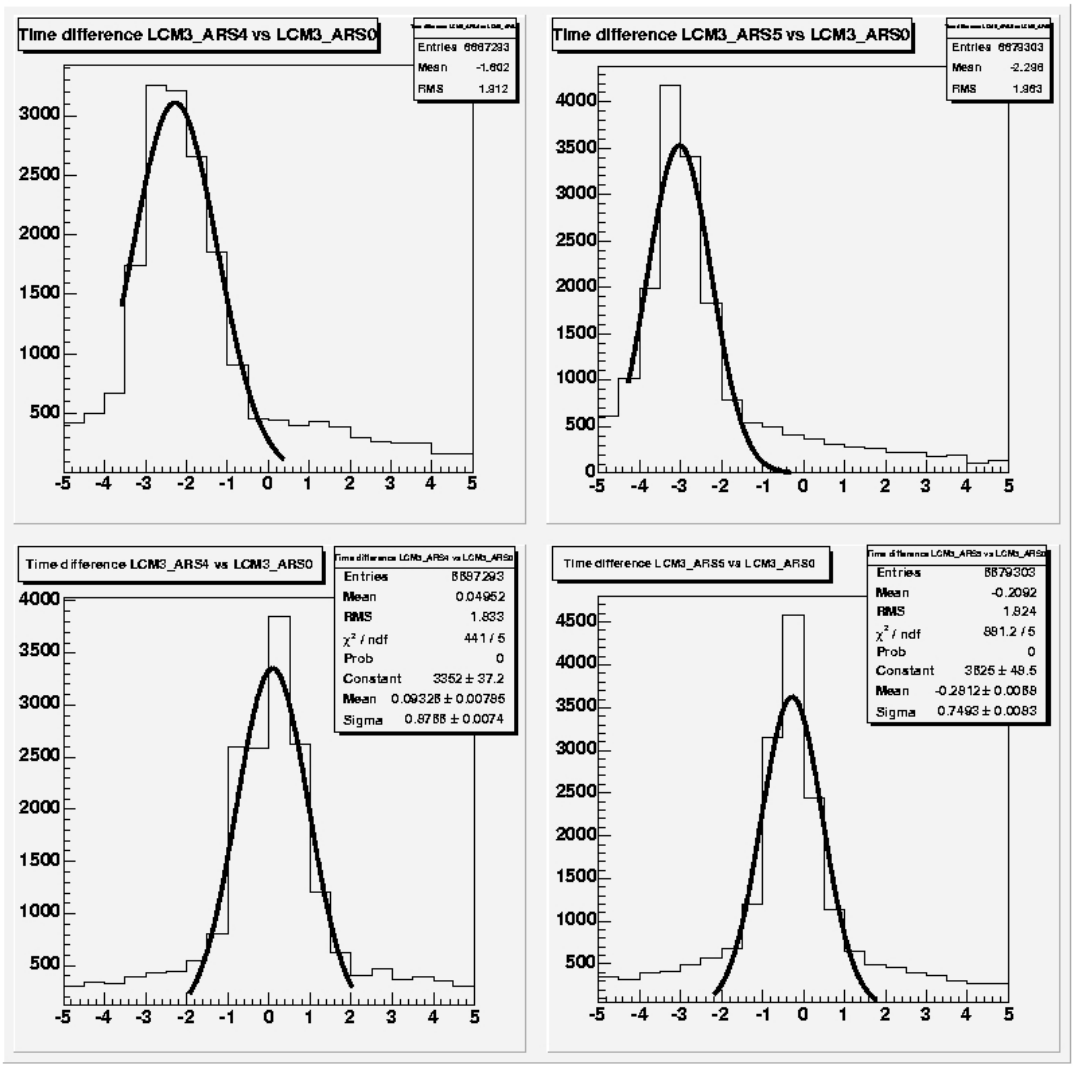

Figure 13: Sea LED beacon run 11303. Time difference distribution between ARS0, OM1 and the two ARSs of OM3, before (top) and after correction for the OMs offset as measured in dark room.

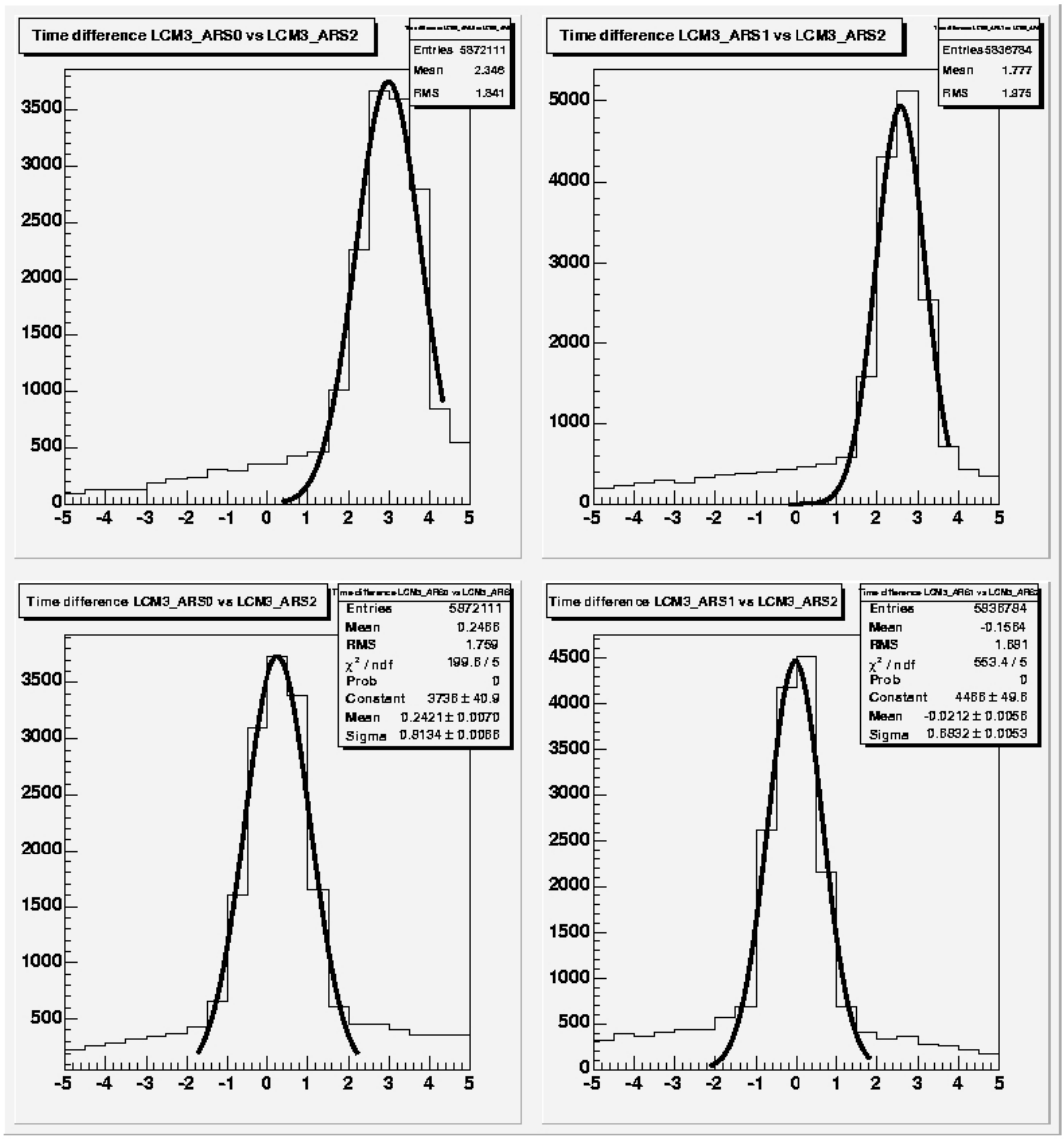

Figure 14: Sea LED beacon run 11303. Time difference distribution between ARS2, OM2 and the two ARSs of OM1, before (top) and after correction for the OMs offset as measured in dark room.

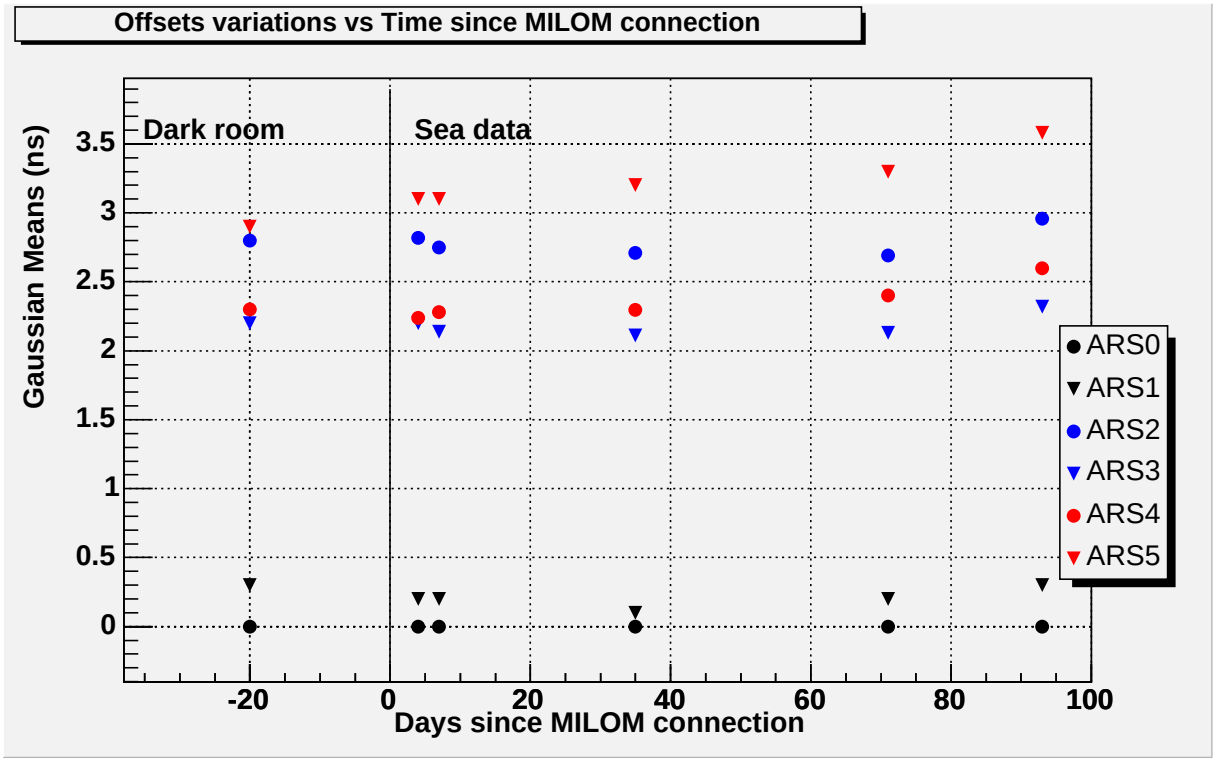

Figure 15: Data on the stability of the timing calibration from the LED Beacon system in the sea and the optical fibre/laser system in the dark room before deployment.

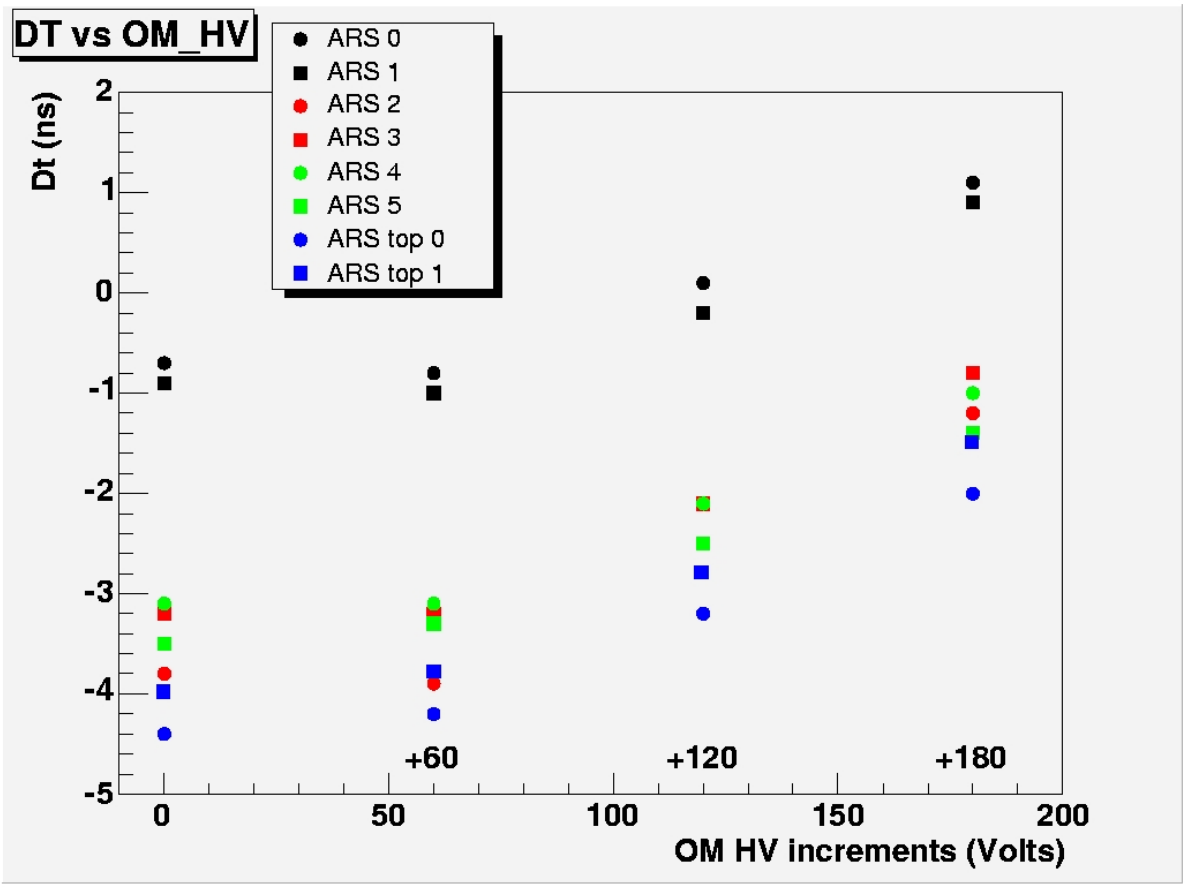

Figure 16: OMs time offsets as a function of High Voltage (+60 Volts step increase).

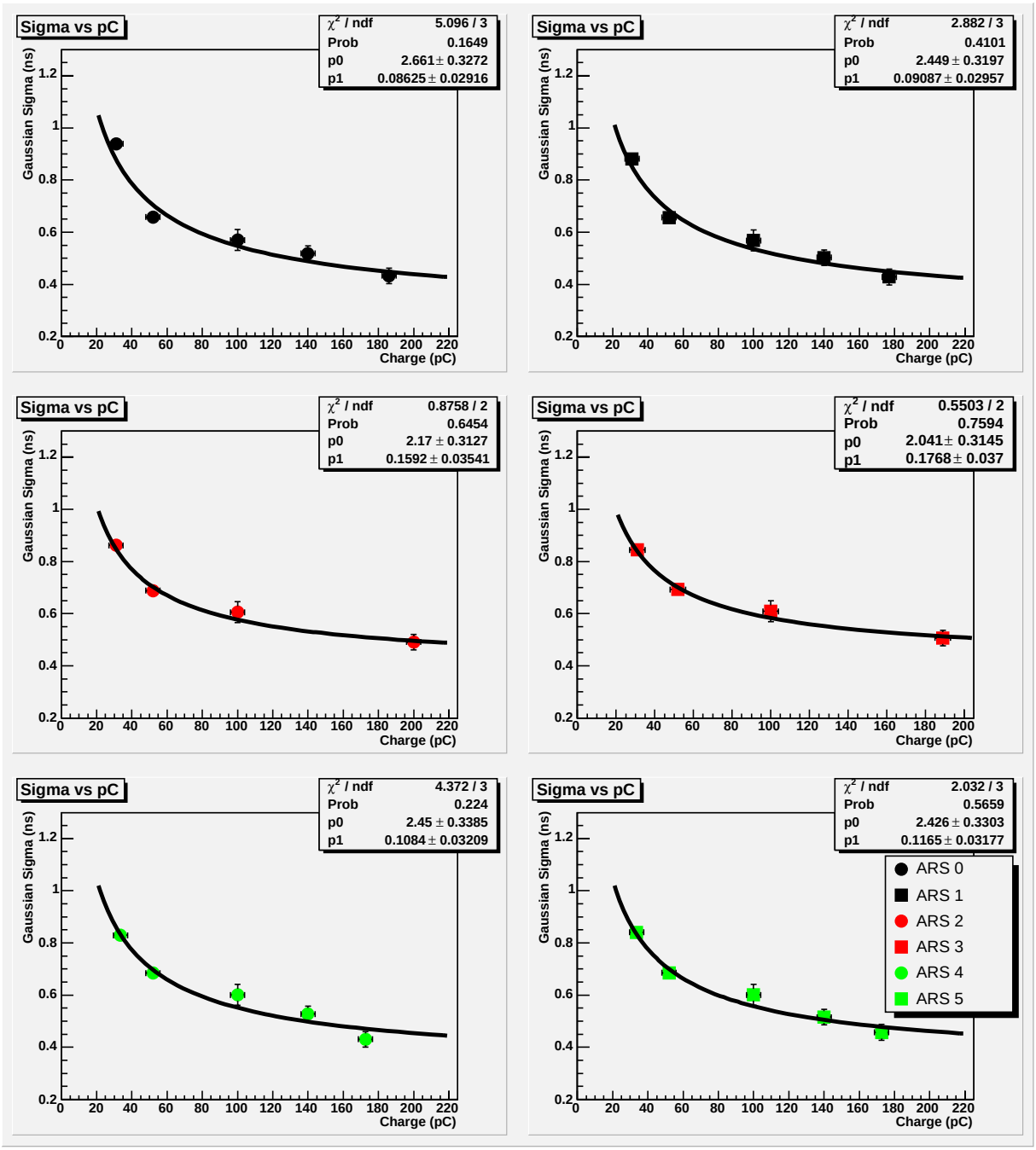

Figure 17: OMs time resolution *vs* charge.

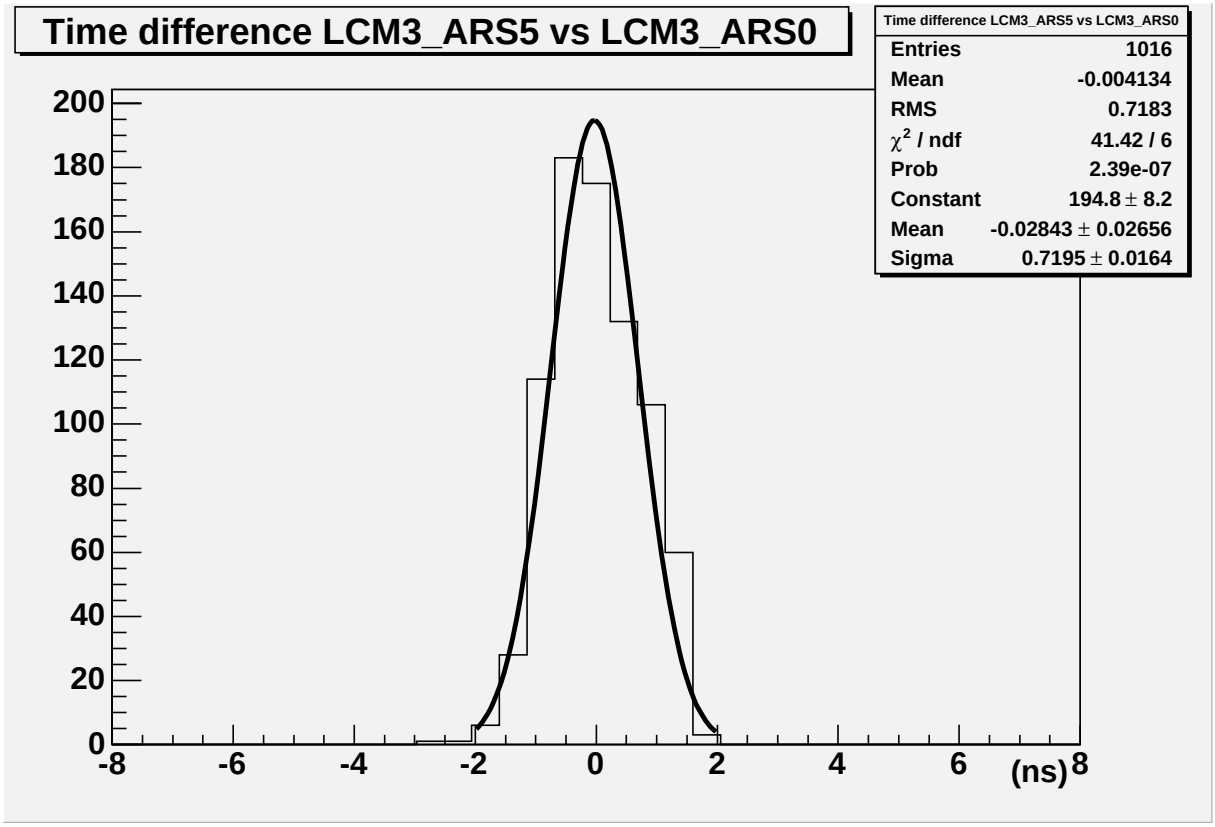

Figure 18: Sea data LED beacon run 11928: example of the distribution of difference in time between signals between adjacent optical modules in the MLCM.

ANTARES-Cali/2006-003

Line 1 time calibration.

V. Bertin, J. Busto, P. Coyle, G. Lamanna, G. Lambard, J.Lavalle, G. Lelaizant, P. Payre

Abstract

In this note we report the results of the ANTARES Optical Modules' time calibration performed in the CPPM dark room during the Line 1 integration.

Introduction

In this note we present measurements of the OMs' time response offsets during the line 1 integration. The purpose of the Dark Room OM time calibration is to measure the characteristic time-offset for each OM, which is due to the specific PMT transit time and the front-end electronics. Such time-offsets are then stored in the database and retrieved at the time of sea data taking in order to correct for the relative delays between the OMs. The dark room calibration of the relative delays of the OMs is a redundant validating measurement of the same calibration which is expected to be performed after deployment in the sea by means of the LED beacon system.

The methodology of the calibration consists of the measurement of the time difference between two coincident signals: the reference time of the laser pulse (provided by the laser internal photodiode) and the arrival time of the hit registered by the OM: T_{PD-ref} - T_i. The distribution of the difference between these signals are then analyzed within a time window of few hundreds of nanoseconds. These distributions follow a Gaussian behavior whose mean value is the time offset of the specific ARS (ARS_T0) and the sigma is an estimation of the time resolution of the system.

1 Set-up description

The set-up for the dark room tests of the Line1 is based on a similar configuration adopted earlier for the MILOM as described in [1]. The technical details of the experimental layout for the line 1 calibration, during the integration at CPPM, can be found in [2], while the test procedures and the acceptance criteria are described respectively in [3] and [4].
For the relative time calibration of the ARSs we want to know the time offset between OM's responses to a synchronous signal. Such a signal is provided by a laser equipped with an optical system sitting into the control room [5]. An optical fiber brings the laser light from the control room to the dark room and is then distributed simultaneously to the OMs by a 1-to-16 optical splitter also located into the dark room. Sixteen optical fibers are connected at the output of the splitter. These fibers are then used to bring the laser light to the 15 OMs of one sector a time: 3 OMs (conventionally called OM0, OM1 and OM2 for each storey) for four LCMs plus one MLCM . The end of each fiber is fixed at the bottom of each cylinder (the *flower pot* as shown in Fig.1) containing the OM, where a diffuser allows the spreading of the laser light on the sensitive hemisphere of the OM inside the pot and then on the photocathode [7]. The OMs were operated at the nominal gain of 5×10^7, according to the operating high voltages values provided in the integration data base.
The time calibration of each OM from the Line1 consists to provide their timing response to the photons travelling from the laser to the photocathode with a reference time given by a photodiode signal internal to the laser which is stable in amplitude and with less than five nanoseconds in rise time. This latter is read by an independent LCM_Ref dedicated to the Line calibration.

2 TVC calibrations

The arrival time of each pulse (SPE_ITEM) is coded using a 50 ns resolution *timestamp* as provided by the LCM clock and the TVC (Time-to-Voltage Converter) value between 0 and 255 corresponding to the precise time of arrival inside the clock period. To get the exact time of each *spe* some corrections are needed.

For each ARS, two TVCs (TVC A and TVC B) are used sequentially, they are needed because the time the electronics takes to come back from the maximum slope value to the minimum is not

negligible at the high precision we work [7]. Ideally TVC values of 0 and 255 bits would correspond to 0 and 50 ns respectively with a theoretical resolution of (50 ns / 255 bits) $\times 1/\sqrt{12} \simeq 0.06$ ns. We need to know the real transfer function bit/ns and the dynamic range of every TVC before adding the corresponding TVC value in ns to the *timestamp* of a *spe*. The TVC calibration methodology consists in plotting the TVC values (one histogram for each TVC; two per ARS, i=1,2). For each histogram, the average (*ave*) occupancy over the 256 bins is computed. The lower and upper bounds were defined as the first bin (T_min) the last bin (T_max) in which the number of entries exceeds 10% of *ave*. With the assumption that the real dynamic response of the TVC is still linear, the slope of the transfer function is computed as T_slope (bit/ns) = (T_max - T_min) / 50 ns.

The T_min, T_max and T_slope values for every ARSs are measured for each run to monitor their stability as a function of the operational temperatures. A well defined constant series of values for such parameters is then assumed for the following calibrations of the line. In Fig. 2, an example of TVC histograms for the OM0, OM1, OM2 of the LCM1 is shown. In Fig. 3, a sample of T_min and T_max for the Line 1 is provided while the corresponding values of T_slope are shown in Fig. 4.

3 OMs' Time Offset Calibration

Before to proceed, three basic corrections have to be applied in order to get the best results of the time calibrations: fiber lengths offsets correction, clockphase correction and walk effect correction.

3.1 Fiber lengths correction

The laser light which is distributed to all OMs simultaneously follows different paths along different fibers starting from the 1-to-16 splitter to the diffusers of the OMs' containers. The correction for unequal fiber lengths has been measured by taking data in the dark room and swapping the position of an OM among the fifteen containers. Fig. 5 shows the relative time delays of each fiber w.r.t. the fiber 15 with the OM1 (in the 'flower pot' 15) as reference.

3.2 Clock-Phase correction

The clock transmission to every storey of the line uses optical fibers within the electro-optical cable. Such connection induces a relative delay between storeys which is measured with the *ps* precision by the clock system (see [6] for more details). The relative delays *clock − phases* are measured conventionally with respect to the SCM of the Line 1 at which is then assigned a clock-phase equal to 0. This clock-phase is taken into account to provide exactly the characteristic time-offset for each ARS as: T_{PD-ref} - T_i - $ClockPhase_i$. The clock-phases values ($(T_{SCM/LCM} + T_{LCM/SCM})/2$) considered during the dark-room calibrations are stored in the database and summarized in Fig. 6. As you can see, the time delays distribution is non-linear because the optical path dedicated to the clock isn't the same on all the line. There is a different optical path from the SCM to the first floor of each sector and this difference in optical path induces a delay between each sector.

3.3 Walk effect correction

The walk effect is caused by variations in the amplitude of pulses coming from the PMs and discriminated by the ARSs at a fixed voltage threshold. Coincident signals but with different amplitudes will cross the threshold at different times. The ARSs' walk effect has been already studied and parameterized [8]. The correction to be applied consists in the estimation of such walk by monitoring

the response of the ARSs to laser pulses of different intensities. For every ARS the T_{PD-ref} - T_i - $ClockPhase_i$ distribution is examined as a function of the charge and then fitting the profile of such correlation with the polynomial function:

$$\frac{p_0 + p_1 Q}{p_2 + Q} + \frac{p_3}{Q}, \ with\ p_0, p_1, p_2 > 0\ and\ p_3 < 0\ , \tag{1}$$

where p_i are the four free parameters of the fit and Q is the charge in pC (see Fig.7 for an example). Compared to the past (*e.g.* see the MILOM case [1]), in this specific study, we keep constant the p_0 parameter with the intent to obtain approximately the same best fit function for all ARSs of the line and we have added the p_3 parameter which allows for a better fit results at lower values of the integrated charge. The charge Q for each i ARS is obtained from the AVC counts by considering a linear dependence as confirmed by earlier qualification tests of the ARS mother boards: AVC_i = $Slope\ Q_i + Int_i$. A constant *Slope* value of 1.1 is considered due to the tiny variation among ARSs [9], while the specific intercept Int_i is measured from the pedestal run calibration in the dark room and corresponds to the mean value of the ARSs' pedestals (see fig.9). Finally the best fit parameters p_i are then used to correct every spe-time for its own walk-delay. The delays introduced by the walk effect are systematically subtracted to all spe-times , as a function of the total integrated charge of the signals by which they are generated. In Fig.8 we show the charge Q *vs* (T_{PD-ref} - T_i - $ClockPhase_i$) after correction and AVC counts (to better illustrate the difference the AVC counts has been plotted negative) *vs* (T_{PD-ref} - T_i - $ClockPhase_i$) before correction. Finally in Fig.10 and Fig.11 we show an example of the time-difference histogram before and after walk correction for a low intensity.

3.4 Led Optical Beacon tests

Line1 is equipped with four LOBs, Led Optical Beacons, for the OMs time calibration in the sea. LOBs positions along the line were chosen to optimize the lighting of all OMs. They are connected on the storey 2, 9, 15 and 21 and read by a dedicated 6^{th} ARS of the corresponding LCM.

The methodology of the Beacons calibration is the same than for the OMs. As you can see in Fig.12, a dedicated fiber coming from the optical system in the control room to the LOB in the dark room, allows to bring the laser light to the mini-PM of the beacon without passing by the splitter to prevent from further laser attenuation. Finally, the time-offset is measured by taking into account the clock-phases of the corresponding LCM and the difference of optical paths between the OMs and LOB itself.

4 Results

As shown in Fig. 13 in the case of high laser intensity, for each ARS of all OMs, the time distributions have a common offset of about 50 ns which corresponds to the difference between the laser optical path and the electric path of the photodiode reference signal. This offset in time is not really important because it's the relative time difference of distributions which is relevant. The relative time difference between the mean value of the ARS0 Gaussian fit of the LCM1 from the Sector1, taken as reference, and the mean value of Gaussian fit of other ARSs.

A truncated copy of the final table is in Tab. 14 (See in [10] for the complete version) : we have all LCMs from 1 to 25, ARSs for each LCM from 0 to 6 (with ARS6 only in case a led_beacon is connected), TVCs A(B) min and max coming from the TVC calibration for each ARS, the Clockphase, the time differences (Dts) for each ARS with the LCM1_ARS0 as reference. Then, we have the statistical errors due to the Gaussian fit performed on the LCM1_ARS0 distribution and that performed on

each ARS' distribution, equally due to the cut on each fiber exiting to the splitter we made to obtain approximately the same time difference everywhere and finally to the statistical error performed on the clockphase of about 10ps. After we have the systematic errors mainly due to the systematic error on the clockphase of about 50ps, the electronic which induces a random noise estimated to 50ps and to the time difference variations on the timeslices range used. Indeed, we have just used ten thousand timeslices window from the hundred first timeslices and an other window used to induce a variation of the entries number giving a time difference appreciably different. Then there are the total error which is the quadratic sum of both precedents and the sigma values for the Gaussian fit of each ARS. Finally, we have the intercept and slope values to obtain the pC values from the AVC counts and the fit parameters p_0, p_1, p_2, p_3 relative to the walk effect correction.

We have performed the same work for the four led_beacons as shown in Fig.15. The four Gaussian fit are approximately distributed around 105 ns. The difference from that obtained using the OMs fits comes from the difference in transit time between the led_beacon microPM and the PM of OMs. This latter is approximately equals to 55 ns. The results concerning time-offsets (without Transit-Time correction), with the LCM1_ARS0 as reference, are also stored in the results table for each ARS6 on which the led_beacons are connected.

Summary plots of the resulting time offsets for all OMs of the line 1 are provided in Fig. 16 and 17, while the same results for the PMs of the four optical beacons are shown in Fig. 18. The full list of examined plots for the totality of seventy-five OMs of the line1: TVC occupancies, time-offsets before and after Walk effect correction, AVC and pC versus (T_{PD-ref} - T_i - $ClockPhase_i$) Histograms and Profiles can be found elsewhere [10]. To ensure clearness in this note, just a few examples of those plots are shown, but we recall that the totality of the results, which are critical for the time calibration of the detector, are listed in tables available in [10] and soon on the ANTARES database.

5 Time resolution

In order to estimate the time resolution the system can reach, data with different laser light intensity have been taken in dark room. The OM time resolution has three independent contributions: σ_{TTS} due to the spread in the transit time of the photo-electrons laser pulse width, $\sigma_{syst.calib.}$ the resolution due to the calibration system and finally a constant contribution $\sigma_{elec.}$ related to the front-end electronics. This results in:

$$\sigma^2_{t_{OM}} = \frac{\sigma^2_{TTS}}{N_{pe}} + \frac{\sigma^2_{syst.calib.}}{N_{pe}} + \sigma^2_{elec.}, \tag{2}$$

where N_{pe} is the number of photoelectrons.

For each ARS the Gaussian sigmas of the time difference w.r.t. the PD signal, T_{PD-ref} - T_i, have been analyzed as a function of signal amplitude (integrated charge in PC). We have performed the best fit (see Fig.19) of the function

$$\sigma_{t_{OM}} = \sqrt{p0/x + p1} \tag{3}$$

where x corresponds to $N_{pe} \simeq$ charge (pC)/Q_{spe} ($Q_{spe} = 8pC$) ; $p0$ corresponds to $\sigma^2_{TTS} + \sigma^2_{syst.calib.}$ which is actually dominated by the σ_{TTS} due to the transit time spread.; $p1$ corresponds to $\sigma^2_{elec.}$.

For all the ARSs we obtained the best fit parameters corresponding to $\sigma_{elec.} \simeq 0.35$ ns and a $\sqrt{\sigma^2_{syst.calib.} + \sigma^2_{TTS}} \simeq 1.45$ ns. From these results we can deduce that the best time resolution that we expect to reach in the sea for a high amplitude signal is less than 0.5 ns. A crosscheck of this important

figure of merit with sea data will be performed with the LED beacon and will be reported in an other note.

Conclusions

The methodology and results of the Line1 time calibrations in the dark room have been detailed in this note. Information regarding the calibrations parameters critical for the initial sea operation are also provided.

References

[1] V. Bertin, J. Busto, P. Coyle, G. Lamanna, M. Melissas, Internal Note Antares-Cali/2005-05

[2] G. Hallewell, G. Lamanna, ANTARES Note 5-ASS-02-55-A.

[3] G. Lamanna, ANTARES Note 5-ASS-02-62-A.

[4] G. Hallewell, G. Lamanna, P. Lamare, ANTARES Note 5-ASS-02-58-B.

[5] J. Busto, ANTARES Note 5-ASS-02-66-A.

[6] V. Bertin, J. Carr, P. Coyle, F. Feinstein, G. Hallewell, J.J. Hernandez, S. Karkar, C. Tao, L. Thompson, Internal Note ANTARES-Cali/2002-002

[7] S.Karkar, Internal Note ANTARES-Cali/2003-003.

[8] J.S.Ricol, PhD thesis, 2002, CPPM.

[9] S.Loucatos, private communication.

[10] http://antares.in2p3.fr/users/lambard/LINE1

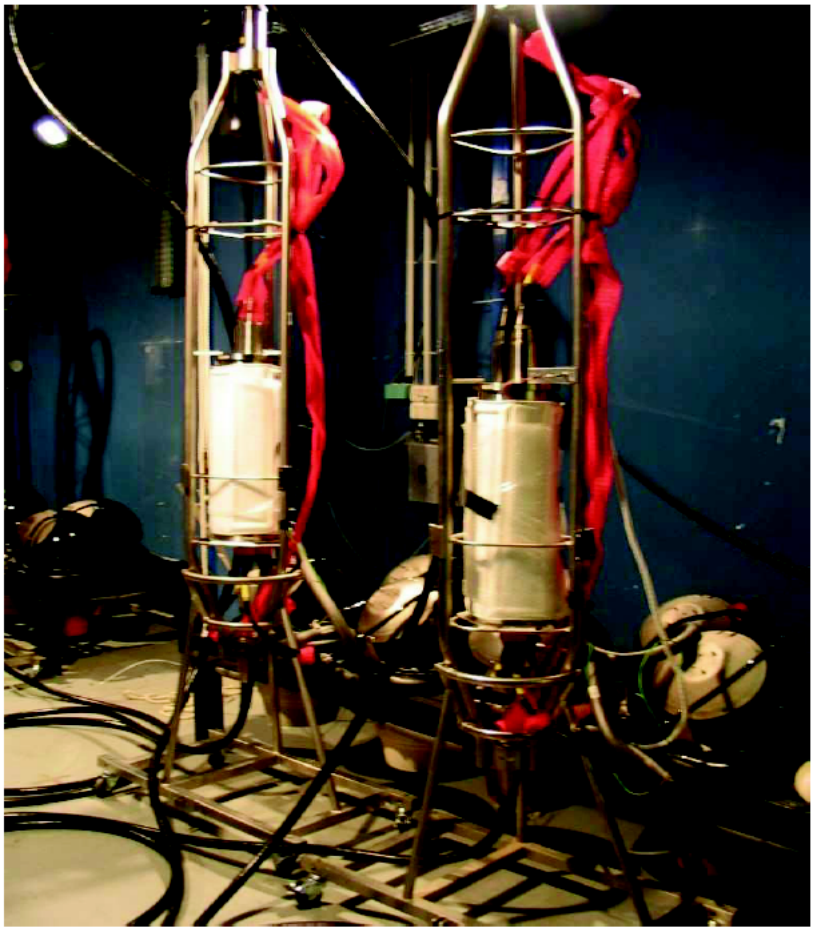

Figure 1: Laser test of OMs in the Dark Room.

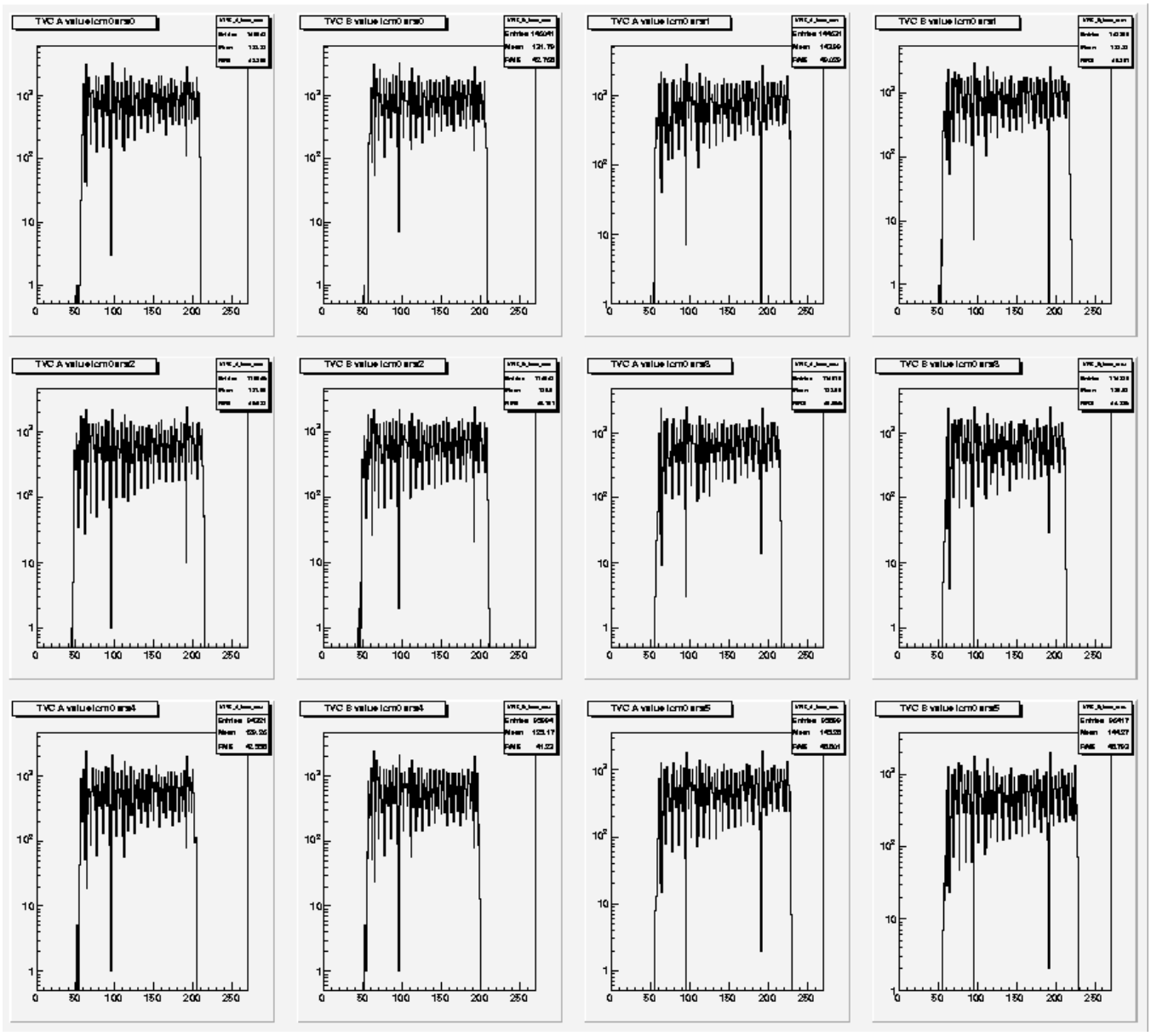

Figure 2: TVC occupancy histograms for the three OMs of the MLCM of Sector 1, during dark room calibrations. From top to bottom: TVCs related to the acquisition of the OM1 (ARS0 and ARS1), OM2 (ARS2 and ARS3) and OM3 (ARS4 and ARS5).

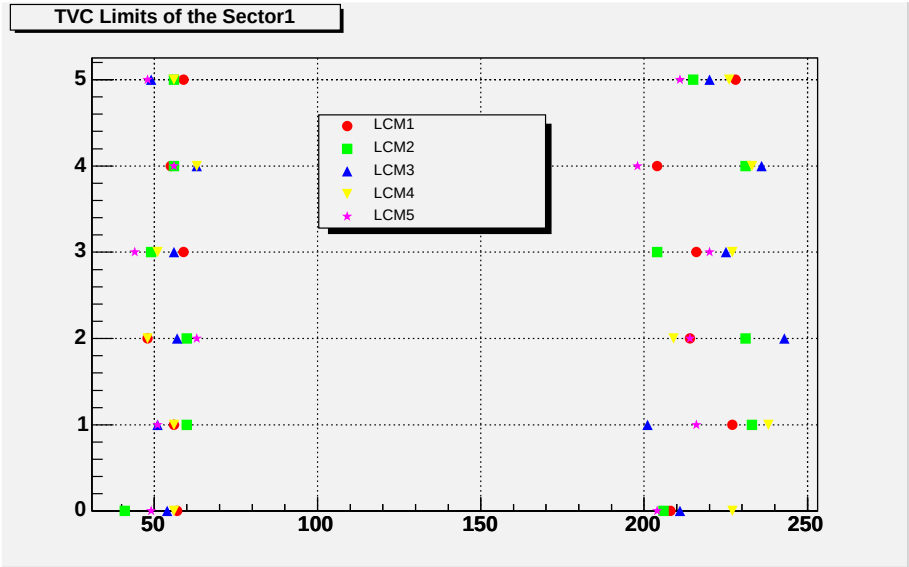

Figure 3: Upper and lower limits of the real dynamic range of the Line1 TVC A for the sector 1.

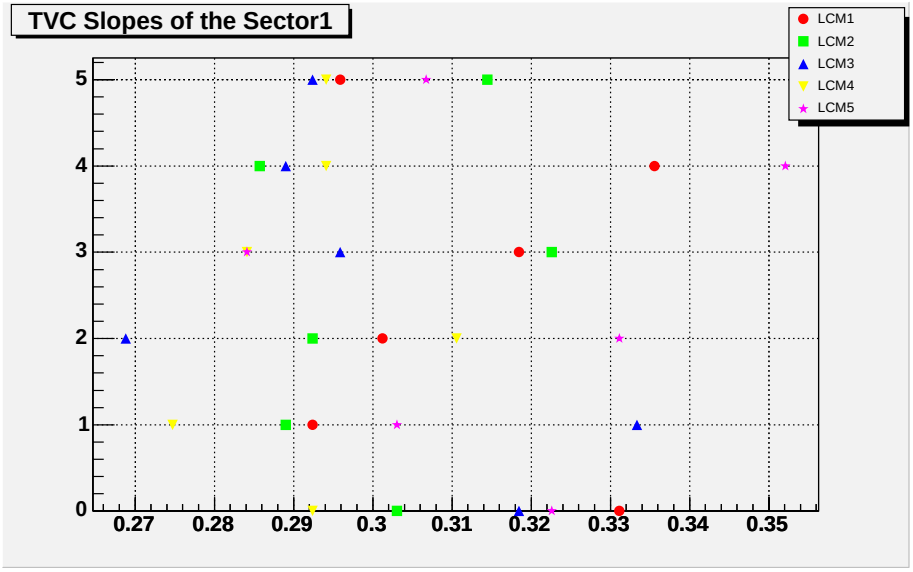

Figure 4: Slopes of the transfer function bit/ns computed for Line1 TVCA for the sector 1.

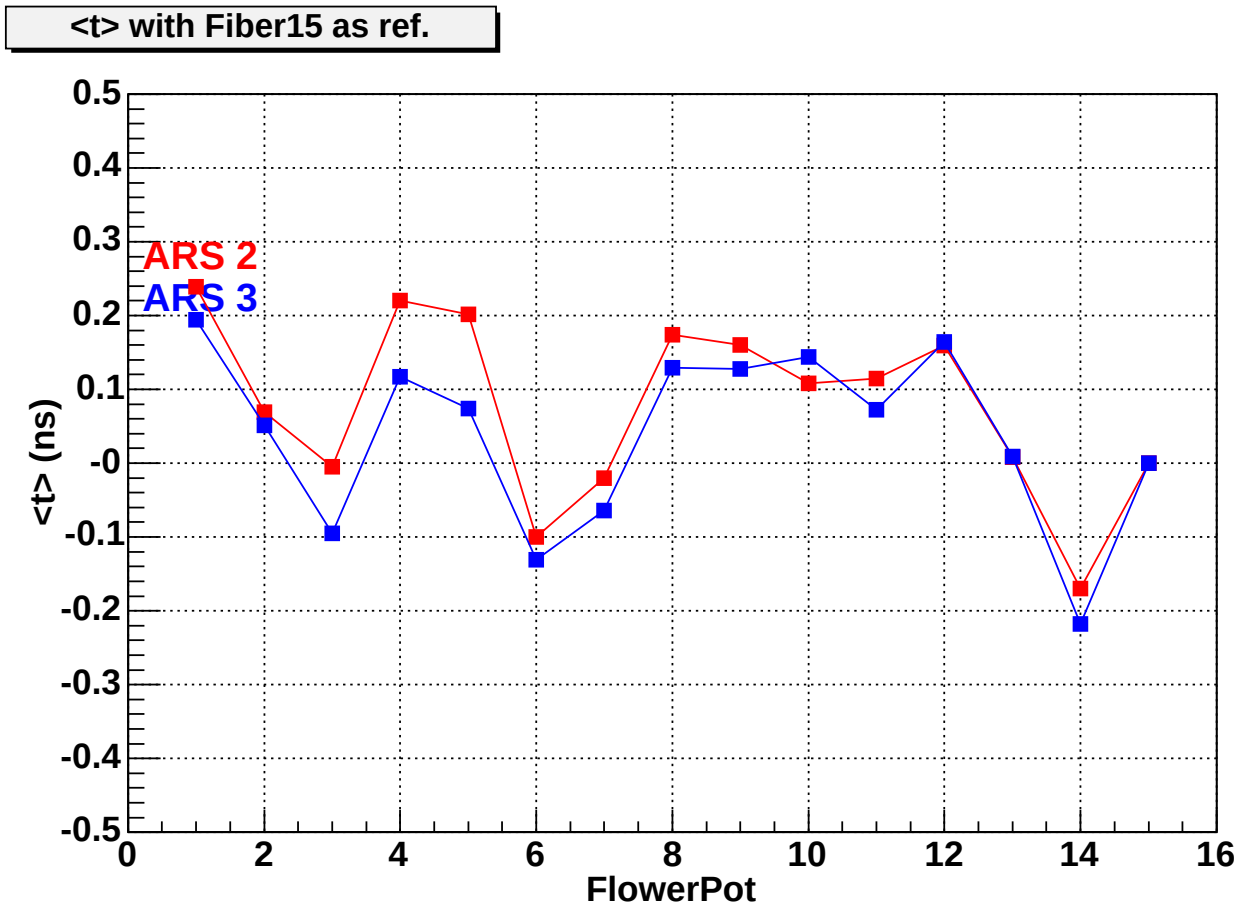

Figure 5: The relative time delays of each fiber w.r.t. the fiber 15.

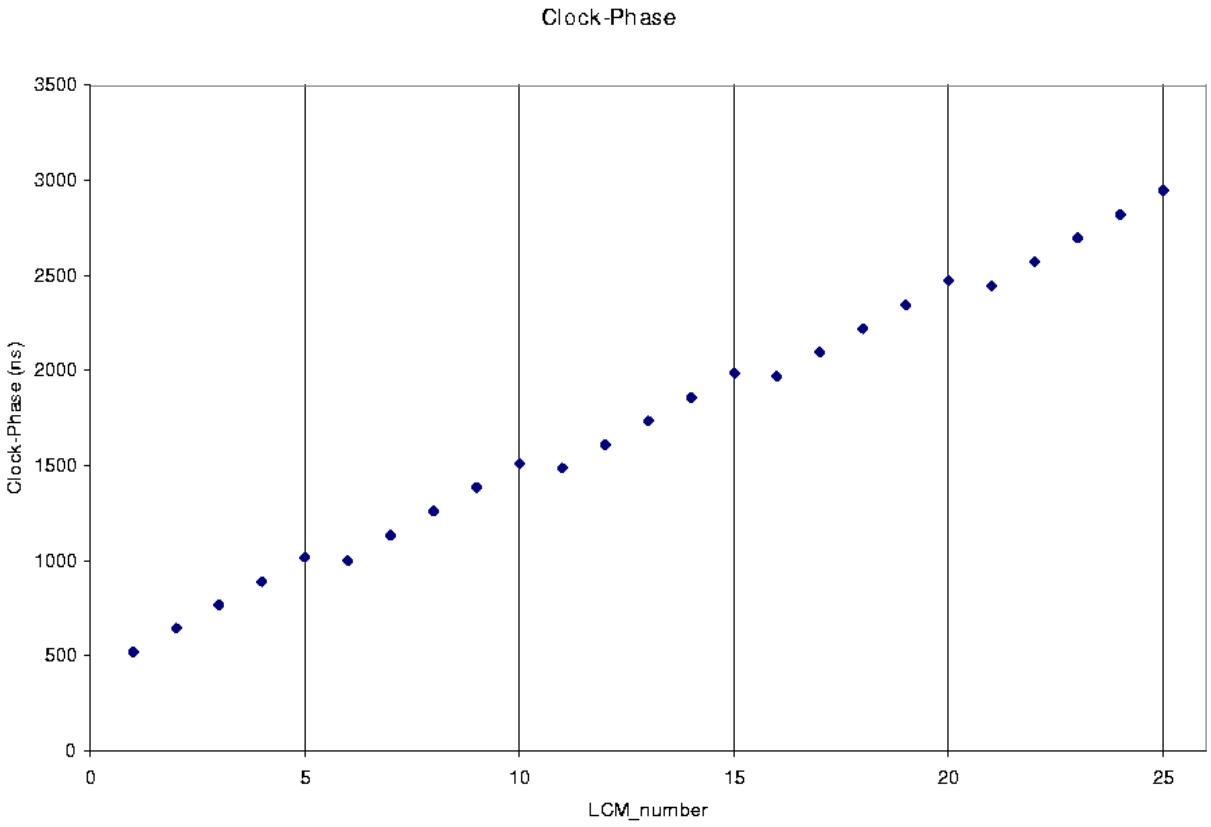

Figure 6: Clock-phase values (ps) for each storey as measured during dark room tests.

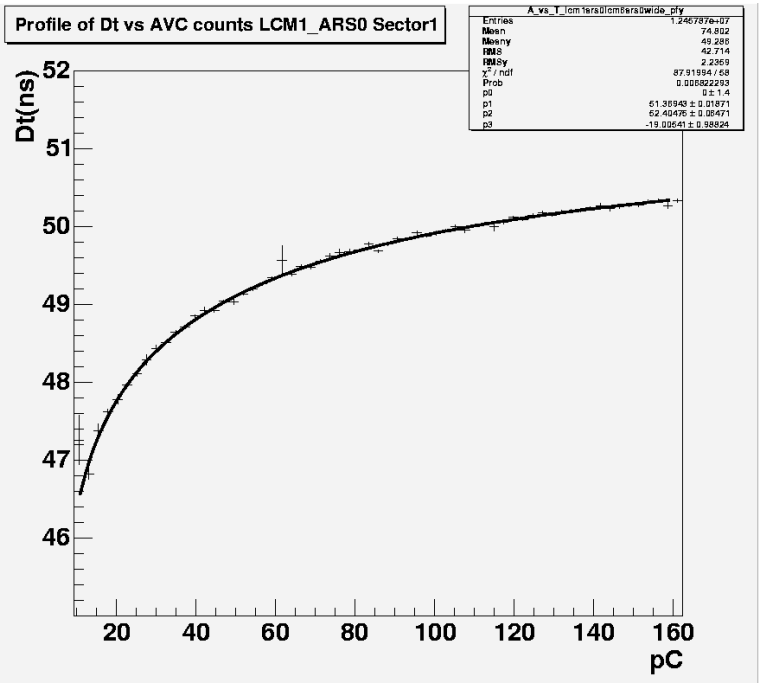

Figure 7: Example of best fit of walk function to the time-charge correlation for the ARS0 of the LCM1_OM0.

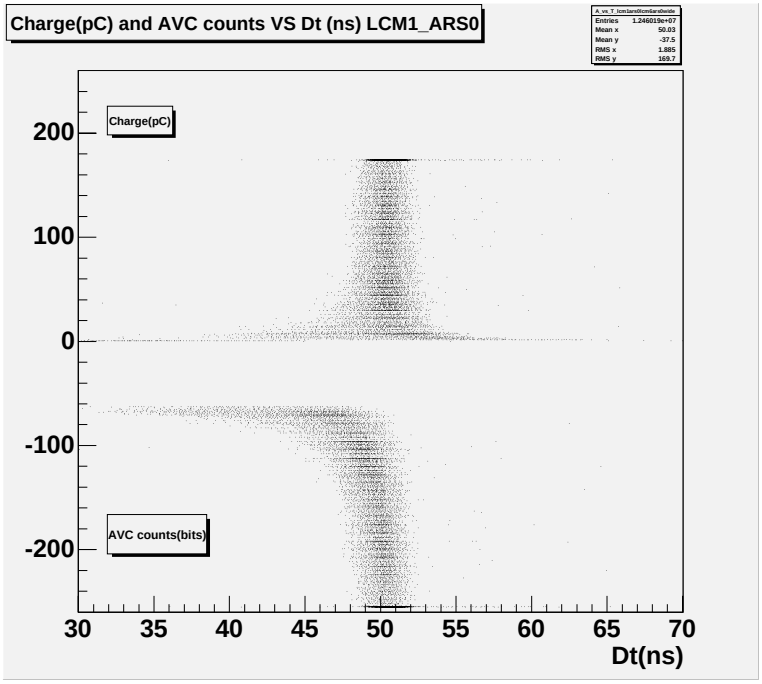

Figure 8: AVC counts-time before Walk correction for the ARS0 of the LCM1_OM0(lower plot). Charge-time correlation after walk correction(upper plot).

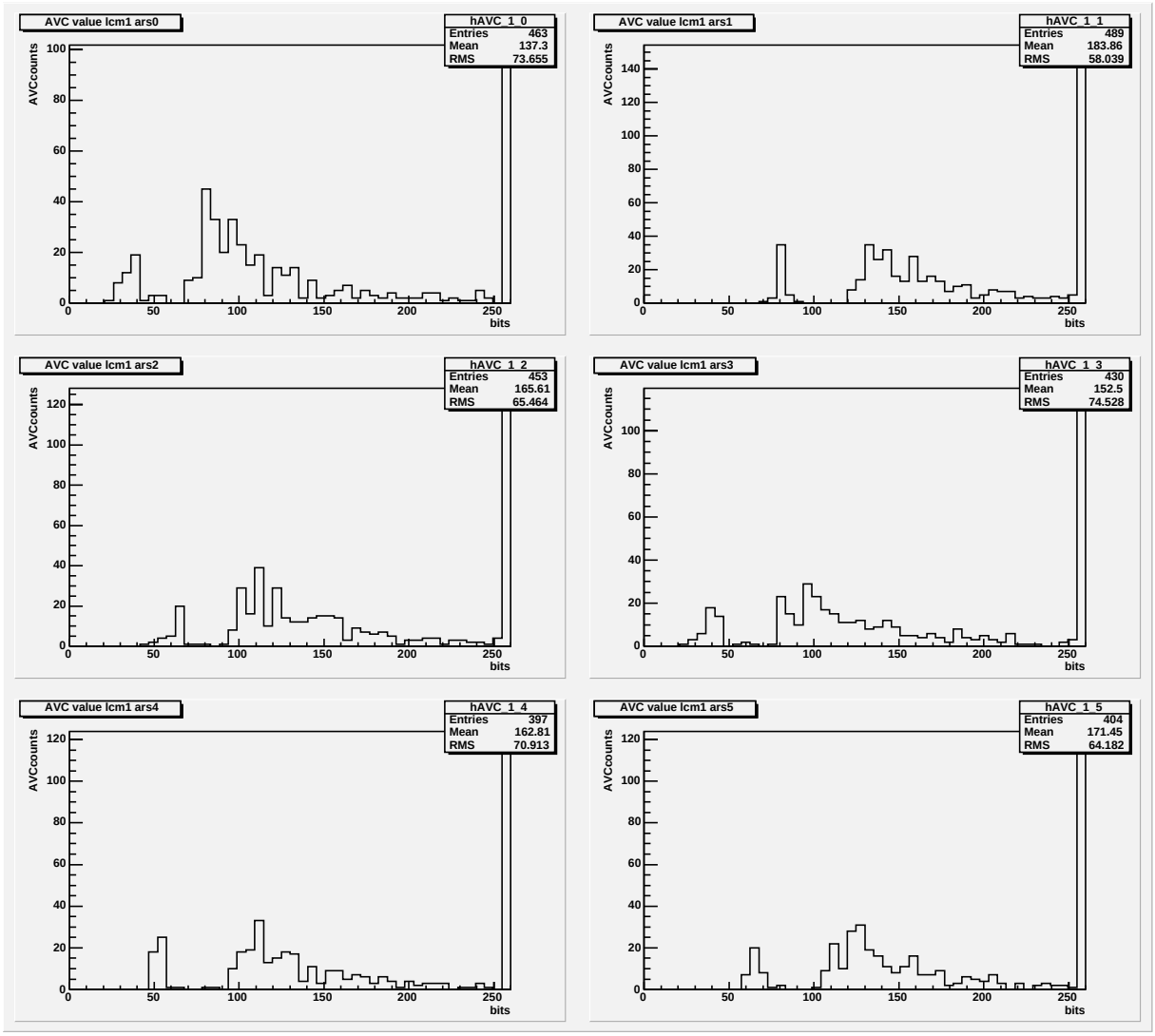

Figure 9: Pedestal Run distribution in AVCcounts for the LCM1 of the sector1 in example where the first peak (pedestal peak) is used for the AVCcounts/pC conversion (mean value equivalent to the intercept value for the AVC/pC conversion).

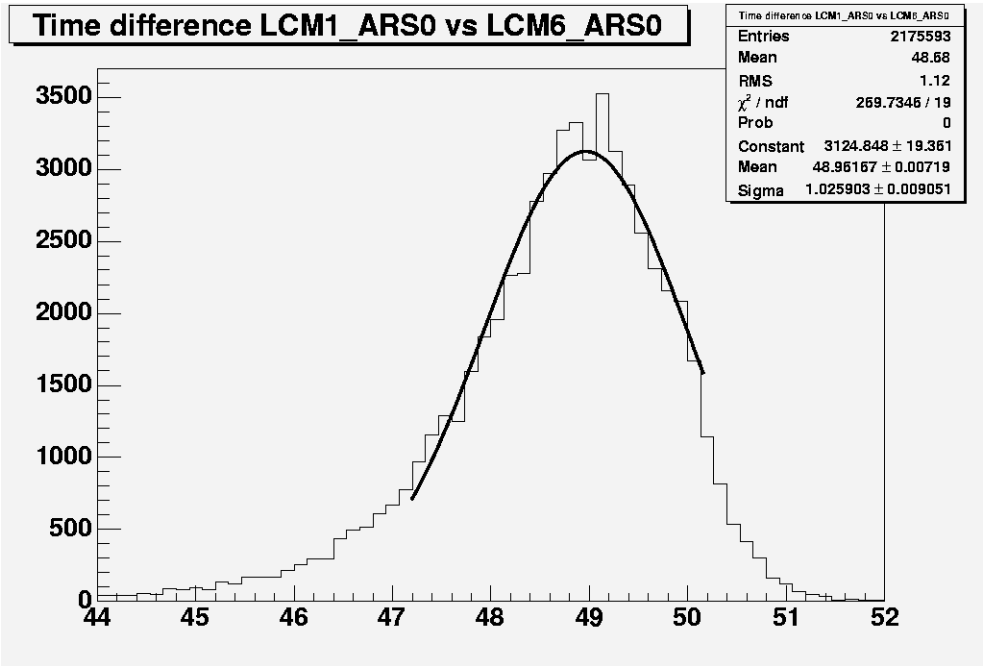

Figure 10: Example of time difference distributions before corrections for the walk effect.

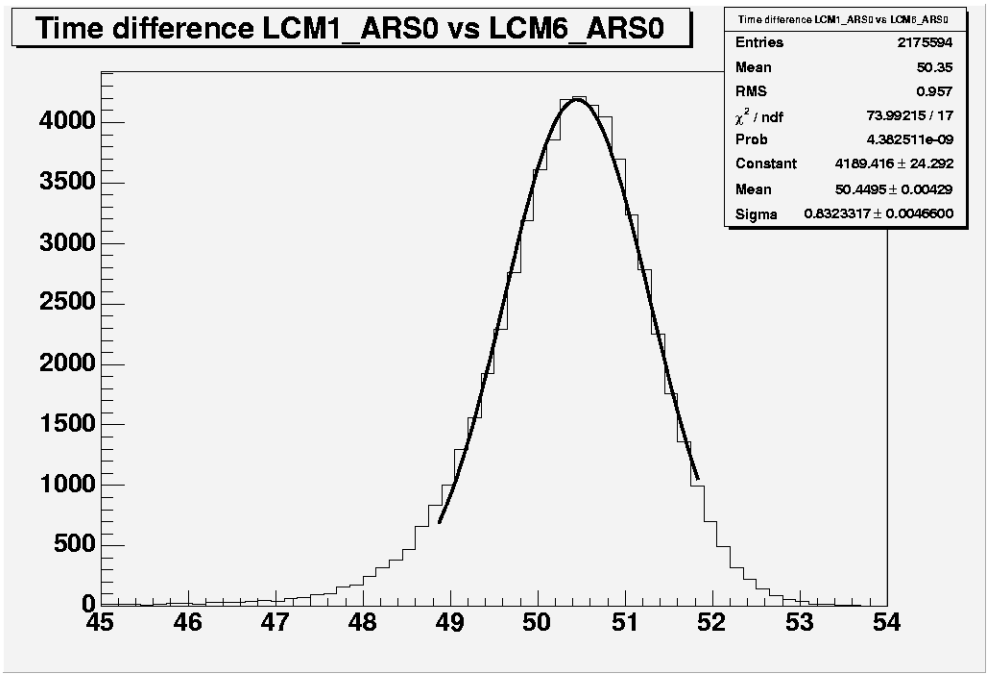

Figure 11: Example of time difference distributions after corrections for the walk effect.

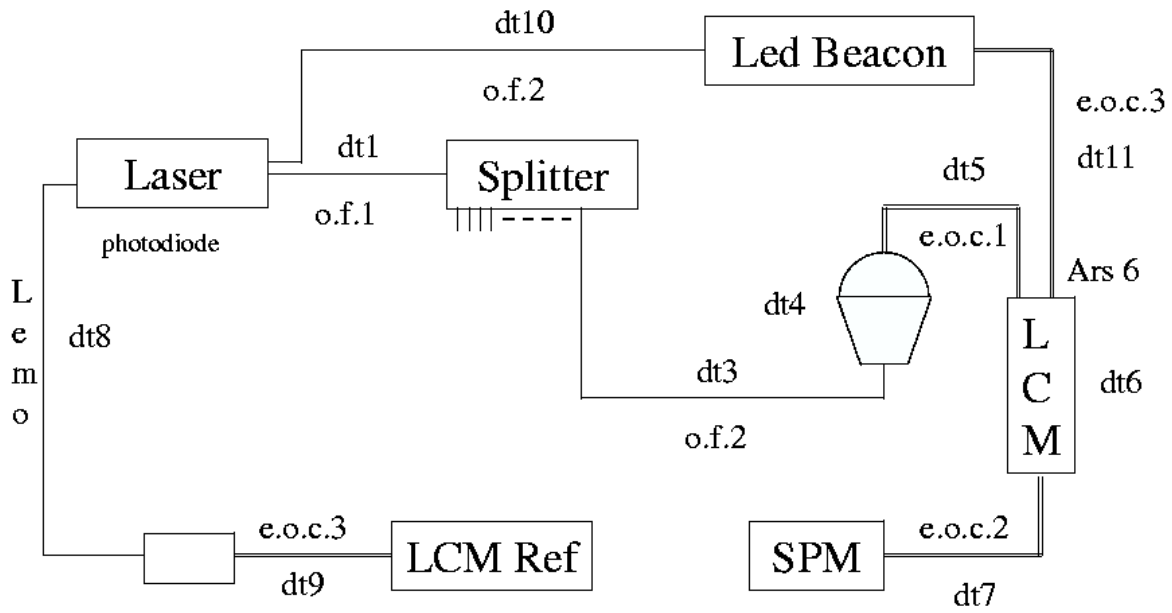

Figure 12: Optical structure for the distribution of the laser light for all OMs and the LED_Beacon. As you can see, the optical paths for an OM and the LED_Beacon are differents.

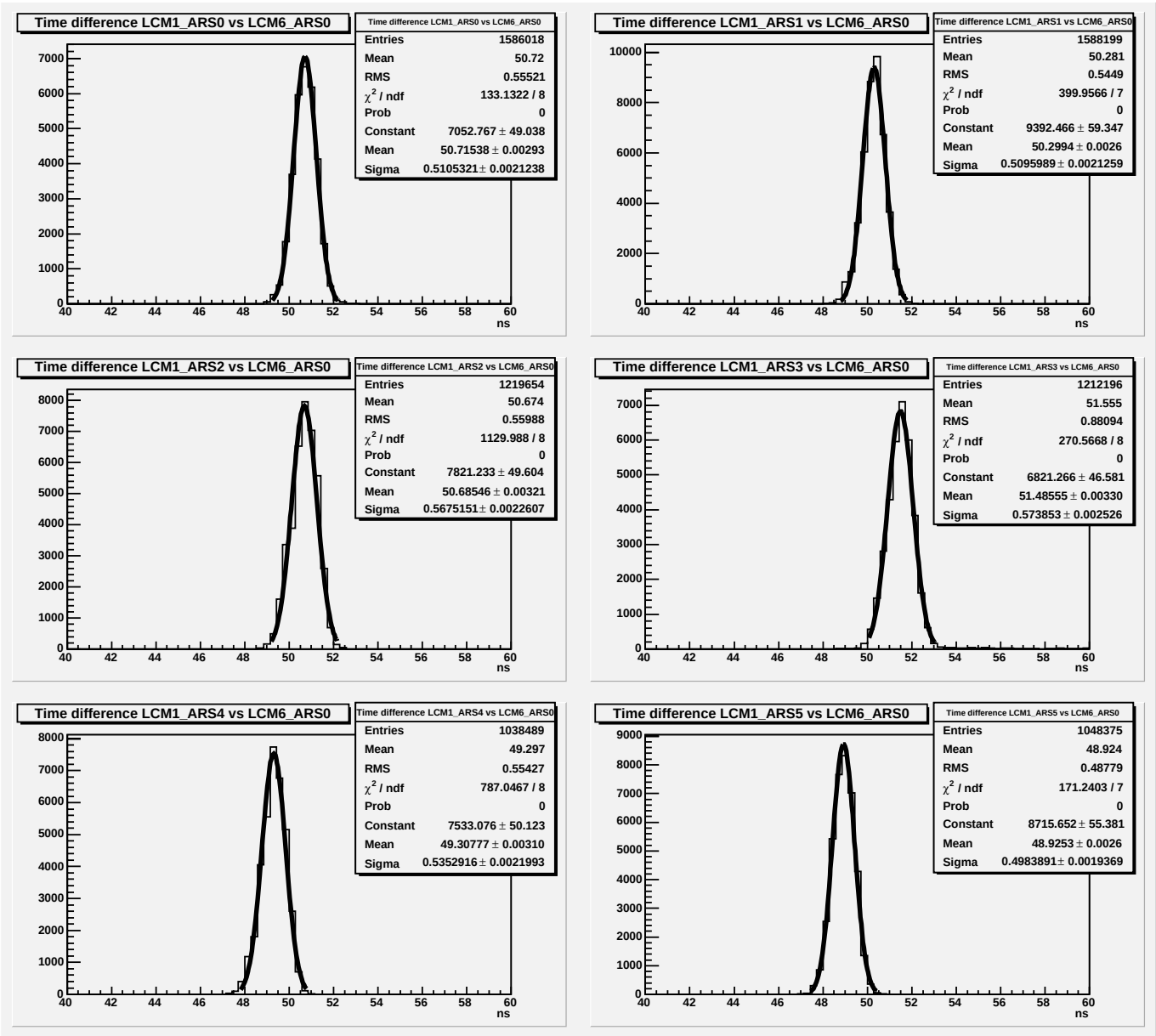

Figure 13: Example of time difference distributions after walk effect corrections for the first storey of the sector1.

LCM_DAQ_Id	LCM	ARS	TVCAmin	TVCAmax	TVCBmin	TVCBmax	ClkPh (ns)	Dt (ns)	ErrStat	ErrSyst	ErrTot	Sigma	Int	Slope	P0	P1	P2	P3
1624	1	0	57	208	57	207	520.896	0	0.01693	0.075	0.07689	0.51053	63.35	1.1	2499.79	51.3694	52.4048	-19.01
1624	1	1	56	227	56	217	520.896	0.41599	0.01641	0.07075	0.07263	0.5096	63.22	1.1	2499.79	50.8662	53.2794	-21.17
1624	1	2	48	214	48	209	520.896	-0.1401	0.01656	0.07141	0.07331	0.56752	25.92	1.1	2499.79	51.6029	52.0692	-21.65
1624	1	3	59	216	59	212	520.896	-0.9882	0.01737	0.07348	0.07551	0.57385	79.61	1.1	2499.79	52.2202	51.0256	-21.38
1624	1	4	55	204	54	198	520.896	1.41562	0.01711	0.07681	0.07869	0.53529	75.91	1.1	2499.79	49.6536	54.7696	-17.94
1624	1	5	59	228	59	228	520.896	1.79909	0.01628	0.07141	0.07325	0.49839	64.01	1.1	2499.79	49.1004	55.3255	-23.87
1624	1	6	0	270	0	270	520.896	0	0	0	0	0	0	0	0	0	0	0
1631	2	0	41	206	43	206	645.806	-1.1741	0.01565	0.075	0.07661	0.42598	36.92	1.1	2499.79	51.2202	52.7256	-21.38
1631	2	1	60	233	60	231	645.806	-0.9134	0.01596	0.07075	0.07253	0.42784	81.74	1.1	2499.79	50.8202	53.5256	-21.38
1631	2	2	60	231	60	231	645.806	-1.2412	0.01724	0.07141	0.07347	0.54217	64.21	1.1	2499.79	51.0502	53.2256	-12.38
1631	2	3	49	204	49	201	645.806	-0.9278	0.0162	0.07348	0.07525	0.49869	41.93	1.1	2499.79	51.0502	53.9256	-15.38
1631	2	4	56	231	56	230	645.806	1.31388	0.01655	0.07681	0.07858	0.47285	54.75	1.1	2499.79	49.0002	56.5256	-15.38
1631	2	5	56	215	56	212	645.806	0.46554	0.01602	0.07141	0.07319	0.44469	67.59	1.1	2499.79	49.6502	54.2756	-20.38
1631	2	6	67	233	67	227	645.806	54.183	0.0132	0.07071	0.07193	0.29558	0	0	0	0	0	0
1622	3	0	54	211	56	214	767.939	2.36786	0.01671	0.075	0.07684	0.52123	69.26	1.1	2499.79	49.167	54.4025	-17.14
1622	3	1	51	201	52	203	767.939	2.69954	0.01628	0.07075	0.0726	0.51763	66.3	1.1	2499.79	48.8565	54.9276	-20.54
1622	3	2	57	243	57	236	767.939	3.11549	0.01647	0.07141	0.07329	0.49491	67.01	1.1	2499.79	48.2536	56.0788	-20.36
1622	3	3	56	225	56	218	767.939	2.84682	0.01614	0.07348	0.07524	0.51686	49.74	1.1	2499.79	48.6311	55.9038	-20.16
1622	3	4	63	236	63	233	767.939	0.66431	0.01557	0.07681	0.07837	0.43376	73.79	1.1	2499.79	48.8502	55.3256	-20.38
1622	3	5	49	220	49	212	767.939	-0.1514	0.01637	0.07141	0.07327	0.48142	60.26	1.1	2499.79	49.7002	53.7256	-20.38
1622	3	6	0	270	0	270	767.939	0	0	0	0	0	0	0	0	0	0	0

Figure 14: Example of table’s structure for 3 LCMs of the sector1.

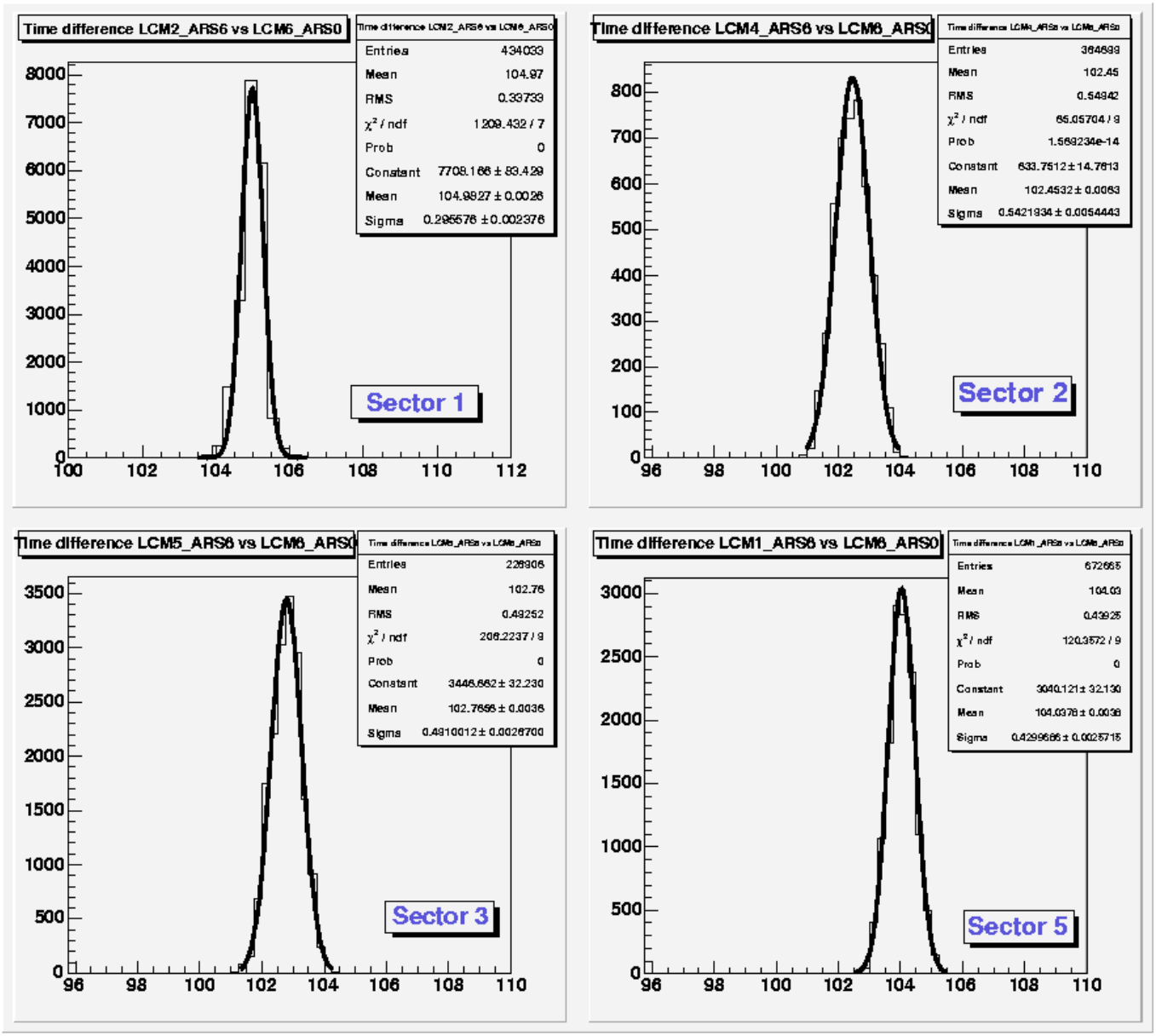

Figure 15: Time difference distributions for the four LED_Beacons of the Line1 after optical path correction between the laser system for an OM and that for a LED_Beacon (without Transit-Time correction and difference with the LCM1_ARS0 taken as reference).

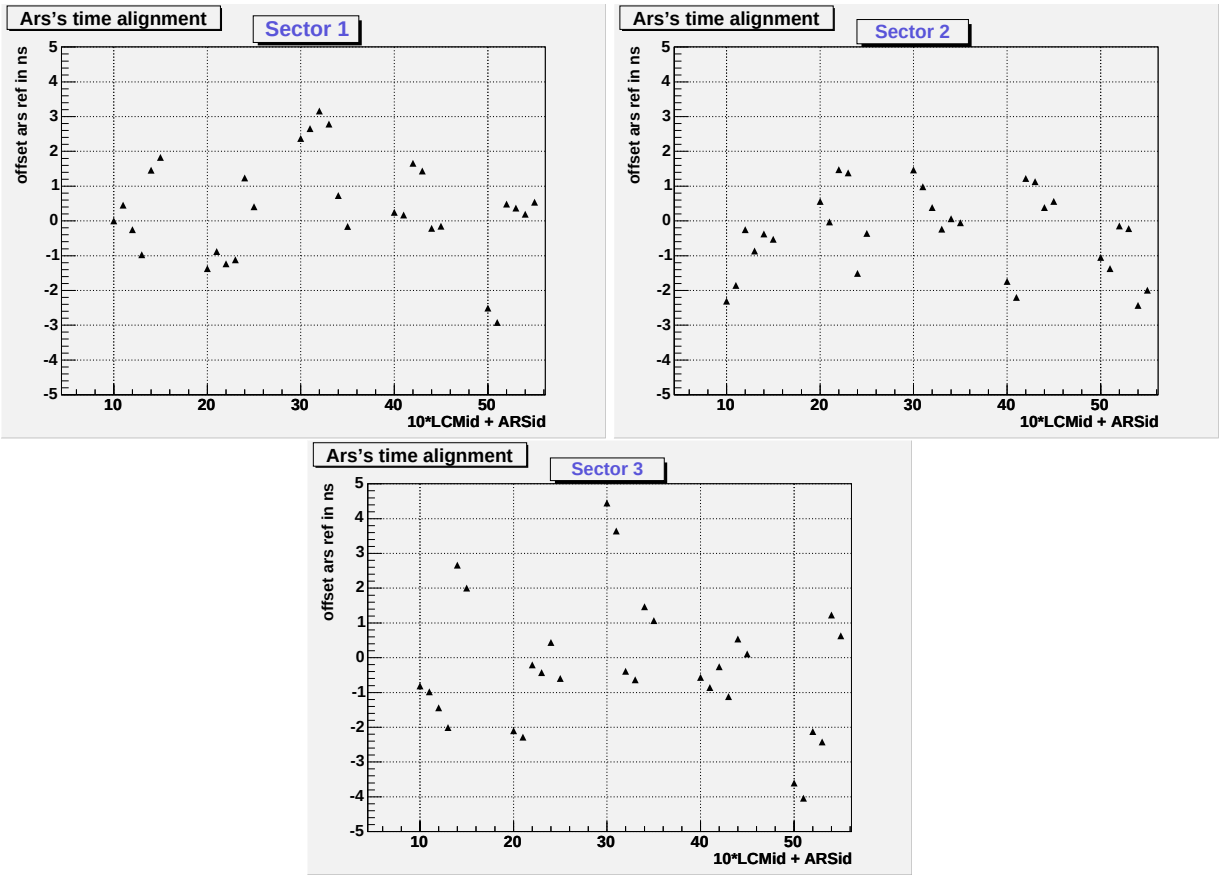

Figure 16: Resulting time offsets for the ARSs in Sector 1,2 and 3.

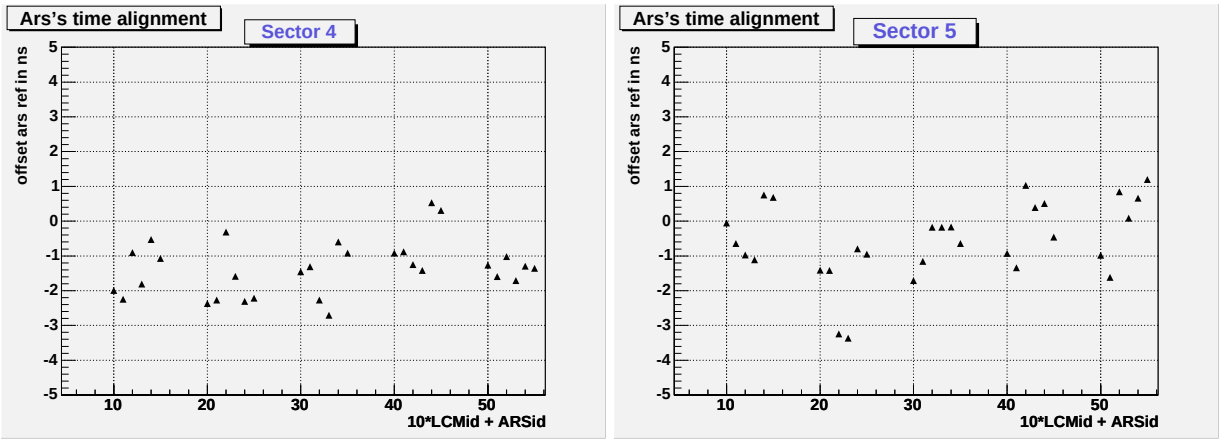

Figure 17: Resulting time offsets for the ARSs in Sector 4 and 5.

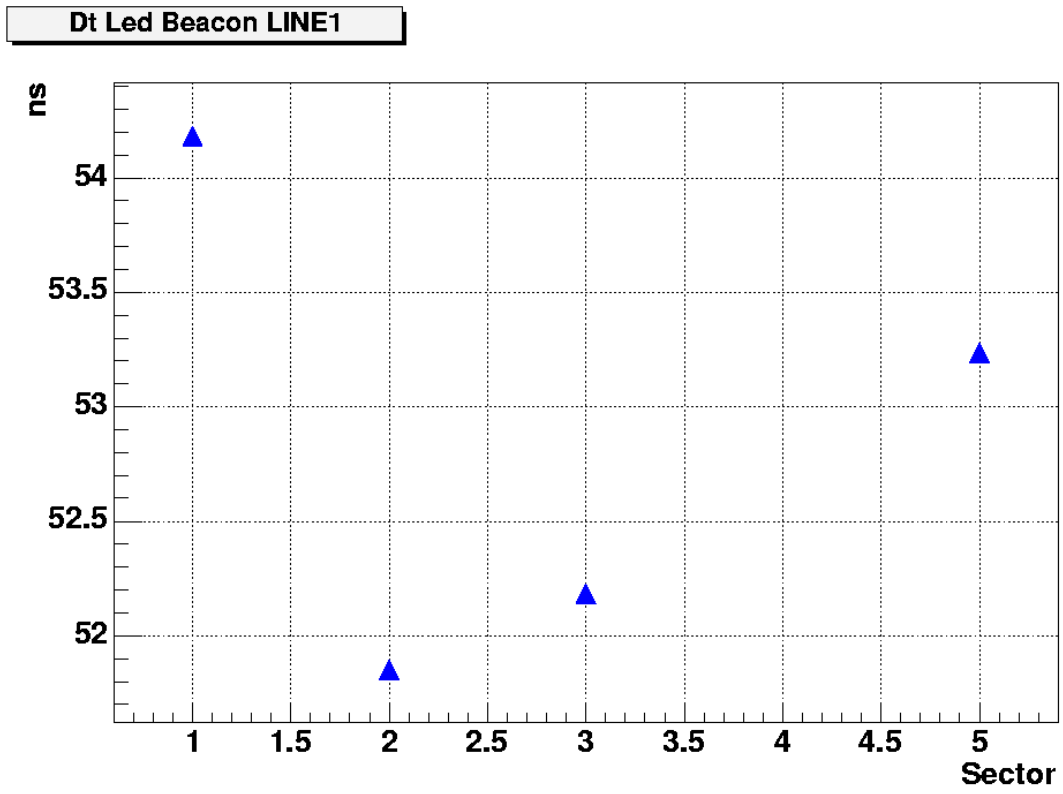

Figure 18: Resulting time offsets for the four LED-Beacons (without Transit-Time correction).

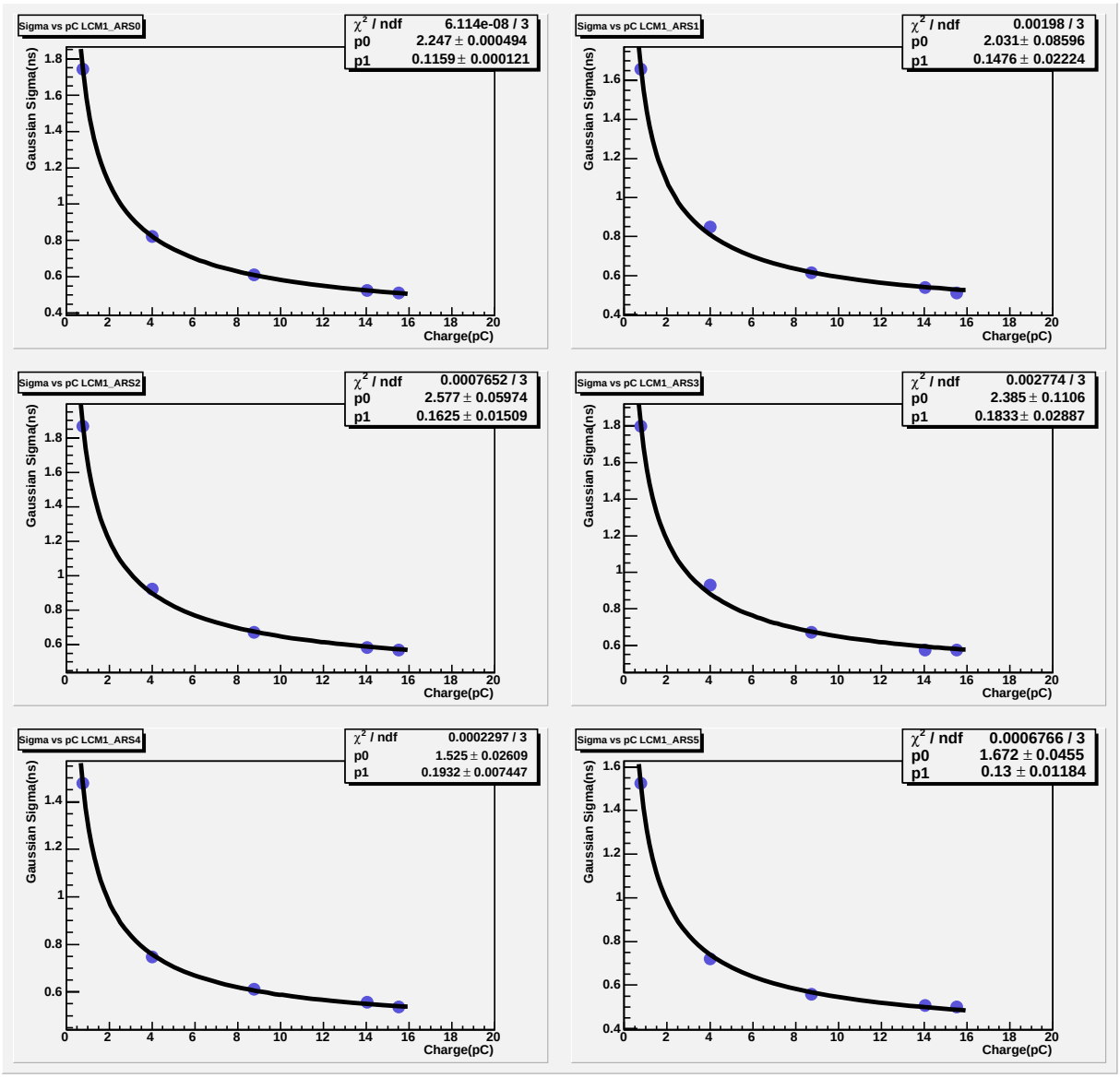

Figure 19: Example of OMs time resolution in function of the charge(pC) for the LCM1 of the Sector1.

First results of the Instrumentation Line for the deep-sea ANTARES neutrino telescope

J.A. Aguilar[j], A. Albert[u], F. Ameli[x], M. Anghinolfi[i], G. Anton[g], S. Anvar[y], E. Aslanides[e], J-J. Aubert[e], E. Barbarito[b], S. Basa[r], M. Battaglieri[i], Y. Becherini[c], R. Bellotti[b], J. Beltramelli[y], V. Bertin[e], A. Bigi[w], M. Billault[e], R. Blaes[u], N. de Botton[y], M.C. Bouwhuis[v], S.M. Bradbury[t], R. Bruijn[v,ab], J. Brunner[e], G.F. Burgio[f], J. Busto[e], F. Cafagna[b], L. Caillat[e], A. Calzas[e], A. Capone[x], L. Caponetto[f], E. Carmona[j], J. Carr[e], S.L. Cartwright[z], D. Castel[u], E. Castorina[w], V. Cavasinni[w], S. Cecchini[c,m], A. Ceres[b], P. Charvis[h], P. Chauchot[k], T. Chiarusi[x], M. Circella[b], C. Colnard[v], C. Compère[k], R. Coniglione[s], N. Cottini[w], P. Coyle[e], S. Cuneo[i], A-S. Cussat-Legras[d], G. Damy[k], R. van Dantzig[v], C. De Marzo[b],I. Dekeyser[d], E. Delagnes[y], D. Denans[y], A. Deschamps[h], F. Dessages-Ardellier[y], J-J. Destelle[e], B. Dinkespieler[e], C. Distefano[s], C. Donzaud[y], J-F. Drogou[ℓ], F. Druillole[y], D. Durand[y], J-P. Ernenwein[u], S. Escoffier[e], E. Falchini[w], S. Favard[e], F. Feinstein[e], S. Ferry[n], D. Festy[k], C. Fiorello[b], V. Flaminio[w], S. Galeotti[w], J-M. Gallone[n], G. Giacomelli[c], N. Girard[u], C. Gojak[e], Ph. Goret[y], K. Graf[g], G. Hallewell[e], M.N. Harakeh[q], B. Hartmann[g], A. Heijboer[v,ab], E. Heine[v], Y. Hello[h], J.J. Hernández-Rey[j], J. Hößl[g], C. Hoffman[n], J. Hogenbirk[v], J.R. Hubbard[y], M. Jaquet[e], M. Jaspers[v,ab], M. de Jong[v], F. Jouvenot[y], N. Kalantar-Nayestanaki[q], A. Kappes[g], T. Karg[g], S. Karkar[e], U. Katz[g], P. Keller[e], H. Kok[v], P. Kooijman[v,aa], C. Kopper[g], E.V. Korolkova[z], A. Kouchner[a], W. Kretschmer[g], A. Kruijer[v], S. Kuch[g], V.A. Kudryavstev[z], H. Lafoux[y], P. Lagier[e], R. Lahmann[g], G. Lamanna[e], P. Lamare[y], J.C. Languillat[y], H. Laschinsky[g], V. Layshuk[p], Y. Le Guen[k], H. Le Provost[y], A. Le Van Suu[e], T. Legou[e], G. Lim[v,ab], L. Lo Nigro[f], D. Lo Presti[f],

H. Loehner [q], S. Loucatos [y], F. Louis [y], F. Lucarelli [x], M. Marcelin [r], A. Margiotta [c], R. Masullo [x], F. Mazéas [k], A. Mazure [r], J.E. McMillan [z], R. Megna [b], M. Melissas [e], E. Migneco [s], A. Milovanovic [t], M. Mongelli [b], T. Montaruli [b], M. Morganti [w], L. Moscoso [y,a], M. Musumeci [s], C. Naumann [g], M. Naumann-Godo [g], V. Niess [e], C. Olivetto [n], R. Ostasch [g], N. Palanque-Delabrouille [y], P. Payre [e], H. Peek [v], C. Petta [f], P. Piattelli [s], J-P. Pineau [n], J. Poinsignon [y], V. Popa [c,o], T. Pradier [n], C. Racca [n], N. Randazzo [f], J. van Randwijk [v], D. Real [j], B. van Rens [v], F. Réthoré [e], P. Rewiersma [v],G. Riccobene [s], V. Rigaud [ℓ], M. Ripani [i], V. Roca [j], C. Roda [w], J.F. Rolin [k], M. Romita [b], H.J. Rose [t], A. Rostovtsev [p], J. Roux [e], M. Ruppi [b], G.V. Russo [f], F. Salesa [j], K. Salomon [g], P. Sapienza [s], F. Schmitt [g], J-P. Schuller [x], R. Shadnize [g], I. Sokalski [b], T. Spona [g], M. Spurio [c], G. van der Steenhoven [v], T. Stolarczyk [y], K. Streeb [g], D. Stubert [u], L. Sulak [e], M. Taiuti [i], C. Tamburini [d], G. Terreni [w], L.F. Thompson [z], C. Tao [e], P. Valdy [ℓ], V. Valente [x], B. Vallage [y], G. Venekamp [v], B. Verlaat [v], P. Vernin [y], R. de Vita [i], G. de Vries [v,aa], R. van Wijk [v], P. de Witt Huberts [v], G. Wobbe [g], E. de Wolf [v,ab], A-F. Yao [d], D. Zaborov [p], H. Zaccone [y], J.D. Zornoza [j], J. Zúñiga [j]

[a] *AstroParticule et Cosmologie, UMR 7164 (CNRS, Université Paris 7, CEA, Observatoire de Paris), 11, place Marcelin Berthelot, 75005 Paris, France*
[b] *Dipartimento Interateneo di Fisica e Sezione INFN, Via E. Orabona 4, 70126 Bari, Italy*
[c] *Dipartimento di Fisica dell'Università e Sezione INFN, Viale Berti Pichat 6/2, 40127 Bologna, Italy*
[d] *Centre d'Océanologie de Marseille, CNRS/INSU Université de la Méditerranée Aix-Marseille II, Station Marine d'Endoume-Luminy, Rue de la Batterie des Lions, 13007 Marseille, France*
[e] *CPPM – Centre de Physique des Particules de Marseille, CNRS/IN2P3 Université de la Méditerranée Aix-Marseille II, 163 Avenue de Luminy, Case 907, 13288 Marseille Cedex 9, France*
[f] *Dipartimento di Fisica ed Astronomia dell'Università e Sezione INFN, Viale Andrea Doria 6, 95125 Catania, Italy*
[g] *Friedrich-Alexander-Universität Erlangen-Nürnberg, Physikalisches Institut, Erwin-Rommel-Str. 1, D-91058 Erlangen, Germany*
[h] *UMR GéoScience Azur, Observatoire Océanologique de Villefranche, BP48, Port de la Darse, 06235 Villefranche-sur-Mer Cedex, France*
[i] *Dipartimento di Fisica dell'Università e Sezione INFN, Via Dodecaneso 33, 16146 Genova, Italy*

[j] *IFIC – Instituto de Física Corpuscular, Edificios Investigación de Paterna, CSIC – Universitat de València, Apdo. de Correos 22085, 46071 Valencia, Spain*
[k] *Centre de Brest, BP 70, 29280 Plouzané, France*
[ℓ] *Centre de Toulon/La Seyne Sur Mer, Port Brégaillon, Chemin Jean-Marie Fritz, 83500, La Seyne sur Mer, France*
[m] *INAF-IASF, via P. Gobetti 101, 40129 Bologna, Italy*
[n] *IPHC – Institut Pluridisciplinaire Hubert Curien, 23 rue du Loess, BP 28 – 67037 Strasbourg CEDEX 2, France*
[o] *Institute for Space Sciences, 77125 Bucharest, Magurele, Romania*
[p] *ITEP – Institute for Theoretical and Experimental Physics, B. Cheremushkinskaya 25, 117259 Moscow, Russia*
[q] *Kernfysisch Versneller Instituut (KVI), University of Groningen, Zernikelaan 25, 9747 AA Groningen, The Netherlands*
[r] *Laboratoire d'Astrophysique de Marseille, CNRS/INSU - Université de Provence Aix-Marseille I, Traverse du Siphon – Les Trois Lucs, BP 8, 13012 Marseille Cedex 12, France*
[s] *INFN – Labaratori Nazionali del Sud (LNS), Via S. Sofia 44, 95123 Catania, Italy*
[t] *School of Physics & Astronomy, University of Leeds LS2 9JT, UK*
[u] *GRPHE – Groupe de Recherche en Physique des Hautes Energies, Université de Haute Alsace, 61 Rue Albert Camus, 68093 Mulhouse Cedex, France*
[v] *Nationaal Instituut voor Kernfysica en Hoge-Energiefysica (NIKHEF), Kruislaan 409, 1098 SJ Amsterdam, The Netherlands*
[w] *Dipartamento di Fisica dell'Università e Sezione INFN, Largo B. Pontecorvo 3, 56127 Pisa, Italy*
[x] *Dipartimento di Fisica dell'Università "La Sapienza" e Sezione INFN, P.le Aldo Moro 2, 00185 Roma, Italy*
[y] *DSM/DAPNIA – Direction des Sciences de la Matière, Département d'Astrophysique de Physique des Particules de Physique Nucléaire et de l'Instrumentation Associée, CEA/Saclay, 91191 Gif-sur-Yvette Cedex, France*
[z] *Dept. of Physics and Astronomy, University of Sheffield, Sheffield S3 7RH, UK*
[aa] *Universiteit Utrecht, Faculteit Betawetenschappen, Princetonplein 5, 3584 CC Utrecht, The Netherlands*
[ab] *Universiteit van Amsterdam, Instituut voor Hoge-Energiefysica, Kruislaan 409, 1098 SJ Amsterdam, The Netherlands*

Abstract

In 2005, the ANTARES Collaboration deployed and operated at a depth of 2500 m a so-called Mini Instrumentation Line equipped with Optical Modules (MILOM) at the ANTARES site. The various data acquired during the continuous operation from April to December 2005 of the MILOM confirm the satisfactory performance of the Optical Modules, their front-end electronics and readout system, as well as the calibration devices of the detector. The in-situ measurement of the Optical Module yielded a timing resolution better than 0.5 ns. The performance of the acoustic positioning system, which enables the spatial reconstruction of the ANTARES detector with a precision of $\sim$ 10 cm, is verified. These results demonstrate that with the full ANTARES neutrino telescope the design angular resolution of better than 0.3° can be realistically achieved.

1 Introduction

The ANTARES Collaboration is building a large underwater neutrino telescope located at a depth of 2500 m in the Mediterranean Sea offshore from Toulon in France [1]. The experiment aims to detect neutrinos with energies above 10 GeV by means of the Cherenkov light emitted in sea water by charged particles produced in the neutrino interaction with the surrounding medium. Photons are recorded by a lattice of Optical Modules (OMs) [2], consisting of 10" hemispherical photomultiplier tubes (PMTs) [3] housed in pressure resistant glass spheres, installed along a set of mooring lines. The ANTARES detector will consist of 12 lines of 25 storeys, each storey being equipped with a triplet of Optical Modules and an electronic container mounted on a titanium frame, giving thus a grand total of 900 OMs. Some storeys also support a hydrophone for acoustic positioning or a LED Optical Beacon used for interstring time calibration. Every line is individually connected to a Junction Box by an interconnecting cable of length of a few hundred metres laid down on the sea bed. The Junction Box is itself linked to the shore station by a 40 km long electro-optical cable equipped with 48 optical fibres. The installation of the 12 lines of the ANTARES detector is starting in February 2006 with completion expected in 2007.

In Spring 2003, two prototype lines, the Prototype Sector Line (PSL) equipped with 15 Optical Modules (OMs) and the Mini Instrumentation Line (MIL) hosting calibration and environmental measurement devices, were deployed, connected and operated for a few months at the ANTARES site. This operation allowed a demonstration of the main aspects of the design of the detector and measurement of the background counting rates, due to bioluminescence and ^{40}K decays, in the OMs over a period of about four months [4]. The study also revealed that both lines suffered some problems. After the experience of the PSL and MIL lines, significant changes were made to the detector design. In parallel to the launching of the mass production of all detector elements, the ANTARES Collaboration built a new version of the Mini Instrumentation Line based on the final design of all electronic boards and mechanics. This line, which also includes an extra storey with three OMs, has been christened the MILOM. The main objective of the MILOM operation is to provide an in-situ check of the modified detector elements and a validation of the performance of the time calibration and the acoustic positioning devices. It was also an excellent opportunity to validate the tools and procedures used during the integration and deployment of a line before their application to the first complete ANTARES detector line. Furthermore, the MILOM houses environmental instruments needed for the calibration of the detector and the monitoring of the water physical properties.

Completed in December 2004, the MILOM line was deployed on the ANTARES

site, located at 42°48′N-6°10′E, in March 2005 and connected into the existing Junction Box with the Remote Operated Vehicle (ROV) VICTOR of IFREMER in April 2005. It has operated since then with almost permanent shift crews from the ANTARES shore station located in La Seyne-sur- Mer. This paper highlights the main results obtained from the MILOM operation in 2005, in particular the analysis of the Optical Module signals and of the calibration device data.

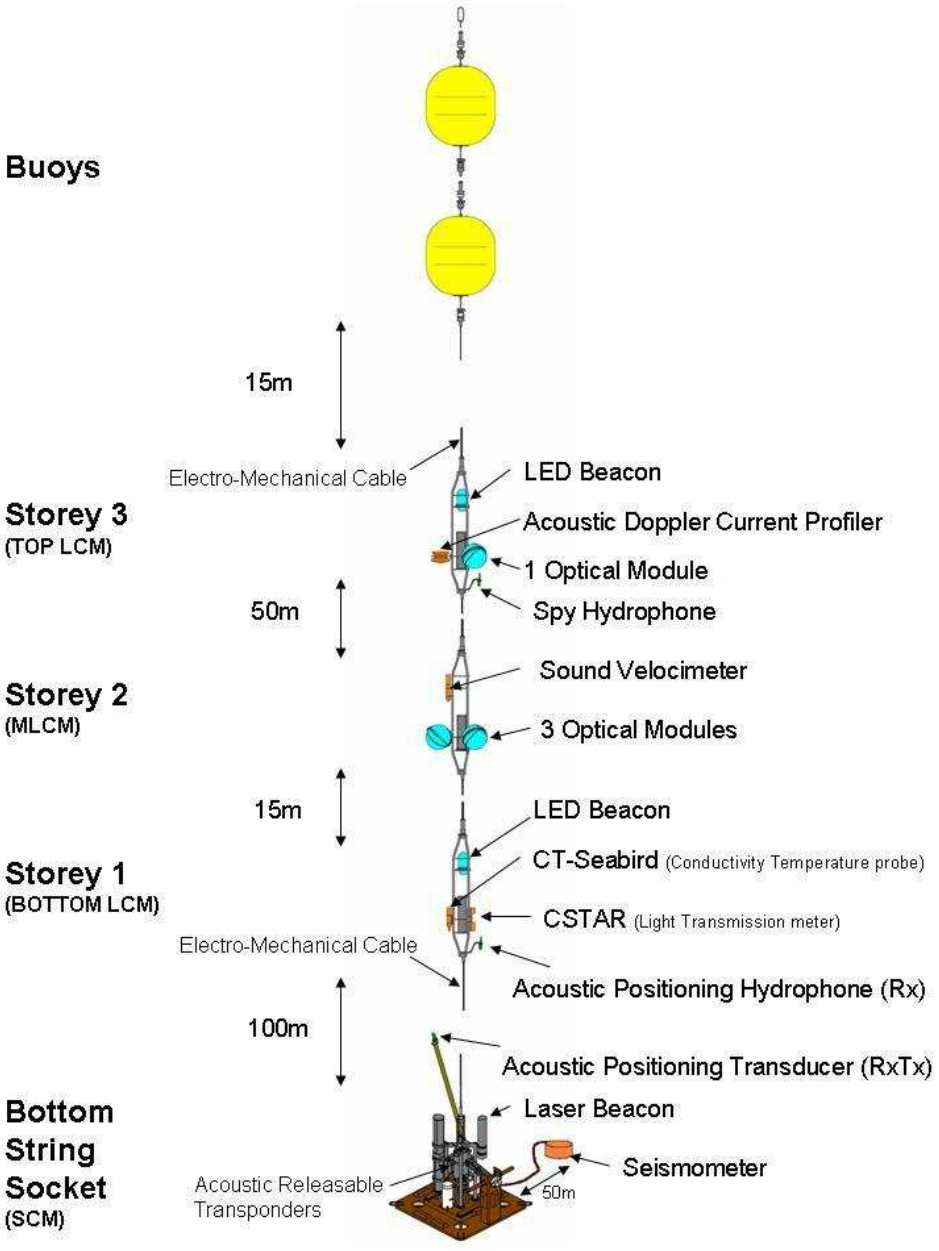

Fig. 1. Layout of the MILOM line.

2 The MILOM line

As shown in figure 1, the MILOM consists of an instrumented releasable anchor, the Bottom String Socket (BSS), and of three storeys located respectively at 100 m, 117 m and 169 m above the sea bed (the inter-storey spacings indicated in figure 1 correspond to the cable lengths). The line is maintained in an almost vertical position by two buoys located at the top.

The MILOM is equipped with four Optical Modules: a triplet of OMs on the second storey, as for a standard ANTARES optical line storey, and a single additional OM fixed on the top storey. The line also supports three intense light sources used mainly for the OM timing calibration: the Laser Beacon located on the BSS and two LED Optical Beacons attached to the bottom and top storey respectively. In order to allow the reconstruction of the line shape geometry, the MILOM is equipped with biaxial tiltmeters and compasses located in the electronic container of every storey, and with two acoustic positioning modules: an emission/reception (RxTx) module with its transducer on the BSS and a reception (Rx) module with its hydrophone on the bottom storey. In addition, the MILOM hosts various environmental devices: an acoustic current profiler [5] monitors the intensity and direction of the underwater flow; a sound velocimeter [6] records the local value of the sound velocity; a CT probe [7] measures the conductivity and temperature of the sea water; a transmission meter [8] monitors the light attenuation of the water; a Spy Hydrophone records the acoustic activity from the positioning beacons, surface noise or a biological origin; and a broadband seismometer [9] installed into the sea bed sediment 50 m away from the MILOM anchor monitors the seismic activity at the site. Finally, the MILOM BSS is equipped with two releasable autonomous transponders [10] which enable the monitoring of the line anchor position during its deployment and allow the release of the BSS from its dead weight in order to recover the line.

All instruments deliver their data in real time and can be remotely controlled from the ANTARES shore station through the Gb Ethernet network of the detector. Every storey is equipped with a Local Control Module Container (LCM) which contains the electronic boards for the OM signal processing, the instrument readout, the acoustic positioning, the power system and the data transmission. On the middle storey, the Master Local Control Module (MLCM) also contains an Ethernet switch board, which multiplexes the data acquisition (DAQ) channels from the other storeys. At the bottom of the line, the BSS is equipped with a String Control Module (SCM) container which contains the local readout and DAQ electronics, as well as the power conversion and delivery system for the whole line. Finally, both MCLM and SCM include a Dense Wavelength Division Multiplexing system used for data transmission in order to merge several 1Gb/s Ethernet channels on the same pair

of optical fibres by using different laser wavelengths. Although a local trigger requiring time coincidences between Optical Modules of the same storey can be activated into each LCM, the large bandwidth of the DAQ system allows most of the time a transmission of all recorded OM signals to shore. A dedicated computing farm, the data filter, can then perform a global selection of the OM hits of the interesting "physics events" from the data recorded by the whole detector during a certain time slice [11].

While the recording of the OM signals and instrument data of the MILOM started immediately after its connection, the first months of operation have been dedicated to online software development and tuning of the detector settings. The smooth data taking of the MILOM mainly started in September 2005 after an implementation of an optical amplifier at the shore station and an upgrade of the DAQ software.

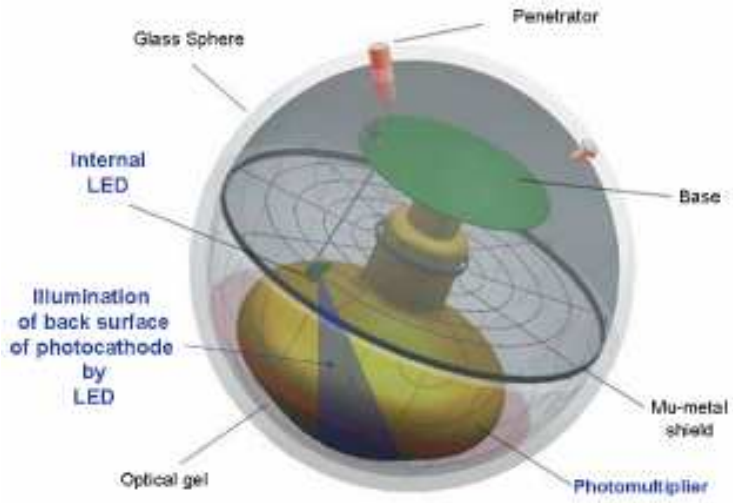

Fig. 2. Sketch of the ANTARES Optical Module.

3 The Optical Module data

The ANTARES Optical Module consists of a 10" Hamamatsu photomultiplier tube housed in a pressure resistant glass sphere (see figure 2). The 900 PMTs foreseen in the ANTARES detector have been selected and fully characterized to work with a threshold below the single photo-electron level with a mean transit time spread of $\sigma \sim 1.3$ ns (FWHM ~ 3.0 ns). The PMT signal is processed by the Analogue Ring Sampler (ARS) ASICs which measure the arrival time and the charge of the pulse [12]. Only this information is sent to shore in the case where it is compatible with a single photo-electron (SPE) pulse, while the ARS can perform a full digitisation of the PMT signal for larger amplitudes. In order to minimize the dead time, every OM is read out

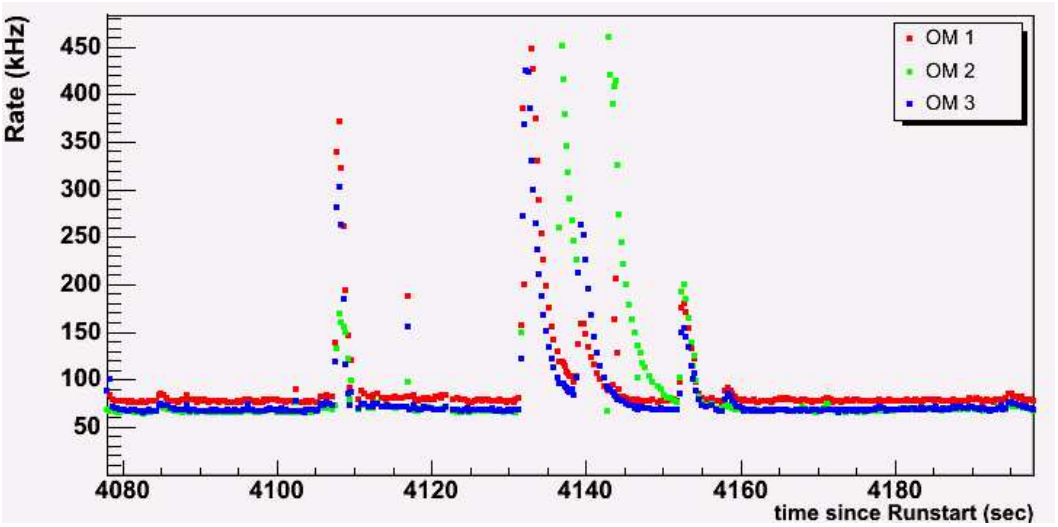

Fig. 3. Example of counting rates for the three OMs located on the second storey of the MILOM during 120 seconds.

by a pair of ARS chips which treat the signal alternatively according to a token ring.

During normal operation, the PMT high voltage is set so as to obtain a gain of 5×10^7 leading to a SPE signal amplitude of about 60 mV. The readout trigger threshold of the ARS is set to 0.5 photo-electrons. Figure 3 shows an example of the counting rates recorded by the three OMs located on the MILOM second storey during a period of 120 seconds. The counting rates exhibit a baseline largely dominated by optical background due to ^{40}K decays and bioluminescence coming from bacteria, as well as bursts of few seconds duration produced by bioluminescent emission of macro organisms [13]. The fourth OM located on the top storey is exhibiting a faulty power supply since the beginning of the MILOM operation; it is thus not read out. A visual survey of the MILOM line has recently been performed in-situ by the ROV VICTOR. It revealed that the Optical Beacon, located on that same top storey and powered with the same supply, is full of water due a leak of its glass container.

For each OM, the baseline rate is defined as the average of the minimum counting rate during periods of 15 minutes. Figure 4 shows the summary of the baseline rates extracted from the data recorded by the three OMs of the MILOM second storey for a period of three months during Autumn 2005. The variability of the bioluminescence component of the baseline, already observed during the operation of the Prototype Sector Line in 2003, is confirmed by the data measured with the MILOM. The baseline counting rates decrease from 80-90 kHz in mid-September to about 60 kHz in November 2005. Figures 3 and 4 also clearly reveal that the counting rate of one Optical Module (OM1) is systematically larger by about 15% with respect to the two other OMs of the storey. Studies are in progress to determine whether this difference can

be attributed to a larger quantum efficiency or to a possible lower threshold value of the PMT of this Optical Module with respect to the others.

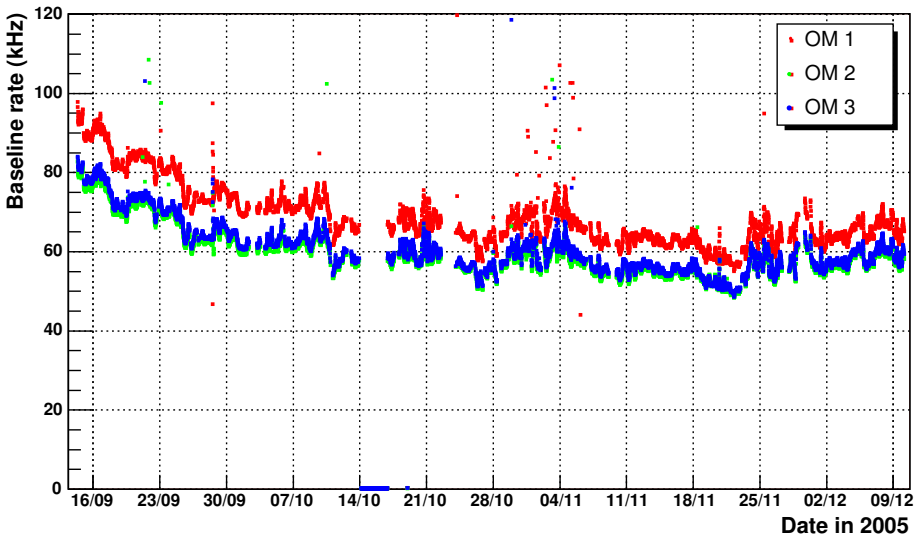

Fig. 4. Baseline rates for the three OMs located on the second storey of the MILOM during Autumn 2005.

The time coincidences between the signals of two OMs have also been studied. Figure 5 shows such distributions as a function of the time delay between the OM signals, for the three pair combinations of the OMs located on the MILOM second storey. The distributions exhibit a flat background due to random coincidences of OM hits and a Gaussian distribution centred around $\Delta t \sim 0$ due to genuine coincidences of two photon signals coming from ^{40}K radioactive decays. The genuine coincidence rates estimated from the Gaussian fits to the distribution are found to be 13.0 ± 0.5 Hz for the OM1-OM2 and OM1-OM3 pairs and 10.5 ± 0.4 Hz for the OM2-OM3 pair respectively. This is in very good agreement with a simulation of a simulation of the signal induced by the ^{40}K decays which leads to a coincidence rate of 12 Hz with a 4 Hz systematic error due to uncertainties on effective area and angular response of the OMs. These measurements also confirm that the larger counting rate observed with OM1 is not due to electronic background of its front-end electronic channel but probably due to a higher quantum efficiency.

As mentioned previously, the ARS has also the capability to perform a full sampling of the OM signal, called WaveForm (WF), in addition to the charge measurement of the PMT pulse and its arrival time. Although this functionality is mainly used to record double pulses or large amplitude signals, it is useful to cross-check the computation of the SPE charge by the integrator circuit of the ARS. In WF mode, the OM anode signal is digitised with 128 records at a sampling rate of 640 MHz. In order to obtain a precise time stamping of the WF data, a synchronous sampling of the 50 MHz internal ARS clock

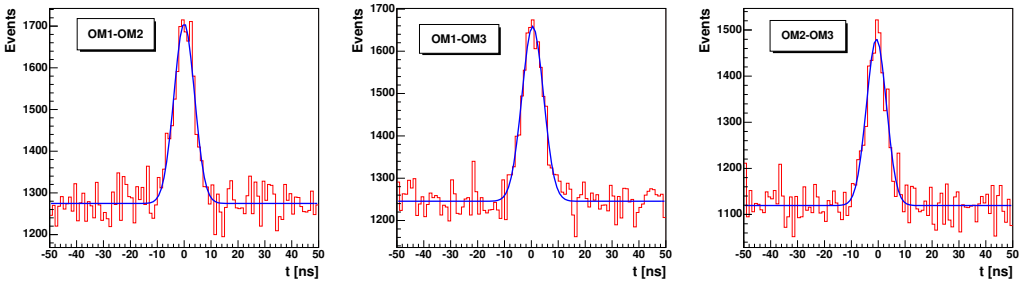

Fig. 5. Time coincidence distributions between the signals of two OMs of the MILOM second storey as a function of the time delay of the two signals. The three OM pair combinations are shown.

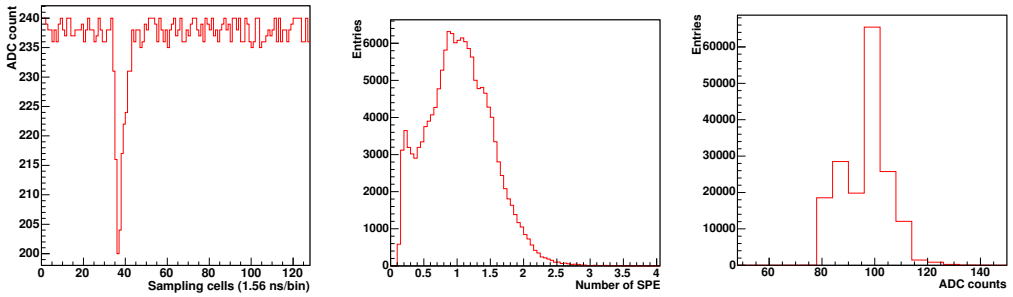

Fig. 6. Example of a WaveForm sampling of an OM signal (left). Charge distribution of the PMT signal obtained by integrating the WF samples (middle) and measured by the AVC circuit of the ARS (right).

is also produced and readout in addition to the OM data. An example of a WF record is shown on figure 6 (left). Figure 6 (middle) displays the charge distribution of the OM signal for SPE events obtained by integrating the WF samples after baseline subtraction. The single photo-electron peak is clearly identified well above the electronic noise. Figure 6 (right) also shows as a comparison the charge distribution measured by the analogue to voltage converter (AVC) circuit of the ARS. The AVC has a dynamic of 8 bits (256 channels) but the circuit is subject to significant non linearities which disturb the charge distribution when displayed with maximum granularity.

The stability of the measurements of the signal charge obtained with the integrator circuit of the ARS is shown in figure 7. This figure displays the variation of the mean charge measured by every ARS AVC circuit as a function of time for the three OMs on the second storey of the MILOM. The normalised mean charge is computed as the ratio between the mean value of the charge distribution to the mean value of their first measurement appearing in the plot. This figure is obtained from the analysis of minimum bias data largely dominated by SPE events. As can be seen in figure 6, the charge distributions remain stable within $\pm 1\%$ for all ARSs during more than two months of monitoring. This indicates that PMT gain, the trigger threshold and the charge

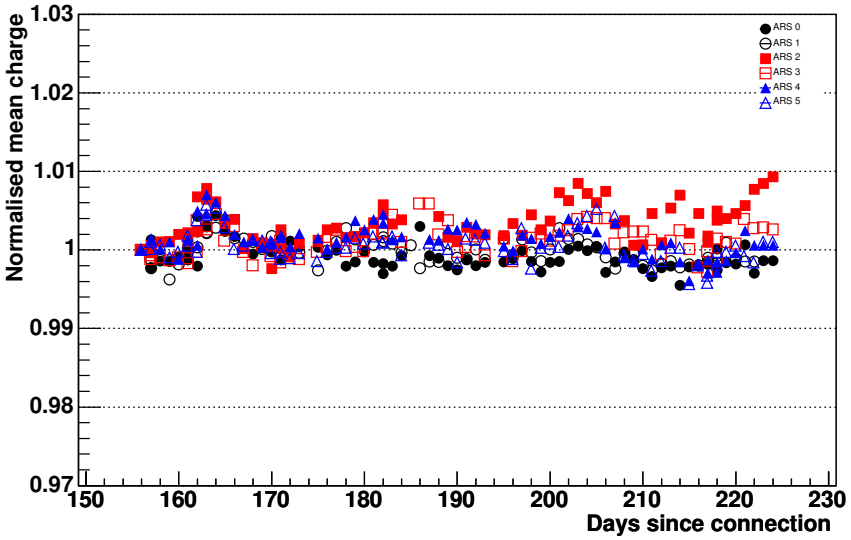

Fig. 7. Variation of the mean charge measured by the analogue to voltage converter (AVC) of every ARS as a function of time for the three OMs located on the second storey of the MILOM. The normalised mean charge is computed as the ratio between the mean value of the charge distribution to the mean value of their first measurement appearing in the plot.

integrators did not fluctuate by more than a few percents during that period.

4 Optical Module timing precision

The ANTARES neutrino telescope is designed to have an excellent angular resolution of less than 0.3° for neutrino energies in excess of 10 TeV, which relies on good timing resolution of the signals recorded by the Optical Modules. The specification for the detector is that the timing resolution should be limited by the transit time spread of the PMTs which have $\sigma \sim 1.3$ ns and by the effect of scattering and chromatic dispersion of the light during its transmission in water, which will contribute with a similar amount to the time uncertainty. To achieve this all electronics and calibration systems are each required to contribute less than 0.5 ns to the overall timing resolution.

The complete timing resolution of the Optical Modules has been measured with the MILOM using the LED Optical Beacon system [14]. As indicated in figure 1, an LED beacon is located in the bottom storey underneath the OM triplet of the second storey at a distance of about 15 metres. The LED beacon contains 36 individual blue LEDs ($\lambda = 470$ nm, typical dominant wavelength) synchronised in time and arranged to give a reasonably isotropic light emission. A small PMT internal to the LED beacon monitors the output

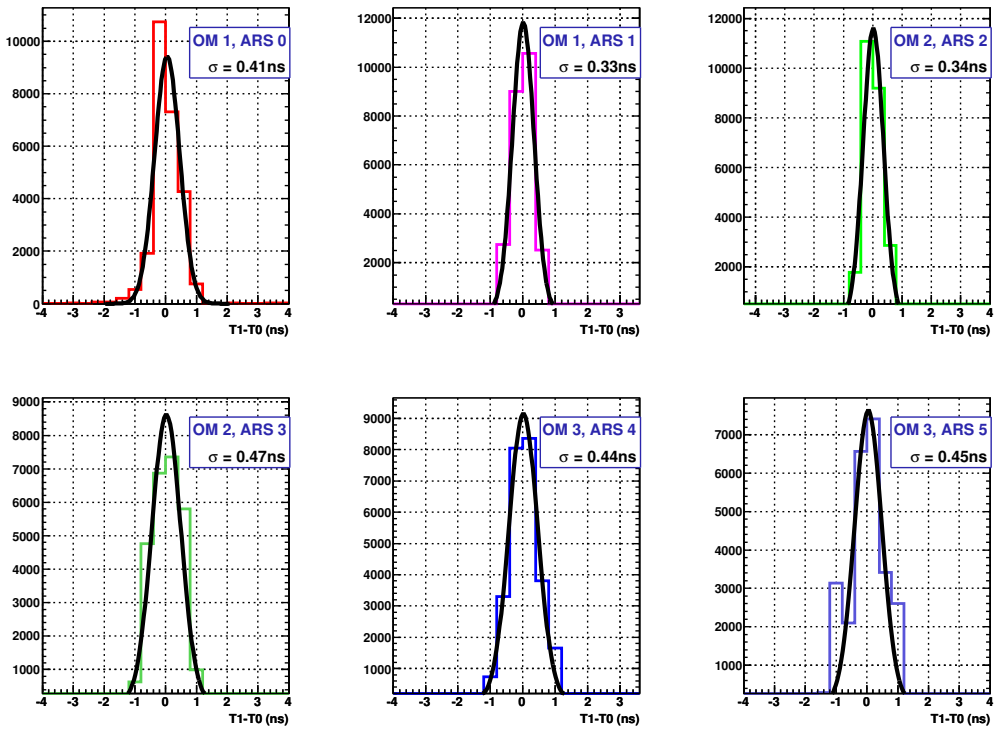

Fig. 8. Distribution of signal arrival times in the Optical Module (T1) with reference to the time of the LED Optical Beacon flash (T0). The measurement obtained by every ARS readout channel of the OM triplet located on the second storey is shown. Each distribution has been centred to 0 by subtracting its mean value before the fit of a Gaussian function. The resulting resolution value (σ) is indicated in each panel.

light pulse timing and amplitude and provides the time reference of the light flash.

The measurement of the OM timing resolution is performed by pulsing the LED beacon at a frequency of 30 Hz. Figure 8 shows the distribution of signal arrival times in the three OMs relative to the reference PMT in the LED Beacon. For every OM, the measurement obtained by both ARS readout channels are shown, since every front-end chip can induce a (possibly) different intrinsic electronic contribution to the timing measurement. In the time distribution shown in figure 7, the contribution of the small PMT inside the LED beacon is small since it has a fast rise time of 0.78 ns, and so the measurement is dominated by the OM contribution. As can be seen from the distribution shown in figure 8, the timing resolution of all Optical Module readout channels is measured to be $\sigma \sim 0.4$ ns. This resolution is obtained for large intensity light pulses and so is not dominated by the PMT transit time spread but by the intrinsic electronic resolution. A detailed analysis of the dependence of timing resolution with light intensity is in progress to separate the various contributions, but this result already shows that the complete electronics contribution

is smaller than 0.5 ns as required.

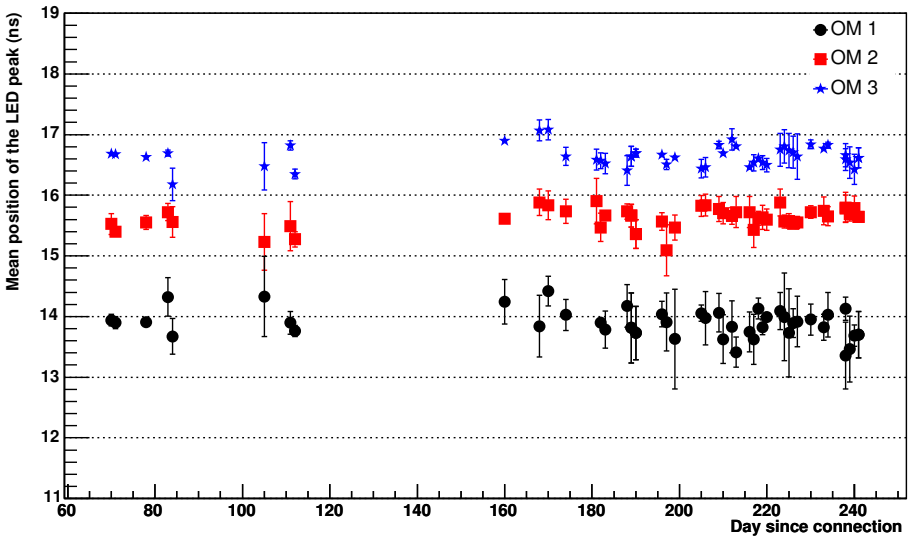

Fig. 9. Mean values of the arrival times of the OM signal induced by an internal LED flash with respect to the time of the flash. The mean time is displayed with reference to the start of the time to voltage converter (TVC) of the ARS. The plot displays the measurements obtained for the three OMs located on the second storey of the MILOM during six months of data taking. For every OM, the data points display the average value measured by its two ARS channels.

Every Optical Module also contains an internal blue LED in order to monitor the stability of the photomultiplier tube. This LED is mounted on the back of the PMT and illuminates a large fraction of the photocathode through the phototube, as shown in figure 2. The transit time of the PMT is monitored by flashing the internal LED at a rate of about 100 Hz and by looking at the OM signal arrival time with respect to the time of the LED flash. Figure 9 shows the mean of the peaks in such distributions for the triplet of OMs on the MILOM second storey as a function of time. It confirms that the transit time of the Optical Module remains stable within 0.5 ns during the operation of the MILOM in the sea.

5 Acoustic positioning system resolution

The second essential element to achieve the necessary angular resolution of the neutrino telescope is a real time measurement of the position in space of the Optical Modules with a precision of $\sim$ 10 cm. These positions are obtained by triangulation from distance measurements provided by the acoustic positioning system. The full acoustic positioning system will consist of a

three dimensional array of emitting transducers (RxTx modules), fixed on the sea bed, together with receiving hydrophones (Rx modules), attached on several storeys along every detector line. These devices exchange precisely timed acoustic signals in the 40-60 kHz frequency range. In addition, the acoustic system includes four autonomous transponders which emit an acoustic "ping" at a precisely given frequency, in response to a special interrogation by one RxTx module. These transponders will be located all around the ANTARES detector field in order to enlarge the triangulation basis and to make its geometry more uniform. At the present time, only a limited number of acoustic devices are installed at the site: one RxTx module on the MILOM anchor and one Rx module on its first storey. A first autonomous transponder has also been installed at the ANTARES site, its transducer being fixed at about 4 m above the sea bed on top of a pole supported by a pyramidal structure at a horizontal distance of $\sim$ 175 m from the MILOM anchor.

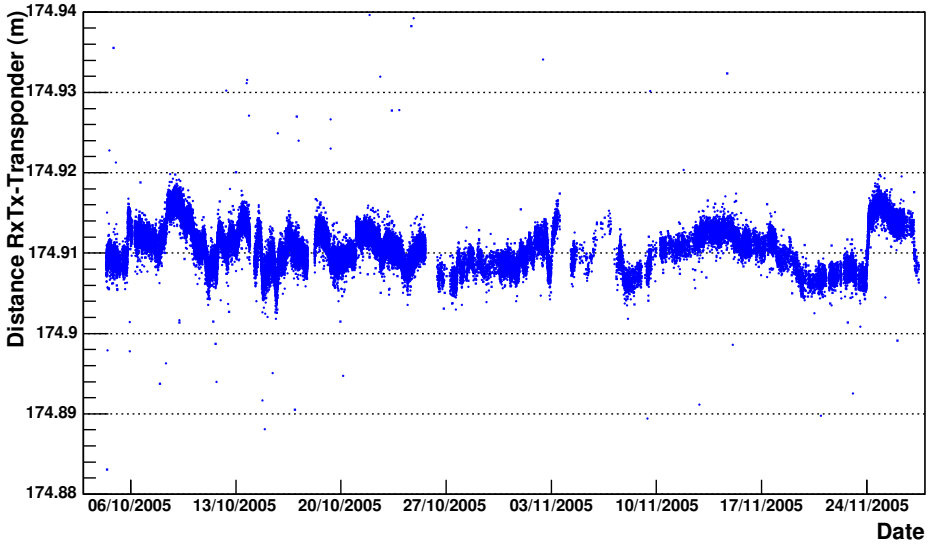

Fig. 10. Distance measured by the acoustic positioning system between the RxTx module and the autonomous transponder, both being fixed at a few metres above the sea bed. The measurement is displayed as a function of time during two months of monitoring.

Although the limited number of installed acoustic emitters does not allow the triangulation reconstruction, the MILOM operation demonstrates the resolution and the stability of the acoustic system by monitoring the distance measured between two fixed points. This is illustrated in figure 10 which displays the acoustic distance measured between the RxTx transducer attached on the MILOM anchor and the autonomous transponder. The acoustic system measurements show a resolution of a few mm and a stability of $\sim$ 1 cm on a distance of 174.91 m during two months of monitoring. The absolute distance obtained by this system is well in agreement with the value of 175.6 m obtained with the long base line acoustic navigation system used onboard the

surface boat during the marine operation to monitor the deployment and installation of the lines. This navigation system, based on $\sim$ 10 kHz acoustic signal exchanges, allows range measurements of several thousands of metres with an accuracy limited to $\sim$ 1 m. With the MILOM operation, the performance of the acoustic positioning system are confirmed to be well within the specifications required to obtain a precision of $\sim$ 10 cm on the spatial reconstruction.

6 Examples of instrumentation measurements

In parallel to the Optical Module data taking and to the operation of the calibration devices, the various instruments of the MILOM dedicated to environmental measurements have been regularly read out. This allows a continuous monitoring of some physical quantities of the sea water at the ANTARES site which might have an influence on the calibration of the detector or on the bioluminescence background: the water current flow, the water temperature, the sound velocity and the water transparency. As an example, the measured water current velocity recorded by the Doppler current profiler located on the MILOM top storey is displayed in figure 11 as a function of time during eight months of monitoring. These measurements confirm that the water current remains usually small at the ANTARES site, with a velocity < 20 cm/s and with an average speed of ~ 5 cm/s.

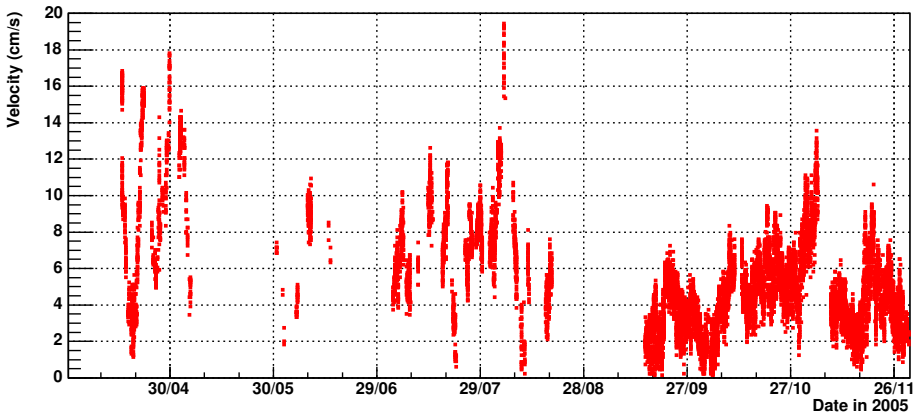

Fig. 11. Velocity of the water current flow measured by the Doppler current profiler as a function of time during eight months of the operation of the MILOM in 2005.

Figure 12 shows the individual heading of the three storeys of the line measured by the compass in each electronic container as a function of time for the same period. Although each storey has its own relative orientation due to the uncontrolled alignment in construction, one can notice that the rotation changes affect the whole line. As expected, the top storey also shows a

larger rotation amplitude as compared to the others. The measurements also indicate that the two lower storeys, separated by a shorter cable of 12.5 m, tend to remain at a constant orientation with respect to each other. Some correlation between the storey rotations and the water direction changes can also be noticed especially when the current velocity is large, as during the first days of November 2005.

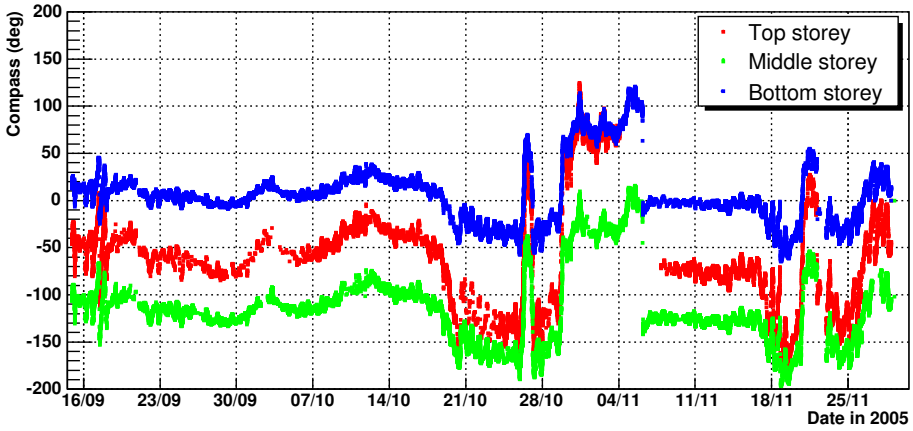

Fig. 12. Individual headings of the three MILOM storeys, measured by the compass included into every electronic container, as a function of time during two months of monitoring.

The seismometer readout by the MILOM has been delivering continuous data to the ANTARES shore station. It provided clear signals from several earthquakes around the world, such as the one in Japan on August 30^{th} 2005 and in Peru on September 24^{th} 2005. Further analyses of the seismometer data are currently in progress. Their results will be detailed in a forthcoming dedicated publication.

7 Conclusions

Since April 2005, the ANTARES Collaboration has been operating a Mini Instrumentation Line equipped with Optical Modules (MILOM) immersed at a depth of 2500 m on the ANTARES site. The main purpose of this line, built with pre-production elements of the ANTARES detector, was to allow an in-situ check of all the equipment and in particular to validate the time calibration and acoustic positioning device performances.

The various data regularly acquired during the MILOM operation confirm the capability of the Optical Modules and of its front-end electronics to trigger and readout single photo-electron signals. The continuous data collection of the OM signals and the MILOM instruments during several months val-

idate the whole electronics and the DAQ readout system designed for the ANTARES detector. The operation of the light source calibration devices, such as the LED Optical Beacon or the OM internal LED, shows that a time calibration of all Optical Modules can be achieved in-situ with an accuracy better than 0.5 ns. The results yield an electronics contribution to the OM timing resolution smaller than 0.5 ns, as required. Finally, the operation of the acoustic positioning system shows that its performance is well within the specification required to achieve the spatial reconstruction of the detector with an accuracy of $\sim$ 10 cm. All these results confirm the excellent performance of the ANTARES detector electronics and calibration devices as required to obtain the desired angular resolution of the neutrino telescope. The experience with the MILOM gives confidence for the operation of the first complete lines of the ANTARES detector which are scheduled to be deployed during 2006.

Acknowledgement

The authors acknowledge financial support by the funding agencies in particular: Centre National de la Recherche Scientifique; Commissariat à l'Énergie Atomique; Commission Européenne (FEDER fund); Région Alsace (contrat CPER); Région Provence-Alpes-Côte d'Azur; Département du Var; Ville de La Seyne-sur-Mer, France; Bundesministerium für Bildung und Forschung, Germany; Istituto Nazionale di Fisica Nucleare, Italy; the foundation for Fundamenteel Onderzoek der Materie (FOM) and the Nederlandse organisatie voor Wetenschappelijk Onderzoek (NWO) in the Netherlands; Russian Foundation for Basic Research, Russia; Ministerio de Educación y Ciencia, Spain.

References

[1] E. Aslanides et al. ANTARES Collaboration, preprint CPPM-P-1999-02, DAPNIA 99-01, IFIC/99-42, SHEF-HEP/99-06 (astro-ph/9907432).

[2] P. Amram et al., ANTARES Collaboration, Nucl. Inst. Meth. A 484 (2002) 369 (astro-ph/0112172).

[3] J.A. Aguilar et al., ANTARES Collaboration, Nucl. Inst. Meth. A 555 (2005) 132 (astro-ph/0510031).

[4] V. Bertin on behalf the ANTARES Collaboration, "Status of the ANTARES neutrino detector", 8th International Workshop on "Topics in Astroparticle and Underground Physics" (TAUP 2003), Nucl. Phys. B 138 (2005).

[5] 300 kHz direct reading ADCP Workhorse Monitor from Teledyne RD Instruments, http://www.rdinstruments.com/monitor.html

[6] Sound velocimeter Ref QUUX-3A(A) from Genisea/ECA, http://perso.wanadoo.fr/genisea/sound_velocimeter.htm

[7] MicroCAT C-T sensor SBE 37-SI from Sea Bird Electronics, http://www.seabird.com/products/spec_sheets/37sidata.htm

[8] C-Star transmissiometer from WET Labs, http://www.wetlabs.com/products/cstar/cstar.htm

[9] Triaxial broadband seismometer CMG-3T from Güralp Systems, http://www.guralp.net/products/

[10] Acoustic releasable transponder RT661B2S from IXSEA, http://www.ixsea.com/php/contenu/en/p-oceano_ocean.php

[11] J.A. Aguilar et al., ANTARES Collaboration, "The data acquisition system of the ANTARES neutrino telescope", in preparation.

[12] J.A. Aguilar et al., ANTARES Collaboration, "The Optical Module front-end electronics of the ANTARES neutrino telescope", in preparation.

[13] J.A. Aguilar et al., ANTARES Collaboration, "The ANTARES telescope reveals unexpected intense and variable deep-sea bioluminescence", in preparation.

[14] J.A. Aguilar et al., ANTARES Collaboration, "The ANTARES Optical Beacon system", in preparation.

Astroparticle Physics 32 (2009) 73–88

Contents lists available at ScienceDirect

Astroparticle Physics

journal homepage: www.elsevier.com/locate/astropart

A multivariate analysis approach for the imaging atmospheric Cherenkov telescopes system H.E.S.S.

F. Dubois [a,*], G. Lamanna [a,*], A. Jacholkowska [b]

[a] LAPP, Laboratoire de Annecy-le-Vieux de Physique des Particules, UMR/IN2P3-CNRS, Université de Savoie, 9 Chemin de Bellevue – 74941, Annecy-le-Vieux, France
[b] LPNHE, Laboratoire de Physique Nucléaire et de Hautes Energies, UMR/IN2P3-CNRS, Universités Paris VI & VII, 4 Place Jussieu – 75252 Paris, France

ARTICLE INFO

Article history:
Received 23 March 2009
Accepted 19 June 2009
Available online 25 June 2009

Keywords:
Multivariate analysis
H.E.S.S.
Gamma-rays
Cherenkov
IACT

ABSTRACT

A multivariate particle classification approach is proposed and applied to the analysis of the data from H.E.S.S. (High Energy Stereoscopic System). The combination of results from the three shower reconstruction methods: Hillas, model and 3D-model, leads to a substantial gain in the discrimination power between photons and hadrons. The construction and use of a combined effective estimator improves by several factors the signal-to-background ratio which is extremely important in case of studies of the faint and extended sources. The results of this approach are presented for a typical set of sources. The consequent gain in the sensitivity is shown through a comparison to the H.E.S.S. published results.

1. Introduction

In the past decade, the High Energy Stereoscopic System (H.E.S.S.) successful observations [1] resulted in a multitude of revolutionary results in the VHE gamma domain for various types of galactic and extragalactic sources. The H.E.S.S. experiment, an array of four of new generation Imaging Air Shower Telescopes (IACT) located in Namibia, is presently the most sensitive detector of the astrophysical VHE gamma-ray sources (>100 GeV). The four telescope array system provides a sensitivity to a 1% of the Crab Nebula flux in ~25 h observation. A fifth telescope (twice in size) is presently under construction and will improve the sensitivity of the H.E.S.S. array below 100 GeV. Till now, the H.E.S.S. collaboration has published the detection of more than 50 sources of different types: SNRs, PWNs, unidentified galactic sources and AGNs.

One limiting factor in the standard H.E.S.S. analysis is the identification of photons against the hadron cosmic-rays which constitute a major part of the measured candidates. At present, the hadron discrimination procedures do not allow the morphological studies of the faint and extended sources or the detection of the very tiny fluxes expected from the exotic gamma-ray signals as from the galactic dark matter. To improve the hadron rejection, a promising approach is based on a use of the maximum information that is provided by the shower reconstruction and the Monte Carlo simulations in case of photons and hadrons. At present, three reconstruction methods are qualified in H.E.S.S.: Hillas parameter reconstruction [2], model reconstruction [4] and 3D-model reconstruction [5], which yield complementary discriminating variables for the hadron background suppression. Although most of the published analysis have been performed by applying the standard method of *Hillas parameterization*, with the advent of the H.E.S.S. telescopes with large mirrors and fine-pixel cameras together with the stereoscopy, new and more elaborate techniques have been introduced and also applied in a good fraction of the H.E.S.S. analysis:

- a *model analysis* technique based on the comparison of the shower images with a more realistic semi-analytical pre-calculated model of the image [3,4].
- a 3*D-model analysis* method based on a simple three-dimensional elliptical reconstruction of the gamma-ray induced air shower [5].

In this paper, a combination of the discriminating variables from the three reconstructions is proposed, resulting in an estimator called later as X_{eff}, which was successfully used for the particle identification in LEP[1] analysis. Moreover, a construction of an estimator varying between 0 and 1, characterizing particle type, may lead in future to analysis with weighted event techniques. In the following, after a brief description of the three different reconstruction methods in Section 2, a multivariate classification approach based on

* Corresponding authors.
E-mail addresses: duboisf@lapp.in2p3.fr (F. Dubois), giovanni.lamanna@lapp.in2p3.fr (G. Lamanna).

[1] The CERN particle physics experiment at LEP – the Large Electron Positron collider.

0927-6505/$ - see front matter © 2009 Elsevier B.V. All rights reserved.
doi:10.1016/j.astropartphys.2009.06.003

the combination of the various discriminating variables is defined and detailed in Section 3. In Section 4 the combined energy and direction estimators are discussed. In Section 5, in order to validate the proposed procedure, a sample of astrophysical observation data published by H.E.S.S. are re-analysed with X_{eff} estimator and the results are compared with those from the standard analysis.

2. The H.E.S.S. data analysis methods

2.1. Hillas analysis

The classical analysis method for IACT data was first introduced by Hillas in 1985 [2], where so-called Hillas parameters of the shower images in the camera focal plane are defined: the length L and the width W of the elliptical image; the total image amplitude (image size); the *angular distance d* between the center of the camera and the image center of gravity; the azimuth angle ϕ of the image main axis and the orientation angle α, as shown in (Fig. 1).The use of the Hillas parameters leads to a robust and efficient reconstruction and analysis method, as detailed elsewhere (see [6] for a review). In general, in single telescope observations, the image parameters *length* and *width* provide a way to estimate the shower direction, while the shower energy is usually estimated from the image *size* and nominal distance (d). The stereoscopic imaging technique [3] provides a simple geometric reconstruction of the shower: the source direction is given by the intersection of the shower image main axes in the camera. The energy is estimated from a weighted average of each single telescope energy reconstruction. The discrimination of gamma events against the dominant background of the charged cosmic-ray atmospheric showers may be faced in different ways [3,13,14], taking the advantage of existing correlations between Hillas parameters and particle type. Among them the *Scaled Cuts* technique is usually applied and commonly used in the H.E.S.S. standard analysis. The geometric parameters of the shower image, width w and length l, are compared to the averaged expected values ($\langle w\rangle, \langle l\rangle$) and their variances ($\sigma_w, \sigma_l$) as obtained from Monte Carlo simulated gamma-ray data as a function of the image total charge amplitude q and the reconstructed *impact distance* ρ of the shower. According to this technique the main Hillas image parameters renormalized to the expected values are the *Scaled Width* (*SW*) and *Scaled Length* (*SL*):

$$SW = \frac{w(q,\rho) - \langle w(q,\rho)\rangle}{\sigma_w(q,\rho)}, \tag{1}$$

$$SL = \frac{l(q,\rho) - \langle l(q,\rho)\rangle}{\sigma_l(q,\rho)}. \tag{2}$$

The scaled parameters are then easily combined in stereoscopic observations in *Mean Scaled Width*:

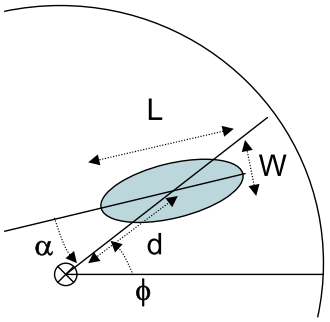

Fig. 1. Definition of the geometrical parameters used for the Hillas shower reconstruction.

$$MSW = \frac{\sum_{tels} SW}{\sqrt{ntels}} \tag{3}$$

and *Mean Scaled Length*:

$$MSL = \frac{\sum_{tels} SL}{\sqrt{ntels}} \tag{4}$$

ntels being the number of telescope of the IACT array (e.g. four in case of H.E.S.S.). These two variables are almost uncorrelated for gamma-ray showers (as it will be shown further in the text with Monte Carlo simulations) therefore are often combined in a single discriminating variable *Mean Scaled Sum* (*MSS*):

$$MSS = \frac{MSW + MSL}{\sqrt{2}} \tag{5}$$

2.2. Model analysis

A more elaborate analysis technique pioneered by the work of the CAT (Cerenkov Air Telescope) collaboration and now extensively applied in the H.E.S.S. data analysis is the Model analysis whose details can be found in [4] and references therein. Here in short recall, the so-called model method is based on the comparison between the registered shower images and a predicted pixel-by-pixel modeling of the expected image within a realistic detector simulation. The event reconstruction is based on a maximum likelihood fit of the shower direction and energy, with use of all available pixels in the camera, without requirement on the image cleaning. The probability density function (p.d.f.) of observing a signal S in a given pixel, under the assumption of an expected amplitude μ, a fluctuation of the pedestal σ_p (due to the night sky background and electronics) and a fluctuation of the single photo-electron ($p.e.$) signal $\sigma_s \approx 0.4$ (which matches the photomultiplier resolution) is given by $P(S|\mu,\sigma_p,\sigma_s)$, defined as:

$$P(S|\mu,\sigma_p,\sigma_s) = \sum_{n=0}^{\infty} \frac{e^{-\mu}\mu^n}{n!\sqrt{2\pi(\sigma_p^2 + n\sigma_s^2)}} exp\left(-\frac{(S-n)^2}{2(\sigma_p^2 + n\sigma_s^2)}\right) \tag{6}$$

The reconstruction of the events e.g. the primary energy, the direction and the impact parameter of the detected photon (identically for the case of a single telescope or a stereoscopic array), is obtained through the maximization of a log-likelihood function:

$$L = 2\sum_{i=1}^{Pixels} log[P_i(S_i|\mu,\sigma_p,\sigma_s)] \tag{7}$$

In the model analysis the separation between γ and hadron candidates relies on a *goodness—of—fit* (G) variable. The average value of the log-likelihood can be calculated analytically following to:

$$\begin{aligned}\langle lnL\rangle &= \sum_{i=1}^{Pixels} \int_{S_i} P(S_i|\mu_i,\sigma_{p_i},\sigma_{S_i}) \times lnP(S_i|\mu_i,\sigma_{p_i},\sigma_{s_i}) dS_i \\ &= \sum_{i=1}^{Pixels} [1 + ln(2\pi) + ln(\sigma_{p_i}^2 + \mu_i \times (1+\sigma_{S_i}^2))]\end{aligned} \tag{8}$$

As the variance of $\ln L$ being close to 2, the *goodness—of—fit* (G) can be defined as a normal variable:

$$G = \frac{\langle lnL\rangle - lnL}{\sqrt{2 \times N_{dof}}} \tag{9}$$

where N_{dof} is the number of degree of freedom.

2.3. 3D-model analysis

A 3D-model reconstruction method of the gamma-ray induced air shower has been recently introduced and applied in the

H.E.S.S. data analysis. The atmospheric shower is modeled as a Gaussian photosphere with anisotropic light angular distribution and then used to predict the collected light in each pixel of a camera. The main shower parameters, e.g. incident direction, shower core position on the ground, slant depth of shower maximum, average lateral spread of the Cerenkov photosphere and primary energy, are derived from the fit of the pixel content in the images. The 3*D-model analysis* selects electromagnetic showers on the basis of their rotational symmetry with respect to the incident direction. Details on the 3*D-model analysis* can be found in [5]. Monte Carlo simulation studies have demonstrated the dependency of the photosphere 3D-width (in units of radiation length) on the slant depth of the shower maximum. This property together with the assumption of a rotational symmetry of the electromagnetic shower allows to reject most of the background hadrons through a dimensionless and almost zenith angle independent quantity ω, the reduced 3D-width:

$$\omega = \frac{\sigma_T \rho}{D_S} \tag{10}$$

where σ_T is the transverse standrad deviation of teh 3D shower, ρ is the density of air and D_S is the column density at shower maximum (see [5] for furtehr details).

The ω discriminating variable, the reduced 3D-width, which shows excellent abilities for the photon/hadron separation, together with Hillas parameters, will contribute to the over-all combination of the discriminating variables as described in Section 3. The three methods have been applied in the H.E.S.S. data analysis mainly for cross-check purposes while the Hillas analysis has been always considered as the reference standard method. In some cases a linear combination of the Hillas and Model approaches have produced competitive background rejection and the corresponding results have been published by the H.E.S.S. collaboration. At present, the need of improving the sensitivity of the experiment for more detailed studies, requires the combination of the complementary performances of these three methods. The terms of their comparison can be found elsewhere [4]. Here it is important to summarize the main differences among them:

- *Sensitivities*: The three methods show very similar sensitivities. If the model and 3D-model analysis have a ∼20% higher efficiency for gamma-rays than the Hillas analysis they also keep more background events and are therefore less competitive in terms of signal-to-background ratio. The gamma efficiency as a function of the OFF-axis angle (distance of the shower axis to the center of the camera) is more flat for the Model and 3D-model analysis since they both do not rely on the images size as in the case of Hillas analysis.
- *Angular resolution:* The model analysis at low energy performs significantly better ($\sigma_{68} \simeq 0.07^\circ$ at 0.4 TeV) than other analysis ($\sigma_{68} \simeq 0.1^\circ$ for 3D-model and $\sigma_{68} \simeq 0.12^\circ$ for Hillas). The Hillas and 3D-model methods at higher energy takes over ($\sigma_{68} \simeq 0.05^\circ$ for 3D model, $\sigma_{68} \simeq 0.07^\circ$ for Hillas and $\sigma_{68} \simeq 0.1^\circ$ for model at 20 TeV). The angular distances to shower true direction (θ parameter) reconstructed by the three methods show low level of correlation due to different pattern reconstruction on ground.
- *Energy resolution:* The model analysis performs significantly better ($\Delta E/E \simeq 12$–13%) for energy up to 20 TeV than other analyses ($\Delta E/E \simeq 30$–16% as a function of energy for 3D-model and $\Delta E/E \simeq 16$–20% for Hillas).

3. The X_{eff} combined method

The classification and regression method approach (e.g. neural-network, random-forest, fisher), usually applied in data analysis, combines parameters from a given reconstruction procedure (the shower image parameters in the case of the IACT analysis) which characterize differently signal and background events. In the presented approach (see [7] for more details), these image parameters, which are already powerful by themselves and applied to the H.E.S.S. analysis providing already excellent background discrimination for bright sources, will be combined in a single estimator. This procedure presents a two-fold aspect: a more powerful hadron background suppression as based on the maximum information obtained with three complementary reconstructions, and a single analysis parameter leading to a simplified study of applied cuts for a global optimization of the photon and hadron efficiencies. Therefore, in the following, the aim of this work will be to combine the main *gamma*-tagging discriminating variables of each of the three reconstruction methods with the purpose of exploiting their complementary discriminating power improving the *gamma*/*hadron* separation, as compared to the standard H.E.S.S. analysis results. The discussed multivariate method consists of a unique resulting discriminating variable X_{eff}, whose value, associated to each event, has the power of an event-by-event gamma-mistag probability (*hardness*) estimator. The definition of the X_{eff} mis-tagging probability function, introduced in [8–10], follows the relation:

$$X_{eff}(\{x_i\}) = \frac{\eta H(\{x_i\})}{(1-\eta)G(\{x_i\}) + \eta H(\{x_i\})} \tag{11}$$

where η is the mistag fraction of the gamma class of events (e.g. the relative background fraction):

$$\eta = \frac{N_{Hadron}}{N_{Hadron} + N_{Gamma}}, \tag{12}$$

where N_{Hadron} is the background number of events while N_{Gamma} the signal events in any data sample. $G(\{x_i\})$ and $H(\{x_i\})$ are the *global* multi-dimensional *probability density functions*(*p.d.f.*) for events in which the tag identifies *G*amma (the right tag) and *H*adron (the wrong tag).

In the following, in order to describe the application of the method and the resulting analysis performance in terms of gamma/hadron separation, two distinct data-sets are used: *Gamma*, corresponding to Monte Carlo simulated data at different zenith and offset conditions and *Hadron*, firstly treated with H.E.S.S. proton Monte Carlo, secondly analysed with real off-source observation data-sets, obtained in stereoscopic mode with at least three telescopes.

The discriminating variables x_i from the three reconstructions entering the X_{eff} combination are respectively: (1) the *Mean Scaled Width* (*MSW*), the *Mean Scaled Length* (*MSL*) for the Hillas reconstruction ([2]); (2) the *Mean Scaled Goodness* (*MSG*) for the model reconstruction ([4]); (3) the *Rescaled Width* (3*RW*), for the 3D-model reconstruction ([5]). The use of multi-dimensional global *p.d.f.*s describes properly the possible correlations between the discriminating variables, while they are quite well approximated by the product of the corresponding one-dimensional probability density functions, when the variables are not correlated:

$$X_{eff}(\{x_i\}) = \frac{\eta \prod_i h_i(x_i)}{(1-\eta)\prod_i g_i(x_i) + \eta \prod_i h_i(x_i)} \tag{13}$$

where $g_i(x_i)$ and $h_i(x_i)$ are the gamma and *h*adron respective probability density functions *p.d.f.*s of any discriminating variable x_i. The simplified assumption of the factorization of the *p.d.f.*s in the X_{eff} equation is fully justified for the case of *Gamma* sample due to the absence of any correlation (see Fig. 2) between discriminating variables, while a limited correlation is manifested by the variables in the case of the *Hadron* sample. However in the case under exam, these residual correlations in the variable distributions for hadrons,

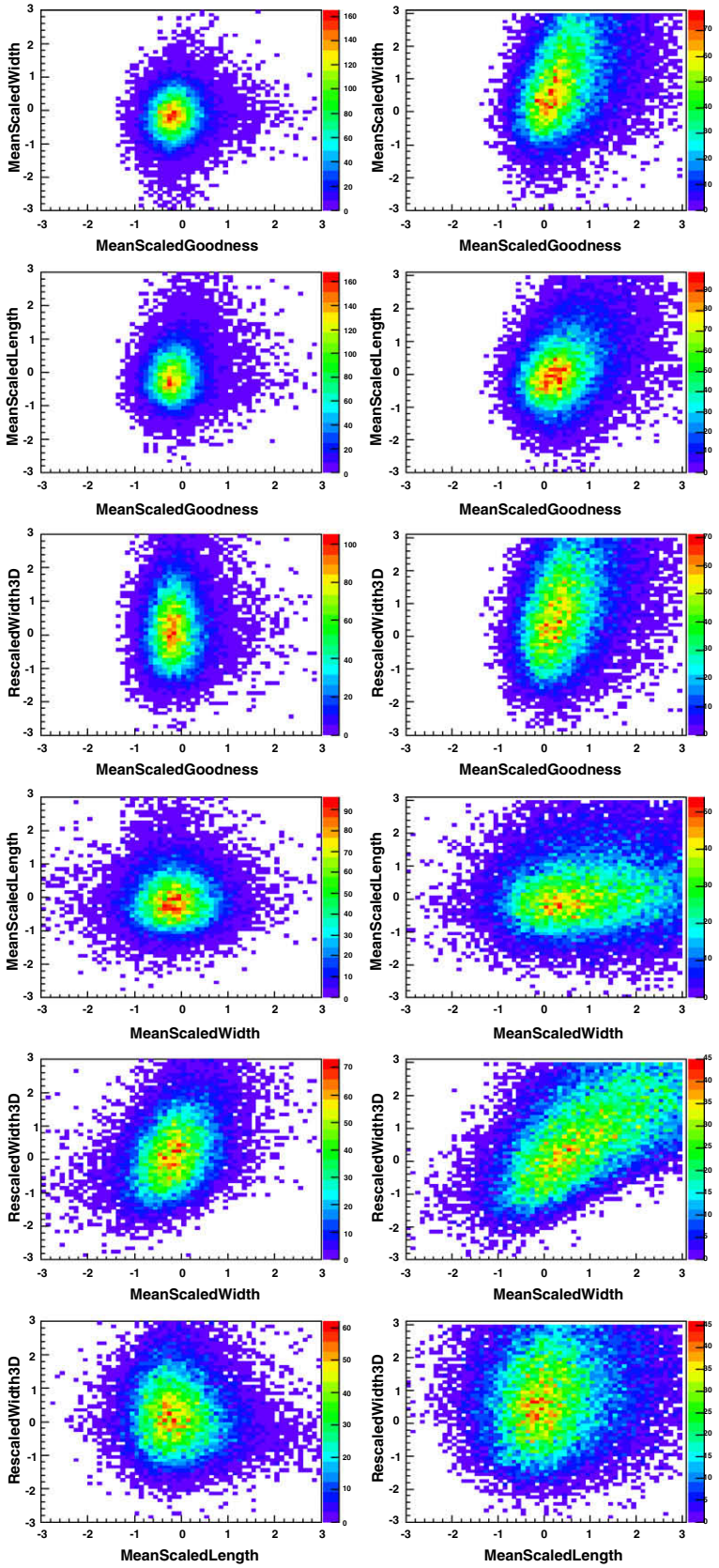

Fig. 2. The reciprocal combinations of pair of discriminating variables among MSL, MSW, MSG and 3RW do not show any correlation for the *Gamma* sample (left panel) while a residual correlation exists for the background-*Hadron* sample (right panel).

have no measurable effects. During various tests performed in the qualification procedure of the X_{eff} method, the possible systematic effect induced by the use of the factorization of the p.d.f. functions has been checked and found negligible. This aspect is discussed la-

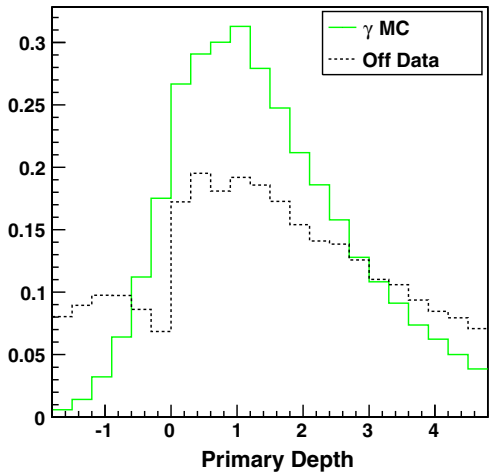

Fig. 3. Reconstructed primary depth in radiation lengths for photon and proton Monte Carlo.

ter in the text (see Section 4.3) when possible systematic effects induced by the X_{eff} are detailed. Therefore, all presented results are derived for simplicity with single discriminating variables *p.d.f.*s.

3.1. Event pre-selection

The first step in the analysis is a series of pre-selection criteria:

- Image cleaning requiring pixels in the image to be above a lower threshold of 5 p.e. and to have a neighbour above 10 p.e., and vice versa. This cut is the first step in the moment analysis and makes γ-ray showers approximating better a narrow elliptical shape, before application of the Hillas reconstruction method.
- Accepting events within a maximum offset angle from the camera center of 2° allows to reduce any zenith angle dependent effects or variations in the NSB (Night Sky Background) level across the field of view as well as to limit the radial variation of the telescope system acceptance (see [15] for more details).
- The first cosmic-ray interaction depth generating showers in the atmosphere is one free parameter of the model analysis and the corresponding reconstructed value in radiation lengths (X_0) ranges from -1 and 4 for γ-ray showers. These two limits are applied to the reconstructed primary depth distribution (Fig. 3) to exclude some fraction of hadrons.
- One more pre-selection cut is mainly devoted to guarantee a certain level of consistency among the different reconstruction methods. It concerns the distribution of the shower directions reconstructed by the three analysis methods. In Fig. 4 the distributions of the relative dispersions of the direction reconstruction for any pair of analysis methods: $|\theta_{Model} - \theta_{Hillas}|, |\theta_{Model} - \theta_{3D}|$ and $|\theta_{Hillas} - \theta_{3D}|$ are shown for the pre-selected samples of *Gamma*-MC events, *Gamma* and *Hadron* data-set events. The good agreement between the *Gamma*-MC and *Gamma* data-set distributions, together with different shape of the distribution of the *Hadron* data-set compared to *Gamma* events, allows to apply a pre-selection aimed to retain only those events for which the above relative dispersions are contained within a limit corresponding to $\sim$90% containment for γ-ray events (namely a common upper limit of $\sim 0.5^\circ$).
- A final event pre-selection criteria, able to decrease the background by more then 20% (removing the tails of the *Hadron* distributions), is based on the application of a lower and an upper cuts (e.g. -3 and +3) on the distribution of the discriminating variables (before computing from them the corresponding *p.d.f.*s): only those events for which all four variables have values contained between these limits are retained (see Fig. 5).

The distributions of the discriminating variables were studied as a function of the dynamical range of the H.E.S.S. system. In previous works, a good agreement between the distributions of the discriminating variables for simulated photons (*Gamma*) and ON–OFF real data were well established and discussed by [4,5]. Training samples of simulated photon and OFF-data-sets were examined as a function of the zeinth angle of the observations (from 0° to 60°), energy range (from $\sim$100 GeV to $\sim$100 TeV), photon spectral index (from 1.8 to 3.4), minimum image size cut (40, 60, 80, 200 p.e.) and finally different offsets, the point source distance from the camera center, (from 0° to 2°). The relative variations of the distribution (in terms of spread, normalization and mean value) are contained within a few percent, without any appreciable effect on the profile of the resulting X_{eff} estimator, neither in the final results of the analysis of a set of astrophysical sources considered for validation purposes (see Sections 4.3 and 5). A common choice was then assumed for the distribution of the four discriminating variables and a unique parameterization of the resulting *p.d.f.*s (Fig. 5) was adopted and applied for all analysis.

Thus the resulting X_{eff} (*hadroness*) estimator applied in the following is defined as:

$$X_{eff} = \frac{\eta \prod_{1\leqslant i\leqslant 4} h_i(x_i)}{(1-\eta)\prod_{1\leqslant i\leqslant 4} g_i(x_i) + \eta \prod_{1\leqslant i\leqslant 4} h_i(x_i)} \tag{14}$$

where h_i and g_i are the *p.d.f.*s for *Hadron* and *Gamma*, respectively, as a function of the four discriminating variables: MSL, MSW, MSG

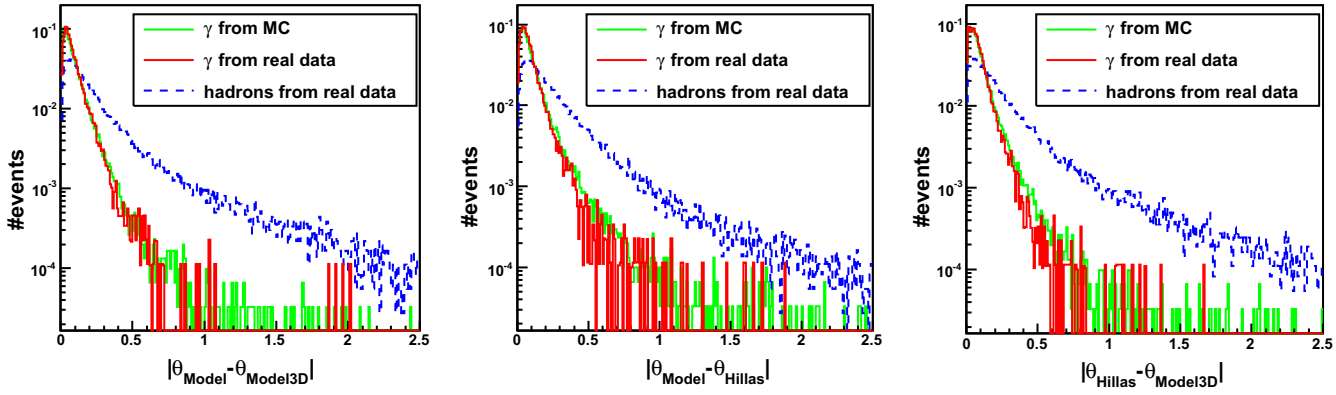

Fig. 4. Dispersion between reconstructed directions for any pair of analysis methods: $|\theta_{Model} - \theta_{Hillas}|, |\theta_{Model} - \theta_{3D}|$ and $|\theta_{Hillas} - \theta_{3D}|$. The distributions for simulated *Gamma* (MC) events together with pre-selected *Gamma*-candidates (ON–OFF) and *Hadron*-candidates (OFF) samples are compared.

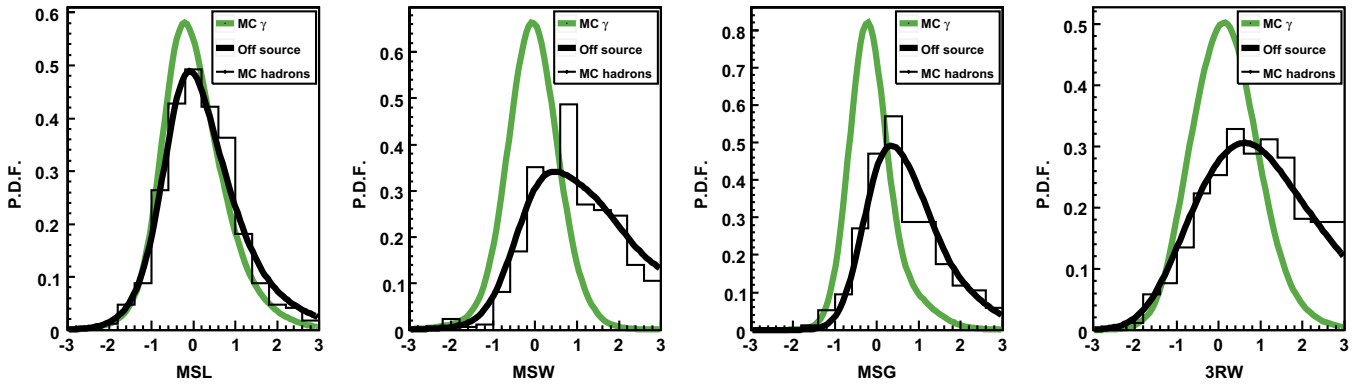

Fig. 5. Probability density functions derived from the best fit resulting functions of the distributions of the discriminating variables (e.g. MSL, MSW, MSG and 3RW from left to right) for, respectively, Monte Carlo simulated *Gamma* and *OFF*-data-sets. The cross represents the *p.d.f.* deduced from Monte Carlo simulated protons.

and 3*RW* (as shown in Fig. 5). The comparison of the *p.d.f.* for *Gamma* and *Hadron* shows a good discriminating power of each variable. The Monte Carlo simulations for protons provide *p.d.f.* distributions in good agreement with the OFF-data. In the following the OFF-data *p.d.f.* will be used. In Fig. 6 an example of the resulting events classification according to the value of the X_{eff} discriminating estimator is shown for *ON*-source, *OFF*-source and *ON—OFF* data samples. The X_{eff} classification allows to quantify the resulting event-by-event mistag probability providing a *hadroness* test statistic for the γ/h separation.

In Eq. (14) the mistag fraction η can be defined a priori or estimated with a likelihood optimization. Since it corresponds to the background fraction related to the effective signal-to-background ratio, which is therefore a function of the specific data-set under study (e.g. the fluency of the specific astrophysical source). In order to adopt the most appropriate η value and to check the compatibility between the X_{eff}(*hadroness*) estimator efficiency in the data and the Monte Carlo a likelihood function composed of the *p.d.f.*s of the discriminating variables was used here:

$$\mathscr{L} = \eta \prod_{1\leqslant i\leqslant 4} h_i(x_i) + (1-\eta) \prod_{1\leqslant i\leqslant 4} g_i(x_i). \tag{15}$$

The optimal η value is the one which minimizes the sum of $-\mathscr{L}(\eta)$ over-all events of the data sample:

$$\min\left[-2\sum_{events} \ln(\mathscr{L}(\eta))\right] \tag{16}$$

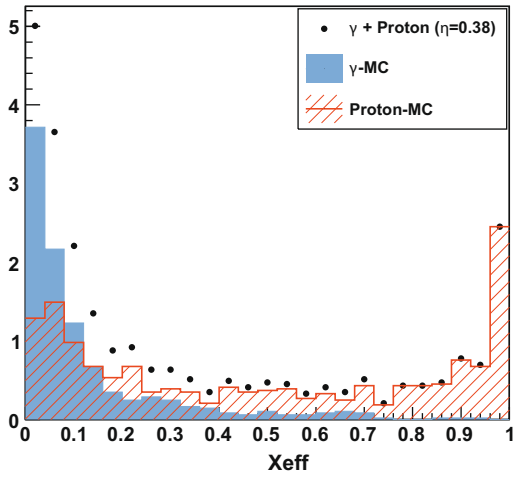

Fig. 6. Example of the X_{eff}-*hardness* (gamma-mistag) estimator distributions for two samples of simulated *Gamma* and *Hadron* events. A specific X_{eff} value is estimated for each event. The two samples are merged in a unique sample corresponding to $\eta = 0.38$ and analysed to validate the analysis method.

Successful tests of this method applied on samples with known amounts of *Gamma* and *Hadron* events (for which therefore η is precisely known) leads to a precise (less than 3% uncertainty) determination of the resulting optimal η. This result demonstrates as well the compatibility and the good agreement between data and Monte Carlo for photon sample (see Fig. 7). However as reported in [10] the effective power of the X_{eff} discriminating method is not given by the value of η. Even for a choice of an a priori value of η, e.g. 50%, the use of the discriminating variables and the resulting X_{eff} function ensures that the γ/h separation is successfully achieved as well as a compatibility with the Monte Carlo results.

In Fig. 8 the distributions of the *S*ignal-to-*B*ackground ratio (S/B) and the significance σ as a function of the X_{eff} value for a *Crab* data-set are shown. Five different distributions are compared for five respective different values chosen for the η factor. Whatever is the choice of the η value, the corresponding values of the maxima of these three analysis quality parameters are not affected. The optimization of the events selection through a cut on the X_{eff} value corresponding to the maximum of these three quality parameters for a specific analysis, will be a function of η.

4. The H.E.S.S.–X_{eff} data analysis method

The X_{eff} data analysis approach aims to take advantage of the complementary properties of the three described reconstruction methods and to improve the background rejection.

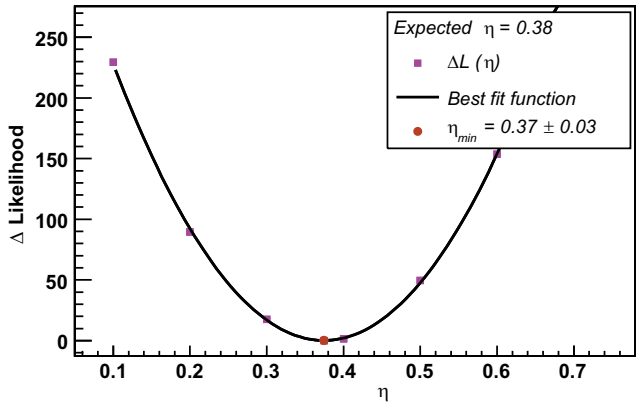

Fig. 7. Two samples of simulated *Gamma* and *Hadron* events are merged and analysed to validate the analysis method. The maximization of the likelihood function for the optimal η value estimation provides a value (0.37 ± 0.03) consistent within 3% with known a priori relative background fraction (being 0.38).

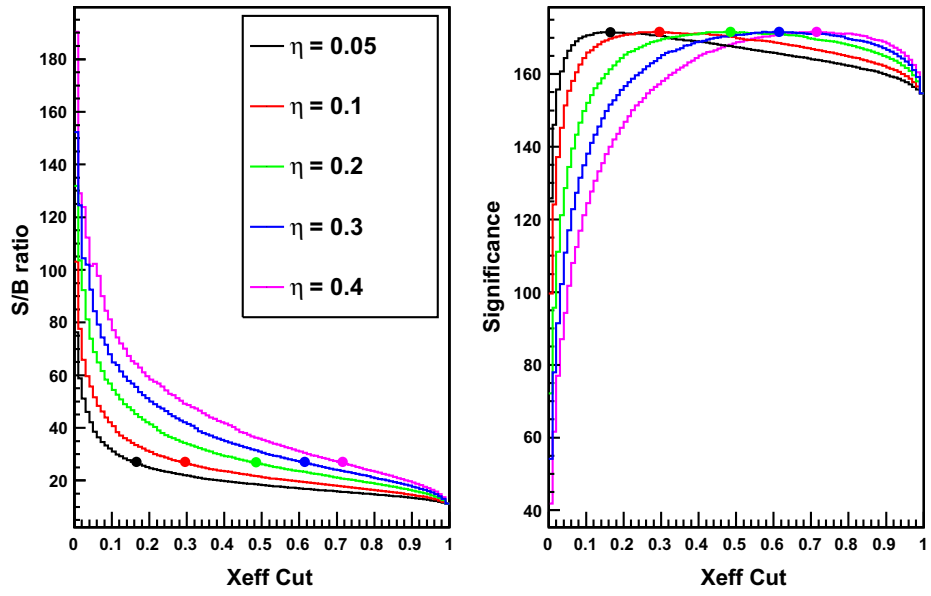

Fig. 8. The signal-to-background ratios (S/B) and the significances N_σ as a function of the $X_{eff} - Cut$ value for the Crab data sample. Five different distributions are compared for five corresponding different values assumed for η. While the choice of the optimal η affects the X_{eff} distribution and the consequent choice of the corresponding X_{eff}-Cut, the correlation between η and the optimal X_{eff}-Cut allows for invariant values of the corresponding quality parameters (see bullet markers).

4.1. Event selection and background rejection

The X_{eff} method, as described above, is then applied to the pre-selected data-sets. An unique value of the X_{eff}, e.g. an $X_{eff}Cut$, is chosen to separate the γ-like events from the bulk of *hadron*-like candidates. The optimum selection cut yields the maximum values of the corresponding quality parameters for the data analysis of a given astrophysical source: namely the significance N_σ level achieved, as defined through the likelihood ratio method described in [11], which also depends on the square root of the observation time $N_\sigma/\sqrt{t}$, the *S*ignal-to-*B*ackground ratio (S/B), the number of photons N_γ and the quality factor $Q_f = \epsilon_\gamma/\sqrt{\epsilon_h}$. The cut selection criteria generally depend on the energy spectrum of the sources and therefore their optimization is achievable with the Monte Carlo simulations, requiring a possible optimization of the $X_{eff}Cut$ selection separately for much harder or much softer energy spectra. However, after having deeply investigated the systematic effects due to the spectral dependent choice, as a rule an universal $X_{eff}Cut = 0.3$ is applied for every analysis and for any kind of source, in order to preserve the a priori nature of the analysis. Such an approach should also be applied in source searches. Furthermore, if for the background estimation, the OFF-source data samples are used instead the Monte Carlo proton simulations, the application of the general and common background *p.d.f.*s avoids a subjective approach to the source discovery procedures and the introduction of the additional biases in statistical optimization of the signal-to-background ratio. Tables 1 and 2 summarize the combination of cut selections together with the choice of the nominal cuts on the distance (θ) from the reconstructed shower position to the source, the image amplitude and the distance from the center of the field of view. Two different values of η are adopted: 0.1 for sources whose flux is intense as much as at least 10% the Crab flux, while $\eta = 0.5$ is the choice for all other fainter sources (as well as for source search and morphological study of extended sources). The stability of the analysis results as a function of selection criteria optimization is addressed later in the text (see Section 4.3).

Table 2
Summary table showing the various estimated contributions to the systematic flux error [15].

Uncertainty	Flux (%)	Index
MC shower interactions	1	
MC atmospheric sim.	10	
Broken pixels	5	
Live time	1	
Selection cuts	8	0.08
Background est.	1	0.01
Run-by-run variability	15	
Data-set variability		−0.05
Total	20	0.09

Fig. 9 shows the resulting energy dependency of the photon effective area for the full H.E.S.S. array as a function of true Monte Carlo simulated photon energy and for observations at zenith angles of $20^\circ, 45^\circ$ and 60° and when the X_{eff} analysis method is applied. In order to establish and summarize the competitive results achieved through the application of the X_{eff} analysis, the receiver operator characteristic (ROC) diagram, showing the fraction

Table 1
The X_{eff} cut selections as well as cuts on the distance (θ) from the reconstructed shower position to the source, the image amplitude and the distance from the center of the field of view, optimized for various cases, as described in the text, are listed.

Configuration Name (*e.g.*)	η	X_{eff}Cut Max.	$\theta^2_{cut}(deg.^2)$ Max.	Amplitude (p.e.) Min.	Distance (°) Max.
Flare (*AGN*)	0.1	0.3	0.02	40	2.0
Bright (*Crab*, *MSH*-1552)	0.1	0.3	0.0125	80	2.0
Faint (*AGN*, *PWN*)	0.5	0.3	0.0125	80	2.0
Search (*J*1849)	0.5	0.3	0.0125	200	2.0

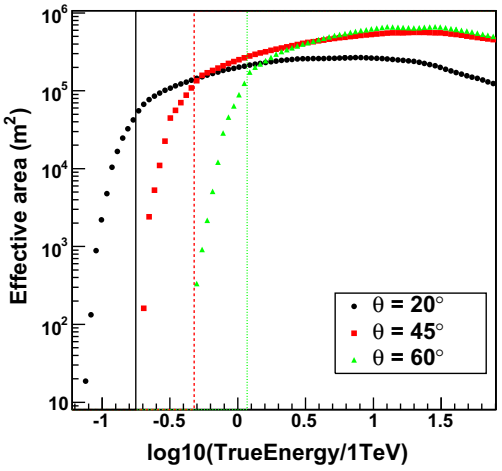

Fig. 9. The effective collecting area of the full H.E.S.S. arrays for the X_{eff} analysis as a function of true Monte Carlo simulated photon energy and for observations at zenith angles of 20°, 45° and 60°. The vertical lines denote the safe energy thresholds for each zenith angle, increasing in zenith angle form left to right.

of accepted gamma (e.g. photon efficiency ϵ_γ) as a function of the corresponding fraction of accepted hadron (e.g. proton efficiency ϵ_h), is presented (see Fig. 10). Same diagram is produced for both the *standard* H.E.S.S. *Hillas* analysis and the X_{eff} analysis. The *ROC* diagram for model and 3D-model analysis are comparable to the Hillas one within a few percents. In fact even if they have higher efficiency for γ-rays compared to Hillas (~20%), they also keep more background events, which in turns leads to very similar sensitivities for all three methods. The results here presented are based on Monte Carlo simulation analysis and validated with a H.E.S.S. data sample of the Crab observation. This comparison shows a general superiority achieved in the γ/h separation by combining the three different reconstruction methods (through the X_{eff} approach) against the standard selection based exclusively on optimized cuts on the Hillas scaled parameters. It is also useful to compare the different approaches in terms of the corresponding quality factors $Q_f = \epsilon_\gamma/\sqrt{\epsilon_h}$. In Fig. 11 the energy and zenith angle dependencies of the ratio between the X_{eff} and the Hillas quality factors $(Q_f(X_{eff})/Q_f(Hillas))$ are shown. For the computation of the $Q_f(X_{eff})$ and $Q_f(Hillas)$ the γ and *hadron* efficiencies are estimated starting from an identical original sample of simulated events pre-selected only according to the image cleaning requirements (e.g. pixels in the image to be above a lower threshold of 5 p.e. and to have a neighbour above 10 p.e.).

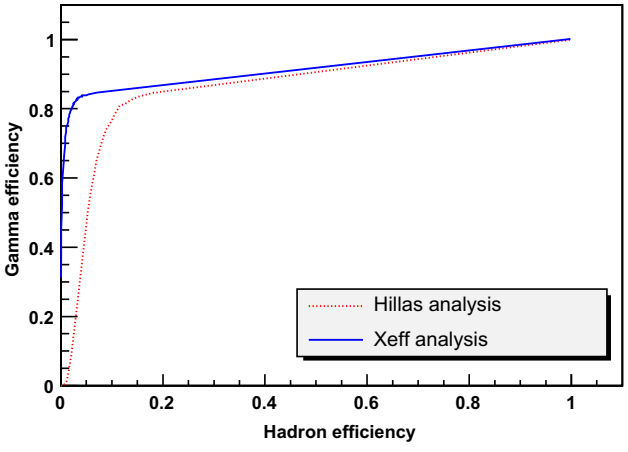

Fig. 10. Receiver operator characteristic diagram applied to the γ/h separation for the case of the *standard* H.E.S.S. *Hillas* analysis and the X_{eff} analysis.

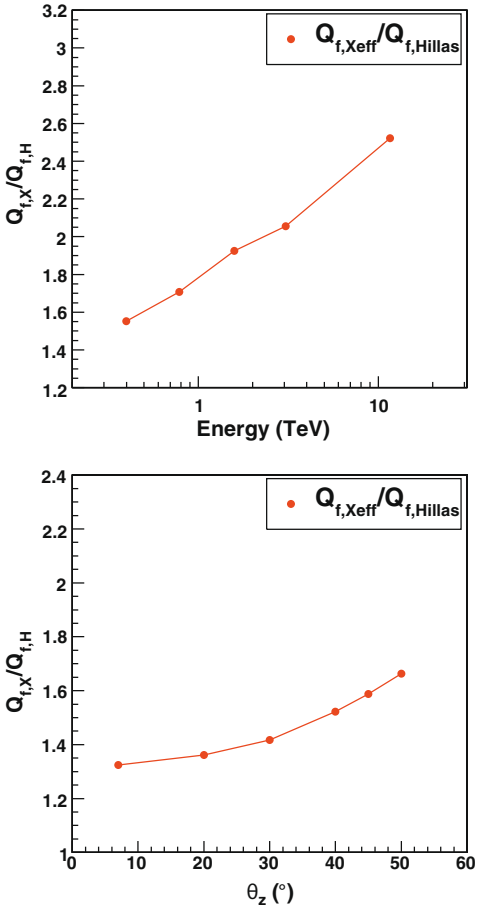

Fig. 11. Ratios between the X_{eff} quality factor $Q_f(X_{eff})$ and the Hillas one $Q_f(Hillas)$. The $Q_f(X_{eff})/Q_f(Hillas)$ ratio is shown as a function of zenith angle (bottom) and reconstructed energy (top).

4.2. Combined direction and energy estimations

The X_{eff} approach is here proposed to optimize the γ-event selection, however since it is based on the combination of the three independent reconstruction methods, a combination of the correlated estimates of single physical quantities, namely the primary γ energy and direction, has also to be studied. After having selected γ candidate events through the X_{eff} analysis it is clearly desirable to quote a single quantity to characterize the energy and direction of the photon which is critical for the following spectral and morphological analysis of any astrophysical sources. As already shown, for the event pre-selection, a certain agreement was already required among the three reconstruction methods in terms of primary photon directions. This guarantees that the distributions of the reconstructed observables have almost a Gaussian behaviour for the three methods (see Fig. 12). This also happens for the primary photon energy. It is shown in Fig. 13 with an example of the distribution of the relative error in the reconstructed energy per event for Monte Carlo simulated 0.8 TeV energy γ for the three analysis methods. Choosing the physical quantity reconstructed by one method out of three would be one of the solutions. The alternative one is to combine different estimates by weigthing each result x_i by a factor which takes into account the covariance matrices between estimates (see [12] for more details). Supposing the physical quantity x is measured using M ($M = 3$ in our case) different methods,

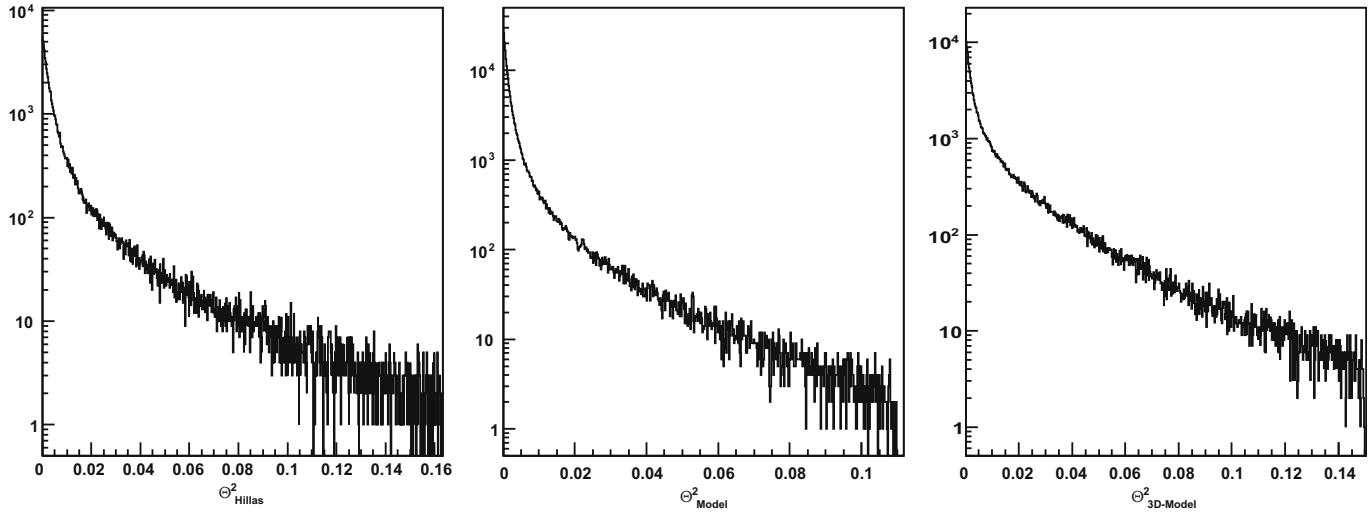

Fig. 12. The distribution of the relative error in the reconstructed square angular distances to the shower true direction (θ^2) for Monte Carlo simulated 0.8 TeV energy γ sample and for the three analysis methods. The resulting σ_{68} containments, commonly used for the angular resolution estimation, are 0.08° (Hillas), 0.05° (model) and 0.1° (3D-model).

and x_i the unbiased estimate through the ith method, an improved $\hat{x}$ estimate of the studied quantity is obtained by requiring a linear combination of the individual estimates:

$$\hat{x} = \sum_{i=1}^{M} w_i x_i, \tag{17}$$

where the weighting factors w_i for various estimates x_i are constant and are related to unbiased estimates, which means

$$\sum_{i=1}^{M} w_i = 1 \tag{18}$$

The variance of $\hat{x}$ is thus defined as:

$$\sigma^2(\hat{x}) = \sum_{i=1}^{M}\sum_{j=1}^{M} E_{ij} w_i w_j, \tag{19}$$

where E_{ij} are elements of the covariance matrix between estimates of the ith and jth methods, the diagonal elements giving the variance of the individual estimates (σ_H, σ_M and σ_{3D}, for *H*illas, *M*odel and 3*D*-model methods, respectively), while the off-diagonal elements describe the correlations between pairs of estimates:

$$\mathbf{E} = \begin{bmatrix} \sigma_H^2 & E_{H,M} & E_{H,3D} \\ E_{H,M} & \sigma_M^2 & E_{M,3D} \\ E_{H,3D} & E_{M,3D} & \sigma_{3D}^2 \end{bmatrix} \tag{20}$$

The *Best Linear Unbiased Estimates* (BLUE) method is then applied which consists in looking for the M values of w_i which provide the best unbiased estimates of the observable $\hat{x}$ and minimize the corresponding variance $\sigma^2(\hat{x})$.

Such a method is specifically applied to the determination of the best estimate of the primary photon direction and energy (which correspond to the observable $\hat{x}$) of the γ-candidate events as reconstructed by the $M = 3$ reconstruction methods. The error matrix **E** is estimated by Monte Carlo simulation, by applying to a γ sample simulated at conditions similar to the real data sample (e.g. for the Crab data analysis, MC photon spectrum generated with $\Gamma = 2.6$ and 50° zenith angle was considered) the same selection criteria as for real data. Therefore covariances between esti-

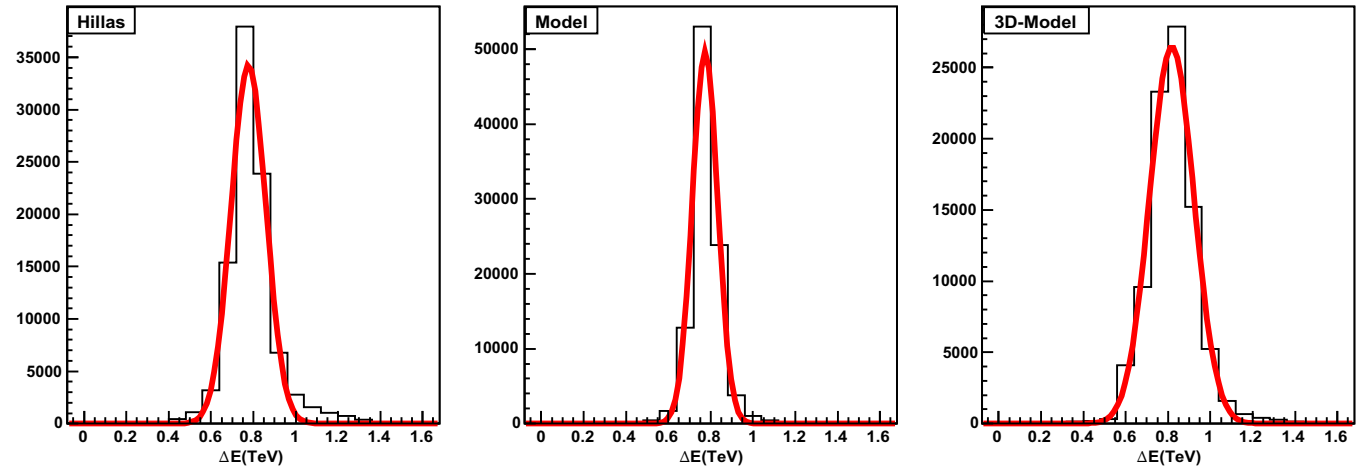

Fig. 13. The distribution of the relative error in the reconstructed energy per event for Monte Carlo simulated 0.8 TeV energy γ for the three analysis methods. The root mean square widths of the energy distributions are 13% (Hillas), 9% (model) and 19% (3D-model), while the gaussian σ from the fit are, respectively, 9%, 7% and 15%.

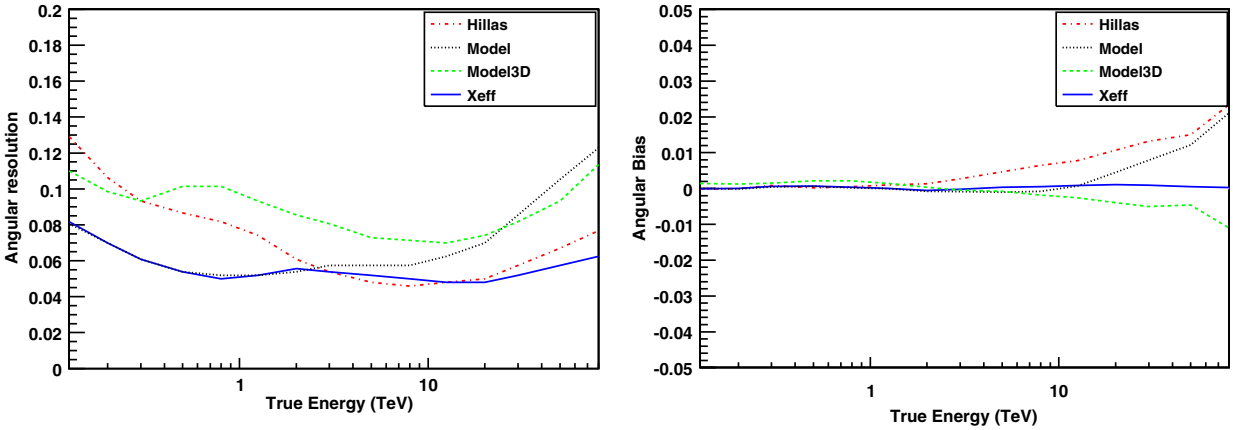

Fig. 14. The angular resolution (left panel) and the angular bias (right panel) as a function of *Gamma* energy, resulting from the X_{eff} analysis and estimated through the correlated combination of the directional measurements provided by the three reconstruction methods. The X_{eff} results are compared with expected angular resolution and bias from the three methods separately.

mates is computed as a function of different data-set conditions: e.g. energy and spectral index, camera offsets and zenith angles. The **E** error matrix determines the weights w_i of the three different estimates by satisfying the unbiased condition (in Eq. (18)) and miminmizing the Eq. (19). Finally the obtained weights w_i are applied to combine together, respectively, the observables for the three different reconstructions. Fig. 14 shows the angular resolution (68% containment) as a function of *Gamma* original energy for simulated showers. The events candidates are selected according to the X_{eff} analysis, while the chosen reconstruction is respectively the Hillas, Model, 3D-model to be compared with the estimated combined directional measurement referred as X_{eff}. One can deduce the expected improvement when the X_{eff} results are compared with expected angular resolutions from the other three methods separately: at lower energy (0.1–1 TeV) the combined 68% containment angular resolution follows the most competitive model reconstruction, while at higher energy (greater than few TeV) the Hillas and 3D-model methods perform better. For completeness in Fig. 14 the angular bias is also shown in order to provide the order of magnitude of relative systematic uncertainties in the direction reconstruction for different reconstructions. Here it is also important to remind that the reconstructed angular distances to the shower true direction (the θ parameter) from the three methods show low level of reciprocal correlation due to different pattern reconstruction on ground and which makes envisagable the combination of their estimates. The Hillas analysis reconstructs better the events that are well within the array, whereas the model analysis performs better with events that are not too close to one telescope. The 3D-model does its best with high telescope-multiplicity events, which concentrate at the center of the array (see [4] and references therein for more details).

The same combinatorial approach is applied to obtain a better estimate of the reconstructed energy of the gamma candidates. Fig. 15 shows the energy resolution and the energy bias as a function of *Gamma* original energy for simulated showers for the combined result (referred as X_{eff}) and the three independent reconstructions.

4.3. Systematic uncertainties

The systematic effects to the spectral measurements of a source, related to the detector inefficiencies and reconstruction have been studied with Crab Nebula data [15]. The following table summarizes the most important factors contributing to the systematic error estimation as extracted from the H.E.S.S. publication [15]:

At first order, these uncertainties affect in similar way the results obtained with the three methods of shower reconstruction. In the following, the systematic effects specific to the use of the X_{eff} composed estimator are discussed.

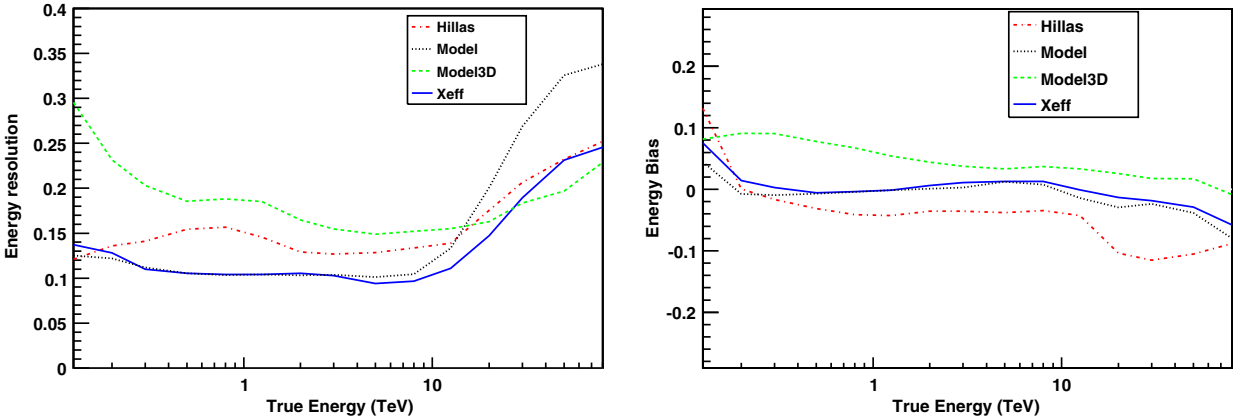

Fig. 15. The energy resolution (left panel) and the energy bias (right panel) as a function of *Gamma* true energy, resulting from the X_{eff} analysis and estimated through the correlated combination of the energy measurements provided by the three reconstruction methods. The X_{eff} results are compared with expected energy resolution and bias from the three methods separately.

The first point that should be underlined is related to the domain of the validity of the Eq. (11) with parameter η value comprised between 0.05 and 0.95 which implies the necessity of performing a strong pre-selection of events in the initial sample. This guarantees a correct behaviour of the formula and the lowest possible dependency on the background fluctuations – a pre-selected signal/background ratio of the order of 1 would be an optimal choice. The inherent systematic effects of each reconstruction method were checked with MC simulations and extensive studies as a function of the zenith angle and the offset for different types of sources have been performed in the past analyses as described in [2,15,4,5]. It is assumed in the presented analyses, that a proper simulation of the discriminating variables leads to a correct description of the X_{eff} construction in the MC simulations. This shows the importance of the description of the H.E.S.S. detector in the simulations and of the comparisons of the X_{eff} mis-tagging performances between MC and data samples. Related to this point, it was necessary to compare the correlation factors concerning the discriminating variables produced by Hillas, Model and 3D-model reconstructions which show, as well for MC as for Data, no correlation for photons and some residual values for the hadron background. There are at least two possibilities to overcome the correlation problem: reconstruct X_{eff} with global multi-variable $p.d.f$.s for photons and hadrons, or perform an iteration on X_{eff} variable by fitting the $p.d.f.$ from the X_{eff} distribution. The first solution has been studied and the differences in results on signal-to-background separation found with global, multi-variable $p.d.f$.s were below few %, to be considered here as negligible. In order to provide a quantitative example of such results, a test on a Crab data-set is here considered. The differences between the S/B-ratios and significance levels N_σ for an X_{eff} function built through the factorisation of single $p.d.f$.s and same estimators obtained with an X_{eff} using instead a single multi-variable correlated $p.d.f.$ are shown in Fig. 16. One can deduce the relative differences contained within few percents, second that the approach X_{eff} with the factorisation of single $p.d.f$.s performs better as expected. The stability of the results was checked as a function of the X_{eff}-cut for three values: 0.1, 0.3 and 0.5, as also shown in Fig. 16.

Finally, a good test when determining possible systematic effects on the results of data analysis, is to study the implication of variation of cut selection (the X_{eff} cut) within a reasonable domain. The stable dependency of the S/B ratio and the significance level N_σ on the X_{eff} cut can be deduced by Fig. 8. In this example, always referred to a Crab data-set, when considering X_{eff} cut variation at fixed η value or by varying η as well, one can deduce the low level systematic contribution due to the employed method corresponding to $\leqslant 10\%$ variation on the resulting S/B ratio and $\leqslant 3\%$ in the obtained N_σ. The stability plot of the spectral analysis results is shown in Fig. 17. Here the powerlaw best fit results for the same Crab data-set are compared through the correlation between spectral index Γ vs. differential flux dN/dE ($E > 1$ TeV) for different values of X_{eff}-cut = 0.1, 0.5, 0.7 and 0.9. The spectral analysis is stable within the statistical uncertainties, showing the total negligible systematic effect of the choice of X_{eff} cut.

In conclusion the systematic effects introduced by the multivariate X_{eff} approach is totally negligible compared to the main sources of uncertainties listed in Table 2.

5. The H.E.S.S.–X_{eff} data analysis validation

The improvement achieved with the X_{eff} data analysis in terms of sensitivity, reconstruction and background rejection, is validated by the re-analysis of some astrophysical sources already observed with the H.E.S.S. system. The X_{eff} data analysis results are here shown and compared to the corresponding results obtained with a standard Hillas analysis already published by the H.E.S.S. collaboration.

5.1. Point-like sources

A first cross-check required to validate the method is to study some point-like sources at different background condition, namely

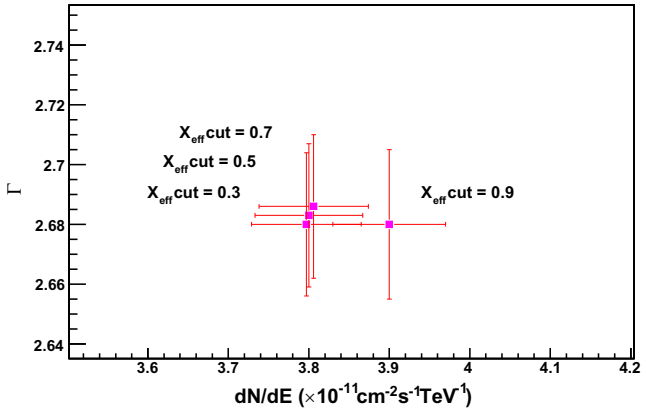

Fig. 17. Stability plot of the results of the spectral analysis for a Crab data-set, by varying the value of the X_{eff} cut selection = 0.1, 0.5, 0.7 and 0.9.

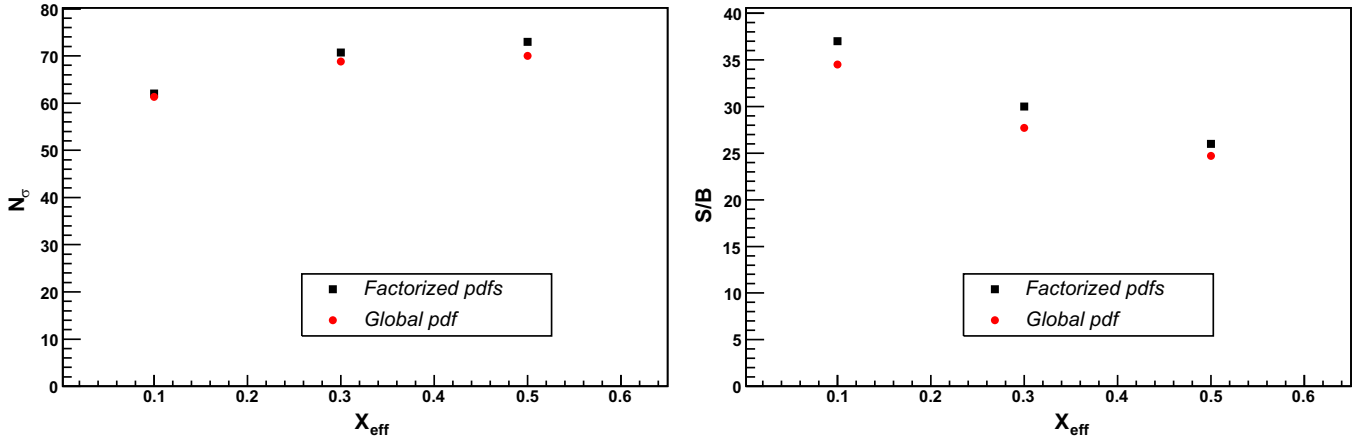

Fig. 16. The significance levels N_σ and the S/B-ratios for three chosen X_{eff}-cut (0.1, 0.3 and 0.5) in the case the X_{eff} function is built through the factorisation of single $p.d.f$.s and same estimators obtained with an X_{eff} using instead the single global correlated $p.d.f.$

Table 3
Comparative results for the analysis of the Crab nebula, listed by data-set along with excesses, significance and signal-to-background ratios. The X_{eff} analysis is competitive in terms of background rejection power when compared to standard Hillas analysis published results as well as the model and 3D-model analysis standalone.

Source	Data-set	Method	*ON*	*OFF*	α	Excess	Significance N_σ	S/B
Crab	III	*Hillas*-stand. (publ.)	4759	2417	0.20	4283	94.2	8.8
	III	*Model*	10,079	37,635	0.07	7293	99	2.7
	III	*3D-model*	7460	15,732	0.1	5958	99	3.8
	III	X_{eff}-bright	5013	902	0.20	4833	115.1	26.8

Table 4
Flux and spectral measurements of the Crab, divided up by data-set. The results of powerlaw plus an exponential cut-off best fits with the X_{eff}-*bright*-cuts analysis for a data-set (III) is compared to published results (*Std.*) with *Hillas* − *Standard*-cuts analysis. The results of the powerlaw (PL) best fits are also compared. The quoted errors do not take into account the systematic effects.

Data-set	Method	$I_0(1\text{TeV}) \times 10^{-11}$ (cm^{-2} s^{-1} TeV^{-1})	Γ	E_c (TeV)	$F_{>1\text{ TeV}} \times 10^{-11}$ (cm^{-2} s^{-1})
ALL	*Std.*	3.76 ± 0.07	2.39 ± 0.03	14.3 ± 2.1	2.26 ± 0.08
III	*Std.*	3.84 ± 0.09	2.41 ± 0.04	15.1 ± 2.8	2.31 ± 0.10
III	X_{eff}	4.01 ± 0.09	2.52 ± 0.04	19.4 ± 5.3	2.32 ± 0.08
ALL	*Std.* (PL)	3.45 ± 0.05	2.63 ± 0.01		2.11 ± 0.03
III	X_{eff} (PL)	3.81 ± 0.07	2.67 ± 0.02		2.27 ± 0.06

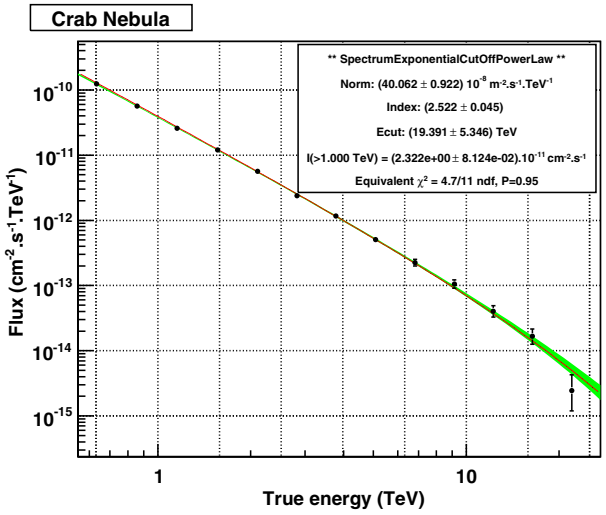

Fig. 18. Energy spectrum resulting from the X_{eff} analysis for data-set III, fit residuals to the power law and exponential cut-off fit are also shown.

Galactic (e.g. the Crab nebula, SNR G0.9+0.1) and extragalactic (e.g. PKS2155, ES0347 and H2356).

5.1.1. Crab nebula

The Crab nebula, a reference source in VHE gamma-ray astronomy, has a size comparable with the H.E.S.S. point-spread function (PDF), therefore it is usually treated as a point-like source even if it belongs to the family of extended pulsar wind nebulae (PWN). First observed at high energies in 1989 the Crab was then re-observed and confirmed by a number of other experiments (see [15] and reference therein).

The H.E.S.S. collaboration has published the analysis of the Crab data based on different observations from 2004 to 2005 and for a total time of 22.9 h after data quality selection [15]. A sub-sample of those data (quoted as the III data-set), with four telescopes, limited average zenith angle observation (47.9°) and longer live time (10.6 h), has been re-analysed by applying the X_{eff} method and with the choice of so-called *Bright*-cuts. The results of this analysis are summarised in Table 3. As expected the X_{eff} analysis applied to this data-set provides better results in terms of background rejection, with S/B ratio more than a factor 3 better than in Hillas-standard analysis and an improved significance of 22%.

The differential energy spectrum of the Crab signal as observed by the H.E.S.S. instrument, has been determined with a parameterization described by a power law with slope $\Gamma = 2.39 \pm 0.03_{stat} \pm 0.09_{sys}$ and an exponential cut-off at $(14.3 \pm 2.1_{stat} \pm 2.8_{sys})$ TeV. The integral flux above 1 TeV is $2.26 \pm 0.08_{stat} \pm 0.45_{sys} \times 10^{-11}$ cm^{-2} s^{-1} TeV^{-1}. The energy spectrum of the Crab for the data-set III has been measured with the X_{eff} analysis. The results are consistent with the one published in [15] (see Table 4). The reconstructed X_{eff} integral flux is compatible with the Hillas-standard result within the statistical uncertainties, which indicates that the reconstructed flux is not strongly dependent on the details of the analysis method. The differential spectra are also in agreement in case of power law fit function plus exponential energy cut-off as well as in the case of a power law best fit function (PL), compared to the results of the published analysis on the full Crab data sample (ALL). Even if compatible within the uncertainties, the X_{eff} Crab spectrum (Fig. 18) shows less steepening at an energy cut-off (E_c) of $(19.4 \pm 5.3_{stat} \pm 3.9_{sys})$ TeV, slightly higher than in the Hillas spectrum.

5.1.2. SNR G0.9+0.1

The H.E.S.S. instrument has detected for the first time a VHE (> 100 GeV) gamma-ray emission from the composite supernova remnant G0.9+0.1. The flux and the location of this point-like source make it an important case for the X_{eff} analysis validation purpose: it is one of the weakest source ever detected at TeV energies (with a flux representing only 2% of the flux from the Crab above 200 GeV); it is located in the region around the Galactic Center where the cosmic-ray and diffuse gamma-ray background make the source signal more difficult to detect. The H.E.S.S. collaboration has published results on the G0.9+0.1 emission based on a 2004 data-set corresponding to a total live time of about 50 h [16]. The Hillas-standard analysis resulted in a highly significant detection with 13 σ. The data-set is fitted by a power law in energy with photon index $\Gamma = 2.40 \pm 0.11$. The X_{eff} analysis was conducted on exactly the same data-set and with the choice of *Faint*-source *cuts*. For cross-check a classic Hillas analysis through the application of *Standard* cuts and requiring a 200 p.e. threshold was also conducted. The comparison among the results of the two analysis

Table 5
Comparative results for the analysis of the SNR G0.9+01, listed by data-set along with excesses, significance and signal-to-background ratios. The X_{eff} analysis is competitive in terms of background rejection power when compared to standard Hillas analysis.

Source	Method	*ON*	*OFF*	α	Excess	significance N_σ	S/B
G0.9+01	*Hillas* (200 p.e.)	1069	10801	0.065	368	13 (publ. in [16])	0.5
	X_{eff}-bright (200 p.e.)	348	1715	0.071	225	16	1.8

Table 6
Comparative results for the analysis of the MJD 53944 PKS2155-304 flare, listed by methods (published *Hillas-loose* cuts analysis and X_{eff}-*Flare* cuts analysis) along with radius of integrated region around the source, excesses, significance and signal-to-background ratios.

Source	Method	$\theta^2_{cut}(deg.^2)$	*ON*	*OFF*	α	Excess	N_σ	S/B
PKS2155-304	*Hillas-looses* [17]	0.04	12480	3296	0.215	11771	168	17
	X_{eff}	0.02	8420	399	0.20	8340	165	105

methods are detailed in Table 5. The gain in significance with the X_{eff} analysis is ~30%, and the background rejection is improved of a factor ~3, for a reduced number of excess events.

The H.E.S.S. collaboration has published the detection (and the discovery in same cases) of VHE γ-ray emission from distant extragalactic sources: AGNs, Blazars and BL Lac objects. For our validation purpose a sample of such sources is considered since they exhibits various level of spectral hardness and corresponding integral flux for a similar background level. In the follow the results of the X_{eff} analysis are summarized.

5.1.3. The PKS2155-304 big-flare

The 28 July 2006 flare of the PKS 2155-304 blazar observed by H.E.S.S., for its peculiar fluency, energy spectrum, time variability and for the point-like size of the source, is an excellent prototype for the validation of the multivariate analysis. The H.E.S.S. published results are based on a standard analysis [17] of an equivalent exposure of 1.32 h live time at a mean zenith angle of 13° in the early hours of MJD 53944. As reported in the corresponding publication [17] the analysis was perfomed with Hillas method and *loose cuts* [15] (40 p.e. minimal amplitude; looser cuts on Hillas discriminating variables with consequently higher gamma statistics but lower background rejection power), yielding to an energy threshold of about 170 GeV. This approach could be sensitive to systematic bias due to important inalienable background on short time scale even if, at first sight, it could not be an issue since the average flux observed during this outbust corresponds to about seven times the Crab flux. Furthermore, it would simplify the analysis avoiding low-statistics issues on short time scale flux estimation. The standard analysis is based on ON-source data taken from a circular region of radius $\theta = 0.2^\circ$ centered on PKS 2155-304, which corresponds to a 99% containment of ON–OFF candidate events and in agreement with the angular resolution (68% containment) provided by the Hillas reconstruction method at low energies (see Fig. 14).

The X_{eff}-analysis was conducted on exactly the same data-set and with the choice of *Flare cuts* applied to ON-source data taken from a circular region of radius $\theta = 0.14^\circ$ centered on PKS 2155-304, corresponding to 95% events containment according to the angular resolution provided by the combined method at low energies (see Fig. 14). The comparison between the two approaches is shown in Table 6. In Fig. 19 the distributions of *ON* and *OFF* source events in θ^2 resulting from the Hillas analysis and X_{eff} analysis are compared. The vertical arrows denote the θ^2 selection cuts corresponding to respectively 90% and 95% containment of excess events after background subtraction. Both distributions, which are in perfect agreement with their expected point-spread functions, show the different level of backgorund rejection achieved

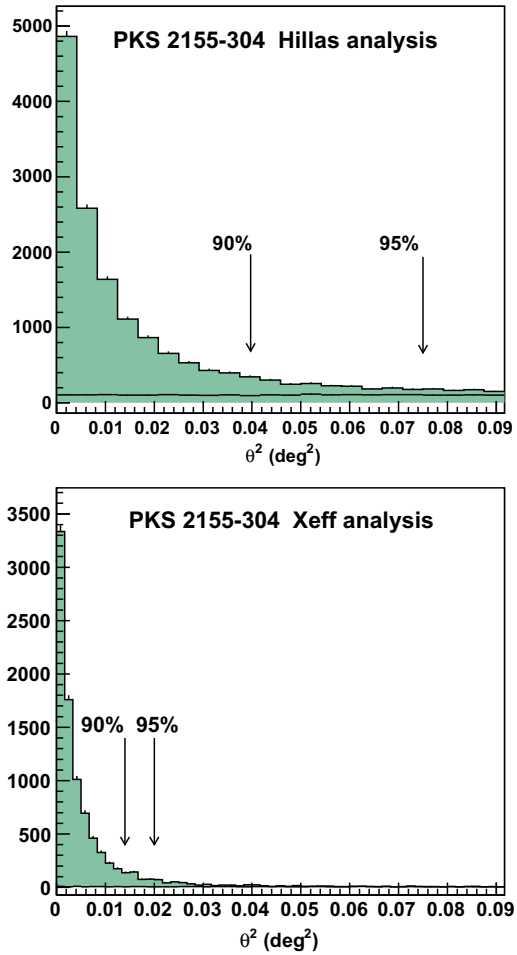

Fig. 19. Distributions of *ON* and *OFF* source events in θ^2 for the PKS2155-304 MJD 53944 flare data-sets resulting from the Hillas analysis (top) and X_{eff} analysis (bottom). The vertical arrows denote the θ^2 selection cuts corresponding to, respectively, 90% and 95% containment of excess events after background subtraction. Both distributions are in perfect agreement with their respective Monte Carlo derived point-spread functions.

with the two methods as well as the improvement in terms of angular reconstruction when the X_{eff} method is applied: 90% of the excess γ-events are reconstructed within $\theta^2 = 0.02^\circ$, while they are within $\theta^2 = 0.075^\circ$ in the *Hillas* analysis.

The X_{eff}-analysis is applied to a selected sample of 8420 events, which is about 30% less candidates ON source than the sample

selected for the Hillas analysis. The excess events selected by the two analysis differ each other for the same extent but with a comparable resulting level of significance for both methods. The X_{eff} approach shows also in this analysis a competitive background rejection power, resulting in about one order of magnitude higher value of the signal-to-background ratio. All these considerations support the hypothesis that the measured gamma-ray flux from the PKS 2155-304 2006 flare as studied with the X_{eff}-analysis is based on a statistically significant sample of photon events with a high level of purity, e.g. lowest possible level of background contamination.

The spectral analysis has been performed with the X_{eff} method. The fit to the data with a simple power law function resulted in a spectral index $\Gamma = 3.35 \pm 0.02_{stat} \pm 0.1_{sys}$ compatible with the published one ($\Gamma = 3.19 \pm 0.02_{stat} \pm 0.1_{sys}$) and an average integral flux above 200 GeV equal to $\Phi_{>200\ \mathrm{GeV}} = 1.66 \pm 0.05_{stat} \pm 0.33_{sys} \times 10^{-9}$ cm^{-2} s^{-1} consistent with the published result of $\Phi_{>200\ \mathrm{GeV}} = 1.72 \pm 0.05_{stat} \pm 0.34_{sys} \times 10^{-9}$ cm^{-2} s^{-1}.

The almost pure sample of photons from PKS2155-304 Big-flare obtained with X_{eff} selection may be further used in the energy-time analysis and calibration studies between data and Monte Carlo simulations.

5.1.4. 1ES 0347-121

The BL Lac object 1ES 0347-121 was observed for a total live time of 25.4 hours and at zenith angles ranging from 12° to 40° [18]. The H.E.S.S. observation results in an excess of 327 events, corresponding to a statistical significance of 10.1 standard deviations for an energy spectrum ranging from 250 GeV to 3 TeV and described by a power law with photon index $\Gamma = 3.10 \pm 0.23$. The same data-set have been analysed through the X_{eff} approach resulting in 290 excess events corresponding to about 50% higher statistical significance and a factor of three improved S/B ratio (see Table 7).

5.1.5. H 2356-309

The BL Lac object H 2356-309 was observed with a total exposure of about 40 h live time. The H.E.S.S. collaboration has published the results of a standard Hillas analysis and a 3D-model standalone analysis, both allowing for corresponding 9.7σ and 11.6σ significance levels [19]. The differential energy spectrum of this source is well-described by a power law with a photon index $\Gamma = 3.09 \pm 0.24$. The competitive results of the X_{eff} analysis of the same data-set are shown in Table 7: the high level of background rejection power allows to get a factor of two significance level for about the same number of excess events.

For the above studied sources the agreement between the results of spectral analysis with the standard Hillas method and the X_{eff}-approach, already shown in previous examples, is confirmed. This consolidates the applicability of the multivariate approach for the H.E.S.S. analysis.

5.2. Extended sources

The X_{eff} method is conceived with the purpose of improving the morphological studies of extended sources and the sensitivity to faint γ-emission thanks to its background rejection power together with the best estimation of the direction and energy of the photon candidates. To validate such achievement a test has been performed on some Galactic sources (e.g. Vela-X, MSH 15-52 and J1849).

5.2.1. Vela-X

The Vela-X cocoon is an extended region to the south of the Vela pulsar and part of the Vela supernova remnant (SNR) complex region which is source of non-thermal radiation. H.E.S.S. has observed a strong signal originated from this region. Vela-X is an important prototype for the validation of the analysis method introduced here: it is one of the most extended source ever detected by a IACT observatory and it has a peculiar energy spectrum showing the first clear evidence of a peak from VHE gamma-ray sources. The published H.E.S.S. Hillas analysis of Vela-X [20] resulted in an excess of 2152 events for a total live time of 16.4 h, within an integration region of 0.8° around the best fit center of gravity of the emission region. The background level in the Vela-

Table 7
Comparative results for the analysis of extragalactic sources (1ES 1101-232, 1ES 0347-121 and H 2356-309), listed by methods (published *Hillas* analysis and X_{eff} analysis) along with excesses, significance and signal-to-background ratios.

Source	Method	*ON*	*OFF*	Excess	N_σ	S/B
1ES 0347-121	Hillas [18]	1167	9241	327	10.1	0.4
	X_{eff}	553	3067	290	14.7	1.1
H 2356-309	Hillas [19]	3776	35,280	591	9.7	0.4
	3D-model [19]	1706	13,784	453	11.6	0.4
	X_{eff}	1213	6593	618	22.2	1.0

Table 8
Comparative results for the analysis of the 2004–2005 Vela-X nebula cocoon observations, listed by methods (the published standard Hillas-*hard cuts* analysis and the X_{eff}-*Faint-cuts* analysis, both applied to a $\theta^2 = 0.64°$ integration angle) along with excesses, significance and signal-to-background ratios.

Source	Method	*ON*	*OFF*	α	Excess	N_σ	S/B
Vela-X	Hillas-*hard* (200 p.e.) [20]	9610	7879	0.94	2152	16.7	0.29
	X_{eff}-Faint (200 p.e.)	3505	2230	0.9	1515	22	0.76
	X_{eff}-Faint (80 p.e.)	8789	8006	0.9	1945	13.5	0.27

Table 9
Flux and spectral measurements of Vela-X. The results of the powerlaw plus an exponential cut-off best fits with the X_{eff}-*Faint* analysis (with 80 p.e. threshold) is compared to published results with *Hillas-hard* analysis (with 200 p.e. threshold). The uncertainties associated to each measurement are in order the statistical and systematic ones.

Method	E_{MIN} (GeV)	E_{MAX} (TeV)	Γ	E_c (TeV)	$F_{>1\mathrm{TeV}}$ ($\times 10^{-11}$ cm^{-2} s^{-1})
Hillas	550	65	$1.45 \pm 0.09 \pm 0.2$	$13.8 \pm 2.3 \pm 4.1$	$1.28 \pm 0.17 \pm 0.38$
X_{eff}	250	65	$1.46 \pm 0.07 \pm 0.2$	$13.6 \pm 2.9 \pm 3.9$	$1.71 \pm 0.14 \pm 0.41$

X analysis (both the published and the X_{eff} ones) was estimated using the *ON—OFF* method, based in a sample of runs taken at similar zenith angles which contain no excess gamma-ray signal. This method allows the background level to be estimated in cases where the integration region from the source is comparable to the size of the field of view. For the published analysis the choice of Hillas-*hard* cuts (200 p.e. image amplitude threshold) was motivated by the need of improving the angular resolution and reducing systematic effects due to uncertainties in the background estimation. On the contrary the X_{eff} analysis with the choice of *Faint*-source cuts (implying only 80 p.e. minimal threshold) is supposed to be at least performant as the Hillas-*hard* analysis due to a competitive background rejection and an improved angular resolution without being obliged to increase the minimal image amplitude to 200 p.e.. In Tables 8 and 9 the published and the X_{eff} results are compared: the X_{eff} *Faint* cuts (with a choice of integration region of 0.8° around the best fit center of gravity of the emission region)resulted in slightly reduced statistics of selected γ-events and ~32% improvement in the resulting significance and about almost factor of three increase of the signal-to-background ratio. Furthermore for completeness the X_{eff} analysis with 80 p.e. amplitude threshold was applied and the results are comparable to those obtained with Hillas analysis but at 200 p.e. amplitude threshold. In conclusion the X_{eff} analysis leads to global improvement in γ-events precision identification critical for morphological studies and in lower energy sensitivity for further spectral investigation.

These results validate and confirm the X_{eff} multivariate approach as a successfull way to analyse faint extended sources.

The published energy spectrum of Vela-X as observed by H.E.S.S, has been measured with a differential spectrum described by a power law with slope $\Gamma = 1.45 \pm 0.09_{stat} \pm 0.2_{sys}$ and an exponential cut-off at energy of $(13.8 \pm 2.3_{stat} \pm 4.1_{sys})$ TeV. The integral flux above 1 TeV is $1.28 \pm 0.17_{stat} \pm 0.38_{sys} \times 10^{-11}$ cm^{-2} s^{-1} TeV^{-1}.

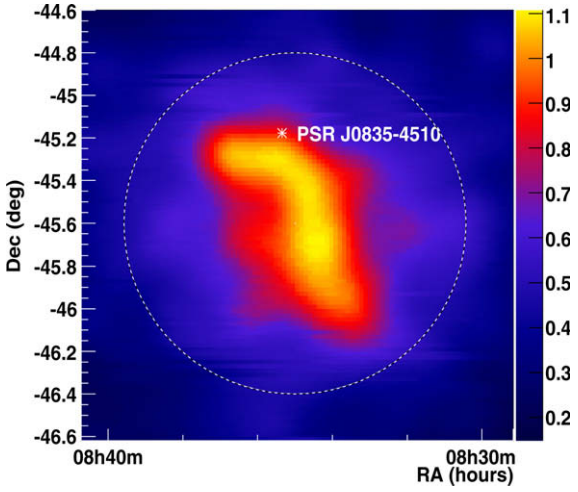

Fig. 20. Gaussian smoothed sky map of the Vela-X cocoon region obtained with the X_{eff} analysis with 200 p.e. threshold and 0.09° smoothing width.

The energy spectrum as measured with the X_{eff} analysis is consistent with the published ones (see Table 4) but it is extended at lower energy (250 GeV against the 550 GeV) with competitive results obtained for 80 p.e. threshold. This last achievement is what one has to look forward when exploiting the introduced multivariate analysis potential. This result combined with a competitive angular resolution, which is better than 0.07° even at the energy threshold of the measured flux (see Fig. 14), allows to investigate more in details the morphology of extended sources and as a function of the energy regime of the non-thermal emission. Fig. 20 shows the gaussian smoothed sky map of the Vela-X cocoon region with smoothing width of 0.09° (as performed in the published map [20]) and obtained with the X_{eff} analysis with 200 p.e. threshold. The circle represents the H.E.S.S. integration region for the spectral measurement (0.8°).

The comparison with the published map [20] shows a good agreement as far as we apply a smoothing width compatible with the Hillas reconstruction point-spread function (PSF). When a smaller smoothing width, more consistent with the improved X_{eff} PSF, and a lower energy threshold are applied, some new morphological features are revealed. Further model investigation on the Vela-X region morphology is therefore envisaged [7]. It goes far behind the aim of this paper and will be detailed in a dedicated analysis of the H.E.S.S. collaboration [21].

5.2.2. MSH 15-52

The Supernova Remnant MSH 15-52 is an other extended prototype source chosen for validation purpose. It has been observed by H.E.S.S. and a γ-ray signal was detected at 25 sigma level during an exposure of 22.1 h live time [22]. The published results by the H.E.S.S. collaboration concern a selected sample of data taken at a mean zenith angle of 37° and analysed using the standard Hillas method. The data are consistent with a power law energy spectrum from 280 GeV to 40 TeV and a photon index $\Gamma = 2.27 \pm 0.03 \pm 0.2$. The energy spectrum as measured with the X_{eff} analysis is consistent with the published one. In Table 10 the published and the X_{eff} results are compared: the X_{eff} *Bright*-source cuts resulted in slightly reduced statistics of selected γ-events and 50% improvement in the resulting significance and about factor of two increase of the signal-to-background ratio. The Hillas analysis of the morphological study of MSH 15-52 was conducted with a higher energy threshold (~ 900 GeV) by applying a 400 p.e. amplitude threshold on the image size of the γ-candidates. This cut is meant to reduce the Hillas angular resolution to $\leqslant 0.07°$ and improve the morphological investigation: the resulting extended emission reveals an elliptically shaped region around the pulsar PSR B1509-58, with semi-major axis ~ 6′ in the NW–SE direction and semi-minor axis ~ 2′. This morphology coincides with diffuse pulsar wind nebula as observed at X-ray energies by ROSAT [22]. As in the case of Vela-X also for MSH 15-52 the X_{eff} analysis leads to a global improvement in γ-events precision identification and to a lower energy improved sensitivity, critical for further morphological investigation: the improved X_{eff} PSF would allow for more detailed studies and at a lower energy regime since the 400 p.e. amplitude threshold is not required to achieve a comparable angular resolution (0.07°). Further model investigation on the MSH 15-52 PWN morphology is therefore envisaged [7].

Table 10
Comparative results for the analysis of the Supernova Remnant MSH 15-52 2004 observations, listed by methods (the published standard Hillas analysis and the X_{eff}-*bright-cuts* analysis, along with excesses, significance and signal-to-background ratios.

Source	Method	*ON*	*OFF*	Excess	N_σ	S/B
MSH 15-52	Hillas-*standard* (80 p.e.) [22]	3706	10,154	1469	25	1.0
	X_{eff}-*bright* (80 p.e.)	2069	6249	1371	39	2.0

Finally the X_{eff} analysis method has demonstrated competitive performance in searching for signal from a series of faint sources. As an example the IGR J18490-0000 was observed by the H.E.S.S. system during scans of the Galactic plane [23]: the preliminary results of Hillas (hard cuts and 200 p.e. image amplitude threshold) analysis have been published in [24]. The analysed dataset includes 49 h of live time with an average zenith angle of 30°. An excess was detected with a peak significance of $6.4-6.7\sigma$. The X_{eff} analysis (with *Search − cuts*) provides an excess detection for $> 6\sigma$ average significance and a $\sim 8\sigma$ peak significance level.

6. Conclusions

A multi-variable-classification approach based on a composed estimator for the photon and hadron selection in H.E.S.S. experiment has been studied.

The proposed method aims to use the results of the three reconstructions of the photon candidate shower parameters by combining the identification estimators as well as the kinematical variables: angle and energy. This leads to optimizations of the signal-to-background ratios in a multi-variable space (here four dimensions) by use of the maximal information derived from the individual reconstruction methods. The followed approach ensures, by its principle, the best optimization of the quality factor and allows to reach the lowest energy threshold in the X_{eff} analyses. The gain in the quality factor is due also to a more stringent pre-selection possibility offered by comparing the reconstructed kinematical parameters, and to be applied before the X_{eff} combination. It has also been checked, that the error weighted combination of the kinematical variables provides improved resolution functions in a large energy range.

The results from X_{eff} analysis of a series of benchmark sources are very competitive as compared to the standard H.E.S.S. analyses based only on one reconstruction procedure. For these sources, the main improvement obtained with X_{eff} estimator concerns the signal-to-background ratio and the quality factor in general. For the point-like or the extended sources, keeping the photon efficiency on about the same level, the improvement factor varies between 3 and 10 depending on the analysis type, while the resulting significance increases of about 30%.

The future developments with combined estimators will follow different directions: inclusion of other possible discriminating variables, preferentially uncorrelated with those presented in this paper, and comparison and testing of the other commonly used procedures [25].

Finally, it should be underlined, that the X_{eff} estimator is well suited for the weighted event-by-event analyses and a Likelihood parameterization approach for the investigation of the theoretical modeling of the morphological properties of the extended sources.

Acknowledgements

The authors would like to thank the H.E.S.S. collaboration for the technical support and the fruitfull discussions about the three different methods in use for the data analysis. The authors thank Prof. W. Hofmann, spokesperson of the H.E.S.S. collaboration for allowing us to use H.E.S.S. data in this publication.

References

[1] H.E.S.S. Collaboration. <http://www.mpi-hd.mpg.de/hfm/HESS/pages/publications>/.
[2] A. Hillas, in: Proceedings of the 19th I.C.R.C. (La Jolla), vol. 3, 1985, p. 445.
[3] A. Daum et al., Astropart. Phys. 8 (1997) 1.
[4] M. de Naurois, in: Proceedings of the Cherenkov, astro-ph/0607247v1, 2005.
[5] M. Lemoine-Goumard, B. Degrange, M. Tluczykont, Astropart. Phys. 25 (2006) 195.
[6] W. Hoffmann et al., Astropart. Phys. 12 (1999) 135.
[7] F. Dubois, Ph.D. Thesis, LAPP, 2009.
[8] D. Buskulic et al., ALEPH Collaboration, Phys. Lett. B 377 (1996) 205.
[9] D. Buskulic et al., ALEPH Collaboration, Phys. Lett. B 384 (1996) 449.
[10] D.E. Jaffe, F. Le Diberder, M.-H. Schune, LAL 94-67 and FSU-SCRI 94-101.
[11] T.-P. Li, Y.-Q. Ma, Astroph. J. 272 (1983) 317.
[12] L. Lyons, D. Gibaut, P. Clifford, Nucl. Instrum. Methods A270 (1998) 110–117.
[13] G. Mohanty et al., Astropart. Phys. 9 (1998) 15.
[14] P.T. Reynolds et al., Astroph. J. 404 (1993) 206.
[15] H.E.S.S. collaboration, F. Aharonian, et al., Astron. Astrophys. 457 (2006) 899.
[16] F. Aharonian et al., H.E.S.S. collaboration, Astron. Astrophys. 432 (2005) L25–L29.
[17] F. Aharonian et al., H.E.S.S. Collaboration, Astrophy. J. Lett. 664 (2007) L71.
[18] F. Aharonian et al., H.E.S.S. Collaboration, Astron. Astrophys. 473 (2007) L2–L25.
[19] F. Aharonian et al., H.E.S.S. Collaboration, Astron. Astrophys. 455 (2006) 461.
[20] F. Aharonian et al., H.E.S.S. Collaboration, Astron. Astrophys. 448 (2006) L43.
[21] F. Dubois et al., for the H.E.S.S. Collaboration, in: Proceedings of the 31st I.C.R.C. (Lodz), 2009.
[22] F. Aharonian et al., H.E.S.S. Collaboration, Astron. Astrophys. 435 (2005) L17–L20.
[23] F. Aharonian et al., H.E.S.S. Collaboration, Astrophy. J. 636 (2006) 777.
[24] R. Terrier et al., H.E.S.S. Collaboration, in: Proceedings of the Gamma-2008, vol. 312, Heidelberg, 2008.
[25] Toolkit for Multivariate Data Analysis (TMVA). <ttp://tmva.sourceforge.net>/.

ANNEXE B

- A. Jacholkowska, **G. Lamanna**, et al., Physical Review D 74,(2006) 023518
- J. Carr, **G. Lamanna,** J. Lavalle, Rep. Prog. Phys. 69 (2006) 2475-2512
- **G. Lamanna,** Modern Physics Letters A, vol.18 (2003) n.28, 1951
- **G. Lamanna**, Proc. "SNGHEGE", 2007.
- F. Dubois, **G. Lamanna** et al. for the H.E.S.S. collaboration. Proc. ICRC, 2009

Indirect dark matter search with diffuse gamma rays from the Galactic Center with the Alpha Magnetic Spectrometer

A. Jacholkowska,[1,*] G. Lamanna,[2] E. Nuss,[1] J. Bolmont,[1] C. Adloff,[3] J. Alcaraz,[4] R. Battiston,[5] P. Brun,[3] W. J. Burger,[5] V. Choutko,[6] G. Coignet,[3] A. Falvard,[1] E. Fiandrini,[5] L. Girard,[3] C. Goy,[3] K. Jedamzik,[1] R. Kossakowski,[3] G. Moultaka,[1] S. Natale,[7] J. Pochon,[3] M. Pohl,[7] S. Rosier-Lees,[3] M. Sapinski,[1,†] I. Sevilla Noarbe,[4] and J. P. Vialle[3]

[1]*Laboratoire de Physique Théorique et Astroparticules, UMR5207-UM2/IN2P3-CNRS, Place Eugène Bataillon—CC70, 34095 Montpellier, France*

[2]*Centre de Physique des Particules de Marseille, UMR/IN2P3-CNRS, 163 avenue de Luminy—Case 902, 13288 Marseille, France*

[3]*Laboratoire d'Annecy-le-Vieux de Physique des Particules, LAPP/IN2P3-CNRS et Université de Savoie, F-74941 Annecy-le-Vieux, France*

[4]*Centro de Investigaciones Energèticas, Medioambientales y Tecnològicas, CIEMAT, E-28040 Madrid, Spain*

[5]*University and Sezione INFN of Perugia, Italy*

[6]*Laboratory for Nuclear Science, MIT, 77 Massachusetts Avenue, Cambridge, Massachusetts 02171-9131, USA*

[7]*DPNC, University of Geneva, 24, Quai Ernest-Ansermet, 1211, Geneva 4, Switzerland*

(Received 1 February 2006; published 18 July 2006)

The detection of nonbaryonic dark matter through its gamma-ray annihilation in the center of our galaxy has been studied. The gamma fluxes according to different models have been simulated and compared to those expected to be observed with the Alpha Magnetic Spectrometer (AMS), during a long-term mission on board of the international space station. Under the assumption that the dark matter is composed of the lightest, stable supersymmetric particle, the neutralino, the results of the simulations in the framework of minimal supergravity models, show that with a cuspy dark matter halo profile or a clumpy halo, the annihilation gamma-ray signal would be detected by AMS. More optimistic perspectives are obtained with the anomaly mediated supersymmetry breaking (AMSB) model. The latter leads also to a cosmologically important ^{2}Li abundance. Finally, the discovery potential for the massive Kaluza-Klein dark matter candidates has been evaluated and their detection looks feasible.

DOI: 10.1103/PhysRevD.74.023518 PACS numbers: 95.35.+d

I. INTRODUCTION

The nature of dark matter is one of the outstanding questions and challenges in cosmology. The existence of cosmological dark matter is required by a multitude of observations and arguments, such as the excessive peculiar velocities of galaxies within clusters of galaxies, or the observations of gravitational arcs indicating much deeper gravitational potentials within clusters than those inferred by the presence of the luminous matter [1,2]. On the galactic scale, extensive dark matter halos are required to explain the observed rotation curves in spiral galaxies, or the velocity dispersion in elliptical galaxies [3,4]. Furthermore, big bang nucleosynthesis predicts a fractional contribution of baryons to the critical density, Ω_b, significantly smaller than the total Ω_m in form of clumpy matter. The Wilkinson Microwave Anisotropy Probe (WMAP) has provided the most detailed measurements of the cosmic microwave background (CMB) anisotropies [5]. In the framework of the standard cosmological model, WMAP quotes a total matter density of $\Omega_m = 0.27 \pm 0.04$ and a baryon density of $\Omega_b = 0.044 \pm 0.004$, which confirms that most of the matter is nonbaryonic, in agreement with the results obtained from primordial nucleosynthesis studies.

Various nonbaryonic dark matter candidates require physics beyond the standard model of particle physics (for a recent review see e.g. [6]). N-body simulations of structure formation [7] suggest a nonrelativistic, weakly interacting massive particle (WIMP) as a dark matter component, thus favoring the cold dark matter scenario [8,9]. The WMAP measurement of the density of the nonbaryonic dark matter provides constraints in the range of $0.095 < \Omega_{\mathrm{CDM}} h^2 < 0.129$, at the 2σ level.

Supersymmetric theories offer an excellent WIMP candidate, which satisfies the CDM paradigm and the constraints on Ω_{CDM}, namely, the neutralino (χ_1^0) of the minimal supersymmetric standard model (MSSM), assumed to be the lightest supersymmetric particle (LSP) and stable due to R-parity conservation [10]. At present, lower limits on the LSP neutralino mass in the MSSM are about 50 GeV from LEP experiments (although the mass may be significantly smaller depending on the assumptions relative to gaugino mass universality). Less conventional scenarios than the neutralino within the minimal supergravity (mSUGRA) context have been proposed [11]:

(i) In the anomaly mediated supersymmetry breaking (AMSB) scenario [12,13] the neutralino LSP is predominantly a W-ino [the supersymmetric partner of the electrically neutral component of the $SU(2)_L$

*E-mail address: Agnieszka.Jacholkowska@cern.ch

†On leave from Henryk Niewodniczanski Institute of Nuclear Physics in Cracow

gauge bosons]. Endowed with a relatively large annihilation cross section this particle may constitute the bulk of the dark matter when subsequently to its thermal freeze-out, it is further generated non-thermally (e.g. via Q-ball evaporation or gravitino decay). By virtue of its large annihilation cross section the W-ino may lead to possibly large gamma fluxes [14].

(ii) In extra-dimension models, ultimately motivated by string theories, it has been argued [15] that the lightest Kaluza-Klein excitation can provide under certain conditions, a very good CDM candidate. In the present paper we will restrict ourselves to the possibility of low scale extra-dimensions as an extension of the nonsupersymmetric standard model [16] with a perfectly viable dark matter Kaluza-Klein particle [17].

In this paper, we present the predicted γ-ray fluxes from the Galactic center from neutralino annihilations in the frame of mSUGRA and AMSB models, as well as from Kaluza-Klein dark matter annihilations. The predicted fluxes are used to assess, for the different scenarios, the discovery potential for nonbaryonic dark matter provided by a three-year observation of the diffuse γ-ray differential spectrum by the AMS on the ISS.

II. MODEL DESCRIPTIONS AND SIMULATIONS

The limited knowledge of dark matter structure and the density profile near the Galactic center represent the principal astrophysical uncertainties when evaluating the discovery potential of the dark matter through indirect detection. On the other hand, the predicted γ-ray fluxes depend on the assumptions made within the framework of the particle physics models associated with the different dark matter candidates.

A. Dark matter halo parametrization

One may parameterize the mass density profile of our Galaxy by the following equation:

$$\rho_\chi(r) = \rho_0\left(\frac{R_0}{r}\right)^\gamma\left\{\frac{R_0^\alpha + a^\alpha}{r^\alpha + a^\alpha}\right\}^\epsilon, \tag{1}$$

assuming a simple spherical Galactic halo. An isothermal profile with core radius a corresponds to $\gamma = 0$, $\alpha = 2$ and $\epsilon = 1$ as proposed by [18]. A Navarro, Frenk, and White (NFW) profile [19] is obtained with $\gamma = 1$, $\alpha = 1$, and $\epsilon = 2$, whereas Moore's distribution [20] is recovered if $\gamma = \epsilon = 3/2$ and $\alpha = 1$. Only the NFW and Moore models are considered in this study. The two models predict large values of the neutralino density in the Galactic center (GC).

The parameters of the halo modeling are:

(i) R_0—distance from Earth to GC,

(ii) ρ_0—halo density at R_0,

(iii) a—the core radius—for $r < a$ the halo density is constant and equal to $\rho(a)$ in case of the isothermal parametrization.

As shown in [21], ρ_0 and a cannot be chosen arbitrarily. The total mass of the Galaxy restricts the (ρ_0, a) parameter space. For the NFW-*Standard* model the generic parameter values are: $R_0 = 8.0$ kpc, $\rho_0 = 0.3$ GeV/cm^3, $a = 20$ kpc. Another possible combinations of (ρ_0, a) parameters allow, given the uncertainties: $R_0 = 8.5$ kpc, $\rho_0 = 0.4$ GeV/cm^3, $a = 4$ kpc (NFW-*cuspy*). The two configurations were considered. The values for the Moore profile have been chosen as follows: $R_0 = 8.0$ kpc, $\rho_0 = 0.3$ GeV/cm^3, $a = 28$ kpc.

The WIMPs located around the Galactic center should annihilate and produce high-energy photons. The corresponding photon flux near the Earth, Φ_γ—per unit time, surface, and solid angle—may be expressed as

$$\Phi_\gamma = \frac{1}{4\pi}\frac{\langle\sigma v\rangle N_\gamma}{2m_{\rm wimp}^2}\int_{\rm los}\rho_{\rm wimp}^2(r)ds. \tag{2}$$

In Eq. (2), $m_{\rm wimp}$ is the mass of the WIMP-dark-matter candidate; $\langle\sigma v\rangle$ denotes the thermally averaged annihilation rate ; $\rho_{\rm wimp}(r)$ is the mass density of the dark matter and r is the distance from the Galactic center. The flux Φ_γ is proportional to the number of annihilations per unit time and volume, $\langle\sigma v\rangle\ \rho_{\rm wimp}^2(r)/m_{\rm wimp}^2$ and to the number of secondary photons per annihilation, N_γ. Finally to obtain the flux at the Earth it is necessary to integrate the WIMP density squared along the line-of-sight (los) connecting the observer to the Galactic center. The integral can be expressed in the form:

$$J(R) = 2\int_0^{\sqrt{R_0^2 - R^2}}\rho^2(\sqrt{s^2 + R^2})ds, \tag{3}$$

assuming a spherical halo with radial extension R_0. The coordinate s extends along the line-of-sight. R is the radial distance from the center of the Galaxy for such a direction.

Because the density decreases steeply at large distances (see Eq. (1)), a radial cutoff $R_{\rm c}$ has been applied. It has been checked that our results are not sensitive to the value of $R_{\rm c}$, which is set to 8.0 or 8.5 kpc depending on the chosen halo profile.

We integrate the function J over a solid angle around the Galactic center, subtended by the detector acceptance, e.g. a circular region with angular radius $\theta_{\rm obs}$:

$$\Sigma = 2\pi\int_0^{\theta_{\rm obs}} J(R)\sin\theta d\theta, \tag{4}$$

where $R/R_0 = \tan\theta \simeq \theta$. Thus the resulting value for I_γ—flux of high-energy photons collected per unit of time and surface—can be written as:

$$I_\gamma = (3.98 \times 10^{-18}\ \text{photons cm}^{-2}\,\text{s}^{-1})\left(\frac{\langle\sigma v\rangle N_\gamma}{10^{-29}\ \text{cm}^3\,\text{s}^{-1}}\right) \times \left(\frac{1\ \text{TeV}}{m_\chi}\right)^2 \Sigma_{19}, \quad (5)$$

where Σ_{19} denotes Σ expressed in units of 10^{19} GeV^2 cm^{-5} and integrated over the AMS acceptance, $\Delta\Omega = 10^{-3}$ sr. We have integrated the relation (4) as a function of galactic halo profiles leading to the following results:

(i) For a NFW-*standard* profile: $\Sigma_{19} = 2.7\ 10^2$, thus $\tilde{J}(0)(\Delta\Omega) = 1.2\ 10^3$
(ii) For a NFW-*cuspy* profile: $\Sigma_{19} = 117.7\ 10^2$, thus $\tilde{J}(0)(\Delta\Omega) = 50.0\ 10^3$
(iii) For a Moore profile: $\Sigma_{19} = 336.7\ 10^2$, thus $\tilde{J}(0) \times (\Delta\Omega) = 142.9\ 10^3$

where $\tilde{J}(0)(\Delta\Omega)$ corresponds to the notation used in [21]. For integration, we have defined an inner cutoff radius at $R_c = 10^{-5}$ pc such that for $R > R_c$ the flux vanishes.

For completeness, two astrophysical factors may enhance the expected gamma fluxes from neutralino annihilations:

(i) clumpiness of the dark matter halo as indicated by N-body simulations [7],
(ii) the presence of a supermassive black hole (SBH) with a mass of $\sim 2.6 \times 10^6 M_\odot$ creating unstable conditions due to baryon infall by the adiabatic compression process, studied by [22,23]

The overall enhancement factor of the expected flux is estimated in [24] to be between 5 and 100, depending on the clumpiness of the galactic halo. The enhancement of the annihilation signal in presence of a spike in the dark matter halo is significant with respect to ordinary dark matter cusp, even in case of gravitational scattering of stars and the self-annihilating dark matter particles, as pointed by [22,25,26].

B. Models for WIMP candidates

In this section, we describe briefly the physics models associated with selected dark matter candidates, including the methodology and assumptions used to investigate the different hypotheses.

1. mSUGRA parametrization

The two supersymmetric scenarios considered belong to the class of models where supersymmetry (SUSY) breaking is effectively communicated to the visible sector via (super)-gravitational effects. We use the conventional mSUGRA scenario [11] with common values for the soft supersymmetry breaking scalar and gaugino masses and trilinear couplings, m_0, $m_{1/2}$, A_0, taken as initial conditions at a given high energy universality scale. We require the three gauge couplings to take a common value at a unification scale M_{GUT} and, for simplicity, identify this scale with the universality scale of the soft SUSY parameters. With these initial conditions and with the value of $\tan\beta$ (the ratio of the two Higgs vacuum expectation values $\frac{\langle H_2^0\rangle}{\langle H_1^0\rangle}$) defined at the electroweak scale, the relevant low energy quantities are obtained throug the running of the parameters from M_{GUT} down to a scale of the order of the electroweak scale. Electroweak symmetry breaking is then required at that scale with the correct Z boson physical mass, thus fixing the supersymmetric μ parameter (up to a sign) and its soft supersymmetry breaking counterpart.

The flux predictions are obtained by use of computational tools which allow to scan over various SUSY parameters. This is achieved through an interface of the two codes, DarkSUSY [27] and SUSPECT [28], which we dub hereafter DSS (DarkSUSY-SUSPECT). Significant features of particle physics and cosmology are thus combined in our approach, taking into account various phenomenological constraints (consistency of the top, bottom and τ masses, present experimental limits on the superpartner and Higgs masses, limits from $b \to s\gamma$, no charged LSP, ..., relic density constraints), some of which are implemented in SUSPECT and others in DarkSUSY. We have checked in the mSUGRA framework the compatibility of the results obtained with the DSS software package and the ISASUGRA interface provided with DarkSUSY.

2. Anomaly mediated supersymmetry breaking parametrization

The anomaly mediated supersymmetry breaking (AMSB) is a gravity-mediated mechanism where the SUSY breaking is communicated to the observable sector by the super-Weyl anomaly [12,13]. In particular, the masses of gauginos are generated at the one-loop level as in [29]:

$$M_i = b_i\left(\frac{\alpha_i}{4\pi}\right)^2\langle M\rangle, \quad (6)$$

where α_i are the gauge coupling constants and b_i the associated β-function coefficients. M is the auxiliary field in the supergravity multiplet whose vacuum expectation value $\langle M\rangle$ is expected to be of the order of the gravitino mass $m_{3/2}$, the latter being generically in the range: $10\ \text{TeV} < m_{3/2} < 100\ \text{TeV}$.

In the minimal AMSB model, the sleptons suffer typically from a tachyonic problem. One way to fix this problem is to add a scalar mass parameter m_0^2, accounting for a nonanomalous contribution to the soft SUSY breaking.

The most important message from the gaugino mass formula above is the hierarchy:

$$M1{:}M2{:}M3 = 2.8{:}1{:}8.3$$

as opposed to $M1{:}M2{:}M3 = 1{:}2{:}7$ which is expected for the gravity- or gauge-mediated models. This implies that

the lightest neutralino ($\tilde{\chi}_1^0$) and the lightest chargino ($\tilde{\chi}_1^{\pm}$) are almost pure W-inos and consequently mass-degenerate.

3. Kaluza-Klein dark matter

Models with compact extra dimensions predict several new states, the Kaluza-Klein (KK) excitations. In the case of universal extra dimensions (UED) [16], all standard model fields can propagate in the bulk, and their effective four-dimensional interactions with the KK states conserve a quantum number associated with the latter. The conservation of this KK number implies that the KK modes cannot decay exclusively into standard model particles; the lightest KK mode (LKP) will thus be stable [16,30]. Moreover, the LKP, when electrically neutral and with no baryonic charge, provides a viable dark matter candidate [17]. The mass of the LKP dark matter particle, like all other states of the KK tower, is inversely proportional to the compactification radius R. Accelerator electroweak measurements constrain rather weakly the UED scenario, since in this scenario the observables are sensitive only to the virtual effects of the KK modes. The lower mass bound leads to $R^{-1} \geq 280$ GeV [16]. The most promising LKP dark matter candidate is associated with the first level of KK modes of the hypercharge gauge boson $B^{(1)}$. In our calculation we consider the relic density of $B^{(1)}$ of [17] leading to a $B^{(1)}$ lower bound mass bound constraint of 400 GeV.

III. AMS GAMMA DETECTION AND SENSITIVITY

A. The AMS-02 experiment

The main elements of AMS-02 detector [31] which are shown in Fig. 1 include: a superconducting magnet, a gaseous transition radiation detector (TRD), a silicon tracker (Tracker), time-of-flight hodoscopes (TOF), a ring imaging Cerenkov detector (RICH), an electromagnetic calorimeter (ECAL) and anticoincidence Veto counters. The superconducting magnet has the shape of a cylindrical shell with the inner diameter of 1.2 m and length of 0.8 m; it provides a central dipole field of 0.8 Tesla. The eight layers of double-sided silicon tracker sensors are placed in planes transverse to the magnet axis. The silicon tracker measures the trajectory of relativistic singly charged particles with an accuracy of 10μ in the bending and 30μ in the nonbending coordinates. It provides also measurements of the particle energy loss which allows to distinguish the charge. The time-of-flight system (TOF) containing four detection layers, measures singly charged-particle transit times with an accuracy of 140 psec and also yields energy loss and coordinate measurements. The transition radiation detector (TRD) is situated on the top of the spectrometer and consists of 20 12 mm thick foam radiator arrays, interleaved by arrays of 6 mm diameter gas proportional tubes filled with a Xe/CO_2 mixture. The TRD provides an e^-/hadron separation better than 100 up to an energy of 200 GeV as well as precise charged-particle coordinate measurements. The RICH detector is installed below the last TOF plane and consists of a 3 cm thick aerogel radiator with a refraction index of 1.05, a mirror and pixel type matrix photo-tubes for the light detection measures of the velocity of the single charged particle with an accuracy better than a fraction of a percent. The ECAL detector is situated at the bottom of the AMS-02 setup. It is a three-dimensional ($65x65x17$ cm^3 electromagnetic sampling calorimeter with total length of $16X_0$, consisting of 1 mm diameter scintillating fibers sandwiched between grooved lead plates.

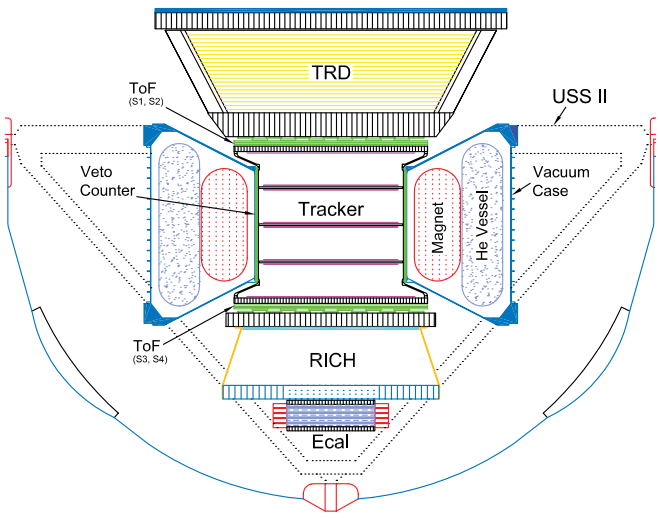

FIG. 1 (color online). Schematic view of the AMS-02 experiment which will operate on the International Space Station.

B. Performance of photon detection

Cosmic γ-rays may be detected in AMS by two different methods. The *conversion mode* involves the reconstruction in the tracker of the e^+e^- pairs produced by γ conversions in the material upstream of the first layer of silicon sensors [32–34]. In the *single photon mode*, the γ-rays are detected in the electromagnetic calorimeter [35].

The performance of AMS-02 detector for γ-rays has been studied with the AMS simulation and reconstruction program based on GEANT [36]. The simulated performances have been validated using the AMS-01 data for the subdetectors present during the shuttle test flight [37] and the test beam data obtained with prototypes of the new or modified modules.

The Monte Carlo sample for the present study includes more than 10^9 reconstructed events including both cosmic γ-rays and charged-particle backgrounds over the relevant energy range. The latter in order of decreasing importance include protons, He and C nuclei and electrons. With a charged-particle background rejection of O(10^4) to O(10^5), we obtain a background-to-signal ratio of the order of a few

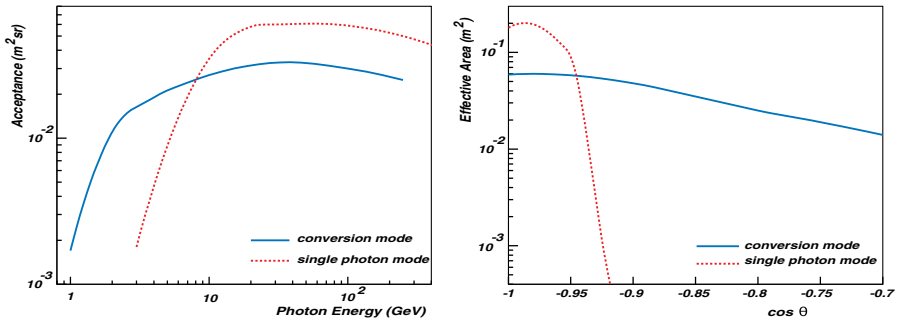

FIG. 2 (color online). AMS acceptance as a function of γ-ray energy for the two detection modes (top panel). The effective areas versus zenith angle at 50 GeV γ-ray energy (bottom panel).

percent. The principal background at this level is due to the galactic diffuse γ-ray emission.

1. The conversion mode

The event signature for this mode are two reconstructed tracks in the Tracker originating from a vertex located upstream of the first silicon layer of the tracker.[1]

The incident γ-ray energy and direction were determined by adding the reconstructed momenta components of the $e^{\pm}$ pair, evaluated at the entrance of the AMS-02 detector.

The main source of background are p and e^- which interact in the AMS detector, producing secondaries, mainly delta rays, which result in double-track events associated with a common origin at the interaction point.

The conversion of the secondary photons produced in the vicinity of the AMS, i.e. in the ISS body and solar panels, was found to be negligible in comparison to the expected γ-ray fluxes.

The following criteria are applied to reject background events:

(i) Identify events with interactions;
(ii) Identify charged particles entering the TRD from the top and fire all the tubes along its reconstructed trajectory.
(iii) Identify reconstructed large invariant mass events.
(iv) Identify particles entering the fiducial volume of the AMS through the side of the TRD).

A preliminary rejection factor of 5×10^4 was obtained for each different cosmic ray species (e^- and p), after all selection cuts have been applied.

2. The single photon mode

The event signature for this mode is the presence of electromagnetic-type energy deposition in the ECAL, while almost nothing is found in the other AMS subdetectors.

The identified backgrounds contributing to the cosmic γ-ray signal are events with charged particles[2] either passing undetected in the gaps of the AMS active tracking volume or entering the ECAL from the side.

The following criteria are applied to reject the background events:

(i) Identify p, He by analyzing the 3-dimensional shower development in ECAL;
(ii) Identify charged particles by requiring the trajectory direction of the reconstructed ECAL shower passes inside the AMS sensitive volume and reject these events.

The rejection factors for different cosmic ray species after all cuts have been applied are : $>6 \times 10^4$ for $e^{\pm}$, $(2.5 \pm 1) \times 10^6$ for p and $>1.7 \times 10^6$ for He nuclei.

3. Acceptances and resolutions

The simulations are used to parameterize the AMS performance for γ detection in terms of acceptance, effective area, angular and energy resolutions, and background rejection. Figure 2 shows the acceptance and effective area for the two detection modes. The corresponding energy and angular resolutions are shown in Fig. 3.[3]

The parameterized performance is used to establish the AMS-02 sensitivity for the different scenarios in which high-energy γ-rays are produced by the annihilation of dark matter near the Galactic center. In a first approximation, we consider a γ-ray source located at galactic longitude $l = 0$ and galactic latitude $b = 0$.

C. The sensitivity to the gamma flux and confidence level determination

We have developed a ROOT-based [39] simulation program, the AMS-γ fast simulator (AMSFS) [40], in order to investigate the AMS capability to localize nonisotropic radiation, either pointlike or diffuse. Here we describe the computational approach implemented in the simulator.

[1]The material in front of the first silicon tracker plane, consists of the TRD, the first two layers of TOF scintillators, and mechanical supports, represents $\simeq 0.23X_0$.

[2]mostly e^-, p and He nuclei

[3]We have chosen a conservative estimate of the single photon mode acceptance; a second study reports a 50% higher acceptance [38].

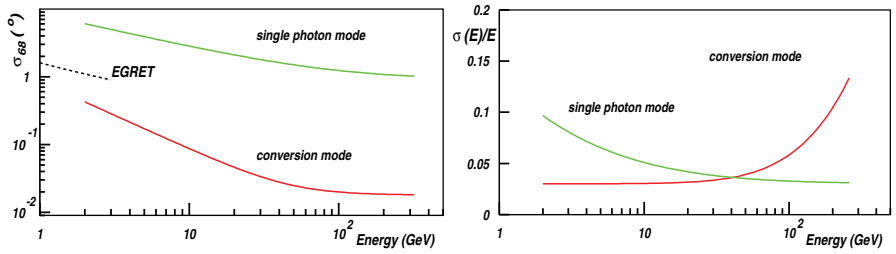

FIG. 3 (color online). The 68% containment angular resolution for both complementary detection modes as a function of energy (top panel). Energy resolutions as a function of original γ-ray energy (bottom panel).

We define the detector's γ-ray source sensitivity as the minimum flux required to achieve a specified level of detection significance. The significance S of a detection is given by:

$$S(E_\gamma > E_t) \sim \frac{N_\gamma^{\rm obs}(E_\gamma > E_t)}{\sqrt{B(E_\gamma > E_t)}}, \tag{7}$$

where $N_\gamma^{\rm obs}(E_\gamma > E_t)$ and $B(E_\gamma > E_t)$ are, respectively, the total number of detected photons from the source and the number of background photons falling within the source area above an energy threshold E_t. $N_\gamma^{\rm obs}$ and B are functions of the effective detection area $A(E)$ of the instrument, the angular resolution expressed in terms of the solid angle $\Omega(E)$, the observation time $T_{\rm obs}$ and the differential spectra:

$$N_\gamma^{\rm obs}(E_\gamma > E_t) = \int_{E_t}^{\infty} \int_\Omega \frac{dN_\gamma}{dEd\Omega} A(E) T_{\rm obs} d\Omega(E) dE, \tag{8}$$

and

$$B(E_\gamma > E_t) = \int_{E_t}^{\infty} \int_\Omega \frac{dB}{dEd\Omega} A(E) T_{\rm obs} d\Omega(E) dE. \tag{9}$$

In order to establish the significance level of the observation, we require a minimum of three detected gamma events.

We use the analytical expressions resulting from the best fit to the curves shown in Figs. 2 and 3 for the energy dependence of the acceptance, the angular and energy resolutions. The solid angle over which the background is integrated for a given source is $\Omega(E) = \pi\sigma_{68}^2(E)$, where σ_{68} is the detector angular resolution defined within which 68% of the source photons fall.

The calculation of the Galactic center observation time $T_{\rm obs}$ is based on a 3-year misssion on the international space station (ISS) [41]. The AMS observation time is not uniformly distributed over the celestial sphere since the ISS is in a 51.6° orbit, and the detector is fixed rigidly to the ISS. Taking into account the precession of the orbital plane of the station about the Earth's pole, a full sky coverage is obtained about 5.3 times per year. The *exposure* (effective area × the observation time) varies with the photon energy due to the energy dependence the effective area, and the position in the sky, due to the orbit precession.

The dependence of the effective area on the inclination of the photon direction (θ), the time $dT_{\rm obs}$ spent by the detector viewing the Galactic center within a specific viewing inclination $d\theta$, has been calculated and then integrated over the field-of-view (θ range up to 42° for the conversion mode and 22° for the single photon mode) and convoluted with the corresponding effective area: $A(E, d\theta) \times dT_{\rm obs}$. The time intervals when ISS orbits over the South Atlantic anomaly region are excluded.

The source spectrum $dN_\gamma/dEd\Omega$ in Eq. (8) corresponds to the photon differential spectrum of the dark matter annihilation calculation incorporating the halo profile model and the choice of the particle physics parameters, including the mass of the WIMP candidate. The background flux $dB/dEd\Omega$ corresponds to the isotropic extra-galactic γ-ray background radiation and the galactic diffuse radiation (the latter is due mainly to the decay of π^0s produced by interactions of the cosmic rays with the interstellar medium). The extra-galactic component has been measured by EGRET to be [42]:

$$\frac{dB_{\rm extragal.}}{dEd\Omega} = \Phi_0 \times \left(\frac{E}{k_0}\right)^{\epsilon} ({\rm cm^2\,s\,sr\,GeV})^{-1}, \tag{10}$$

where $\Phi_0 = (7.32 \pm 0.34) \times 10^{-6}$ $({\rm cm^2\,s\,sr\,GeV})^{-1}$, $k_0 = 0.451$ GeV and $\epsilon = -2.10 \pm 0.03$.

The galactic diffuse flux is enhanced toward the galactic center and the galactic disk as measured by EGRET. In our calculation we use the parametrization of the differential flux provided in [21]:

$$\frac{dB_{\rm gal.}}{dEd\Omega} = \Gamma_0 \times \left(\frac{E}{r_0}\right)^{\alpha} ({\rm cm^2\,s\,sr\,GeV})^{-1}, \tag{11}$$

where $\Gamma_0 = 8.6 \times 10^{-5}$ $({\rm cm^2\,s\,sr\,GeV})^{-1}$, $r_0 = 1$ GeV and $\alpha = -2.7$.

Finally, the Galactic center point sensitivity has to take into account the profile of the energy spectrum of the photons produced as a function of the neutralino mass m_χ. For this purpose we define the following function:

$$\Lambda(m_\chi) = \frac{\int_{E_t}^{\infty} \frac{d\Phi}{dE} A(E) dE}{\int_{E_t}^{\infty} \frac{d\Phi}{dE} dE}. \tag{12}$$

$\Lambda(m_\chi)$ includes the weight of the detector acceptance $A(E)$ on the total rate of photons expected to be detected for a given differential flux

$$\frac{d\Phi}{dE} = \frac{1}{4\pi}\frac{dN_\gamma}{dE}\frac{\langle\sigma v\rangle}{2m_\chi^2}\Sigma_{19}. \tag{13}$$

Therefore we can rewrite the function Λ as

$$\Lambda(m_\chi) = \frac{\int_{E_t}^{\infty}\frac{dN_\gamma}{dE}A(E)dE}{\int_{E_t}^{\infty}\frac{dN_\gamma}{dE}dE}, \tag{14}$$

where

$$\int_{E_t}^{\infty}\frac{dN_\gamma}{dE}dE = N_\gamma(E_\gamma \geq E_t) \tag{15}$$

is the total number of continuum γ-rays above energy E_t mainly due to the decay of π^0 mesons produced in jets from neutralino annihilation. For the computation of N_γ we have considered the parametrization from Ref. [43], after checking its compatibility with PYTHIA parametrization included in DSS as explained in the caption of Fig. 4:

$$N_\gamma(E_\gamma \geq E_t) = \frac{5}{6}\left(\frac{E_t}{m_\chi}\right)^{3/2} - \frac{10}{3}\frac{E_t}{m_\chi} + 5\left(\frac{E_t}{m_\chi}\right)^{1/2} + \frac{5}{6}\left(\frac{E_t}{m_\chi}\right)^{-1/2} - \frac{10}{3}. \tag{16}$$

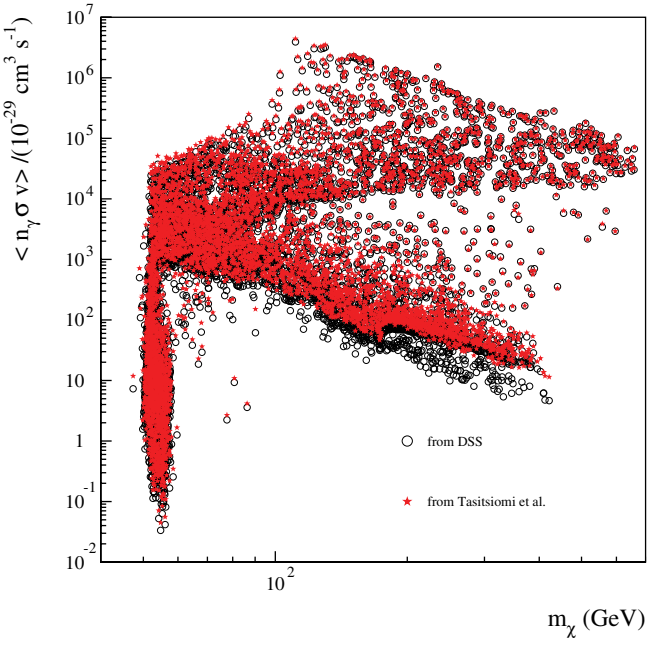

FIG. 4 (color online). The $\langle N_\gamma\sigma v\rangle$ as a function of m_χ with standard set of parameters as compared with parametrization [43]. A threshold $E_t = 1$ GeV has been assumed. A normalization factor of 2.4 was applied to obtain compatibility between the two calculations. This factor is used in our calculations.

The differential continuum spectrum, assuming $N_\gamma(E_t = m_\chi) = 0$, is:

$$\frac{dN_\gamma}{dE} = \frac{1}{m_\chi}\left(\frac{10}{3} + \frac{5}{12}\left(\frac{E}{m_\chi}\right)^{-3/2} - \frac{5}{4}\left(\frac{E}{m_\chi}\right)^{1/2} - \frac{5}{2}\left(\frac{E}{m_\chi}\right)^{-1/2}\right). \tag{17}$$

With formulas (16) and (17) we can compute the function $\Lambda(m_\chi)$ for a given value of the neutralino mass m_χ:

$$\Lambda(m_\chi) = \frac{1}{N_\gamma}\int_{E_t}^{\infty}\frac{dN_\gamma}{dE}A(E)dE \tag{18}$$

and obtain the corresponding confidence level.

The total number of photons detected by AMS is defined as

$$N_\gamma^{\rm obs}(E_\gamma > E_t) = T_{\rm obs}\int_{E_t}^{\infty}\frac{d\Phi}{dE}A(E)dE. \tag{19}$$

or, using the $\Lambda(m_\chi)$ function

$$N_\gamma^{\rm obs}(E_\gamma > E_t) = T_{\rm obs}\Lambda(m_\chi)\int_{E_t}^{\infty}\frac{d\Phi}{dE}dE. \tag{20}$$

According to the detectability criterion defined in Eq. (7), the minimum detectable flux $F_{\rm min}$, which corresponds to a significance $S(E_\gamma > E_t) = 3$, is derived by requiring $N\gamma^{\rm obs} = 3\sqrt{B}$. The definition of:

$$\Phi_{95} = \int_{E_t}^{\infty}\frac{d\Phi_{\rm min}}{dE}dE = \frac{3\sqrt{B(E_\gamma > E_t)}}{\Lambda(m_\chi)T_{\rm obs}} \tag{21}$$

leads to conservative 95%–99% Confidence Level values.

IV. RESULTS

A. mSUGRA and benchmark point simulations

The DSS program provides values of the γ-ray fluxes for the SUSY benchmark models [44,45] and the so-called "wild scan" configurations of the mSUGRA parameters.

The SUSY benchmark models have been proposed to provide a common way of comparing the SUSY discovery potential of the future accelerators such as LHC or linear colliders. The 13 SUSY scenarios correspond to different configurations of the five mSUGRA parameters with the trilinear coupling parameter A_0 set to 0. The models fulfill the conditions imposed by LEP measurements, the $g_\mu - 2$ result, and the relic density constraint of $0.094 < \Omega_\chi h^2 < 0.129$.

To derive the gamma-ray fluxes for some of these benchmark models we use our current MC simulation programs: DSS, which was described previously. In particular the value of $\Omega_\chi h^2$ is calculated in the DarkSUSY part, while the simultaneous use of the SUSPECT and DarkSUSY

TABLE I. The lightest neutralino mass m_χ, the mSUGRA parameters m_0, $\tan\beta$, the relic neutralino densities, i.e. $\Omega_\chi h^2$ and the values $\langle N_\gamma \sigma v\rangle$ as described in the text in units of 10^{-29} cm^3 s^{-1}; (masses are in GeV and the stars indicate values from [46]).

model	B	G	I	K	L
M_χ	98.3	153.6	143.0	571.5	187.2
m_0	59	116	178	999	299
$\tan\beta$	10.0	20.0	35.0	38.2	47.0
$\Omega_\chi h^2$	0.12	0.12	0.12	0.11	0.10
$\Omega_\chi h^{2*}$	0.12	0.13	0.13	0.09	0.10
$\langle n_\gamma \sigma v\rangle$	1013	1283	8380	29344	33438
$\langle n_\gamma \sigma v\rangle^*$	782	1032	6303	70903	18739

package allows to perform Renormalization Group Equations evolution from the GUT scale to EWSB scale.

Table I presents values of the lightest neutralino mass m_χ, the mSUGRA parameters m_0, $\tan\beta$, the neutralino relic density $\Omega_\chi h^2$ and the values $\langle N_\gamma \sigma v\rangle$ as described in Sec. III.

The corresponding values of neutralino mass, $\tan\beta$ and m_0 are also quoted. A fine-tuning procedure has been applied as in [44] (to fulfill the relic density constraints). The N_γ were obtained with fast simulation by the convolution of the differential γ-ray fluxes with angular and energy resolution, and applying the acceptance factors of the tracker (TR) and calorimeter (ECAL).

The choice of the benchmark model sample was guided by the requirement of meaningful flux values. These values are low, however, in more favorable astrophysical scenarios, the expected N_γ are enhanced by substantial factors varying from 40 in case of the most cuspy NFW halo profile or about a hundred in case of a Moore profile.

The results in Table I are also compared to those in [46], where a different mSUGRA Monte Carlo was used. Good agreement was found between the results of the two calculations. The observed differences for $\langle N_\gamma \sigma v\rangle$, which are at most ~25% between our results and those in [46], may be explained by more refined interfacing.

In Table II, N_γ detected by AMS during 3-year observation and the significance values for the benchmark models are presented for the NFW halo profile with the standard set of parameter, the most cuspy NFW profile and the Moore profile. The diffuse γ-ray background has been evaluated with the procedure described in Sec. III. The hadron contribution can be considered negligible for a pointlike source, as the proton suppression factors range between 10^{-5} and 10^{-6}. For the standard NFW profile, only the values of the signal-to-background ratio are given as the expected N_γ values are not significant.

TABLE II. The expected number of photons detected in 3 years for different benchmark models and various dark matter halo profiles. Since the benchmark model flux values are low in the scanned (Φ_γ, m_χ) plane, a 3 GeV energy cut threshold has been applied for signal and diffuse gamma background calculations. The sensitivities (N_σ = number of standard deviations above diffuse gamma emission) have been calculated only for photons detected in the tracker assuming 3.0 background photons. In the ECAL detector, we expect 196.0 photons for the galactic diffuse gamma emission.

model	B	G	I	K	L
$N_{\gamma\text{std}}{}^{\text{NFW}}$	0.22	0.14	0.94	0.35	2.48
$N_{\gamma\text{cuspy}}{}^{\text{NFW}}$	9.2	6.0.	40.8	15.2	107.8
N_γ^{Moore}	26.4	17.1	117.3	43.7	309.9
$S/B_{\text{std}}^{\text{NFW}}$	0.04	0.03	0.18	0.06	0.45
$N_{\sigma\text{cuspy}}{}^{\text{NFW}}$	3.2	1.9	13.8	4.7	35.8
N_σ^{Moore}	8.9	5.7	39.6	13.5	102.8

B. Predictions from "wild scan" simulations

1. mSUGRA results

We have performed a "wild scan" in the mSUGRA parameter space. Six thousand models have been simulated in the region of $0.0 \lesssim \Omega_\chi h^2 \lesssim 0.129$. The values below the WMAP lower constraint on $\Omega_\chi h^2$ (0.094) belong to the additional nonthermal neutralino production scenarios.

The ranges of the mSUGRA parameters used in the simulation were:

$$\begin{aligned}
&\text{sign}(\mu)\text{not constraint}\\
&50. < m_0 < 3000.\\
&50. < m_{1/2} < 1600.\\
&0.1 < |A_0| < 2000.\\
&3. < \tan(\beta) < 60.
\end{aligned}$$

The results for the integrated gamma fluxes from the Galactic center as a function of the χ_1^0 mass, presented in Fig. 5, were obtained for a NFW-*standard* profile, and for a γ-ray energy threshold of $E_t = 1$ GeV. Figure 6 shows the results for the more favorable NFW cuspy dark matter profile.

2. AMSB results

For the prediction of the gamma-ray flux in the AMSB framework, the scheme proposed by SUSPECT was used for the evolution of the AMSB parameters up to the EWSB, as for our mSUGRA simulations. Therefore we use the same DSS interface.

The constraints set on the four AMSB parameters (as described in [46]) were:

$$\begin{aligned}
&\text{sign}(\mu)\text{not constraint}\\
&10^4 < M_{3/2} < 10^6.\\
&10^3 < a_0 < 15 \cdot 10^3\\
&3. < \tan(\beta) < 60.
\end{aligned}$$

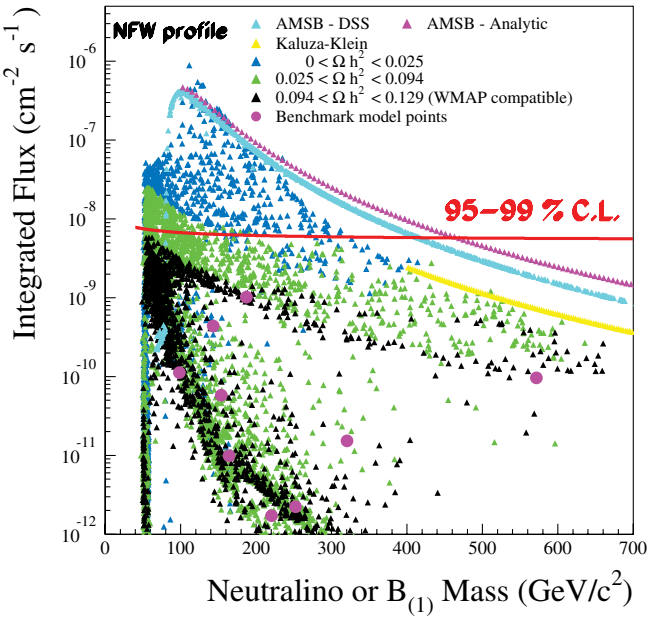

FIG. 5 (color online). The integrated γ flux from the Galactic center as a function of m_χ for the NFW halo profile parametrizations with the standard set of parameters. The considered models are the mSUGRA scheme, AMSB scenario and Kaluza-Klein universal extra-dimensions. The various selections were done by varying Ωh^2 cuts.

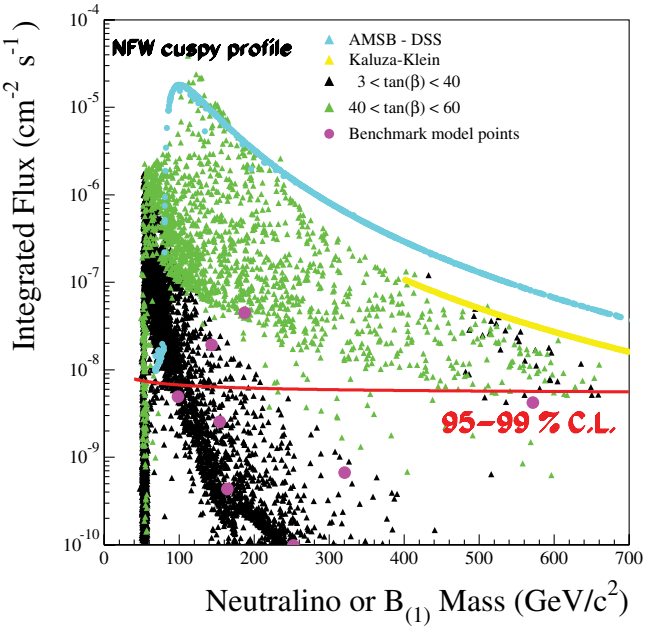

FIG. 6 (color online). The integrated γ flux from the Galactic center as a function of m_χ for a cuspy NFW dark matter halo profile as described in the text. The considered models are the mSUGRA scheme, AMSB scenario and Kaluza-Klein universal extra dimensions. The various selections were done by varying $\tan(\beta)$ cuts.

For completeness, we have checked that this approach was compatible with the analytical approximation as described below.

From Eq. (2) we get:

$$\Phi_\gamma(\Delta\Omega, E_\gamma > E_t) = 1.19\ 10^{-14} N_\gamma \left(\frac{\langle\sigma\beta\rangle}{pb}\right) \times \left(\frac{1\ \mathrm{TeV}}{m_\chi}\right)^2 \Sigma_{19}\ \mathrm{cm}^{-2}\,\mathrm{s}^{-1}, \quad (22)$$

and under the hypothesis of a pure W-ino LSP, the pair annihilation proceeds by exchange of a charged W-ino. The neutral W-ino, here assumed to be the WIMP-LSP, can annihilate into a W-boson pair ($\tilde{W}^0\,\tilde{W}^0 \to W^+W^-$). We have considered the results of [29] for the parametrization of the corresponding annihilation cross section, in the nonrelativistic limit:

$$\langle\sigma\beta\rangle = 9.77\left(\frac{1\ \mathrm{TeV}}{m_\chi}\right)^2 \frac{(1-x_W)^{3/2}}{(2-x_W)^2}\, pb, \quad (23)$$

where $x_W = m_W^2/m_\chi^2$.

Thus the equation for the integral flux of photons from W-ino LSP annihilation becomes:

$$\Phi_\gamma(\Delta\Omega, E_\gamma > E_t) = 1.16\ 10^{-13} N_\gamma \frac{(1-x_W)^{3/2}}{(2-x_W)^2} \times \left(\frac{\mathrm{TeV}}{m_\chi}\right)^4 \Sigma_{19}\ \mathrm{cm}^{-2}\,\mathrm{s}^{-1}, \quad (24)$$

where we have used Eq. (17) for the N_γ value with the scaling factor as described in the caption of Fig. 4.

C. Kaluza-Klein results

The main annihilation channels of LKP into standard model particles are charged lepton pairs for about 59% and quark pairs for about 35% [47]. In our case, the calculation of secondary gamma-ray yield were based on the formulas of $\sigma v(B^{(1)}B^{(1)} \to f\bar{f})$ [17]. The contribution of gamma rays produced from channels with leptons [48] has been neglected, thus providing more conservative results for the gamma fluxes at high energies. As in our previous calculations and following [47] we have used Eq. (25) with again the N_γ value from Eq. (17). To obtain the flux for a given halo profile, we have used the corresponding value of Σ_{19} given in the paragraph 2.1, thus resulting in:

$$\Phi_\gamma(\Delta\Omega, E_\gamma > E_t) = 7.2\ 10^{-15} N_\gamma \left(\frac{1\ \mathrm{TeV}}{m}\right)^4 \times \Sigma_{19}\ \mathrm{cm}^{-2}\,\mathrm{s}^{-1} \quad (25)$$

We checked that our results are compatible with [6]. The expected γ fluxes for the AMSB models and Kaluza-Klein models are also shown in Figs. 5 and 6.

D. Sensitivity for considered models

The 95% CL was obtained by varying, within the uncertainties, the diffuse γ background spectrum as measured by EGRET [49] in the Galactic center area, as described in Sec. III C. With a required minimum of 3 photons over 3σ of the diffuse gamma background and a 1 GeV energy threshold and 3 yr exposure time, the sensitivity to Galactic Center measurements is $(7.0 \pm 0.4)10^{-9}$ cm^{-2} s^{-1} with only a small residual dependence on m_χ. For both sets of astrophysical conditions, the predicted γ fluxes for the AMSB and Kaluza-Klein models are above the 95% CL for WIMP masses below 400 GeV. This indicates the potential of detection or exclusion of AMS-02 in the case of the less conventional SUSY scenario with nonthermal production of neutralinos, or other dark matter candidate proposed by the Kaluza-Klein extra-dimension theories.

It has been recently shown [50] that residual dark matter annihilation during the epoch of big bang nucleosynthesis may result in an efficient production of ^{6}Li. In Fig. 7 we show the resulting ^{6}Li/H ratio in the dark matter models studied in this paper. The ^{6}Li/H yields have been calculated using the parametrizations given in Ref. [50]. The predicted abundances are compared to the value reported for the low-metallicity halo stars, such as HD84937, $^6\mathrm{Li/H} \approx 8.47 \pm 3.10 \times 10^{-12}$ [51], (one of the first stars where a ^{6}Li detection had been claimed). It is seen that, even in a context of a standard NFW profile (Fig. 5), the observed ^{6}Li abundance is consistent with values produced

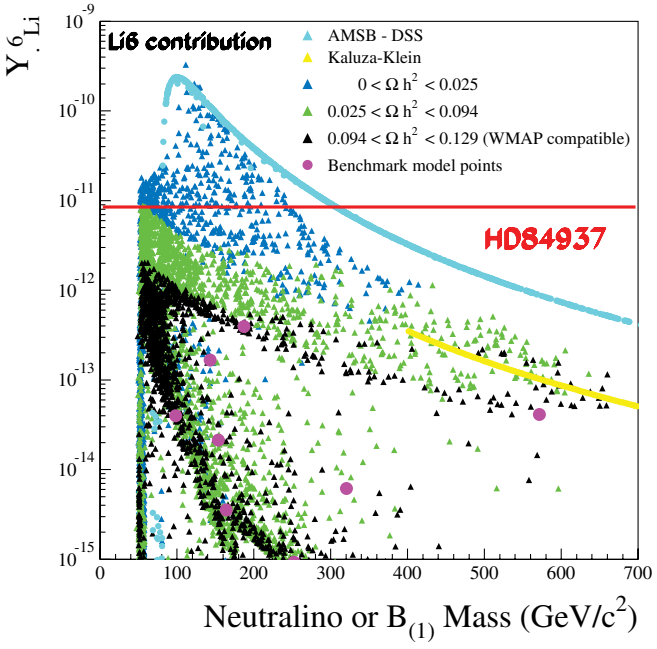

FIG. 7 (color online). The resulting ^{6}Li/H yield synthesized due to residual neutralino/Kaluza-Klein annihilation during the epoch of big bang nucleosynthesis for the same models as considered before. Also shown is the central value of the ^{6}Li/H as observed in the low-metallicity star HD84937.

with certain model configurations, in particular, in nonthermal scenarios for the AMSB model. Detections of ^{6}Li have been reported for ~10 other stars [52,53], with abundances comparable to HD84937. As this is far from what expected in cosmic ray scenarios which may synthesize ^{6}Li, it is possible that the ^{6}Li abundance in low-metallicity stars is in fact an indirect signal of dark matter annihilation during big bang nucleosynthesis.

V. CONCLUSIONS

The DarkSUSY and SUSPECT programs were used to provide the γ-ray flux predictions from the Galactic center region, for the benchmark mSUGRA models, the AMSB scenario and Kaluza-Klein Universal Extra-dimensions models, in order to evaluate the discovery potential of AMS for nonbaryonic dark matter. Only models of mSUGRA scenario with large tanβ yield measurable signals on a realistic time scale. This conclusion is confirmed in a second study with a "wild scan" mSUGRA simulations. Various aspects such as dependence of the results on heavy quark masses or *CP*-odd Higgs pole contributions may change the predictions [24]. The most significant signals correspond to the supersymmetric configurations with the neutralino mass $m_\chi \sim 100$ GeV.

The sensitivity of the AMS-02 detector for γ-ray fluxes from a pointlike source will allow to detect fluxes smaller by a factor of 2 to 3, compared to those measured by EGRET experiment in the GeV range, in the Galactic center region [49]. AMS mission will also extend these measuremnets to a poorly explored energy range around 10 GeV, important for the detection of a low mass neutralino. In the TeV range, the Galactic center was observed by ground-based Air Shower Cherenkov Telescopes (ACTs), which have detected several intensive astrophysical sources [54,55]. The signal from the central source, as observed by different ACT experiments, has been analyzed in the context of SUSY dark matter by [56]. More recently, the HESS Collaboration has published a discovery of a diffuse γ emission in the galactic plane in TeV range, nearby the SgrA* emitter, possibly produced by the hadronic interactions of the Galactic cosmic rays with a complex of molecular clouds [57]. These results indicate that the choice of the observed dark matter source is crucial, and the intense astrophysical environment may be an obstacle for an exotic signal detection. A more promising type of dark matter source could be a nearby Dwarf Spheroidal Galaxy such as DRACO, Sagittarius or Canis Major, presenting lower standard astrophysical backgrounds. These sources have been considered by several authors for the SUSY dark matter flux predictions [58,59], and their observation campains have been scheduled by ACT telescope experiments in the coming future.

In the frame of the present study with the Galactic center source, the 3 yr observation with AMS detector would provide 95% CL exclusion limits for several mSUGRA

models in the case of a favorable dark matter galactic halo configuration, such as the cuspy or very cuspy NFW profiles. Furthermore, if the halo is made of clumps with inner profiles of cuspy type, or if there is a strong accretion around the central black hole, the expected signal would increase by 2 orders of magnitude. For such cases, given the excellent energy resolution of the detector, the discovery of a dark matter annihilation signal would be possible. In particular, the nonthermal SUSY Breaking scenarios, as in case of the AMSB model, result in cosmologically significant ^{6}Li abundances, which, when confronted with the results for ^{6}Li abundances in low-metallicity stars offer interesting perspectives for indirect dark matter searches and the detection of an annihilation signal by AMS. We conclude, that a survey of the Galactic center by AMS has the potential to contribute significantly to our understanding of dark matter.

ACKNOWLEDGMENTS

We thank all our colleagues from AMS for expressing their support and interest in this study.

[1] N. Bahcall and X. Fan, Astrophys. J. **504**, 1 (1998).
[2] N. Dalal and C. R. Keeton, astro-ph/0312072.
[3] M. Azzaro, F. Prada, and C. M. Gutierrez, astro-ph/0310487.
[4] D. Zaritsky *et al.*, Astrophys. J. Suppl. Ser. **478**, 39 (1997).
[5] C. L. Bennett *et al.* Astrophys. J. Suppl. Ser. **148**, 1 (2003).
[6] G. Bertone, D. Hooper, and J. Silk, Phys. Rep. **405**, 279 (2005).
[7] J. R. Primack, Proceedings of International School of Space Science 2001, edited by Aldo Morselli, Frascati Physics Series (to be published).
[8] G. Jungman, M. Kamionkowski, and K. Griest, Phys. Rep. **267**, 195 (1996).
[9] L. Bergstrom, Rep. Prog. Phys. **63**, 793 (2000).
[10] H. Goldberg, Phys. Rev. Lett. **50**, 1419 (1983); J. Ellis *et al.*, Phys. Lett. B **127**, 233 (1983).
[11] R. Barbieri, S. Ferrara, and C. A. Savoy, Phys. Lett. B **119**, 343 (1982); A. H. Chamseddine, A. Arnowitt, and P. Nath, Phys. Rev. Lett. **49**, 970 (1982); L. J. Hall, J. Lykken, and S. Weinberg, Phys. Rev. D **27**, 2359 (1983); N. Ohta, Prog. Theor. Phys. **70**, 542 (1983).
[12] L. Randall and R. Sundrum, Nucl. Phys. **B557**, 79 (1999).
[13] G. Giudice *et al.*, J. High Energy Phys. 12 (1998) 027.
[14] D. Hooper and L. Wang, Phys. Rev. D **69**, 035001 (2004).
[15] E. W. Kolb and R. Slansky, Phys. Lett. B **135**, 378 (1984).
[16] T. Appelquist, H. C. Cheng, and B. A. Dobrescu, Phys. Rev. D **64**, 035002 (2001).
[17] G. Servant, and T. M. P. Tait, Nucl. Phys. **B650**, 391 (2003).
[18] G. Gentile *et al.*, Mon. Not. R. Astron. Soc. **351**, 903 (2004).
[19] J. F. Navarro, C. S. Frenk, and S. D. M. White, Astrophys. J. **462**, 563 (1996).
[20] B. Moore *et al.*, Phys. Rev. D **64**, 063508 (2001).
[21] L. Bergstrom, P. Ullio, and J. H. Buckley, Astropart. Phys. **9**, 137 (1998).
[22] G. Bertone and D. Merritt, Phys. Rev. D **72**, 103502 (2005).
[23] P. Gondolo and J. Silk, Phys. Rev. Lett. **83**, 1719 (1999).
[24] A. Falvard *et al.*, Astropart. Phys. **20**, 467 (2004).
[25] P. Ullio, H. S. Zhao, and M. Kamionkowski, Phys. Rev. D **64**, 043504 (2001).
[26] J. Edsjo *et al.*, J. Cosmol. Astropart. Phys. 09 (2004) 004.
[27] http://www.physto.se/~edsjo/darksusy/.
[28] A. Djouadi, J.-L. Kneur, and G. Moultaka, hep-ph/0211331.
[29] T. Moroi and L. Randall, Nucl. Phys. **B570**, 455 (2000).
[30] T. G. Rizzo, Phys. Rev. D **64**, 095010 (2001); C. Macesanu, C. D. McMullen, and S. Nandi, Phys. Rev. D **66**, 015009 (2002); H. C. Cheng, K. T. Matchev, and M. Schmaltz, Phys. Rev. D **66**, 036005 (2002).
[31] AMS Collaboration, Nucl. Instrum. Methods, (to be published).
[32] R. Battiston *et al.*, Astropart. Phys. **13**, 51 (2000).
[33] G. Lamanna, Nucl. Phys. B, Proc. Suppl. **113**, 177 (2002).
[34] G. Lamanna, AMS-Note 2003-03-03.
[35] V. Choutko, G. Lamanna, and A. Malinin, Int. J. Mod. Phys. A **17**, 1817 (2002).
[36] S. Agostinelli *et al.* (Geant4 collaboration), NIM A **506**, 250 (2003).
[37] M. Aguilar *et al.*, Phys. Rep. **366**, 331 (2002).
[38] L. Girard, Proceedings to Moriond—Astroparticle 2005 and references therein.
[39] http://root.cern.ch.
[40] J. Bolmont, Ph.D. thesis, Univ. Montoellier II, 2005.
[41] I. Sevilla Noarbe, AMS-Note 2004-03-03.
[42] P. Sreekumar *et al.*, Astrophys. J. **494**, 523 (1998).
[43] A. Tasitsiomi and A. V. Olinto, Phys. Rev. D **66**, 083006 (2002).
[44] M. Battaglia *et al.*, Eur. Phys. J. C **24**, 311 (2002).
[45] J. Ellis *et al.*, Eur. Phys. J. C **24**, 311 (2002).
[46] P. Gondolo *et al.*, J. Cosmol. Astropart. Phys. 07 (2004) 008.
[47] G. Bertone, G. Servant, and G. Sigl, Phys. Rev. D **68**, 044008 (2003).
[48] L. Bergstrom, *et al.*, Phys. Rev. Lett. **94**, 131301 (2005).
[49] S. D. Hunter *et al.*, Astrophys. J. **481**, 205 (1997).
[50] K. Jedamzik, Phys. Rev. D **70**, 063524 (2004); **70**, 083510 (2004).
[51] R. Cayrel *et al.*, Astron. Astrophys. **343**, 923 (1999).
[52] P. E. Nissen *et al.*, astro-ph/0004251.
[53] P. E. Nissen *et al.*, Astron. Astrophys. **348**, 211 (1999).
[54] F. Aharonian *et al.* (HESS Collaboration), Astron. Astrophys. **425**, L13 (2004); L. Rolland and J. Hinton (HESS collaboration), Proceedings of ICRC conference, Pune, India (2005).

[55] M. Mori (CANGAROO collaboration), Proceedings of 28th ICRC conference (2003), vol. 5.
[56] S. Profumo, Phys. Rev. D **72**, 103521 (2005).
[57] F. Aharonian *et al.* (HESS collaboration), Nature (London) **439**, 695 (2006).
[58] N. W. Evans, F. Ferrer, and S. Sarkar, Phys. Rev. D **69**, 123501 (2004).
[59] D. Hooper *et al.*, Phys. Rev. Lett. **93**, 161302 (2004).

INSTITUTE OF PHYSICS PUBLISHING REPORTS ON PROGRESS IN PHYSICS

Rep. Prog. Phys. **69** (2006) 2475–2512 doi:10.1088/0034-4885/69/8/R05

Indirect detection of dark matter

J Carr, G Lamanna and J Lavalle

Centre de Physique des Particules de Marseille, UMR/IN2P3-CNRS, 163 avenue de Luminy - Case 902, 13288 Marseille, France

Received 13 April 2006, in final form 26 June 2006
Published 25 July 2006
Online at stacks.iop.org/RoPP/69/2475

Abstract

This article is an experimental review of the status and prospects of indirect searches for dark matter. Experiments observe secondary particles such as positrons, antiprotons, antideuterons, gamma-rays and neutrinos which could originate from annihilations of dark matter particles in various locations in the galaxy. Data exist from some experiments which have been interpreted as hints of evidence for dark matter. These data and their interpretations are reviewed together with the new experiments which are planned to resolve the puzzles and make new measurements which could give unambiguous results.

(Some figures in this article are in colour only in the electronic version)

This article was invited by Professor J Silk.

Contents

1. Introduction

The existence of dark matter in the universe was first proposed by Zwicky in the 1930s to explain the dynamics of clusters of galaxies where the observable luminous matter was insufficient to provide gravitational stability. The presence of dark matter in galaxy clusters has been confirmed by more recent studies including gravitational lensing and inside galaxies dark matter is required to explain the rotation curves measured for many, including the Milky Way.

Numerous observational cosmology experiments now combine to give the standard picture of the composition of matter/energy in the universe as 72% dark energy, 23% non-baryonic dark matter, 4% baryonic dark matter, 1% normal matter in luminous star systems and a small fraction of radiation in various forms. The limited amount of 'normal' matter in the form of luminous stars and baryonic dark matter is given in independent ways from the predictions of nucleo-synthesis and the measurements of the spectrum of fluctuation of the cosmic microwave background. The total amount of matter, baryonic plus non-baryonic comes, again, from two independent sets of measurements: in galaxy clusters and on the cosmic microwave background. It is simulations of structure formation which indicate that the non-baryonic dark matter is 'cold' rather than 'hot' in the sense that to explain the observed structures in the universe the dark matter must behave in a non-relativistic manner in the self-interactions. The baryonic dark matter could be concentrated in molecular clouds or small stellar objects with masses too low to be luminous, although searches for these latter objects have not proved fructuous. The nature and detailed distribution in the galaxy of cold dark matter is at present unknown and the search for dark matter in this form is the subject of this review.

After a brief description of the evidence for dark matter and its nature, the review concentrates on the status of searches for cold dark matter with the so-called indirect method. For all search methods, but especially for the indirect method, the distribution of dark matter in the local galaxy is essential and the present knowledge and hypotheses for the dark matter location are presented. The indirect dark matter search method uses the probe of secondary particles from the annihilation of dark matter at particular locations in the galaxy with current experiments measuring the flux of charged cosmic rays, gamma rays and neutrinos. Existing data will be presented together with example interpretations of this data and prospects for the future. Although in the current data there are features which could be due to annihilations of cold dark matter, the spirit of the present review is that new data is needed before any conclusions can be made and that the various phenomenological studies presented should be viewed as relevant for the preparation and analyses of the next generation of experiments.

2. Evidence and nature of dark matter

The concept of dark matter was introduced as the solution to the discrepancy between estimates of the masses of astrophysical objects, based on the luminous and visible parts, and based on the dynamical behaviour of the components. At almost every cosmic scale, observations infer a larger dynamic mass than the visible mass implying a significant dark matter contribution to the gravitational potential. The mass-to-light ratio, M/L is used to quantify this discrepancy, with $M/L \sim 1$ for a star like the Sun.

2.1. Evidence

Since Zwicky's article in 1933 [1] in which the virial theorem was used to reconstruct the gravitational potential of the Coma cluster concluding that a huge amount of matter was invisible, dark matter has been pointed out at almost every scale in the universe. Since the

indirect detection methods in this review are concerned with the local universe this is where the details in this section are focused.

Most galaxies exhibit a dark matter component. In spiral galaxies, composed of a central bulge surrounded by a luminous disk, stellar motions are dominated by rotation within the disk [2]. The luminous component decreases exponentially from the centre, with a characteristic radius of a few kpc, and so the expectation is that the star rotation velocities decrease beyond this radius, scaling as $r^{-1/2}$ according to Kepler's laws; however, star rotation curves usually remain flat far from galactic centres, typically beyond 30–40 kpc, where gas and stars are not dominant implying a massive dark component. The mass-to-light ratio in spiral galaxies is typically $M/L \sim 5$–10. In elliptical galaxies, where the dynamical equilibrium is dominated by pressure rather than the rotation motion, observations also indicate a large contribution of dark matter, with $M/L \sim 10$–25. Among galaxy types, two are particularly dominated by dark matter: the low surface brightness galaxies (LSB) and the dwarf spheroidal galaxies (DSph). These objects are often characterized by a huge mass-to-light ratio $M/L > 100$ at the border of the field of stars. For indirect dark matter searches, in particular with γ-rays, the DSph galaxies which exist in the local galaxy neighbourhood (e.g. Draco) and have low numbers of stars and a very low gas contribution, are very attractive as possible sources.

At the scale of galaxy clusters, different independent methods such as that of Zwicky, x-ray measurements of inter cluster gas temperature, weak/strong lensing, luminous arcs and multiple images confirm the presence of dark matter at higher fractions than in galaxies, with $M/L \sim 200$ [3]. Mass-to-light ratios seem to remain stable beyond a few Mpc, and translate in terms of matter density as $\Omega_{\rm m} \sim 0.2$–0.3. The recent cosmological scale measurements, like the cosmic microwave background (CMB) [4], large scale structure and supernovae surveys (for instance SNLS [5]), confirm this matter density and favour the so-called cosmological *concordance* (or $\Lambda_{\rm CDM}$) model: that is a cold dark matter universe dominated by a cosmological acceleration term.

2.2. Possible nature of dark matter

Although discrepancies exist between observational amounts of baryonic matter and predictions coming from Big Bang nucleosynthesis calculations indicating the existence of dark baryons, dark matter is essentially non-baryonic. From hierarchical structure formation theories and simulations, the non-baryonic dark matter is compatible with a gas of *cold* and weakly interacting massive particles (WIMPs). No candidate exhibits this cold dark matter (CDM) property within the standard model (SM) of particle physics. However, rather by chance, theories beyond the SM, mainly built in order to solve problems inherent to particle physics, like the unification of couplings at high energy and the *hierarchy* and *naturalness* problems [6, 7], do have dark matter candidates. The currently most popular candidates for WIMPs come from the supersymmetric and extra-dimensional theories which are described below. More exhaustive reviews of particle physics candidates can be found in [8, 9]. Among the candidates not detailed in this review and for which the indirect search experiments are not sensitive, is the axion. The axion was proposed in the 1970s as an extension to the standard model of particle physics as a solution to the problem of strong CP violation, e.g. in the neutron electric dipole moment. This particle must be very light, $\sim 10^{-5}$ eV, and the experiments which search for it look for conversions to photons in strong magnetic fields.

2.3. Supersymmetric theories

Supersymmetry (SUSY) is a symmetry between bosons and fermions which is broken at the currently accessible energy scale. Early attempts to associate known fermions and bosons

in super-multiplets failed [10] and any SUSY theory necessarily adds at least one extra bosonic/fermionic superpartner (called sparticle) to each standard fermion/boson. An extra doublet of Higgs bosons is needed to give masses to *up*- and *down*-type quarks, which cannot belong to the same super-multiplet. Any SUSY generator is defined as a spin-$\frac{1}{2}$ spinor operator obeys anti-commutation relations and commutes with the Poincaré group momenta, preventing the minimum energy of the theory to be negative. SUSY is expected to appear beyond the electroweak energy scale between ∼0.1 and 1 TeV. With such an extension of the Poincaré algebra, requiring the local invariance of SUSY automatically involves gravity.

The mechanism of breaking the supersymmetry is a major issue in the theory. Phenomenological models in which ad hoc (*soft*) terms express this breaking improve the fundamental basis of particle physics at low energy. The minimal version of these models containing only one generator, the minimal supersymmetric extension of the standard model (MSSM), has a coherent frame for the unification of interactions (except gravity) at the high energy scale, breaks the EW symmetry dynamically and solves partly the hierarchy and naturalness problems. Although the general MSSM contains more free parameters than the SM (127 compared with 19), different universality assumptions either at the EW or GUT scales can considerably reduce them and will be discussed later. With the implementation of a discrete symmetry called R-parity, which ensures the conservation of baryon and lepton, B–L, quantum number and proton stability, SUSY particles are bound to be created in pairs, and the lightest supersymmetric particle (LSP) is stable. In this framework, among the dark matter candidates, two have been widely studied for the last two decades: the lightest of the four neutralinos (which will be referred to as the neutralino) and the gravitino. The neutralino is a linear combination of the Majorana fermionic superpartners of the gauge and Higgs bosons [11] (gauginos—bino and wino—and higgsinos), while the gravitino is the superpartner of the graviton (in the local realization of SUSY). From fundamental considerations, these different phenomenologies can be shown to be connected with the SUSY breaking scenarios.

The building of a phenomenological model requires SUSY to be explicitly broken. This is usually realized by means of *soft* terms in the Lagrangian where *soft* means that these terms break SUSY but softly enough to preserve its benefits. These *soft* terms explicitly carry that breaking and are somehow related to its origin. In local SUSY scenarios, which imply supergravity (SUGRA), that breaking not only gives rise to the gravitino mass (like a super Higgs mechanism), but also allows for universality assumptions at the high energy scale that translate in terms of parameter correlations in the MSSM and drastically reduce the number of free parameters. The whole content of the low energy scale theory is then determined by the evolution of the renormalization group equations (RGE) from the scale of SUSY breaking, Λ_{SUSY} to Λ_{EW}.

In the most popular simplified model, called the minimal supergravity model (mSUGRA), the supersymmetry breaking is due to an additional *hidden* sector containing at least the goldstino and its bosonic partner (in opposition to the *visible* SM particles and their superpartners), whose effects are mediated to the observable one by supergravity. This phenomenon is such that the *soft* terms become independent from the hidden sector details and exhibit very simple universality features at the scale Λ_{SUSY}. This modelling assumes universal gaugino, $m_{1/2}$, and scalar, m_0, masses at high energy scale. In this scenario, the MSSM can be described with only 5 parameters at this scale: the unified scalar masses, m_0, the unified gaugino masses, $m_{1/2}$, the universal trilinear coupling, A_0, the Higgs doublet vacuum expected value ratio, $\tan\beta = v2/v1$ and the sign of the Higgs mass mixing parameter, μ, which is itself fixed by dynamically breaking the EW symmetry. In most of the parameter space of this model, the neutralino is the LSP. Its mass is related to those of bino, wino and two-higgsino fields (respectively M_1, M_2, and the Higgs mixing μ). In mSUGRA the neutralino is mainly bino-

like, with its mass related to the unified gaugino mass as: $m_\chi \sim M_1 \sim 0.43 m_{1/2} < M_2, \mu$. Its higgsino component can nevertheless increase by taking an arbitrary high m_0 with respect to low fine-tuning trajectories of the renormalization group equations (the so-called *focus point* regions [12]), or as soon as the gaugino mass unification is relaxed (μ is then driven lighter than M_1, M_2).

Another scenario of SUSY breaking invokes conformal anomalies without any additional hidden sector: the anomaly mediated supersymmetry breaking scenario (AMSB). In this scenario, quantum anomalies, which are well known loop effects, generate the *soft* terms, and the sparticles acquire masses due to the breaking of scale invariance [13]. Nevertheless, the slepton masses are usually tachyonic in this scenario and require other mechanisms of SUSY breaking like the input of a scalar mass parameter, m_0, that should at the end be connected to a hidden sector. In AMSB models, the neutralino is usually the LSP, but with a strong wino component.

Finally, gauge mediated supersymmetry breaking (GMSB) models [14] mediate the breaking to the observable sector from a hidden sector through messenger fields which have gauge interactions. In this scenario, the LSP is mostly the gravitino, which is not observable with the indirect detection methods.

2.4. Theories with extra-dimensions

Full reviews of modern extra-dimension (ED) theories can be found in [15–17] on which the details in the following sections are based.

In 1919, Kaluza [18] tried to explain electromagnetism as a consequence of the curvature of an additional dimension to the classical 4D space-time. He pointed out that if general relativity were extended to a 5D space-time, the resulting equations could split up to the standard 4-dimensional gravitation with an extra term equivalent to Maxwell's equation making electromagnetism similar to gravity. In 1926, Klein [19], applying this idea to quantum mechanics, suggested that the extra dimension should be compactified to a very small radius, as small as the Planck scale. These ideas were revived by string theorists who worked on fundamental theories with 26 (bosonic strings) or 10 (superstrings) dimensions and later to the building of phenomenological models which allowed solutions to the hierarchy and naturalness problems without introducing SUSY.

Among the best known extra-dimension models is that of Arkani-Hamed *et al* [20] which assumes that gravity is the only interaction mediated in the extra-dimensions (called the bulk) and thus modifies the fundamental meaning of the Planck scale as usually defined. One has to define a reduced Planck scale related to the fundamental scale of theory through the volume of the compactified dimensions, which characterizes the gravitational interaction in the effective 4D theory. Taking a fundamental scale at the order of TeV, partly eliminates the hierarchy problem. Another model is due to Randall and Sundrum [21] and rests on a non-trivial background 5D geometry of finite extent. The simplest picture for its boundaries is drawn by two rigid branes of 4D, onto one of which the SM fields are confined (such a model is called RS1). This theory allows a *warped* metric which inverse-exponentially depends on the location of the ED and a curvature scale. In order to obey low energy constraints, gravity is bound to the distant brane, its effects being strongly depleted in the SM one, as required. The reduced Planck scale is then related to both the fundamental scale of theory and the curvature scale. By taking them all on the order of the traditional Planck mass, the EW (TeV) scale is naturally realized on the SM brane. Neither of these models gives detectable dark matter candidates. In general in ED theories, new physical states beyond the SM are expected as soon as the EDs are compactified, due to excitations in the bulk of all fields which propagate

therein. These fields are expanded into a complete series of modes, thus building the so-called Kaluza–Klein (KK) tower; however, only gravity is concerned in these two models.

Other scenarios in which the whole field content of the theory may propagate in all dimensions have been motivated by various arguments. Such models characterize a framework called *universal extra-dimensions* (UED) [22], which contrasts with previous ED theories by allowing translation invariance along the EDs. This leads to momentum conservation at the tree level and then the ED effects can only appear at higher orders of the perturbation theory.

In UED, the momentum conservation in the bulk implies that the KK mode masses are degenerate, and also that KK quantum numbers are conserved in the interactions of the 4D effective theory. This degeneracy is broken at the loop level. In addition, orbifold boundary conditions are usually necessary to suppress some fermionic degrees of freedom, and also manifest at the loop level by breaking of the KK number conservation, leading instead to the conservation of the so-called KK parity. In analogy with SUSY, the consequence of KK parity conservation is the stability of the lightest KK particle (LKP) [16]. In these models the dark matter candidates are first KK excitation of the $B^{(1)}$ boson and the neutrino $\nu^{(1)}$ which can annihilate and provide signatures for indirect searches.

Finally, extensions of the RS1 model in which only the Higgs boson is bound to the TeV brane allow detectable dark matter candidates. In [17] a model is detailed that embeds the RS1 phenomenology in the $SO(10)$ grand unified theory (GUT) framework, defining then a *warped* GUT (wGUT). The mechanism that generates the stability of the lightest non-standard particle is once again related to the proton stability, and emanates from the baryon number conservation. This is characterized by a new symmetry called Z_3, which is a combination of colour and baryon numbers. The partners of SM particles are Z_3-charged which leads to consequences analogous to R-parity conservation in SUSY with the lightest Z_3-charged particle (LZP) stable. In this model, the only viable dark matter candidate has the properties of a right-handed neutrino and is a Dirac fermion.

3. Search methods for dark matter

There are two distinct search methods for cold dark matter in the form of WIMPs referred to as 'Direct' and 'Indirect'. The direct method looks for interactions of dark matter particles in Earth-based detectors and the indirect method looks for secondary particles emanating from dark matter annihilations at a distant location. The two methods, being very different, are complementary; positive evidence seen with the distinct methods would provide convincing confirmation of the discovery of cold dark matter. In some cases the two methods are sensitive in different regions of the parameter phase space for the nature of the CDM particle.

The direct search method relies on the relative motion of a detector fixed on Earth and WIMPs fixed in the galactic halo. A short review of the direct method can be found in [23]. There are two components to this relative motion: the Sun orbiting the centre of the galaxy and the Earth orbiting the Sun. Typical estimates of this relative motion are $\sim 300\,\mathrm{km\,s^{-1}}$, with modulations of $\sim 10\%$ depending on the season of the Earth's orbit around the Sun. A WIMP entering a block of detector material would cause the recoil of a struck nucleus in the detector. There exist a great number of types of direct search detectors using diverse materials and methods to reject backgrounds. The active detector material range between scintillators (e.g. NaI), semiconductors (e.g. Ge), and noble liquids (e.g. Xe). Often the instruments employ two independent measurements of the energy deposited by the recoil nucleon, such as total energy and specific ionization, in order to facilitate the reject background. Some detectors look for annual modulations in the rate as a signature of dark matter due to the change in the relative motion of the Earth in the dark matter halo as the Earth's direction changes as it orbits the Sun.

Other methods search for directionality in the angle the dark matter particle enters the detector to demonstrate the average relative velocity of the dark matter impacting the Earth.

The indirect search method aims to observe rare species of cosmic radiation emitted from annihilation interactions of pairs of WIMPs at locations in the galaxy. Different experiments search with different annihilation products and currently searches are in progress with charged cosmic rays, gamma rays and neutrinos. Depending on the particle type employed, the experiments have distinct features. Due to their weak interactions, neutrinos can search for concentrations of dark matter at the cores of massive astronomic objects such as the centre of the Sun, the centre of the Earth and the centre of the galaxy. Gamma rays would be absorbed from the centre of the Sun and Earth but could emerge from the hypothesized concentration of dark matter around the black hole at the centre of the galaxy. Further γ-ray experiments could observe dark matter concentrations throughout the local galaxy and also in neighbouring galaxies. Charged cosmic rays below energies of $\sim 10^{19}$ eV are deviated in traversing the interstellar magnetic fields and so cannot be used to trace back to any particular annihilation location. The charged cosmic ray searches typically use rare species of particles: positrons, antiprotons and antideuterons and for these experiments it is essential to have accurate estimates of the background flux produced throughout the galaxy of each particle species from sources other than dark matter. The clear signature of a particular source location would be extremely powerful evidence for dark matter and is possible with the gamma ray and neutrino searches.

4. Distribution of dark matter in the galaxy

The self-annihilation rate of any type of WIMP is proportional to the square of the particle density and so the rates and experimental sensitivities for all indirect searches are strongly affected by the dark matter distribution. For the cosmic ray and gamma ray searches it is directly the distribution of matter in the halo of the galaxy which is relevant, while for the neutrino searches the relevant density is that concentrated in the centres of the various possible sources which is itself related to the halo density at the position of the concentrating body.

The estimate of the density, ρ, involves both observational and theoretical astrophysics. The density profile can be constrained with galaxy star rotation curves, which allow the reconstruction of the mass profile and by disentangling the baryon contribution, constrain the dark matter distribution. This technique first led to empirical laws for the density distribution, referred to as *isothermal* profiles [24], with constant rotation velocities and spherical r^{-2} density distributions. Nevertheless, it is rather difficult to estimate the dark matter profile at the centre of galaxies; from the observational point of view, the centres are often difficult to observe and characterize and from the theoretical point of view, the determination of the profile involves highly non-linear calculations. The current theoretical understanding of hierarchical cosmologies rests on the Press–Schechter (PS) formalism [25], which characterizes the growth of structures with gravitational instabilities.

In 1967, Lynden-Bell attempted an analytical treatment of the violent relaxation [26] for a gravitationally bound system of collision-less stellar-like objects and showed that it could drive their distribution to be isothermal with Maxwellian velocities. Much later, with sophisticated computational methods, numerical N-body simulations were applied to the hierarchy picture of structure formation with different cosmological models, finally favouring the Λ_{CDM} model. These methods led to estimates of galactic halo profiles which were often based on the formula

$$\rho_\chi(r) = \rho_0 \left(\frac{r_0}{r}\right)^\gamma \left(\frac{r_0^\alpha + a^\alpha}{r^\alpha + a^\alpha}\right)^\varepsilon , \tag{1}$$

where $\rho_0 = \rho(r_0)$ is a convenient normalization (often taken at $r_0 = R_{\rm Sun}$ for our galaxy), and a characterizes a scale radius below which the profile goes as $r^{-\gamma}$. Two well-known profiles have been proposed by Navarro *et al* [27] (NFW), with $\gamma = 1$, $\alpha = 1$, $\varepsilon = 2$ and Moore [28] with $\gamma = 3/2$, $\alpha = 1$, $\varepsilon = 3/2$, whereas a cored isothermal profile is recovered with $\gamma = 0$, $\alpha = 2$, $\varepsilon = 1$. These profiles differ mainly in the central region. Nevertheless, the resolution of these early simulations was not good enough to scrutinize the very centre of any CDM halo and the logarithmic coefficient γ was extrapolated down to small radii. More recent work shows that the profile seems to become shallower towards the centre of galaxies. This is supported by many observations, especially of LSB galaxies and DSph, which favour cored halos. A minimal core radius can be set by equilibrium arguments so as to regulate the gravitational growth of the central density by the annihilation rate of WIMPs [29]; however, tidal effects [30] can also explain the smearing of the singular density profile and a core formation. On the contrary, the response of dark matter halos to condensation of baryons might lead to more concentrated centres [31], although the merging history of structure could wash out such effects [32]. Finally, the presence of a supermassive central black hole (SBH) at the centre of a galaxy could also steepen the central dark matter profile depending on the cross interaction between stars, DM and the SBH itself.

Another enhancement of the DM annihilation rate could arise from the existence of DM substructures within halos of galaxies, often referred to as clumps. In hierarchical $\Lambda_{\rm CDM}$ cosmologies, the smallest structures formed first and may survive throughout the history of the universe. This phenomenon is natural in the PS formalism which allows a statistical formulation of the hierarchical clustering and is also seen in the numerical simulations. The presence of such over-densities within halos induces the enhancement of the DM annihilation rate, compared with a smooth distribution [33]. In terms of the observable cosmic-ray flux, it is often translated into a so-called *boost factor* applied to the whole primary spectrum. The situation is rather unclear concerning the possible values of this boost factor and further it is likely to be species and energy dependent [34]. Although some N-body simulations favour small values (less than 10) due to the low number of surviving clumps [35], Diemand *et al* [36] suggest that about 50% of the mass in a Milky-Way type galaxy could be bound to dark matter substructures with masses between 10^{-6} and $10^{7}\,{\rm M}_{\rm Sun}$. These authors suggest that about $\sim 10^{15}$ of such substructures may have survived against gravitational disruption, leading to a boost factor of over two orders of magnitude compared with the smooth contribution. Berezinsky *et al* [30, 37] invoke tidal effects that would wash out density fluctuations and lead to a very small surviving population of clumps and so to a small boost factor. Other mechanisms could enhance the DM annihilation rate, such as adiabatic compression around intermediate mass black holes populating galaxies [38].

In the local Galaxy, while there is no direct observational evidence for DM in the galactic disc or in the solar neighbourhood [39], the current estimates of the local DM density are around 0.3–0.4 GeV c^{-2} cm^{-3} [40] which is about 15% of the local matter budget. The centre of the Milky Way is likely to be occupied by a supermassive black hole of $\sim 3 \times 10^6\,{\rm M}_{\rm Sun}$ [41], surrounded by a barred and baryon dominated bulge within a radius of $\sim$4 kpc [42]. The shape of the DM density profile at the very centre is difficult to infer from observations, mainly due to theoretical uncertainties.

The possible clumps of dark matter in the galaxy arise due to seeds from statistical fluctuations in the primordial matter density while the other hypothesized concentrations of dark matter, around the horizon of the black hole at the galactic centre and at the core of massive bodies such as the Sun and Earth, are due to more recent gravitational interactions.

The hypothesized accumulation of dark matter around the central black hole of the galaxy is rather contested. Predictions have been made by Gondolo and Silk [43], where the

distribution of dark matter around the black hole has a spike with a distribution $\rho(r) \propto r^{-A}$ with $2.25 < A < 2.5$, which could give very large fluxes in particular in neutrino searches. There has been an extensive discussion about the existence of this dark matter spike and the situation remains unclear; Ullio *et al* [44] conclude that a null search for annihilation radiation from the galactic centre could not be interpreted as evidence against WIMP dark matter, due to the uncertainty on this matter distribution.

The accumulation of dark matter in massive objects is less controversial and was proposed in the 1980s for the Sun [45] and Earth [46]. Any WIMP-like particle will lose energy elastically in a random encounter with a massive celestial object. Depending on the mass of the celestial object, the particle has a probability to be trapped in a closed orbit around the object and subsequently return to the same point and submit to further encounters and elastic energy losses. If after an encounter, the WIMP velocity becomes less than the escape velocity, it will be gravitationally trapped. The particles then migrate and accumulate at the core of the massive object. At the core, the density of WIMPs is such that annihilations take place and the balance between accumulation and annihilation can lead to equilibrium in very massive bodies such as the Sun. In the case of less massive bodies, such as the Earth, this equilibrium is not yet attained and the lower density continues to increase.

5. Annihilation of dark matter particles

For the indirect search experiments complete rate predictions must rely on calculations on the number and spectra of the relevant particle species in the annihilation reaction final state. In this section, the two main features of the most popular WIMP candidates from supersymmetric and extra dimension theories are briefly presented. More complete details can be found in [8,9,47] for SUSY and [17] for ED. To be able to self-annihilate any dark matter candidate must either be a Majorana particle or a Dirac particle with no matter–antimatter asymmetry. The weak interaction cross-section required by the cosmology constraints means that a high local density of the particles is essential to have an experimentally observable rate with the annihilation rate being related quadratically to the density: $\Gamma \propto \rho^2$. In all annihilation locations the relative velocity of the WIMPs is low and usually annihilation rates are calculated in the null velocity limit i.e. *S*-wave. In this limit, the annihilation products at the leading order in perturbation theory are mostly pairs of standard model fermions/anti-fermions, and neutral pair combinations of gauge or Higgs bosons of all types. Any annihilation product $\chi + \chi \rightarrow A + B$ is potentially created as soon as kinematically allowed, i.e. $2m_\chi \geqslant m_A + m_B$. Pair combinations of massless bosons, photons and gluons, happen only at higher perturbative order, making such final states less probable. The particle species observed in the experiments are the results of decays and hadronization of the tree level final state particles. Further, mainly for the charged particle species, it is essential to take into account propagation and interaction effects between the source and the Earth

5.1. Annihilation channels in supersymmetric theories

For SUSY models, the annihilation products depend intimately on the gaugino/higgsino content of the neutralino. Only the higgsino and wino parts of the neutralino allow couplings to gauge bosons, so that only mixed, higgsino- or wino-like neutralinos can annihilate into massive gauge and Higgs bosons (Z^0Z^0, W^+W^-, $Z^0h(H)$, Z^0A, $W^{+/-}H^{-/+}$, H^+H^- and pair combinations of A, h, H). These configurations occur in the general MSSM when the Higgs mass parameter $\mu \leqslant M_1, M_2$, as well as in the mSUGRA when the unified scalar mass, m_0, is in the multi-TeV range (the *focus point* regions). At the tree level, the main diagrams

involved are neutralino/chargino exchanges in the t-channel and $Z^0/A/h/H$ exchanges in the s-channel. For annihilation in fermion–antifermion pairs, both higgsinos and gauginos are involved and the tree level processes are characterized by s-fermion exchanges in t-channel and again $Z^0/A/h/H$ exchanges in s-channel.

In the low velocity limit, annihilation at rest prevents neutralinos from having their spins parallel, due to Pauli blocking, and implies that two quantum numbers should be conserved by S-wave contributions, i.e. the CP-odd initial state and the null total angular momentum. This, consequently, leads to the suppression of some interactions and final states. For instance, exchanged Higgs bosons in s-channel other than the CP-odd pseudo-scalar, A, are suppressed, as well as pairs of identical/conjugate Higgs bosons in final state (AA, hh, HH, H^+H^-). Moreover, the transverse part of the Z^0 exchange does not contribute, leading to the helicity suppression of low mass and massless fermion–antifermion pairs in the final state. For massive fermions, this favours the pair creation of *down*-type quarks, with an enhancement factor of $\tan\beta$, whereas there is a $(\tan\beta)^{-1}$ suppression factor, from A exchange and destructive interferences, for *up*-type quark pair production. Hence the *bottom* dominates over the *top* quark final states and the τ is the only charged lepton created.

With these considerations, in mSUGRA neutralinos, being bino-like in most of the parameter space, will mainly annihilate into $b\bar{b}$ pairs with pair production of τ also often significant. When massive enough and when carrying a higgsino or wino component, neutralinos will annihilate into massive gauge bosons, for instance, in the general MSSM, in *focus point* regions of mSUGRA, in non-unified gaugino mass models and in AMSB models.

5.2. Annihilation channels in extra dimension theories

In ED theories, as mentioned already, there are different types of dark matter candidates which are interesting for indirect detection experiments. In UED, the LKP is generally the $B^{(1)}$, the first KK excitation of the hypercharge boson and therefore a spin-1 particle. There is no coupling to standard model gauge bosons at the first order of perturbation theory. As a vector, the $B^{(1)}$ annihilation cross-section does not suffer the constraint of helicity suppression of low mass final fermion states. Moreover, the annihilation amplitudes are proportional to the square of the hypercharge of the generated particles, so that the phenomenology is much simpler than in SUSY. The annihilation proceeds mainly in pairs of charged leptons ($\sim$20% per generation), in *up*-type quarks ($\sim$11% per generation), Higgs bosons ($\sim$2.3%), neutrinos ($\sim$1.2% per generation) and *down*-type quarks ($\sim$0.7% per generation). These branching ratios depend little on the $B^{(1)}$ mass or on the KK mass scale m_{KK}. Since the preferred mass range is above 400 GeV for LKPs, all standard model particles are created through annihilation.

In wGUT models, with Z_3 symmetry, the LZP particle is generally taken to be the KK right-handed neutrino ν_Z, a Dirac fermion. As stated previously, the Dirac nature of this particle avoids the helicity suppression of low mass fermion final states. Nevertheless, contrary to the UED LKP, the branching ratios depend strongly on both the LZP and KK scale masses. Below $\sim$100 GeV, LZPs annihilate through Z^0 exchange in the s-channel, providing mainly quarks ($\sim$70%); neutrinos ($\sim$7% per generation) and charged leptons ($\sim$3.5% per generation). For a more massive LZP, above $\sim$200 GeV, the dominant channels are typically $t\bar{t}$, W^+W^- and Zh.

The most significant difference in the annihilation channels in ED theories is the possibility of creating charged lepton and neutrino pairs which are suppressed in SUSY phenomenologies.

5.3. Energy spectrum of final states particles

In order to make predictions for indirect detection, a precise knowledge of the injected cosmic-ray spectrum is essential. In the case of γ-rays and neutrinos the propagation is direct and the detected spectrum can only be affected by absorption and also with oscillations in the case of neutrinos. On the contrary, charged cosmic-ray spectra are sensitive to diffusion in magnetic turbulence and details of their shapes are likely to be deformed during their travel to the Earth. Nevertheless, spectral information is in many cases crucial in trying to disentangle a primary signature of dark matter annihilation from a classical background.

The clearest energy spectrum for a detection would be unique energy lines, either of γ-rays, neutrinos or charged lepton cosmic rays, which give unambiguous signatures related to the WIMP mass. However, γ-ray lines are loop suppressed in all models considered here, making them a weak signal; in the frame of SUSY via box processes $\chi\chi \rightarrow \gamma\gamma$, γZ^0, with energy related to the neutralino mass as $E_\gamma = m_\chi$ or $E_\gamma = (4m_\chi^2 - m_Z^2)/4m_\chi$. In ED theories, due to lepton–antilepton pair production, neutrino lines could emerge from the continuum contribution. Electron–positron pairs can also be produced with significant branching ratios up to 20%, so distorting the primary spectrum despite propagation effects.

All annihilation processes generating quark–antiquark pairs or massive bosons are followed by parton fragmentation, during which charged and neutral pions are created sharing equally the energy budget. These hadronic cascades give rise to a continuum spectra for γ-rays; neutrinos and for anti-matter cosmic rays (positrons, anti-protons, anti-deuterons). The spectrum details are estimated with Monte Carlo simulations based on various QCD modelling [48, 49] or directly from parametrized fragmentation functions with simple phase space arguments [50, 51]. In both cases, the resulting spectra generally exhibit a simple dependence on the WIMP mass. The $W^{+/-}$ decays are characterized by particular spectral structures for positron and neutrino production due to the large branching ratios of $W \rightarrow l\nu$.

6. Searches with cosmic-ray antimatter

The total flux of charged cosmic rays arriving at the Earth is large and the indirect dark matter searches concentrate on rare species, generally antimatter components, which are expected to be irrelevant in the cosmic acceleration sources. The true origin of the bulk of cosmic rays with energies above a few gigaelectronvolts is still uncertain but the main sources in the local galaxy are likely to be supernova remnants, pulsars, stellar winds and binary systems. Hadrons are the main components of cosmic rays arriving above the atmosphere of the Earth, comprising mainly protons, neutrons and helium nuclei with a few per cent of heavier nuclei and with electrons contributing a few per cent of the total. In the cosmic sources, the dominant charged particle species are accelerated and the other species of particles are produced in secondary interactions of these primary particles with matter and radiation fields surrounding the sources. Other secondary interactions take place during the propagation of the primary cosmic rays. To observe an indirect dark matter signal in the data it is essential to have accurate background estimates of all other cosmic-ray sources. Using antiparticles largely removes the primary astrophysical sources as backgrounds but the products of these secondary interactions are a major background which must be calculated with a precise knowledge of fluxes of all species of cosmic rays. The quality of the indirect searches relies on the confidence of the flux and energy spectra used in these background calculations.

Existing data on charged particle spectra in cosmic rays come from experiments flying in the high atmosphere in balloons or above it in satellites, ground-based experiments being

dominated by the particles produced in the atmospheric showers and so being unable to accurately identify the original nature of the cosmic ray. The following sections describe the status of dark matter searches using positrons, antiprotons and antideuterons.

6.1. Cosmic-ray positrons

Positrons are a rare component in cosmic rays; electrons themselves represent only 1–2% of the total of the cosmic-rays flux reaching the Earth with positrons being ∼10% of the electron flux at ∼1 GeV. It is expected that the bulk of electrons are primary particles injected and accelerated in cosmic accelerators while the positrons are secondary interaction products resulting from nuclear collisions in interstellar matter. The interest in positrons as a signal for annihilations of dark matter particles has been animated by a long-standing anomaly in the positron spectrum measured by the high energy antimatter telescope (HEAT) which has been interpreted as a possible WIMP signal by a number of authors.

The anomaly, a step or bump, at energies of around 7 GeV, has been seen in a consistent way in different flights of the HEAT apparatus [52]. The apparatus comprised of a magnetic particle spectrometer with drift tube tracking devices, a transition radiation detector, an electromagnetic calorimeter and time of flight counters. The geometrical acceptance was ∼500 cm^2 sr with a maximum detectable rigidity of 170 GV for electrons. The original data was obtained in balloon flights in 1994 and 1995 for a total of about 50 h and was confirmed in a flight with a different apparatus in 2000.

In the HEAT data, the positron fraction, $e^+/(e^+ + e^-)$, is used to estimate the positron excess by removing any possible overall normalization systematic errors which would affect both the electron and positron fluxes in a similar way. figure 1, from Coutu *et al* [53], shows a compilation of data from various experiments with the HEAT data shown as the red points. To interpret the data, it is necessary to have confidence in the background estimates for the positron fraction. The background calculations are simpler for positrons than, for example anti-protons, because of the absence of hadronic interactions. In propagating through the galaxy, positrons travel in a random walk under the influence of galactic magnetic fields and are affected by electromagnetic energy losses in inverse Compton and synchrotron processes. These effects are taken into account in the 'leaky-box' model of propagation of secondary positrons in our galaxy and diffusion losses in the flux have been calculated by Webber *et al* [54]. The positron background based on these calculations is indicated in figure 1. Even though the data is consistent with the background estimates within their error bars, it is the significant discontinuity and step in the data around 7 GeV which excites interest and attempts to provide alternative explanations to this data beyond the standard processes.

Among the possible explanations of the anomaly not evoking dark matter, is the possibility of a local primary positron component which could arise when e^+e^- pairs are created by near-discrete sources [53, 55]. This could occur through the conversion of high-energy γ-rays in the polar cap region of galactic radio pulsars or by very high-energy γ-rays interacting with optical and ultraviolet radiation in the vicinity of the discrete sources. Another possibility is the generation of electrons and positrons in the interactions of hadronic cosmic rays interacting within giant molecular gas clouds. In this scenario the e^+ enhancement at 10 GeV and the flux deformation would be explained by magnetic turbulence in the cloud forbidding under-threshold momentum cosmic rays to escape. Recently the propagation equation of cosmic rays in the galaxy has been studied using a new approach [56]. The authors succeeded in describing the cosmic-ray propagation on small scales around their sources in three spatial dimensions and time. The results of the calculations have been successfully compared with data; in particular with the boron-to-carbon spectra ratio which is among the most precise experimental

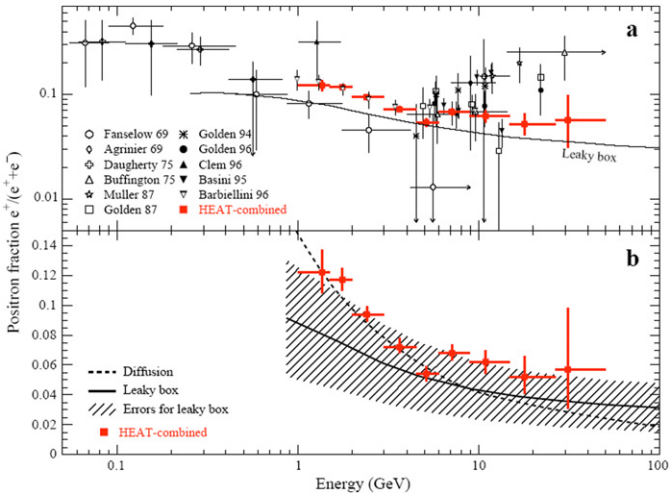

Figure 1. (*a*) A compilation of measurements of the positron fraction versus energy, included the HEAT combined measurement from the 1994 and 1995 flights. A simple leaky-box model prediction is also shown. (*b*) The HEAT-combined positron fraction is compared with a secondary model prediction using galactic diffusion and a leaky-box model prediction curve, surrounded by an estimated band of uncertainty [53].

measurements commonly used for determining cosmic-ray propagation parameters. This recent study pointed out that the cosmic acceleration in supernova remnants has an impact on the rate of cosmic-ray nuclei which could also possibly account for the positrons flux structure as an effect of the acceleration mechanism from such an SNR origin.

Many explanations of this HEAT data using dark matter exist; some of the models are within the SUSY framework [57, 58] and others within the Kaluza–Klein context [59–61]. In Baltz *et al* [58], the authors succeeded in obtaining a better fit to the data using WIMP signals than with the cosmic-ray background alone; however, the form of the WIMP signal in their fits does not reproduce well the shape of the excess step in the data. Figure 2 shows the HEAT data with an example fit from this paper. For this fit, the positron flux is propagated using a true diffusion model with a tangled galactic magnetic field in infinite slab and energy losses due to synchrotron radiation and inverse Compton scattering from the cosmic microwave background and from starlight. The SUSY model in figure 2 has a hard positron spectrum from direct gauge boson decays. To fit the data, an enhancement (clumpiness) of the halo WIMP density by a factor of 117 compared with a smooth galactic halo is required to match the HEAT data. Such factors are not excluded by astrophysical considerations as discussed above.

While in the case of the neutralinos the direct annihilation to e^+e^- is suppressed, it occurs frequently for Kaluza–Klein dark matter. In figure 3(*a*) the positron fraction predicted from Kaluza–Klein dark matter annihilation is shown as a function of positron energy from Hooper *et al* [59]. Here, the authors have considered models with universal extra dimensions where the most natural candidate for the lightest KK particle is the first excitation of the hypercharge gauge boson, $B^{(1)}$, with possible mass ranges from hundreds of GeV up to a TeV. Energetic positrons are copiously produced in $B^{(1)}$ dark matter annihilations both directly and through cascades of muon and tau decays. In figure 3 the HEAT data are compared with the calculation. The solid and dashed lines represent 300 and 600 GeV mass $B^{(1)}$ candidates, respectively, while the dotted line represents the background predicted. Among the possible channels of generic particle dark matter annihilation, the annihilation into charged leptons

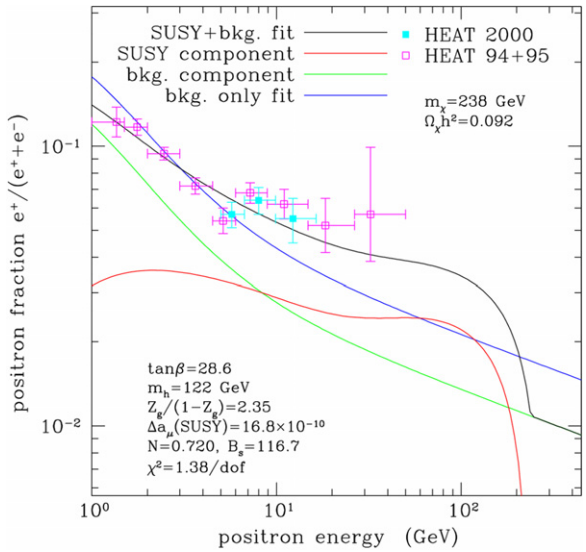

Figure 2. Positron fraction data and fit with a dark matter signal. The positron data is from the HEAT experiment flights in 1994 and 1995 and 2000. The curves show a background only fit, and a fit with background plus a neutralino signal of mass 238 GeV. From [58].

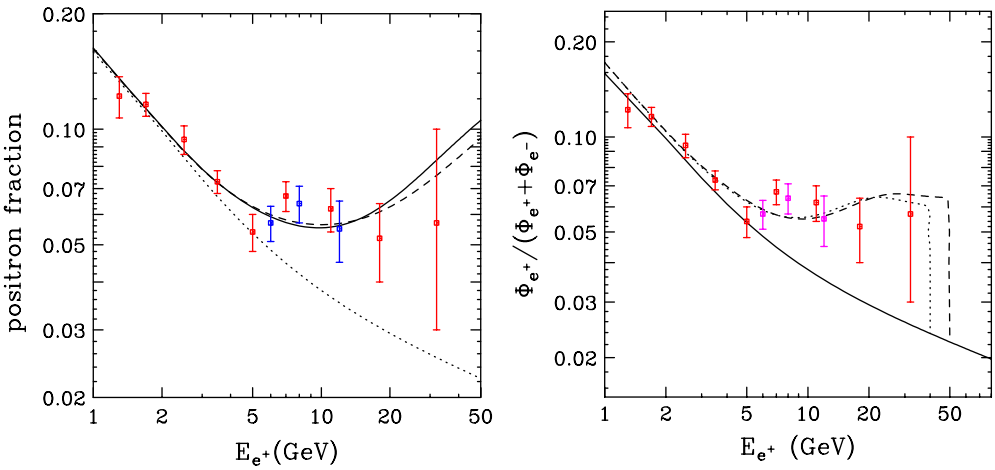

Figure 3. (*a*) (left) The cosmic positron fraction from Kaluza–Klein $B^{(1)}$ dark matter particle for masses of 300 and 600 GeV. Models are compared with HEAT data and dotted line representing the background predicted secondary component. From [59]. (*b*) (right). The cosmic positron fraction from LZP annihilation for masses of 40 and 50 GeV compared with HEAT data. From [60].

$(e^+e^-, \mu^+\mu^-, \tau^+\tau^-)$ produces a much harder spectrum than the modes that typically dominate for supersymmetric dark matter. The positrons produced are then propagated in the galaxy by means of a diffusion constant as found in [61, 62] which results from the best fit of other cosmic-rays flux measurements.

Subsequently in [60] another less massive dark matter candidate has been introduced in extra-dimensional models: a Kaluza–Klein with the quantum properties of a right-handed

neutrino (LZP), and sizable gauge interactions with standard model particles where the possible mass can be less than 100 GeV. This particle can annihilate throughout the galactic halo and can produce high-energy positrons directly as well as through the decays of muon, tauon and quark pairs. In figure 3(*b*) two models corresponding to LZP of masses of 50 and 40 GeV, respectively, fit HEAT data very well. Boost factors of 23 and 17 have been used for the correct normalization.

Finally, [34] has shown that when clumpiness is invoked in the case of positrons, an energy dependence of the corresponding boost factor should be taken into account leading to large variations in the predictions if the number of clumps in the relevant propagation volume is small.

6.2. Cosmic-ray antiprotons

Antiprotons are an even rarer component of the cosmic-ray flux than positrons, with the antiproton/proton flux ratio being $\sim 10^{-5}$ at 1 GeV. As with positrons, antiprotons are mainly produced in collisions of cosmic-ray protons with interstellar matter. Interest in the possibility of exotic signals in the antiproton data was focused following early experimental data where at low energy the measured points were above the background estimates [63, 64].

The most precise antiproton flux data comes from the balloon-borne experiment with a superconducting spectrometer (BESS) detector [65]. BESS is a magnetic spectrometer which was flown with different configurations of the apparatus on a series of balloon flights between 1993 and 2002. The spectrometer had precise tracking with drift chamber and scintillating fibres as well as excellent particle identification in a Cherenkov detector and time of flight counters. Other data comes from the AMS-01 shuttle flight [66] and another balloon experiment, CAPRICE [67].

With later more complete data and with more detailed background estimates it can be concluded that the existing data is consistent with background alone [68]. Figure 4(*a*) shows the various components in the background spectrum which at energies below a few GeV include a 'tertiary' component caused by interactions of higher energy secondary antiprotons and a component from interactions of helium nuclei in the interstellar medium. For the low energy flux the state of solar activity can have a large effect on the cosmic-ray flux able to enter the heliosphere; this effect can be a variation of a factor of 5 in flux between the solar minimum and solar maximum. Figure 4(*b*) gives the comparison with BESS data from 1995 and 1997, which corresponds to a period of minimum solar activity. It can be seen that while the 1995 data has a small excess at low energies, the 1997 is completely consistent with the background.

Despite the present agreement of the measurements with the background many authors have explored the possibility of a contribution of dark matter annihilation in the antiproton data. The same publication of Bergstrom *et al* [68], from which figure 4 is taken, also explores the possibility of a contribution of dark matter in the data and concludes that it is possible to fit the same data with a reduced background contribution and a signal from a 207 GeV mass neutralino. Such fits are possible because the signal and background shapes have very similar energy spectra and so cannot be separated without a precise knowledge of the background flux normalization. In a series of papers, Donato *et al* [69, 70] explore in detail the variation in flux arriving at the Earth due to propagation and diffusion effects in the galaxy for both the background of secondary antiprotons from cosmic-ray interactions and for possible primary antiprotons from neutralino annihilations. These studies conclude that that the background uncertainties are $<25\%$ but that the uncertainties in the arriving signal flux due to the lack of knowledge of the astrophysical parameters of the galaxy are much larger. The two figures 5(*a*) and (*b*) compare the measurements with estimates of background plus an annihilation signal; figure 5(*a*) is for conditions of solar minimum and figure 5(*b*) for solar maximum. In figure 5(*a*)

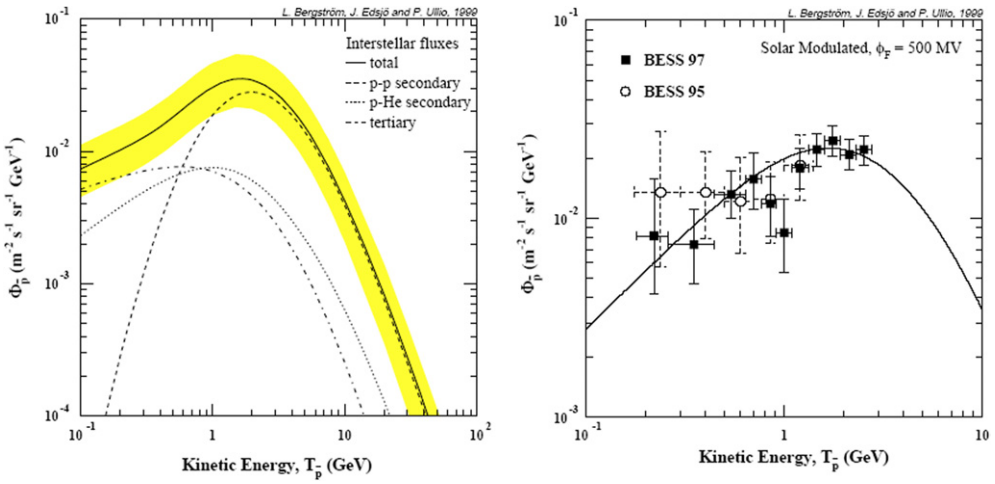

Figure 4. (*a*) (left) Estimates of the antiproton flux with the contribution from secondary and tertiary antiprotons. The uncertainty due to the parametrization of the primary proton spectrum is given as the shaded band. (*b*) (right) Comparison of the BESS data with the background estimate. The figure is from [68].

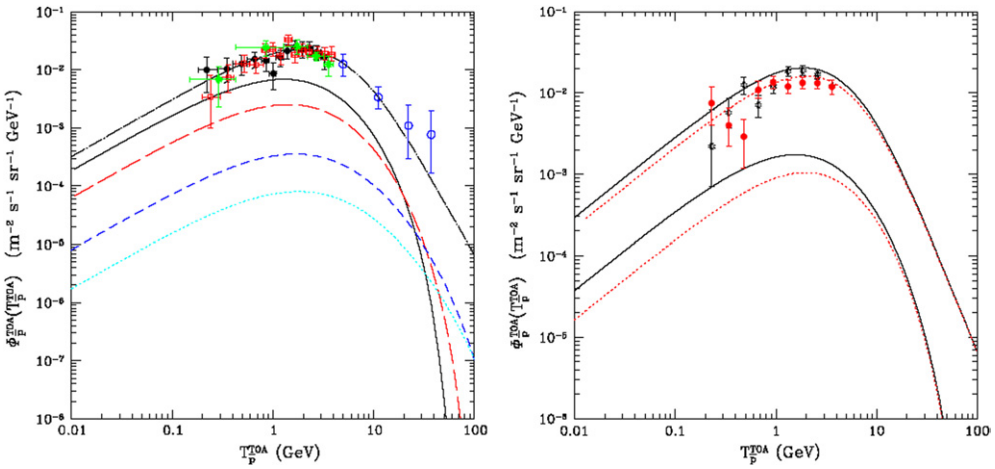

Figure 5. (*a*) (left) Antiproton data from BESS taken in the 1995–97 (●); BESS 1998 (□); AMS (★) and CAPRICE (○). The upper dot-dashed curve shows the background secondary flux and the solid, long dashed, short dashed and dotted lines correspond to $m_\chi = 60$ GeV, 100 GeV, 300 GeV, 500 GeV, respectively. Solar modulation is calculated for a period of minimal solar activity. (*b*) (right) Data from BESS 1999 and 2000 for a period of solar maximal activity. Upper curves are the background lower curves $m_\chi = 100$ GeV [70].

the dot–dashed curve corresponds to the background estimate with the median astrophysical parameter and the other curves give example sets of fluxes for neutralinos with masses between 60 and 300 GeV. In figure 5(*b*) the upper lines show the background and the lower curves a signal for 100 GeV.

From figure 5, it is clearly seen the data is compatible with the background. Within the 25% estimated errors on the background a signal could be accommodated but for $m_\chi = 100$ GeV the shape of the signal spectrum is very similar to that of the background and so cannot be separated

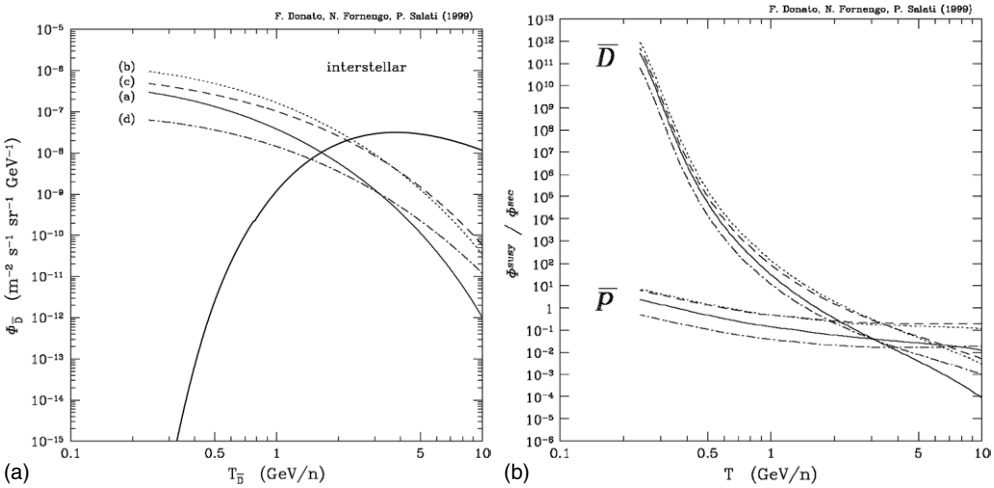

Figure 6. (*a*) (left) Solid line gives estimates of the interstellar flux of secondary antideuterons from cosmic-ray interactions. The various labelled lines give signal predictions for various SUSY models with neutralinos with masses between 37 and 120 GeV. (*b*) (right) The ratio of the signal to background flux, for antiprotons and antideuterons annihilation for the same range of neutralino models. The figure is from [63].

without a very precise knowledge of the background details. Hence, using the antiproton flux to make clear conclusions on a possible dark matter signal requires both much more precise data and also better background estimates needing improved knowledge of the astrophysical parameters that govern the diffusion and propagation in the galaxy.

6.3. Cosmic-ray antideuterons

Cosmic-ray antideuterons are so rare as to have not yet been detected, the existing upper limits from BESS [71] of $\phi < 2 \times 10^{-4}\,\mathrm{m^{-2}\,s^{-1}\,sr^{-1}}\,(\mathrm{GeV/n})^{-1}$ being around 1% of the antiproton flux. For low energies the production of antideuterons by interactions on interstellar material becomes negligible and so any observed flux could be a potential dark matter signal.

Motivated by the difficulties in interpreting the antiproton data, Donato *et al* [63] have investigated the background and signal in the antideuteron flux. Antideuterons from spallation interactions of cosmic-ray protons on the interstellar material proceed via antinucleon pair production and then merge into antideuterons, whereas antideuterons can be produced directly in the annihilations of heavy particles. The propagation of the antideuterons in the galaxy is considered in a similar way as for antiprotons. Figure 6(*a*) gives the estimates of the antideuterons background flux, showing the strong suppression at low energies due to the kinematics, together with the signal flux from various models. In figure 6(*b*) the ratio of signal to background is shown compared with that for antiprotons, indicating a dramatic enhancement at low energies. A study by Duperray *et al* [72] finds much higher predictions for the secondary antideuteron flux, mainly at low energy, due to the inclusion of new production processes.

Figure 7(*a*), from Profumo and Ullio [73], gives the rates from an antideuteron annihilation signal for three SUSY models and two neutralino masses. It can be seen that at an energy of 1 GeV, the highest flux is $\sim 10^{-8}\,\mathrm{m^{-2}\,s^{-1}\,sr^{-1}}$, so 3–4 orders of magnitude less than the existing experimental limit. For comparison figures 7(*b*) and (*c*) show the same models for

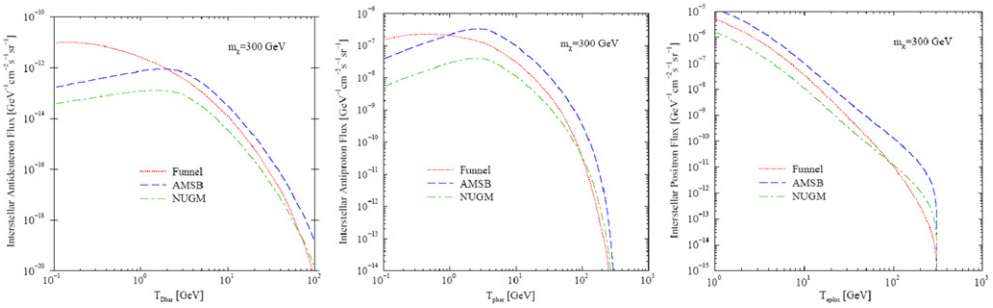

Figure 7. (*a*) (left) Fluxes of antideuteron annihilation signals for three SUSY models as a function of energy, for a neutralino mass of 300 GeV. (*b*) Fluxes of antiproton annihilation signals for the same conditions SUSY models as a function of energy, for a neutralino mass of 300 GeV. (*c*) (right) Fluxes of positron, annihilation signals for three SUSY models as a function of energy, for a neutralino mass of 300 GeV. Figures are from [73].

antiprotons and positrons with fluxes at 1 GeV $\sim 10^{-3}\,\mathrm{m}^{-2}\,\mathrm{s}^{-1}\,\mathrm{sr}^{-1}$ and $\sim 10^{-1}\,\mathrm{m}^{-2}\,\mathrm{s}^{-1}\,\mathrm{sr}^{-1}$, respectively. Hence, although indirect dark matter searches with antideuterons have significant advantages over searches with antiprotons with respect to the ratio of signal to background, the fluxes are very low and the searches must wait for a new generation of cosmic-ray experiments with much higher sensitivities.

6.4. Future perspectives in cosmic-rays searches

A new generation of cosmic-ray experiments is under construction and those most relevant for indirect dark matter searches with antimatter will be space telescopes: AMS-02 [74] and PAMELA [75]. These detectors, which are conceptually similar but with different acceptances and sensitivities, will be in orbit for some years and so have much greater exposure times than the balloon-based experiments which have provided the current data. Another spaced-based detector GAPS [76] has been proposed dedicated for antimatter observations and so also relevant for indirect dark matter searches.

AMS-02 is a high energy particle physics experiment in space scheduled to be installed on the International Space Station by the year 2008 for a three-year mission. After a precursor flight of a prototype detector on board the NASA Space Shuttle in June 1998, the construction of the detector in its final configuration was started and it will be completed by 2006. The AMS-02 detector is a complete particle spectrometer with different elements designed to measure particle type and kinematic parameters. A silicon tracker in a superconducting magnet with a central dipole field of 0.8 T, measures the trajectory of charged particles with an accuracy of $\sim 10\,\mu$m and allows the determination of the charged particle momenta up to a maximum detectable rigidity of ~ 2 TV. The position resolution of the tracker is a factor of ~ 10 better than the gaseous devices used by the balloon-borne magnetic spectrometers. A time of flight system, consisting of four layers of plastic scintillator paddles, triggers on charged particles as well as measuring transit times, energy losses and coordinates. A transition radiation detector provides e^-/hadron separation better than a factor of 100, up to energies of 200 GeV and a ring imaging Cherenkov detector measures the velocity of the charged particles with accuracy better than 1/1000. There is a three-dimensional electromagnetic sampling calorimeter with a total length of $15X_0$, consisting of scintillating fibres sandwiched between grooved lead plates to identify electrons, positrons and photons. The geometric acceptance of AMS is about $1000\,\mathrm{cm}^2$ sr.

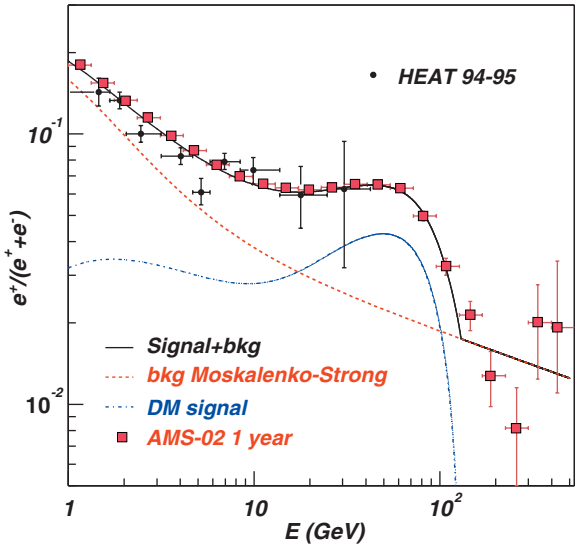

Figure 8. Simulation of the expected AMS-02 performance for the measurement of the positron fraction for a primary e^+ from annihilating neutralinos after 1 year of operation. The figure is from [77].

The PAMELA telescope is also a complete particle spectrometer with a magnetic spectrometer containing a silicon tracker, a time of flight system, an electromagnetic calorimeter and also a neutron detector. The geometrical acceptance of the detector is $\sim$20 cm^2 sr. The detector was launched from Baikonour on 15th June 2006 on the Russian Resurs DK1 satellite.

These two future experiments will provide the sensitivities necessary for indirect searches of dark matter through antimatter cosmic rays and should clarify the existing puzzling measurements. New results will come in the next few years for all the three antiparticle channels: positron; antiproton and antideuteron. For AMS, the positron flux measurement capabilities have been studied [77] indicating that it will be possible to measure the e^+ flux in the energy range 1–400 GeV, with energy resolution of about 2%, statistical uncertainty of 1% at 50 GeV and background rejection power e^+/e^- and e^+/p between 10^4 and 10^6 depending on the energy. The results of the simulation of the positron fraction are shown in figure 8, using the particular choice of SUSY parameters used to fit the data of HEAT shown in figure 2. The antiproton flux will also be accurately measured by AMS up to hundreds of GeV with a good energy resolution and misidentification background, due to p and e^-, below a few per cent. The simulation [78] of the secondary antiproton spectrum detectable by AMS in three years is shown in figure 9 compared with the existing data from previous observations. The detector will be able to reach an antideuteron flux sensitivity of 10^{-7} (m^2 s sr GeV/n)$^{-1}$ which would give between a few and a few tens of antideuteron events depending on the choice of the SUSY model and as a function of the neutralino mass.

The gaseous antiparticle spectrometer (GAPS) is a novel detection approach based on the capture of antimatter in a target with the subsequent formation of exotic atoms. The x-ray emission from the decay of these exotic atoms, together with a correlated pion signature from nuclear annihilation, characterizes uniquely the antiparticle. The experiment, which has been tested [79] on an accelerator beam, is particularly suited for

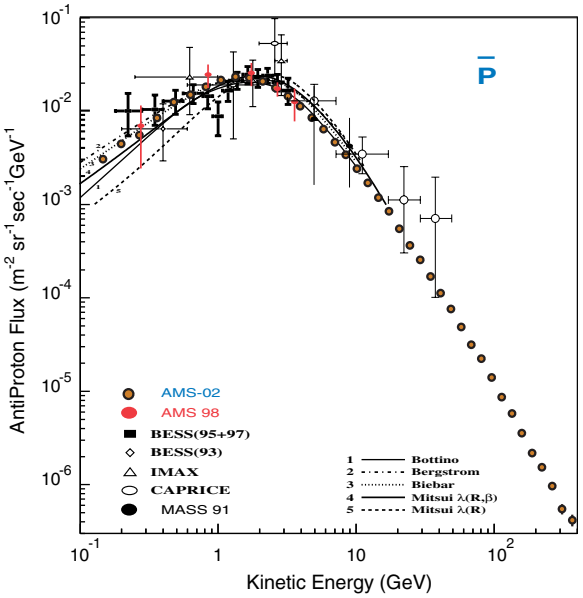

Figure 9. Simulation of the capability of AMS-02 measurements of secondary antiproton flux after 3 years operation compared with existing data. The figure is from [78].

the antideuterons flux measurement in a reduced energy range 0.1–0.4 GeV n^{-1}. GAPS could attain a flux level of 2.6×10^{-9} (m^2 s sr GeV/n)$^{-1}$ and so could explore the lowest energy part of the antideuterons flux, where the secondary antideuterons component is practically absent and where the magnetic spectrometers would be limited by multiple scattering.

7. Indirect search with gamma rays

7.1. High energy gamma ray data

Gamma rays resulting from dark matter annihilations retain the information of their source location in contrast to charged cosmic rays which are diffused by the galactic magnetic turbulence. Hence, gamma rays provide an additional experimental signature in the indirect dark matter searches and further, gamma rays allow searches beyond the local galaxy into other galaxies in the local cluster. The experiments performing dark matter searches with gamma rays are based in space at low energies and on the ground for high energies.

An excess in gamma ray data, measured by the EGRET [80,81] instrument on the Compton gamma ray, has been interpreted as possible evidence for dark matter annihilation in several publications: for example [51, 82–85]. This excess is in a region of the sky located within a few degrees around the position of galactic centre.

EGRET during the 1990s, provided the first gamma-ray sky survey in an energy range from a few MeV to about 20 GeV, resulting in a catalogue [86] of γ-ray sources, many of them unidentified, and measurements of the spectrum of diffuse γ-rays from the inner galaxy [80]. The main γ-ray production mechanism which contributes to the diffuse flux, at energies from 100 MeV to tens of GeV, is the interaction of charged cosmic rays with the interstellar matter which produces π^0 and γ-rays via their decay: $\pi^0 \rightarrow \gamma\gamma$. Another source

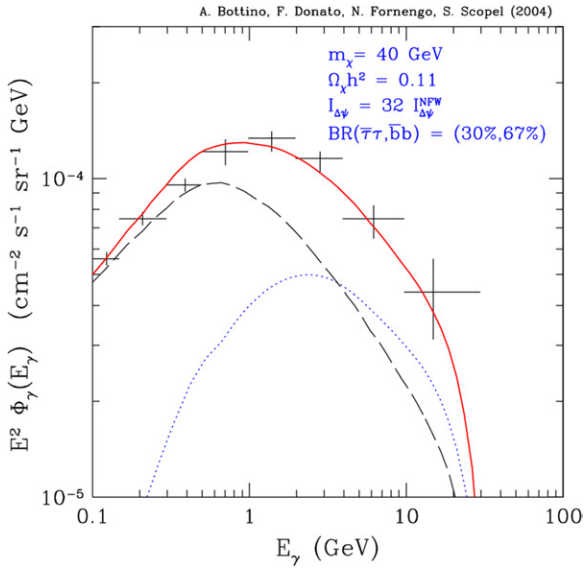

Figure 10. EGRET gamma-ray energy spectrum from the galactic centre. The dashed line is a background calculation as described in the text and the dotted line is the spectrum for a neutralino with mass $m_\chi = 40$ GeV, calculated for a matter density profile with a factor 32 of enhancement with respect to the NFW case. The values of the relic density and of the neutralino annihilation branching ratios are shown. From [82].

of γ-rays is the inverse Compton scattering of cosmic-ray electrons off the interstellar photons where, in particular, energetic electrons may scatter off the infrared, optical and ultraviolet radiation arising from stellar activity and dust. A third γ-rays component originates from electron bremsstrahlung in the interstellar medium. Several detailed calculations [80, 87] have attempted to take into account all these three main γ-rays components giving a deficit of γ-rays compared with the EGRET measurements at the galactic centre and hence possibly indicating an excess due to dark matter annihilation. However, these γ-rays background calculations contain uncertainties from the knowledge of the physics of cosmic rays and of the interstellar medium as well as for the antimatter signals.

A typical analysis of the EGRET excess is shown in figure 10 from Bottino *et al* [82]. The figure shows the measured γ-ray spectra, $\Phi_\gamma(E_\gamma)$, multiplied by E_γ^2, from the galactic centre within galactic latitude and longitude: $|\Delta l| \leqslant 5^\circ$, $|\Delta b| \leqslant 2^\circ$, as a function of the photon energy together with a background estimate and a signal from annihilation. The γ-ray signal has been studied in the framework of an effective MSSM model without gaugino-mass unification at a grand unification scale. For the annihilation of light neutralinos below the thresholds for production of gauge-bosons, Higgs-bosons and t quarks, the γ-rays in the continuum are mainly from the hadronization of quarks and gluon pairs with subsequent π^0 production. The dotted line in figure 10 is the spectrum for a neutralino with mass $m_\chi = 40$ GeV, calculated for a density profile with a factor 32 of enhancement with respect to the NFW case; the dashed line is the gamma ray background calculated in [80], reduced by 10%; the solid line is the total flux, sum of the supersymmetric signal and the background; the experimental points are the EGRET data.

Above a few tens of GeV, cosmic-ray γ-rays can be observed from ground-based telescopes which detect the secondary particles and Cherenkov light produced after the interaction of the

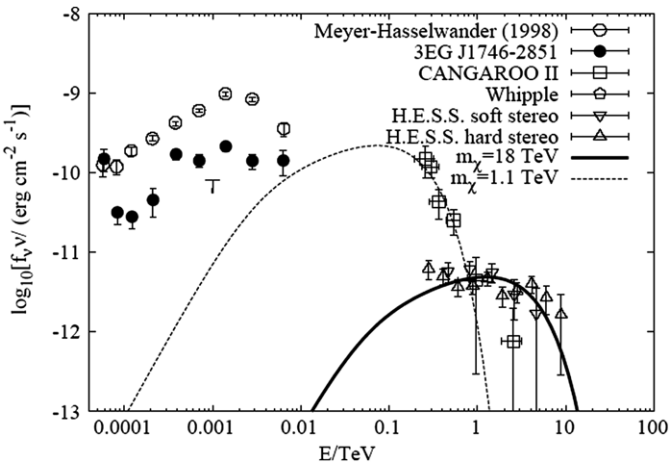

Figure 11. Summary of data from the galactic centre: HESS 2003 (△), CANGAROO (□), EGRET (● and ○), 10 m Whipple telescope of the VERITAS collaboration. Distributions of the spectrum expected from neutralinos with masses 1.1 and 18 TeV c^{-2} are shown. The figure is from [93].

primary γ-rays in the atmosphere. Compared with the direct detection of γ-rays by space-based detectors, the ground Cherenkov detectors have a larger field of view and, necessarily, a higher energy threshold. Atmospheric showers from γ-rays are of the order of 1 per mil of showers caused by charged cosmic rays and so the rejection of hadronic cosmic-ray showers is a critical aspect in the design of γ-ray telescopes. Three telescopes have measured the flux of TeV γ-ray in the region of the galactic centre: CANGAROO [88], Whipple [89] and HESS [90].

The first observation of TeV γ-ray from the galactic centre regions came from the Whipple telescope between 1995 and 2003. The precision of these observations was limited because of the large zenith angles of the source at the Northern Hemisphere location of the instrument. CANGAROO-II, located in Australia, made the first sub-TeV ground detection with a flux measured to have a very steep, $F(E) \propto E^{-4.6\pm0.5}$, spectrum which was incompatible with the Whipple observations. Both these two early observations were consistent with the position of Sgr A* at the galactic centre which has now been identified as a supermassive black hole with intense variable (non-thermal) x-ray and infrared emission.

The HESS telescope array, in Namibia, is a third generation γ-ray instrument with a sensitivity an order of magnitude improved compared to previous telescopes. It consists of four 13 m diameter telescopes operating in stereoscopic coincidence mode and has an energy threshold close to 100 GeV. With HESS, the γ-ray signal was localized within $1'$ and again compatible with the position of Sgr A*. The measurement energy spectrum [91] is consistent with a power law over an extended energy range from ∼125 GeV to ∼20 TeV with spectral index $\Gamma = 2.21 \pm 0.09$ and a flux normalization at 1 TeV of $F_0 = (2.50\pm0.21)\times10^{-12}\,\mathrm{cm}^{-2}\,\mathrm{s}^{-1}\,\mathrm{TeV}^{-1}$. As can be seen in figure 11, the HESS differential spectrum from the galactic centre is in clear disagreement with the CANGAROO-II flux. Further HESS measurements were taken twice during 2004 [92] and confirm the earlier results with higher precision. These data indicate the source has constant flux within statistical and systematic errors on time scales from one year down to ten minutes.

Even with the high resolution of the HESS measurement, the identification of the origin of the radiation remains uncertain given the number of possible sources: the black hole Sgr A*, the supernova remnant Sgr A East, cosmic-ray interactions in the dense matter near the GC or

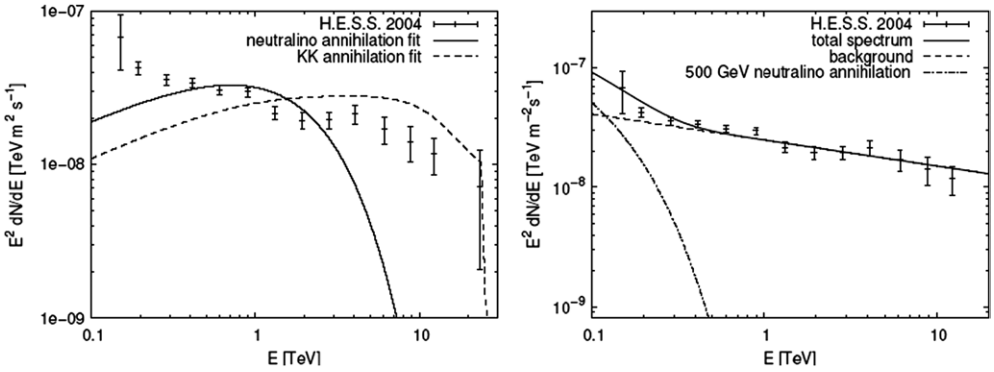

Figure 12. (left) Gamma-ray spectrum for HESS in 2003 and 2004 with fits of annihilation radiation only. The neutralino annihilation spectrum used is from [93] and the Kaluza–Klein annihilation spectrum from [94]. (right) The same data with a two-component fit with a power law plus the annihilation spectrum of a 500 GeV neutralino.

annihilations in a DM halo [91, 92]. Nevertheless several attempts have been made to fit the data with a signal from dark matter annihilations. Figure 11 shows fits to the CANGAROO-II spectrum and the HESS 2003 spectrum with the best fit to the CANGAROO data at 1.1 TeV c^{-2} mass neutralino and the HESS data a mass of 18 TeV c^{-2}; clearly the experimental data are inconsistent. An analysis by Horns [93] finds a good fit to the data with a neutralino of mass 12 TeV c^{-2} with rather high values of the central dark matter density consistent with the formation of a mini-cusp and a halo distribution with a profile $\rho \propto r^{-\alpha}$ with $\alpha > 1$ within 10 pc of the Galaxy Centre. An alternative interpretation [94] fits the data in the Kaluza–Klein dark matter framework also with the assumption of a moderately NFW cuspy (r^{-1}) profile of the dark matter. A fit to the data can be obtained with 10 TeV WIMP particles using a large boost factor of 1000 to reproduce the experimental flux. A more recent analysis of the full HESS spectrum has been performed [95] with the hypothesis that the measured galactic centre spectrum is the sum of two components: a power law astrophysical spectrum plus an annihilation spectrum for a 500 GeV neutralino. Figure 12 shows fits to the HESS 2003 and 2004 data using the annihilation spectra alone and with this two component spectrum. Clearly the annihilation alone cannot describe the data while the two component fit is acceptable. With this latter hypothesis the existence of a dark matter signal in the data cannot be ruled out but clearly the data is dominated by a power law spectrum from an astrophysical origin.

For both the medium energy EGRET data and the high energy HESS data, near and at the galactic centre, any conclusion about a dark matter signal depends totally on a clear understanding of the dominant backgrounds from other sources and so any evidence of the existence of dark matter is very weak. However, interesting new data exists on the neighbouring dwarf spheroid galaxy, Draco, which might contain a relatively large amount of dark matter. Draco, which lies at about 80 kpc from the Earth, has been widely studied and recently the CACTUS experiment [96] has claimed a detection of gamma rays above a 50 GeV energy threshold. Such a detection, if confirmed in the future, is rather exciting since high energy activity is not expected in such a source due to the expected low baryon component and that the fact that it has never been observed at x-ray wavelengths. Profumo and Kamionkowski [97] performed a study of this experimental result in the frame of annihilating DM, with two types of DM profiles and two primary spectra. They show that the standard thermal decoupling picture of the DM candidate with neutralino properties is not compatible with such a detected flux because it would require an annihilation cross-section order of

magnitude too high with respect to the measured value of the cosmological matter density. Interpreting this signal as coming from DM annihilation, they also show that $b\bar{b}$ is disfavoured compared with a $\tau^+\tau^-$ spectrum, when requiring compatibility with limits from EGRET and WHIPPLE.

7.2. Low energy gamma ray data

Some low energy gamma-ray data from the galactic centre region measured by the INTEGRAL satellite has been interpreted by a number of authors as indirect evidence of a low mass dark matter particle, very different from the massive particles so far considered. This data is from the SPI spectrometer on board of the ESA telescope INTEGRAL (INTErnational Gamma-Ray Astrophysics Laboratory) [98] and is a bright 511 keV gamma-ray line from the e^+e^- annihilation originating in the galactic bulge, with a Gaussian shape of $\sim 9^\circ$ FWHM and a copious flux intensity of $9.9^{+4.7}_{-2.1} \times 10^{-4}\,\mathrm{ph\,cm^{-2}\,s^{-1}}$.

The 511 keV γ-ray line, which was first detected in the 1970s [99], is intimately related to the question of the origin of galactic positrons and details of the morphology of the line emission could provide insight to disentangle the different production models. With the advent of the OSSE telescope onboard the Compton Gamma-Ray Observatory a first morphology of the e^+e^- annihilation line was measured at the end of the 1990s. The OSSE observations of at least two emission components, a spheroidal bulge and a galactic disc component, have not been confirmed by INTEGRAL observations. The analysis of the SPI data suggests only an azimuthally symmetric galactic bulge, rather insensitive to a galactic disc component. A recent preliminary analysis [100] of the INTEGRAL imager IBIS/ISGRI, has demonstrated that there is no evidence for 511 keV point sources in the galactic centre with a 2σ upper limit for the flux from any single point source at $1.6 \times 10^{-4}\,\mathrm{ph\,cm^{-2}\,s^{-1}}$.

Both the high injection rate and the quasi-spherical geometry are difficult to attribute to known astrophysical objects or phenomena [101], however for annihilating dark matter models a nearly spherical distribution of annihilations would be natural. Hence, the INTEGRAL detection could support a hypothesis of a signature of light (MeV–GeV) dark matter annihilation into e^+e^- pairs. Although massive dark matter candidates are more popular and these are the main focus of this review, some studies [102] have suggested the predicted dark matter relic density and other constraints would be satisfied even in the hypothesis of a light dark matter candidate. In particular light scalar particles are suggested as a viable possibility.

In [103] the authors discuss the type of halo profile most consistent to the SPI observation and favour a mild cusp in the galactic halo profile with an inner kpc $1/r^\gamma$ profile with $\gamma \sim 0.4$–0.8. The total annihilation cross-section needed to account for the INTEGRAL signal intensity, imposes limits on the mass of the light dark matter candidate, while particle physics constrains its nature. In the case of MeV particles, an S-wave suppressed annihilation cross-section is required and such a cross section would be predicted for interactions in which a new, light, gauge boson was exchanged. For $\sim$100 MeV particles, a nearly constant cross section is needed and for this case the authors suggest that the exchange of new, heavy fermions could be responsible. Different versions of light dark matter particles have been proposed and whether spin-0 or spin-$\frac{1}{2}$, their introduction requires the existence of new coupling and processes responsible for their annihilations. A new interaction mediated by a new neutral light spin-1 gauge boson associated with an extension of the standard model gauge group to SU(3) $\times$ SU(2) $\times$ $U(1)$ $\times$ extra-$U(1)$ is considered in [104].

In order to test the hypothesis of an indirect signature of light dark matter, a new target of observation has been suggested [105]: the Sagittarius dwarf galaxy (SDG), a close-by galaxy dominated by dark matter. SDG is a good place to search for the effect of pure dark matter

since star formation has virtually stopped due to the lack of gas and thus supernovae and hypernovae should be essentially absent. SDG was investigated by INTEGRAL for a limited effective observation time in the year 2003 without detecting any 511 keV emission [106]. The predictions are strongly based on assumptions related to gas extension, environmental conditions (dust density) and shape of the halo profile. Nevertheless, the predicted flux is outside the actual SPI sensitivity and any conclusion must await new observations to increase the exposure and sensitivity to γ-ray emission from SDG.

7.3. Future perspectives in gamma ray detection

The Compton Gamma Ray Observatory, on which EGRET and other gamma ray instruments were based, was de-orbited in 2000. At the present time there are no instruments operating in the same γ-ray energy range but in the coming years data will be available from the GLAST satellites as well as AMS on the ISS and other smaller detectors.

GLAST [107], planned for launch in February 2007, will be a flexible observatory for a wide range of astrophysical phenomena with an imaging γ-ray telescope more capable than instruments flown previously and a secondary instrument for the study of γ-ray bursts. The main instrument, the large area telescope (LAT), will have superior area, angular resolution, field of view, and deadtime that together will provide a factor of $\sim$30 improvements in sensitivity relative to EGRET. The GLAST burst monitor (GBM) will have a field of view several times larger than the LAT and will provide spectral coverage of gamma-ray bursts that extends from the lower limit of the LAT down to 10 keV. The LAT consists of a 4×4 array of identical towers with each $40 \times 40\,\mathrm{cm}^2$ tower comprising a tracker, calorimeter and data acquisition module. The tracking detector consists of 18 XY layers of silicon strip detectors and has high detection efficiency ($>$99%), excellent position resolution ($<60\,\mu$m) and a good signal-to-noise ratio ($>20:1$). The calorimeter in each tower consists of eight layers of 12 CsI bars in a hodoscopic arrangement, readout by photodiodes, with a total thickness of 10 radiation lengths and will allow three-dimensional measurement of the shower profiles for discrimination of hadronic cosmic rays. The anticoincidence shield, which covers the array of towers, employs segmented tiles of scintillator, readout by wavelength-shifting fibres and miniature phototubes.

The advent of GLAST, and also AMS, will allow precise tests of the excess of γ-rays observed by EGRET near the galactic centre. Figure 13 from [108], shows a simulation of the data to be expected from GLAST after two years of operation assuming the result will be the same as the EGRET measured spectrum. To produce this plot a fit is made to the EGRET data with a simplified model where a single dominant annihilation channel is assumed and the neutralino mass is a free parameter. The figure shows the flux which would be measured by GLAST, with the spectrum and normalization for the dark matter source and the normalization for the background as derived from the fit of the EGRET data. Clearly with such statistics GLAST will be able to very accurately measure the energy spectrum; however the interpretation as a dark matter signal will still rely heavily on the background estimates requiring input from many sources. An evaluation of the possibilities of GLAST to observe a dark matter signal from a point-like source at the galactic centre taking into account the HESS results, has been made in [109]. The conclusion of this study is that a dark matter signal with mass above 1.7 TeV would not be observable by GLAST, whereas a signal with mass in the range 20–200 GeV could be possible. The capability of AMS for γ-ray detection have been studied in [74,77,110] and the potential for dark matter detection with γ-rays in [85] in the scenario of mSUGRA with a focus on the expected integrated, instead of differential, flux from the galactic centre.

For the ground based Cherenkov telescopes in the TeV γ-ray region, there are several new projects and upgrades planned. Among the most relevant to the searches for dark

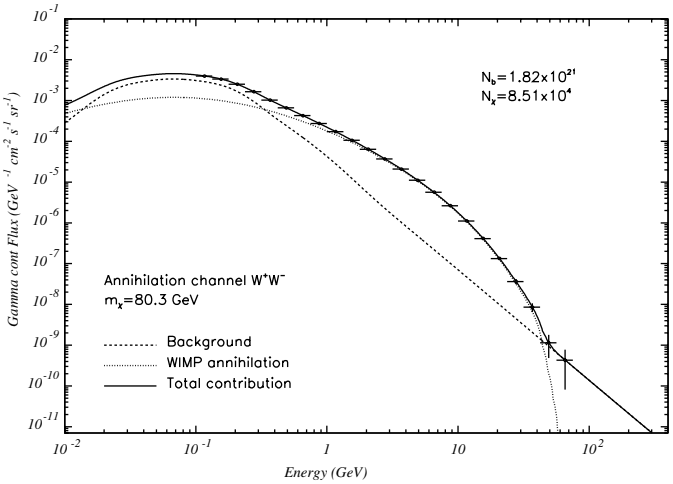

Figure 13. Simulation of a 2 year γ-ray data set which could be obtained with GLAST assuming the spectrum will be the same as that measured by EGRET at the galactic centre. The simulated data points are derived by assuming the angular resolution, $\Delta\Omega = 10^{-3}$ sr, with the energy bin widths $\sim$10% of their central values. The error bars displayed are statistical errors only. The lines are backgrounds and a model with a neutralino mass $m_\chi = 80.3$ GeV and single annihilation channel W^+W^- which fit the EGRET data set well. From [108].

matter are upgrades to HESS and CANGAROO and the MAGIC telescope. HESS currently consisting of four 12 m diameter Cherenkov telescopes will be updated, by adding one larger telescope which, together with the existent ones, will give high sensitivity starting from a lower energy threshold close to 50–100 GeV. Such a perspective is extremely promising in view of complementary observations with the GLAST space telescope within an overlapping energy range from 50 to about 300 GeV. CANGAROO III [111] is an array of four 10 m diameter telescopes being constructed in Woomera, Australia, which started taking data [112] with the intention of moving down the energy threshold from 500 GeV of a single telescope to 100 GeV through the stereoscopic imaging. MAGIC (major atmospheric gamma imaging Cherenkov) [113] at the Roque de los Muchachos astronomical site on the Canary Island of La Palma is the largest and most sensitive air Cherenkov telescope ever built, with a tessellated mirror of 17 m diameter and an energy threshold as low as about 30 GeV (in phase 2 this will be lowered to around 15 GeV). The telescope's more challenging design issues included a mirror support consisting of a carbon-fibre reinforced structure and a low-mass 577 pixel photomultiplier camera with transmission of the analogue signals by optical fibres. Soon MAGIC will be accompanied by a second telescope of equal size, which will then enable the stereoscopic observation of air showers. In the long term, a third telescope with a mirror diameter of 34 m is planned. Among the targets for MAGIC, being located in the Northern hemisphere, is Draco and such observations could confirm, or otherwise, the CACTUS measurements.

8. Indirect search with neutrinos

As for gamma rays, the neutral electric charge of neutrinos means they are not deviated by magnetic fields and so point back to their source. In addition their weakly interacting nature means neutrinos can exit from annihilation sources embedded inside dense matter distributions

such as the centres of the Sun and the Earth. Unfortunately, this same weakly interacting nature means that very massive detectors are needed to detect neutrinos such that, with the present and projected generation of neutrino telescopes, only dark matter concentrations in massive bodies could give detectable annihilation fluxes and those from the galactic halo are negligible. As discussed earlier in section 4, the flux of neutrinos from a spike of dark matter at the galactic centre could be very large but the predictions contain many astrophysical uncertainties. Given this incomplete knowledge of the matter density at the centre of the galaxy and the low mass of the Earth, it is the concentration of dark matter at the centre of the Sun which is the most promising experimental signal.

At present, existing experiments give only upper limits on a possible flux of neutrinos from neutralinos in the Sun, the Earth and the galactic centre. These existing limits come from two classes of detectors: relatively small multipurpose detectors located in caverns underground and large neutrino telescopes in deep water or ice. There are three underground detectors which have given limits on a neutrino flux from the Sun: BAKSAN [114], MACRO [115, 116] and Super-Kamiokande [117, 118] and two neutrino telescopes BAIKAL [119, 120] and AMANDA [121, 122].

Of the underground detectors only Super-Kamiokande is still operational; it consists of 50 000 tons of water instrumented by ∼10 000 photomultipliers and is located in a mine in Japan. The angular resolution of the detector is about 1°. The BAKSAN telescope consisted of ∼3000 liquid scintillator detectors in a cavern in the Soviet Union and had a 2° angular resolution with a mean detected muon energy around 20 GeV. The MACRO detector, in the Gran Sasso underground laboratory in Italy, had 600 tons of liquid scintillator with 20 000 m^2 of streamer tubes and provided an angular resolution of 0.5°. The two operating neutrino telescopes are: BAIKAL at a depth of 1200 m in the water of Lake Baikal in Siberia and AMANDA at a depth of 2000 m in the ice at the South Pole in Antarctica. The BAIKAL detector was operating in 1993 with 36 optical modules and was finished in 1998 with 192 optical modules. Each optical module contains a 15 in photo-tube, 'QUASAR-370', developed specially for the experiment. The detector is located in the Southern part of Lake Baikal at a point where the lake has a depth of ∼1400 m and the distance to the shore is 3.6 km. The light transmission properties of the lake water vary greatly depending on the season due to sedimentation from river in-flow. Typical light absorption lengths are 20 m and light scattering lengths 15 m. The optical modules are deployed on 8 strings arranged at the edges and centre of an equilateral heptagon supported from above by a rigid frame. A special feature of the BAIKAL project, which has facilitated rapid progress, is the fact that the detector is deployed into the water using the platform of frozen surface ice during the winter months. The effective area of the detector is about 2000 m^2 with angular resolution for through-going muons of 4°. AMANDA was installed in stages in holes in the glacial ice made with a hot water drilling technique. The first detector elements were deployed in 1993 at depths of 810 to 1000 m; however, measurements of the ice transparency at those depths showed that the light scattering was unacceptable for operation of a detector. Subsequent strings were deployed at depths of 1500–2000 m where the ice properties are better. In 1997 the AMANDA B10 detector had 300 optical modules on 10 strings and later extra strings were added with improved signal readout technology. The present AMANDA II detector has 19 strings and about 700 optical modules with an effective area of 30 000 m^2 and an angular resolution around 2.5°.

To search for sources of dark matter annihilation these existing experiments select events within a certain cone of the target source. The size of the search cones takes into account the experimental angular resolution and the extent of the expected annihilation region in the source. The experimental limits are then obtained by counting the number of observed events within this search cone and comparing them with the expected number of background events. For

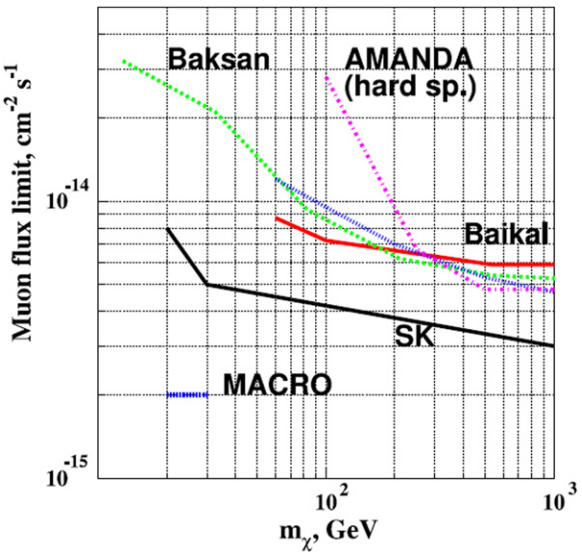

Figure 14. Limits on the excess muon flux from the centre of the Earth as function of the WIMP mass. From [118].

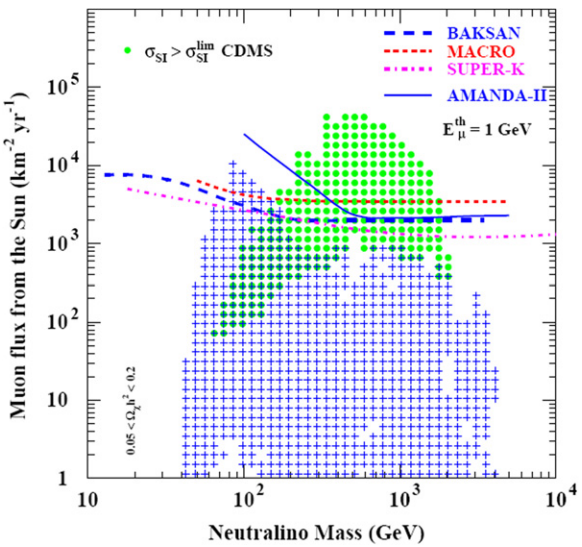

Figure 15. Upper limits on the muon flux from the Sun from neutralino annihilations into W^+W^- as a function of neutralino mass from. The muon energy threshold has been extrapolated to a common value of 1 GeV. The symbols indicate model points in a scan in MSSM parameter space with the dots showing the models disfavoured by recent direct search results from CDMS. The figure is from [122].

neutrino telescopes, the background is usually dominated by the irreducible flux of neutrinos produced by cosmic-ray interactions in the Earth's atmosphere. In figure 14 the limits from the five experiments are compared for a flux of neutralino annihilating at the centre of the Earth. Figure 15 shows a compilation of limits for annihilation in the Sun. It can be seen that in both cases the most stringent limits are set by the Super-Kamiokande experiment even

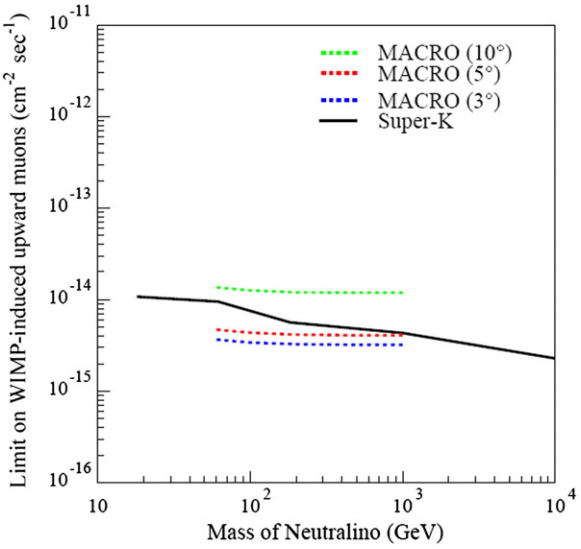

Figure 16. Limits on an annihilation flux from the galactic centre as a function of neutralino mass. From [118].

though the AMANDA experiment is geometrically larger. Among the reasons for this is that at the geographic location of the South Pole where the AMANDA detector is located the Sun is always within $\pm 22^\circ$ of the horizon and at these angles the efficiency of the AMANDA detector is reduced. Only experiments located in the northern hemisphere can observe the centre of the galaxy and figure 16 shows the limits obtained by Super-Kamiokande and MACRO.

Although the existing neutrino indirect dark matter search experiments only have upper limits due to the low detection rates, this technique holds great promise for the future because of the signature of a source of neutrinos with an energy spectrum characteristic of the WIMPs mass emanating from well defined point sources.

8.1. Future perspectives for searches with neutrinos

To complement the sky coverage of AMANDA with a large neutrino telescope in the Northern Hemisphere there are various projects in the Mediterranean Sea. Two neutrino telescope projects, ANTARES [123] and NESTOR [124], are aiming at scientific discoveries with medium sized detectors while the NEMO project is currently undertaking research and development for the construction of a future larger detector. The advantages of sea-water neutrino telescopes are much better angular resolution, up to a factor 10, because of the reduced optical scattering in water compared with glacial ice and a more uniform efficiency due to the homogeneous medium. A disadvantage of a sea-water detector is the higher optical background due to radioactive decay of ^{40}K and light emission from living organisms: bioluminescence. These backgrounds can be overcome in the design of the detector by having a higher density of optical modules and higher bandwidth data readout.

The most advanced sea water neutrino telescope is ANTARES. The ANTARES collaboration started in 1996 to explore sites off the French coast and the site chosen is at $42^\circ 50'$N $6^\circ 10'$E. In the ANTARES detector the optical modules are suspended on individual mooring lines, with a total height of 470 m, which are weighted to the sea bed and held nearly vertical by syntactic foam buoys at the top. The final detector will have 12 lines. The sea bed

at the site is at a depth of 2500 m and the optical modules are positioned at depths between 2400 and 2000 m with each line containing a total of 75 optical modules which are readout to the shore via cables connected to the bottom of the lines. Since November 2001 the site has been linked to the coast via a submarine telecommunication cable 45 km long, to the town of La Seyne-sur-Mer, to the west of Toulon. A series of increasingly complete lines have been used by the collaboration to test the technology chosen. One of these has been operated continually on the site since April 2005 and since March 2006 the first complete line of the detector has been in operation. The construction of the complete detector is in progress and will take place during 2006 and 2007 with full operation of the complete detector expected in 2007. The ANTARES detector will have similar effective area as AMANDA but the angular resolution will be very significantly better reaching around 0.2° above energies of 10 TeV.

A neutrino telescope, ICECUBE [125], with a sensitive volume of the order of 1 km^3 is already in construction at the South Pole. ICECUBE will be installed at the same location at the South Pole as AMANDA and uses the same technology of the latest AMANDA string. ICECUBE will have 80 lines each with 60 optical modules. The first line of the detector was successfully deployed and operated during 2005 and up to 10 more lines will be installed in early 2006. It is expected the detector will be complete by 2011. Because of the larger lever arm compared with AMANDA the angular resolution of ICECUBE will be $<1^\circ$. A design study for a larger undersea telescope in the Mediterranean Sea, with a similar effective area as ICECUBE, is being started by the KM3NET consortium [126].

A study of the capability of future neutrino telescopes of performing indirect searches for dark matter has been made by Bertin *et al* [127]. This study compares the expected experimental sensitivities to models in constrained MSSM (CMSSM or mSUGRA). Figure 17(*a*), from this study, compares the predicted sensitivities of ANTARES and ICECUBE for a muon flux originating from neutrinos emitted in neutralino annihilations in the Sun. The points are the fluxes expected from particular sets of MSSM parameters with the different colours indicating different relic densities for these parameters according to the legend in the figure. Figure 17(*b*) allows a comparison between the sensitivity of the neutrino indirect search and the sensitivity for direct search experiments for the same model points. This figure gives the interaction cross-section of neutralino in the direct search detectors together with existing limits from the CDMS experiment and various projected limits for the future generation of direct search detectors such as EDELWEISS II and ZEPLIN MAX (for details see [127]). From this plot it can be seen that the future neutrino indirect search experiments have similar sensitivities to those of the planned future direct search experiments in this region of the model parameter space.

9. Combined analyses of results

In sections 6 and 7 the anomalies in the observed energy spectra of positrons, antiprotons and gamma rays have been presented together with attempts by several authors to interpret the data as evidence of dark matter. The various fits to the data shown so far treat the data from the different particle species independently; however, if indeed the explanation for the data anomalies were to have a common cause due to dark matter annihilations, then the fluxes of different species must be correlated.

An analysis of the available data has been made by De Boers *et al* [128] considering these correlations. This analysis uses the gamma ray data close to the galactic centre from EGRET, positron from HEAT as well as from the AMS shuttle flight and antiproton data from BESS. The data is fitted with a background simulation plus a neutralino annihilation spectrum. Acceptable fits can be obtained with a range of supersymmetry parameters. Figure 18 shows examples of

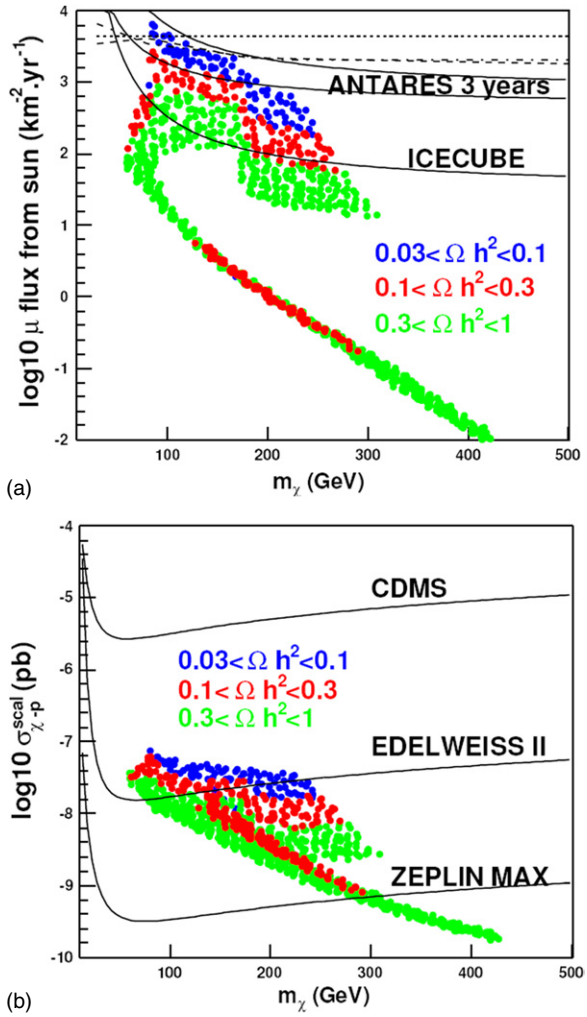

Figure 17. (*a*) Neutrino indirect detection experimental sensitivities on muon fluxes, with a 5 GeV threshold, coming from χ annihilations in the Sun. The points are models in mSUGRA parameter space with the different colours indicating points with different ranges of relic densities for the neutralino dark matter. The figure is from [127]. (*b*) The interaction cross-section for direct dark matter experiments for the same model points as (*a*). The lines are existing and expected future sensitivities of direct search experiments. From [127].

the fits with a value of the neutralino mass at 207 GeV. These results indicate an enhancement (boost) factor of the dark matter density in the halo by a factor of $\sim$6. In the figures the yellow area is the background and the red area the neutralino signal. The fit probability is greatly improved when the dark matter signal is included compared with background alone. This analysis shows a consistent picture of all the data possible but as in all such analyses the question of backgrounds remains.

Any signal of dark matter from the galactic centre must have correlated fluxes between gamma-rays and neutrinos since the region is transparent to both particle species and for any given model, the particle spectra in the annihilation process can be related. Bertone *et al* [129]

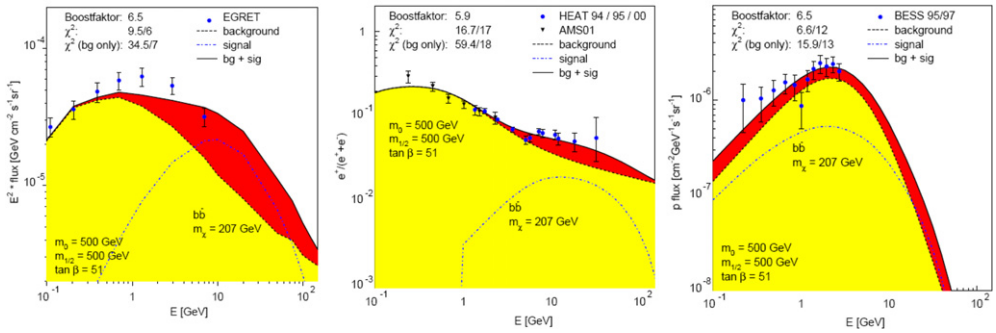

Figure 18. (left). Gamma ray spectrum with contributions from nuclear interactions (grey/yellow) and neutralino annihilation (dark/red) for a neutralino mass of 207 GeV; (centre) corresponding positron spectrum; (right) corresponding antiproton spectrum. From [128].

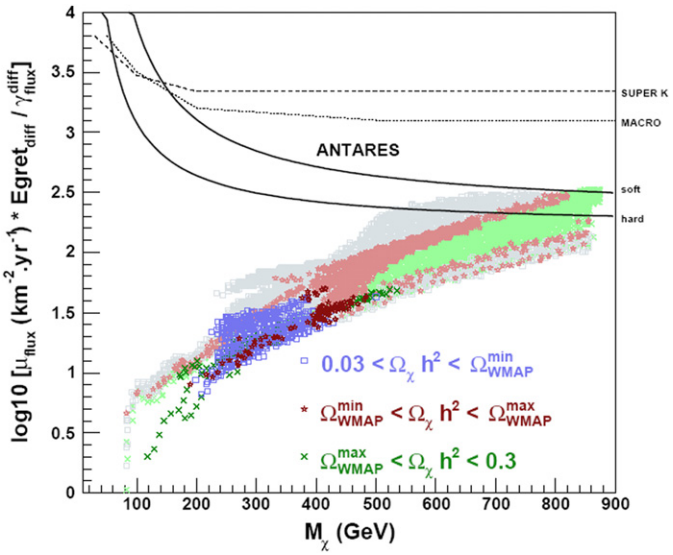

Figure 19. Neutrino induced muon flux from the galactic centre using the EGRET gamma ray flux as an upper limit for the normalization. The coloured points correspond to CMSSM model points in ranges of relic density, with the very light grey shade being the models unfavoured by the latest muon anomalous magnetic moment results. From [129].

have used the EGRET flux from the region of the galactic centre as an upper limit to the gamma-ray and neutrino fluxes from dark matter annihilations. This analysis considers models in the CMSSM parameter space and calculates the number of neutrinos produced in the annihilation relative to the number of gamma-rays. An upper limit on the neutrino flux is calculated by taking the ratio of neutrinos to gamma-rays and normalizing to the EGRET flux. The result is shown in figure 19, giving the muon flux induced in a detector by this neutrino flux. The points in the plot are coloured according to the value of the dark matter relic density and shown relative to the range of measurements of WMAP: $\Omega^{\min}h^2 = 0.095$, $\Omega^{\max}h^2 = 0.119$. The conclusion is that a galactic centre neutrino flux could only be detected by an experiment such as ANTARES for masses above ∼800 GeV.

10. Discussion of different channels

The indirect dark matter searches with the various channels discussed, e^+, $\bar{p}$, $\bar{D}$, γ and ν, have different experimental advantages and problems. In the annihilations, the five channels are produced with differing fluxes, depending on the model details, but generally with higher rates of γ and ν due to their being pion decay products. In some models there are two body final states which could give a unique energy line and a clear experimental signature but usually the rates are too low in these modes to be interesting. Backgrounds also are different for the different channels according to the production rates in cosmic-ray interactions in the interstellar medium.

The experiments detecting the charged particle channels must be carried out above the atmosphere in balloons and satellites and so the effective detection areas are limited; nevertheless, data exists in the positron and antiproton modes which have provoked interest. An essential feature of charge particle channels is the fact that the particles are deviated by magnetic fields such that there is no correlation in the data with the source location. Further, both the signal and background are produced according to the matter distribution in the galaxy and propagate to Earth through the interstellar magnetic fields and interstellar medium. The uncertainty in the knowledge of the interstellar environment gives large uncertainties in both signal and background predictions. Experimentally, the data in the positron channel from HEAT has been taken seriously because the signal could have a different energy spectrum from the background, a situation which is not the case for the antiproton data. For the searches with antimatter, some authors have concluded that the antideuteron channel could be the most promising due to the very low background; however the signal rates are also very low such that large detection areas are needed which can only come from new experiments. It is likely that confidence in the background estimates will continue to be the main problem for the interpretation of any antimatter data.

For the γ channel, at low and medium energies the data comes from satellites with similar limitations on effective detection area as the charged cosmic rays but at high energies ground based telescopes are used which have high detection areas. Being a neutral particle, the γ channel can be associated with the source and avoids the complications of the propagation in the galaxy. The data in this channel below 10 GeV from EGRET is concentrated within a few degrees of the centre of the galaxy whereas the data from the gamma telescopes such as HESS above 200 GeV is more precisely located at the galactic centre. The data of 511 MeV γ from INTEGRAL comes from an extended spherical region at the galactic centre. Interpreted as dark matter, these three γ-ray signals imply totally different natures for the particle candidates. However, given the complexity of this region in the galaxy, there is doubt as to the actual location of the radiation in all cases and it is quite possible their origins are from three different astrophysical sources. A source of dark matter annihilation radiation could exist at the galactic centre but the γ-ray channel alone may not be enough to yield convincing evidence.

The neutral neutrino has the same direction association advantage as the gamma-ray but in addition can exit from sources at the cores of massive objects giving a unique experimental signal at very precise locations. The difficulty for the neutrino channel is the need for massive devices because of the low neutrino interaction cross-section; the same unique property of the neutrino which gives the clear experimental signature also being the cause of the detection limitations. At the present time only experimental upper limits exist and new detectors under construction are needed to advance this area. It is possible that a northern hemisphere neutrino telescope will be able to correlate measurements with the gamma ray telescopes to reach conclusions on the galaxy centre source. However, it is the Sun which is the most promising and unique target for dark matter searches with neutrinos. A positive signal from this source with sufficient statistics would yield two uncontroversial experimental signatures: a well defined

energy spectrum compatible with a particular mass and a point source where backgrounds from other sources are low and easily calculable. These features are unique among all the possible search channels thereby making the neutrino mode a very interesting possibility for the future.

11. Conclusions

This review has investigated the status of experimental searches for dark matter particles via pair annihilations into positrons, antiprotons, antideuterons, gamma rays and neutrinos. In the positron, antiproton and gamma ray channels, features in the data have been associated with possible dark matter signals in a number of publications. This subject has a wealth of literature and only a sample of the interpretations have been presented in this paper.

It is seen that the existing data could be compatible with a signal for dark matter annihilation, in the form of neutralino from supersymmetric theories, or a Kaluza–Klein particle from theories with extra dimensions, with the masses of these particle between 40 and 500 GeV. In all cases the possible signals must be extracted from the data using estimates of the backgrounds from astrophysical sources and from cosmic-ray spallation interactions with interstellar material, both of which have significant uncertainties. Further, the experimental data have systematic normalization errors which may be difficult to take properly into account in the diverse analyses. For these reasons, it is clear that the excesses in the present data are not generally considered as serious evidence of dark matter. In the antideuteron and neutrino channels only upper limits exist. For all channels it is likely that no significant experimental advances will happen without new experiments.

For the antiparticle searches, the PAMELA satellite is expected to be launched in 2006 with AMS possibly following soon afterwards. These experiments will rapidly yield precisely measured positron and antiproton spectra which will verify the existing data spectrum. With these data it is likely that both statistical and systematic errors will be small and understood; however, it is likely the uncertainties in the background estimates will remain. The novel antiparticle experiment, GAPS, is only at the proposal stage but promises interesting advances in the antideuteron channel. There is great activity in the γ-ray field with advances in the HESS, MAGIC and VERITAS ground based telescope and the GLAST launch planned for 2007. The northern hemisphere neutrino telescope ANTARES will be complete in 2007 and the large southern hemisphere telescope ICECUBE around 2011. All these new projects will give major improvements in the quality of the data with great expectations for discoveries.

In the various models for dark matter particles, the different indirect search channels as well as the direct search techniques can all have dominant interest in some parts of the possible parameter phase space. Hence all techniques are equally valid until more experimental knowledge is gained as to the nature of dark matter.

References

[1] Zwicky F 1933 *Helvetica Phys. Acta* **6** 110
[2] Sofue Y and Rubin V 2001 *Ann. Rev. Astron. Astrophys.* **39** 137
[3] Bahcall N *et al* 2003 *ApJS* **148** 243–74
[4] Bennett C L *et al* (WMAP Collaboration) 2003 *Astrophys. J. Suppl.* **148** 1
Spergel D N *et al* 2003 *Astrophys. J. Suppl.* **148** 175
Spergel D N *et al* 2006 *Preprint* astro-ph/0603449
[5] Astier P *et al* 2006 *Astron. Astrophys.* **447** 31
[6] Susskind L 1984 *Phys. Rep.* **104** 181
[7] t'Hooft G (ed) 1979 *Under the Spell of the Gauge Principle* 352, Advanced Series in Mathematical Physics (Singapore: World Scientfic)
[8] Bertone G, Hooper D and Silk J 2005 *Phys. Rep.* **405** 279

[9] Bergstrom L 2000 *Rep. Prog. Phys.* **63** 793
[10] Fayet P 1977 *Phys. Lett.* B **69** 489
[11] Goldberg H 1983 *Phys. Lett.* **50** 1419
[12] Feng J L, Matchev K T and Moroi T 2000 *Phys. Rev.* D **61** 075005
[13] Giudice G F, Luty M A, Murayama H and Rattazi R 1998 *J. High Energy Phys.* JHEP12(1998)027
[14] Dine M, Nelson A E and Shirman Y 1995 *Phys. Rev.* D **51** 1362
[15] Hewett J and March-Russell J 2004 *Phys. Lett.* B **592** 1
[16] Servant G and Tait T 2003 *Nucl. Phys.* B **650** 391
[17] Agashe K and Servant G 2005 *J. Cosmol. Astropart. Phys.* JCAP02(2005)002
[18] Kaluza T F E 1921 *Sitzungsberichte Preussische Akademie der Wissenschaften* **96** 69
[19] Klein O 1926 *Z. Phys.* **37** 895
[20] Arkani-Hamed N, Dimopoulos S and Dvali G R 1998 *Phys. Lett.* B **429** 263
Arkani-Hamed N, Dimopoulos S and Dvali G R 1999 *Phys. Rev.* D **59** 086004
[21] Randall L and Sundrum R 1999 *Phys. Rev. Lett.* **83** 3370
Randall L and Sundrum R 1999 *Phys. Rev. Lett.* **83** 4690
[22] Appelquist T, Cheng H C and Dobrescu B A 2001 *Phys. Rev.* D **64** 035002
[23] Gascon J 2005 *Preprint* astro-ph/0504241
[24] Michie R W 1963 *Mon. Not. R. Astron. Soc.* **125** 127
[25] Press W H and Schechter P 1974 *Astrophys. J* **187** 425
[26] Lynden-Bell D 1967 *Mon. Not. R. Astron. Soc.* **136** 101
[27] Navarro J F *et al* 1996 *Astrophys. J.* **462** 563
[28] Moore B *et al* 2001 *Phys. Rev.* D **64** 063508
[29] Berezinsky V S, Gurevich A V and Zybin K P 1992 *Phys. Lett.* B **294** 221
[30] Berezinsky V S, Dokuchaev V and Eroshenko Y 2003 *Phys. Rev.* D **68** 103003
[31] Gnedin O Y, Kravtsov A V, Klypin A A and Nagai D 2004 *Astrophys. J.* **616** 16
[32] Gao L, Loeb A, Peebles P J E, White S D M and Jenkins A 2004 *Astrophys. J* **614** 17–25
[33] Silk J and Stebbins A 1993 *Astrophys. J.* **411** 439
[34] Lavalle J, Pochon J, Salati P and Taillet R 2006 *Preprint* astro-ph/0603796
[35] Stoehr F, White S D M, Tormen G and Springel V 2002 *Mon. Not. R. Astron. Soc.* **335** L84
[36] Diemand J, Moore B and Stadel J 2005 *Nature* **433** 389–91
[37] Berezinsky V S, Dokuchaev V and Eroshenko Y 2006 *Phys. Rev.* D **73** 063504
[38] Bertone G, Zentner A R and Silk J 2005 *Phys. Rev.* D **72** 103517
[39] Holmberg J and Flynn C 2004 *Mon. Not. R. Astron. Soc.* **352** 440
[40] Olling R P and Merrifield M R 2001 *Mon. Not. R. Astron. Soc.* **326** 164
[41] Schödel R *et al* 2002 *Nature* **419** 694
[42] Gerhard O 2000 *Preprint* astro-ph/0010539
Gerhard O 2001 *Galaxy Disks and Disk Galaxies* ASP Conference Series vol 230 ed J G Funes, S J and E M Corsini (San Francisco: Astronomical Society of the Pacific) pp 21–30
[43] Gondolo P and Silk J 1999 *Phys. Rev. Lett.* **83** 1719
[44] Ullio P *et al* 2001 *Phys. Rev.* D **64** 030504
[45] Press W H and Spergel D N 1985 *Astrophys. J.* **296** 679
[46] Freese K 1986 *Phys. Lett.* B **167** 295
Krauss L M, Srednicki M and Wilczek F 1986 *Phys. Rev.* D **33** 2079
[47] Drees M and Nojiri M M 1993 *Phys. Rev.* D **47** 376
[48] Sjöstrand T *et al* 2001 *Comput. Phys. Commun.* **135** 238
[49] Corcella G *et al* 2001 *J. High Energy Phys.* **0101** 10
[50] Tasitsiomi A and Olinto A V 2002 *Phys. Rev.* D **66** 083006
[51] Bertone G, Servant G and Sigl G 2003 *Phys. Rev.* D **68** 044008
[52] Barwick S W *et al* 1997 *Astrophy. J. Lett.* **482** L191
DuVernois M A *et al* 2001 *Astrophy. J.* **559** 296
[53] Coutu S *et al* 1999 *Astropart. Phys.* **11** 429 and reference therein
[54] Webber W R, Lee M A and Gupta M 1992 *Astrophy. J.* **390** 96
[55] Eichler D and Maor I *Preprint* astro-ph/0501096
[56] Busching I *et al* 2005 *Astrophys. J.* **619** 314
[57] Turner M S and Wilczek F 1990 *Phys. Rev.* D **42** 1001
Kamionkowsky M and Turner M S 1991 *Phys. Rev.* D **43** 1774
Kane G L *et al* 2002 *Phys. Lett.* B **536** 263
Baltz E A and Edsjo J 1999 *Phys. Rev.* D **59** 023511

[58] Baltz E A *et al* 2002 *Phys. Rev.* D **65** 063511
[59] Hooper D and Kribs G D 2004 *Phys. Rev.* D **70** 115004
[60] Hooper D and Servant G 2005 *Astropart. Phys.* **24** 231
[61] Moskalenko I V *et al* 2003 *Astrophys. J.* **586** 1050
[62] Maurin D *et al* 2001 *Astrophys. J.* **555** 585
[63] Donato F, Fornengo N and Salati P 2000 *Phys. Rev.* D **62** 043003
[64] Ullio P *Preprint* astro-ph/9904086
[65] Orito S *et al* 2000 *Phys. Rev. Lett.* **84** 1078
Maeno T *et al* 2001 *Astropart. Phys.* **16** 121
[66] Aguilar M *et al* 2002 *Phys. Rep.* **366** 331
[67] Boezio M *et al* 2001 *Astrophys. J.* **561** 787
[68] Bergström L, Edsjö J and Ullio P 1999 *Astrophys. J.* **526** 215
[69] Donato F, Maurin D, Salati P, Barrau A, Boudoul G and Taillet R 2001 *Astrophys. J.* **536** 172
[70] Donato F, Fornengo N, Maurin D, Salati P and Taillet R 2004 *Phys. Rev.* D **69** 063501
[71] Fuke H *et al Preprint* astro-ph/0504361
[72] Duperray R *et al* 2005 *Phys. Rev.* D **71** 083013
[73] Profumo S and Ullio P 2004 *J. Cosmol. Astropart. Phys.* JCAP07(2004)006
[74] Lamanna G 2003 *Mod. Phys. Lett.* A **18** 28
[75] Sparvoli R (PAMELA Collaboration) 2004 *Proc. 35th COSPAR Assembly* **283**
Adriani O *et al* 2002 *Nucl. Instrum. Meth. Phys. Res.* A **478** 114
[76] Hailey C J *et al* 2004 *Nucl. Instrum. Methods* B **214** 122
Mori K *et al* 2002 *Astrophys. J.* **566** 604
[77] Choutko V, Lamanna G and Malinin A 2002 *Int. J. Mod. Phys.* A **17** 1817
see also Gast H, Olzem J and St Schael *Preprint* astro-ph/0605254
[78] Choutko V 2002 *Proc. Suppl. Nucl. Phys.* B **113** 170
[79] Hailey C J etal *Preprint* astro-ph/0509587
[80] Hunter S D *et al* 1997 *Astrophys. J.* **481** 205
[81] Mayer-Hasselwander H A *et al* 1998 *Astron. Astrophys.* **335** 161
[82] Bottino A *et al* 2004 *Phys. Rev.* D **70** 015005
[83] Berezinsky V, Bottino A and Mignola G 1994 *Phys. Lett.* B **325** 136
[84] Bergstrom L *et al* 1998 *Astropart. Phys.* **9** 137
[85] Jacholkowska A *et al Preprint* astro-ph/0508349
[86] Hartman R C *et al* 1999 *Astrophys. J. Suppl. Ser.* **123** 79
[87] Strong A W, Moskalenko I and Reimer O 2000 *Astrophys. J.* **537** 763
[88] http://www.physics.adelaide.edu.au/astrophysics/index.html
Tsuchiya K *et al* 2004 *Astrophys. J.* **606** L115
[89] http://veritas.sao.arizona.edu/VERITAS_whipple.html
Kosack K *et al* 2004 *Astrophys. J.* **608** L97
[90] http://www.mpi-hd.mpg.de/hfm/HESS/HESS.html
Aharonian F *et al* 2004 *Astrophys. J.* **425** L13
[91] Rolland L and Hinton J (HESS collaboration) Proc. ICRC 2005 Conf.
[92] Hinton J and Aharonian F 2005 *Galactic Center Newsletter* **21** 5
[93] Horns D 2005 *Phys. Lett.* B **607** 225
Horns D 2005 *Phys. Lett.* B **611** 297 (erratum)
[94] Bergstrom L, Brinkmann T, Eriksson M and Gustafsson M 2005 *Phys. Rev. Lett.* **94** 131301
[95] Ripken J *et al* (HESS Collaboration) Proc. ICRC 2005 Conf.
[96] Marleau P 2005 *Proc. TAUP Conf. (Zaragoza, Spain, September 2005)*
[97] Profumo S and Kamionkowski M 2006 *J. Cosmol. Astropart. Phys.* JCAP03(2006)003
[98] Jean P *et al* 2003 *Astron. Astrophys.* **407** L55
[99] Johnson W N and Haymes R C 1973 *Astrophys. J.* **184** 103
[100] De Cesare G *et al Preprint* astro-ph/051123
[101] Casse M and Fayet P *Preprint* astro-ph/0510490
[102] Bohem C, Ensslin T A and Silk J *Preprint* astro-ph/0208458
Bohem C and Fayet P *Preprint* hep-ph/0305261
[103] Bohem C *et al* 2004 *Phys. Rev. Lett.* **92** 101301
[104] Fayet P 2004 *Phys. Rev.* D **70** 023514
[105] Hooper D *et al* 2004 *Phys. Rev. Lett.* **93** 161302
[106] Cordier B *et al* Preprint astro-ph/0404499

[107] http://glast.gsfc.nasa.gov/
[108] Cesarini A *et al* 2004 *Astropart. Phys.* **21** 267
[109] Zaharijas G and Hooper D 2006 *Phys. Rev.* D **73** 103501
[110] Lamanna G 2002 *Proc. Suppl. Nucl. Phys.* B **113** 177
Lamanna G 2002 *Proc. Suppl. Nucl. Phys.* B **119** 119
[111] Kubo H *et al* 2004 *New Astron. Rev.* **48** 323
[112] Enomoto R *et al Preprint* astro-ph/0510300
[113] http://magic.mppmu.mpg.de
[114] Suvorova O V 1999 *Proc. 2nd Int. Conf. on Physics beyond the Standard Model* (Berlin: Springer)
Suvorova O V 1999 *Preprint* hep-ph/9911415
[115] Ahlen S *et al* (MACRO Collaboration) 1999 *Phys. Lett.* B **357** 481
[116] Ambrosio M *et al* (MACRO Collaboration) 1999 *Phys. Rev.* D **60** 082002
[117] Fukada S *et al* (Super-Kamiokande Collaboration) 2003 *Nucl. Instrum. Methods* A **501** 418
[118] Desai S *et al* (Super-Kamiokande Collaboration) 2004 *Phys. Rev.* D **70** 083523
[119] Belolaptikov I A *et al* (BAIKAL Collaboration) 1997 *Astropart. Phys.* **7** 263
[120] Aynutdinov V *et al* (BAIKAL Collaboration) 2005 *Proc. 29th Int. Cosmic Ray Conf. (Pune, India)*
Aynutdinov V *et al* 2005 *Preprint* astro-ph/0507709
[121] Andrés E *et al* (AMANDA Collaboration) 2001 *Nature* **410** 441
[122] Ackermann M *et al* (AMANDA Collaboration) 2006 *Astropart. Phys.* **24** 459
Ackermann M *et al* 2005 *Preprint* astro-ph/0508518
[123] http://antares.in2p3.fr
Aslanides E *et al* 1999 *Preprint* astro-ph/9907432
Amram P *et al* 2002 *Nucl. Instrum. Methods* A **484** 369
[124] http://www.nestor.org.gr
Tzamarias S *et al* 2003 *Nucl. Instrum. Methods* A **502** 150–4
Anassontzis E *et al* 1994 *Nucl. Instrum. Methods* A **349** 242
Anassontzis E *et al* 2002 *Nucl. Instrum. Methods* A **479** 439
[125] Ahrens J *et al* (ICECUBE Collaboration) 2004 *Astropart. Phys.* **20** 507
[126] http://km3net.org
[127] Bertin V, Nezri E and Orloff J 2002 *Eur. Phys. J.* C **26** 111
[128] de Boer W, Herold M, Sander C and Zhukov V 2004 *Eur. Phys. J.* C **33** 981
de Boer W, Herold M, Sander C and Zhukov V 2004 *Preprint* hep-ph/0309229
[129] Bertone G, Nezri E, Orloff J and Silk J 2004 *Phys. Rev.* D **70** 063503

Modern Physics Letters A

ASTROPHYSICS AND PARTICLE PHYSICS IN SPACE WITH THE ALPHA MAGNETIC SPECTROMETER

GIOVANNI LAMANNA

CERN,European Organization for Nuclear Research,
CH-1211 Geneva 23, Switzerland
Giovanni.Lamanna@cern.ch

The Alpha Magnetic Spectrometer (AMS) is a high energy particle physics experiment in space scheduled to be installed on the International Space Station (ISS) by the end of 2005 for a three-year mission. After a precursor flight of a prototype detector on board of the NASA Space Shuttle in June 1998, the construction of the detector in its final configuration is started and it will be completed by 2004. The purpose of this experiment is to provide a high statistics measurement of charged particles and nuclei in rigidity range 0.5GV to few TV and to explore the high-energy ($>$ 1 GeV) gamma-ray sky. In this letter we describe the detector layout and we present an overview of the main scientific goals both in the domain of Astrophysics: cosmic-ray origin, age and propagation and the exploration of the most energetic gamma-ray sources; and in the domain of Astroparticle: the anti-matter and the dark matter searches.

Keywords: space station; cosmic rays; gamma rays; dark matter; antimatter.

1. Introduction

During the last ten years the rate of particle physics discoveries at accelerators is significantly reduced, possibly because of the limited energy scale which can be tested at existing or future facilities. A growing attention is turning to particle astrophysics using new experimental techniques aiming to extend by orders of magnitude the sensitivities reached by past experiments[1]. In particular, a number of space-borne experiments have been proposed to measure, with high accuracy, the composition of primary high energy cosmic rays (CR), searching for new phenomena not accessible to present accelerators. The Alpha Magnetic Spectrometer (AMS) is a particle physics experiment in space. It is a large acceptance, superconducting magnetic spectrometer which will measure, on board of ISS, charged CR spectra of individual elements up to Z$\sim$ 26 and up to TeV region, high energy γ rays up to hundreds of GeV. It will provide the most sensitive search in CR for the existence of antimatter nuclei and for the indirect studies of the origin of dark matter.

2. The AMS-01 Space-Shuttle mission

The primary objective of the flight[2] was the validation of the technical design. During the period June 2^{nd} to June 12^{th} 1998 the Shuttle Discovery performed 154

orbits at an inclination of 51.7^o and at an altitude varying between 390 to 350 km. AMS-01 operated successfully collecting a total of about 100 Million triggers which allowed high statistics measurement of cosmic rays in space. Such measurements enabled, for the first time, the systematic study of the behavior of primary CR near Earth in the rigidity interval from 0.1 GV to 200 GV, at all longitudes and latitudes up to $\pm 51.7^o$, and at the orbital altitude where they were not biased by atmospheric shielding. The main results on CR proton, deuteron, helium, electron, positron fluxes, as well as a new limit for antihelium, $\overline{He}/He \simeq < 1.1 \times 10^{-6}$ in the rigidity range 1-140 GV, are summarized elsewhere [2] [3] [4]. The rigidity measurement and the knowledge of the incident direction of the particle have been used to distinguish in the observed spectra, the contributions of the primary particles and atmospheric secondaries[5]. The knowledge of the primary proton and helium fluxes, as well as the under geomagnetic cut-off secondary proton flux, is important for the interpretation of neutrino oscillation results based on the observation of atmospheric neutrinos[6] [7].

3. The AMS-02 detector

Following the Shuttle flight data analysis, a significant upgrade of the detector, AMS-02, has been planned. The major elements of the AMS-02 detector are shown in Fig.1 and consist of a superconducting magnet (MG), a gaseous transition radiation detector (TRD), a silicon tracker (TR), time of flight hodoscopes (ToF), a ring imaging Cerenkov detector (RICH), an electromagnetic calorimeter (EMC), a star tracker system (AST) and anticoincidence veto counters (ACC).

The superconducting magnet has the shape of a cylindrical shell with 1.2 m inner diameter and 0.8 m length, containing a series of 6 pairs of racetrack shaped coils distributed circumferentially and two main dipole coils. The coils system provides a central dipole field of 0.8 T, and their geometry enables to contain the residual stray field outside the magnet preventing magnetic torque resulting from the interaction with the Earth's field. All superconducting coils are situated inside a vacuum tank and operated at 1.8 K with super-fluid helium. The magnet coils and the toroidal helium storage vessel with a volume of about 2500 liters are screened from heat radiation by a series of cold helium gas cooled thermal shields. The magnet will be launched cold, at the super-fluid helium operational temperature[8].

The AMS-02 silicon tracker detector[9] [10] [11] is the first application in space of the high precision silicon technology developed in Italy by INFN for the ALEPH[12] and L3[13] vertex detectors at the Large Electron-Positron collider (LEP). It has a ~ 7 m^2 large area. It is composed of 2300, high purity, $41.360 \times 72.045 \times 0.300$ mm^3, double-sided silicon microstrip sensors. The silicon sensors are grouped together, for readout and biasing, in ladders of different lengths to match the cylindrical geometry of the magnet. The ladders are arranged in eight circular layers and arrayed transverse to the magnet axis. The tracker measures the trajectory of relativistic singly charged particles with an overall accuracy of about $10\,\mu$ in the bending coordinate and $30\,\mu$ in the non-bending one, allowing the determination of the charged particles

momenta up to a Maximum Detectable Rigidity (MDR) $\sim$ 2 TV. It also provides measurements of the particle energy loss. The high modularity, low voltage levels ($<$ 100 V), and gas-free operation of the devices are well suited for operation in space. The tracker position resolution represents a factor $\sim$ 10 improvement with respect to the different gas devices used by the balloon-borne superconducting magnetic spectrometers.

The time of flight system consists of four layers of plastic scintillator paddles, two above (of 8 counters each) and two below (of 10 and 8 counters respectively) the magnet. The scintillation light is collected by 2 light guides per side and the

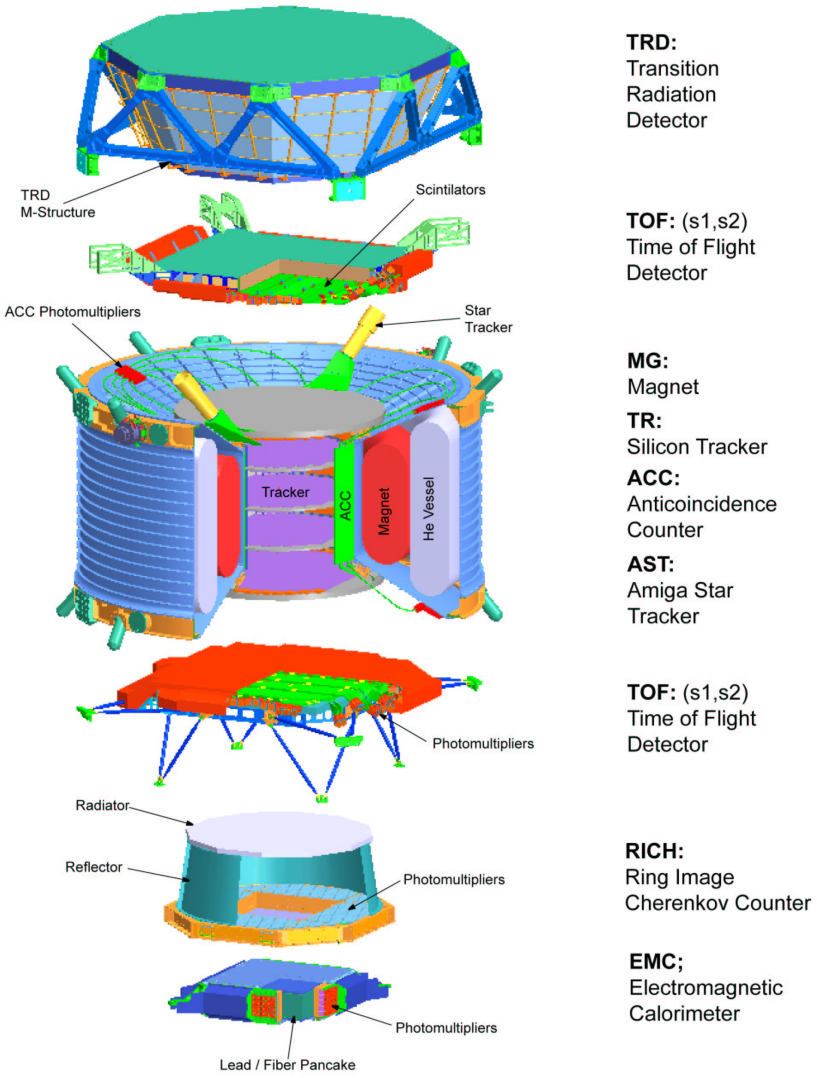

Fig. 1. Schematic exploded view of the AMS-02 experiment on the ISS.

PMT anode and dynode signals are summed together. The ToF system is devoted to trigger every charged particle traversing the spectrometer. It measures singly charged particle transit times with an accuracy of 140 psec and also yields energy loss and coordinate measurements[14].

The TRD is situated on top of the spectrometer and consists of twenty 12 mm thick foam radiator arrays, interleaved by arrays of 6 mm diameter gas proportional tubes filled with Xe/CO_2 mixture. The system is arranged in a conically shaped octagon structure, closed by two honeycomb plates and held by a M-frame (also shown in Fig.1) which is attached to the spectrometer support structure. The TRD provides the e^-/hadron separation better than one hundred up to energy 200 GeV as well as precise charged particle coordinate measurements[15].

The RICH detector is installed below the last ToF plane and consists of a 2 cm thick aerogel radiator with refraction index of 1.05, a reflection mirror and pixel type photo-tubes matrix for the light detection. It assures the measurement of the velocity of the single charged particle with accuracy better than per mil as well as particle flight direction measurement[16].

The EMC detector is situated at the bottom of AMS. It is a three-dimensional electromagnetic sampling calorimeter with total length of $15X_0$, consisting of 1 mm diameter scintillating fibers sandwiched between grooved lead plates[17].

The electronics for the readout of subdetectors is being build based on a total of 650 microprocessors (2-to-4 fold redundant)[18]. The AMS02 detector construction is due to be completed by 2004 and installed in ISS by end 2005 / early 2006. Remote Payload Operations Command Centers (POCC) on the ground segment will allow to monitor and control the experiment. Data will be continuously transmitted at same rate which it is acquired by AMS (2 Mbit/s). The data will also be collected in crew quarters of the Space Station by a dedicated computer, the AMS Crew Operation Post (ACOP).

4. Astrophysics with AMS

4.1. *Cosmic-ray Astrophysics*

Precise measurements of cosmic-ray spectra are relevant for constraining models for galactic CR production, acceleration and propagation. Hadrons are the main component in cosmic rays. Part of them are believed to have a primary origin in a wide energy range. Other nuclei are considered absent at the CR sources and believed to be generated by spallation of heavier nuclei against the interstellar matter. Hydrogen and helium constitute about 99% of the hadronic CR. Precise knowledge of their fluxes is needed to calculate rare secondary CR yield such as antiprotons and positrons, to compute the diffuse gamma ray background spectrum and it is a crucial input for all neutrino calculations, related to solar and atmospheric neutrino deficits and oscillations studies. Although extensively measured for decades, only recent precise measurements have been able to pin down the uncertainties in a limited energy range. The AMS-01 H and He energy spectra are the most pre-

cise measurements in the kinetic energy-per-nucleon range 1 GeV/n $\leq$ E$_k$/n $\leq$ 100 GeV/n with estimated uncertainties of about 5% for protons and 10% for He nuclei. The only existing measurements in the range 100 GeV/n $\leq$ E$_k$/n $\leq$ 1 TeV/n are performed using a balloon-borne calorimeter[19] for protons and a balloon-borne RICH counter[20] for He nuclei. The estimated uncertainty for such measurements is about 25%. The CR proton spectrum assumed in the atmospheric neutrino calculation, which previously followed the Ryan et al.[19] spectra[21], at least at energy around 100 GeV/n, has been revisited[7] following now the more precise AMS-01 and BESS measurements. Fig. 2 shows such a comparison including other previous cosmic-ray protons measurements[7].

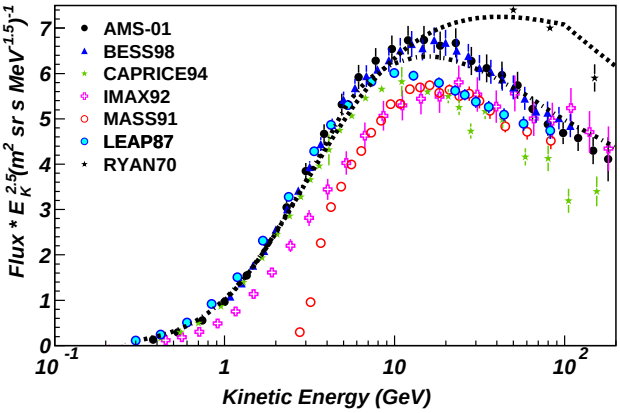

Fig. 2. AMS-01 and other previous measurements of the cosmic proton spectrum, multiply by $E_k^{2.5}$. Simulated p fluxes assumed in atmospheric neutrino calculations are also shown: dotted curve previous the 1998 data from AMS-01 and BESS; dashed-dotted curve updated best fit to AMS-01 and BESS fluxes.

Measurements of the CR element abundances compared to those in the Solar System have helped to understand qualitatively the source composition and propagation properties of galactic CR. Among all nuclei above helium, the most abundant heavier nuclei are C, N and O followed by Fe. This composition is similar to what is observed in the solar system from meteoritic samples and solar spectroscopic measurements. They are related to the injection spectra and can constrain the primary acceleration mechanisms of cosmic rays. AMS-02 will offer the opportunity of a detailed and precise measurements of the most abundant CR components and with particular sensitivity at high energy, determining the fluxes of individual elements with electric charges 1 $\leq$ Z $\lesssim$ 26 in the energy range 0.1 GeV/n $\lesssim$ E$_k$/n $\lesssim$ 1 TeV/n. After 3 years of data taking AMS-02 will collect 10^8 H, 10^7 He and 10^5 C nuclei with energies above 100 GeV/n.

The largest discrepancy in the comparison between CR composition and the Solar System is an overabundance of lighter nuclei as Li, Be, and B, and sub-Fe nuclei in cosmic rays. This feature can be accounted as a result of spallation collisions

of primary heavier nuclei with the interstellar gas. The fluxes of secondaries (absent at the CR sources) and, the ratio of these secondary species to the primaries which produce them through their path in the interstellar matter (ISM) define the amount of material traversed by the CR since their acceleration. AMS-02 will provide precise high-energy measurements by identifying 10^4 B with energies above 100 GeV/n and thus precisely measuring the ratio of boron to its primary carbon up to 1TeV/n. The expected B/C sensitivity after just 6 months of data taking is shown in Fig.3 together with recent measurements. The simulation is performed according to a diffuse-re-acceleration model in which an Alfvèn speed $v_A = 20$ km s^{-1} is assumed and the propagation region is bounded by a Galactocentric radius $R_h = 30$ kpc and a distance from the galactic plane $z_h \sim 1$ kpc[22].

Concerning the stable light isotope measurements, AMS-02 will be able to identify ^{2}H nuclei from protons and ^{3}He from ^{4}He nuclei in the energy range 0.1 GeV/n $\lesssim$ E$_k/n \lesssim$ 10 GeV/n. The few and less precise ^{2}H and ^{3}He nuclei measurements[23] [2] at energy E$_k/n >$ 1 GeV/n leaves room for speculations and predictions based on non-standard propagation models. Precise high-energy measurements will be critical. After 3 years, AMS-02 will identify 10^8 ^{2}H and ^{3}He nuclei. The sensitivity on ^{3}He/^{4}He after 1-day exposure is shown in Fig.3 and it is compared to recent measurements[24] [25]. In this case the ratio is simulated according to a more classical cosmic-ray transport Leaky Box Model (LBM) with a rigidity dependent path-length distribution[26].

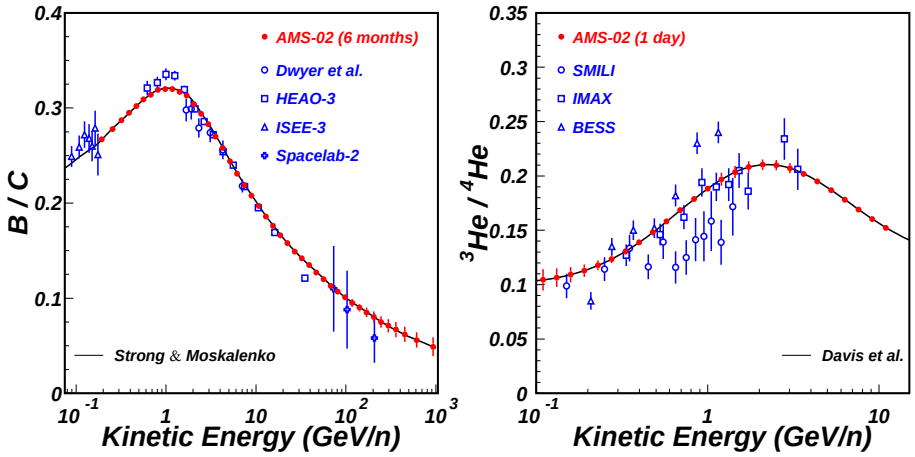

Fig. 3. AMS–02 expected performance on B/C ratio (left) after 6 months of data taking and ^{3}He/^{4}He ratio (right) after 1 day of data taking compared to recent measurements.

Among all unstable secondary nuclei in cosmic rays, ^{10}Be is the lightest isotope having a half-life (t$_{1/2} = 1.51$ Myr) comparable with the confinement time of cosmic rays in the galaxy. The ratio of the unstable to stable secondary nuclei can be used

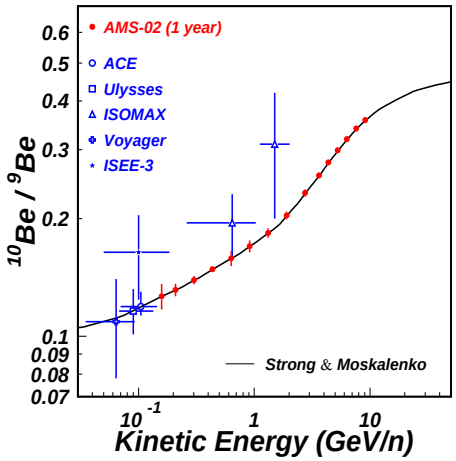

Fig. 4. AMS-02 expected performance on ^{10}Be/^{9}Be ratio after 1 year of data, taking compared to recent measurements.

to determine the cosmic ray confinement time in the galaxy and, in diffusion models, the effective thickness of the galactic halo. AMS-02 will be able to separate ^{10}Be from the stable ^{9}Be in the range 0.15 GeV/n $\lesssim E_k/n \lesssim$ 10 GeV/n. After 3 years, AMS-02 will collect 10^5 ^{10}Be in this energy range. The expected sensitivity on ^{10}Be/^{9}Be after 1 year of data taking is shown in Fig.4 and compared to recent measurements[27]. An unconfirmed measurement[28], which would imply an anomalously high value for this ratio (^{10}Be/^{9}Be > 1), is not included in the figure. The ratio has been simulated according to the propagation model described in Ref.22. The expectation is in average constrained by the assumption on the halo size. The enhancement of the ^{10}Be/^{9}Be ratio at high energy is due to the Lorentz factor. The limiting value at high energy corresponds to the production ratio, whereas at lower energy the ratio decreases according to the combined effect of the finite confinement time of cosmic rays in the galaxy and the effective ^{10}Be half-life $\gamma t_{1/2}$[29].

One more major experimental challenge in cosmic-ray astrophysics is the precise measurements of electrons. Although they represent only a small fraction, O(%), of the CR reaching the earth, the astrophysical importance of their flux measurement and charge composition is fully recognized and has triggered a continuous experimental effort during the last 40 years[30]. The electron flux is dominated by the negative component (90% at 1 GeV) pointing to a primary origin for the bulk of e^-, directly injected at sources, and to a secondary origin of e^+, resulting from nuclear collisions in the ISM. Electrons are distinct from all other CR particles by the absence of hadronic interactions, and, because of their low mass, by significant electromagnetic energy losses during propagation through the galaxy. The imprint of such energy losses on the energy spectrum of electrons allows for interesting conclusions about the containment and source distribution of cosmic rays in the galaxy.

The measurements of electron flux are affected by large statistical and systematic uncertainties and various direct measurements of the e^- spectrum from magnetic spectrometers can differ even by a factor 2. Thanks to its high acceptance and excellent background rejection for e^- in the energy range 1-300 GeV, AMS-02 will detect up to 10^4 electrons with E > 100 GeV, determining a striking improvement in the accuracy of electrons flux and in the composition determination[31].

4.2. *Gamma-ray Astrophysics*

To detect photons in the AMS experiment[32] two complementary methods can be applied[33]. The first method or *conversion mode* consists in the identification and reconstruction of e^+e^- pairs from photons converting somewhere in the material upstream of the first silicon tracker layer[a]. The second method or *single photon mode* is based on the detection of photons in the electromagnetic calorimeter. The event signature is the presence of an electromagnetic shower in EMC, while almost nothing is found in other AMS sub-detectors.

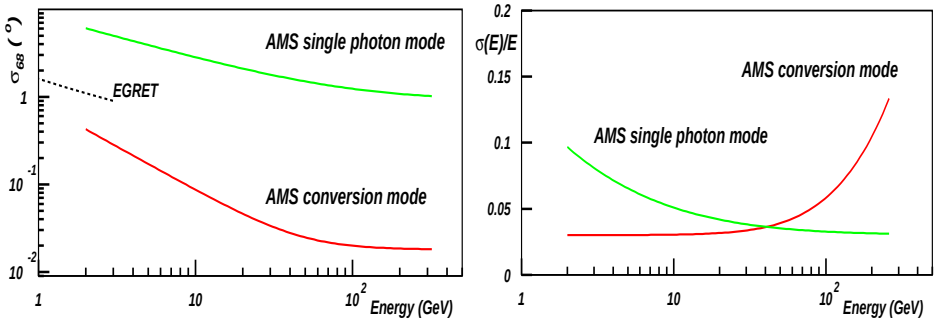

Fig. 5. Angular resolution (left) and energy resolution (right) as a function of energy.

An O(10^6) background rejection level, against the most abundant cosmic rays (p, He, C, e^-), is obtained, allowing a background-to-γ-signal ratio of the order of a few per cent. The average detector acceptance as a function of the γ-ray energy, after all selection criteria are applied, is comparable for the two methods (0.05-0.06 m^2 sr each). The γ energy resolution improves with the energy in the *single photon mode* (few per cent at 400 GeV) while it is dominated by tracker measurement errors in the *conversion mode* (< 15% at 400 GeV) (Fig.5, right). An other important figure of merit is the angular resolution (Fig. 5, left). The EMC detector would allow a 68% containement angular resolution of the order of a degree. More promising resolution as a function of energy can be obtained by the *conversion mode*: $\sigma_{68} \simeq 0.015^o$ at 400 GeV. AMS photons detection capability will be essential for answering fundamental astrophysical questions. For example investigate the mechanism of gammas ejection

[a]The material in front of the first silicon tracker plane, consisting of the TRD, the first two layers of ToF scintillators, and mechanical supports, represents $\simeq 0.3X_0$[31].

from the highest energy particle accelerators, the Pulsars[34]. In Fig.6 we compare the AMS-02 sensitivity to EGRET observation of the higher energy part of the Vela spectrum. In one year sky survey it will be possible to distinguish between the two ejection models: *Polar Cap* and *Outer Gap*[35].

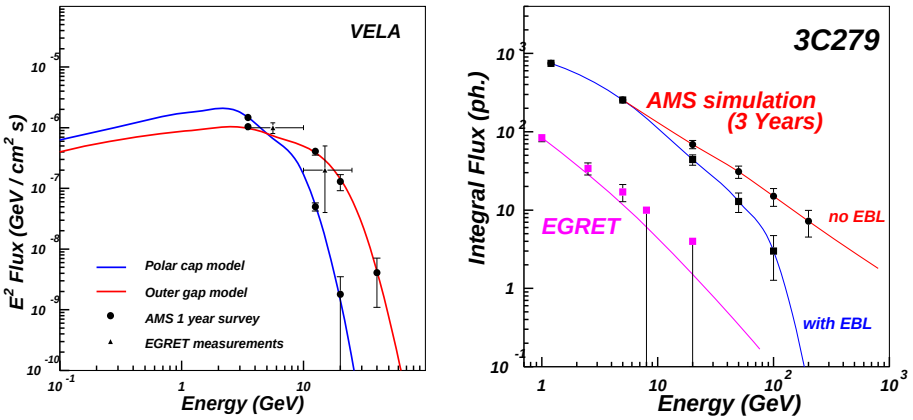

Fig. 6. Vela spectrum expected from AMS in one year (left). 3C279 spectrum expected from AMS in three years γ-ray sky survey (right). EGRET measurements are also shown.

Among the most brilliant astrophysical objects are the Active Galactic Nuclei, AGN. The observational characteristics and classification of AGN vary with the angle between the line of site and the jet axis. When the jet points towards Earth, the resulting violent object is called blazar. EGRET[36] has detected more than 60 blazar AGNs with redshifts ranging from 0.03 to 2.3. All of them will be observed by AMS with high significance. AMS will detect some hundreds such objects possibly back to the time of their formation[37]. This will permit to study more in detail blazars' subclasses and to investigate whether their emissions make up the *isotropic* high-energy gamma radiation detected by EGRET. By observing blazars at various redshifts between the EGRET energy range and that now observed by ground-based Cherenkov telescopes, AMS will explore the first part of the important energy range where the spectra of blazars are expected to cut off. These cut-off could be due either to intrinsic absorption or to interaction of blazar gamma rays with photons of the extragalactic infrared-UV background light (EBL effect[38])(Fig.6).

Gamma-ray bursts (GRBs) are the most intense and most distant high-energy gamma-ray sources (redshift up to $\sim$5) uniformly distributed in the Universe. At GeV energies, the brightest GRBs are 1000-10000 times brighter than the brightest AGN with emitted power of $\sim 10^{51}$ erg. Extrapolating the most energetic and brightest GRBs' spectra detected by EGRET[39] up to the AMS energy range, tens to hundreds of GRBs' photons are expected to be detected depending on the time duration of the bursts. Based on some theoretical assumptions, AMS sensitivity is expected to allow the detection of the high energy tail of up to 10 GRBs per year.

5. Astroparticle Physics with AMS

5.1. *Anti-Matter search*

The mainstream of theoretical studies of the dynamical production of a baryon asymmetry during the early universe, is the baryogenesis approach[40]. Baryogenesis models require conditions which are not presently supported by particle physics experimental data: to date the expected baryon non-conservation and large levels of CP-violation have not been observed. New alternative theory, even if correct, will be untestable because it would be beyond experimental reach like, for example, GUT baryogenesis. According to some alternative models some interesting distant local

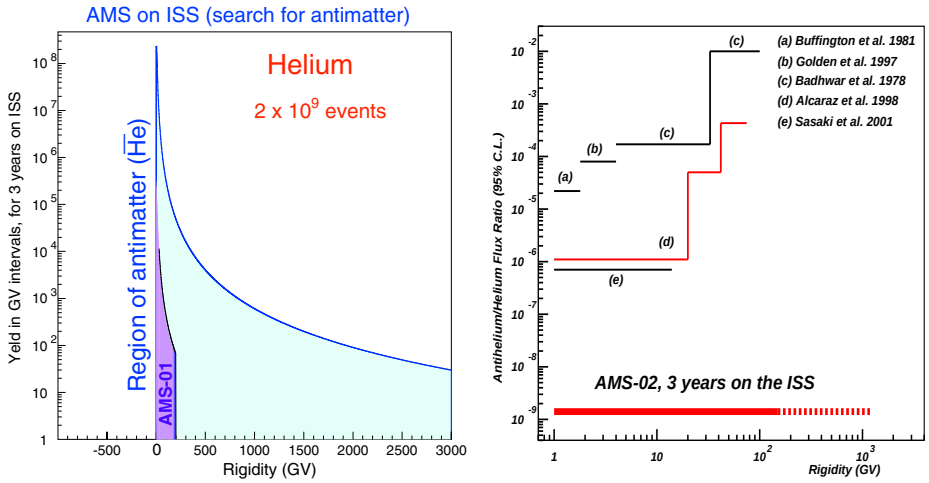

Fig. 7. Left) AMS-02 CR He expected statistics vs AMS-01 data. Right) AMS-02 model independent $\overline{He}/He$ expectation compared with results from AMS-01 (d) and other experiments. For rigidity $>$ 100 GV the prediction is less evident because of the limited resolution.

distribution of antimatter domains can be permitted in our universe. They would pollute space with cosmic antimatter particles which would diffuse through space and eventually reach the vicinity of the Earth. According to modern calculations, the secondary origin of antihelium in cosmic rays is totally negligible and therefore, the detection of just one antihelium nucleus would be a convincing proof of the existence of these domains. Last 20 years of cosmic ray searches for antinuclei have given negative results. A major objective of the AMS physics program is to search for cosmic-ray antinuclei. AMS measures the absolute value of the particle's charge independently in the Tracker, RICH and ToF sub-detectors. The signed particle momentum is measured by the tracking system in the 0.8Tm^2 magnetic field. The velocity is measured by the ToF, TRD and RICH sub-detectors. The AMS detector has a large acceptance (0.5 m^2 sr) and the low material budget along the particle trajectory minimizes the probability for large angle nuclear scattering which could be confused with the signal of anti-nuclei. The AMS-02 sensitivity for He nuclei on

the ISS will be $\sim 10^3$ times larger than AMS-01 (Fig.7, left). In Fig.7 the AMS-02 95% C.L. expectation limit on $\overline{He}/He$ is compared with previous limits from AMS-01[2] and other experiments (see Ref.41). The expected upper limit after 3 years of exposure will reach $\overline{He}/He \simeq 10^{-9}$. By its rigidity range and acceptance, AMS-02 will provide the best sensitivity to these searches.

5.2. *Dark-Matter indirect search*

Astrphysical observations indicate that the Universe may include a large amount dark matter of unknown origin (DM). It could be composed of non-baryonic Weakly Interacting Massive Particles (WIMP). A favored WIMP candidate is the Lightest Supersymmetric Particle in R-parity conserving SUSY models. AMS offers a unique opportunity to study simultaneously SUSY dark matter in four decay channels from the neutralino annihilation: e^+, $\overline{p}$, $\overline{D}$ and γ.

Positron Flux: The AMS-02 e^+ flux measurement capabilities have been recently studied[31]: AMS-02 will be able to measure the e^+ flux in the energy range 1 to 400 GeV, with energy resolution of about 2%, statistical uncertainty of 1% at 50 GeV and high average background rejection power e^+/e^- and e^+/p between 10^4 and 10^6 depending on the energy. An example of three years simulated measurement of secondary e^+ spectrum, according to the theoretical parameterization of Ref.42 and Ref.31 is shown in Fig. 8.

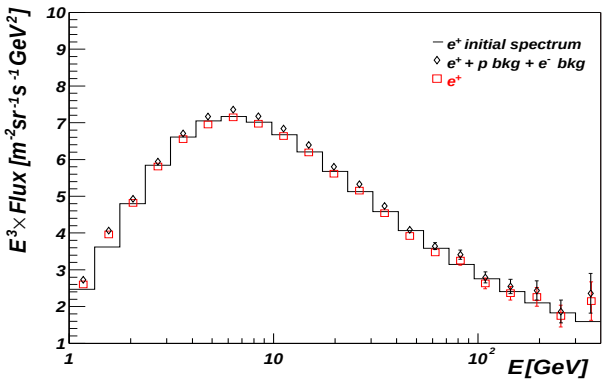

Fig. 8. AMS-02 three years measurement of cosmic e^+ spectrum, multiplied by E^3. The signal and the signal+background estimation are shown and compared to the theoretical spectrum.

Many attempts to predict e^+ production by annihilating neutralinos χ_1^0 in the galactic halo have been published. In recent works[43] the neutralino annihilation has been simulated according to several models, varying 7 free parameters of the MSSM. In each model the e^+ interstellar flux has been calculated by means of a standard diffusion model. Following these calculations, two models assuming m_χ being 336 GeV and 130.3 GeV respectively have been investigated in Ref.44 by means of DARKSUSY. The e^+ signal from χ annihilation was boosted by factors 11.7 and

54.6 to fit the HEAT data, adding the simulated primary positron fluxes to the secondary e^+ spectrum[42]. The results of the simulation of the positron fraction, as expected to be measured by AMS-02 in 1 year, are shown in Fig.9 for this particular choice of SUSY parameters.

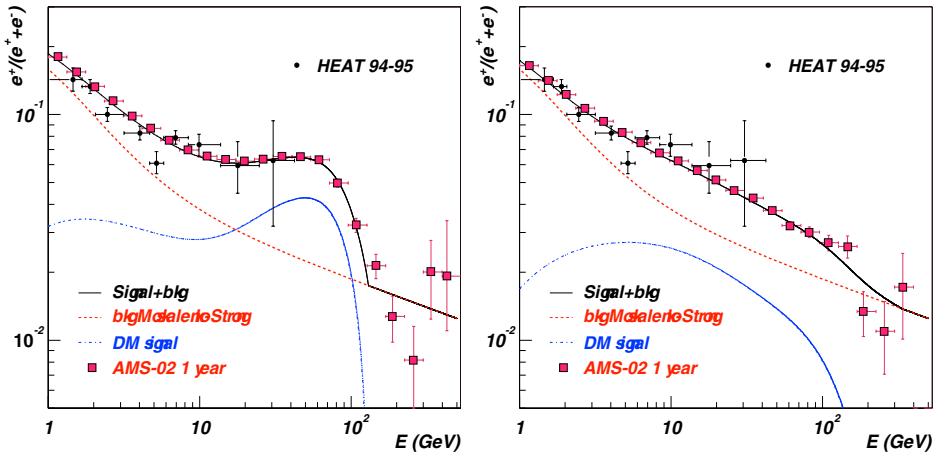

Fig. 9. AMS-02 e^+ fraction in the case of a primary e^+ from annihilating χ.

Antiproton Flux: Measurements of CR $\bar{p}$ flux are few and, at high energy, not very precise. Several attempts of interpreting these measurements have shown the difficulty of deducing $\bar{p}$ propagation properties since an exotic origin such as neutralino annihilation cannot be excluded[45]. For high m_χ a high-energy excess of $\bar{p}$ would be measurable[46] even if it would imply $\bar{p}$ spectrum distortions less evident than in the case of the e^+ spectrum (Fig.10, left). At energy below few GeVs, considerable uncertainties spoil the knowledge of the $\bar{p}$ energy spectrum of the secondary component. AMS-02 will measure accurately the $\bar{p}$ spectrum up to hundreds GeV with a few percent energy resolution[48] and an irreducible background (due to p and e^-) to signal ratio below a few percent level. The simulation of secondary $\bar{p}$ spectrum detected by AMS-02 in three years is shown in Fig.10 together with previous measurements[49].

Antideuteron Flux: Recently a few GeVs secondary production of $\overline{D}$ by annihilating neutralinos has been considered[50]. For some supersymmetric configurations the expected flux of primary antideuterons, below few GeV/n is several orders of magnitude above the background. Due to its large acceptance AMS-02 offers the unique opportunity of exploring the $\overline{D}$ channel for the indirect evidence of supersymmetric dark matter.

Gamma-ray Flux: Gamma rays might be a possible indirect signature of dark matter through processes of direct annihilation like $\chi\chi \rightarrow \gamma\gamma$ and $\chi\chi \rightarrow Z\gamma$, and the continuum photons flux mainly due to the decay of π^0 mesons produced in jets from neutralino annihilations. The γ-ray flux at Earth depends on two factors: the

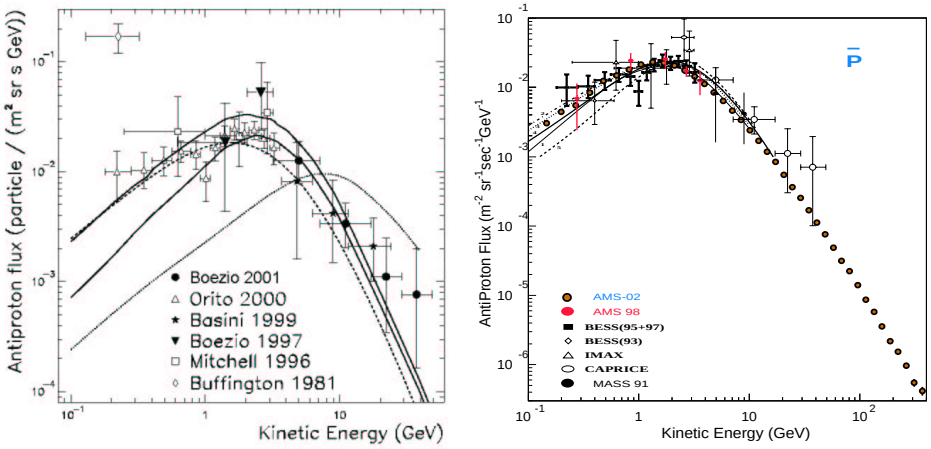

Fig. 10. Left) Example of predicted distortions of the $\bar{p}$ flux due to χ signal according to particular chioices of SUSY paramters and m_χ (see Ref.46, 47). Right) AMS-02 3 years secondary $\bar{p}$ flux compared with previous measurements.

average annihilation rate of gammas which is related to supersymmetrical models and therefore with a wide range of variability and to the neutralino density along the line of sight of the Galactic Center (GC), which is related to the astrophysical model of the halo dark matter profile. Halo models with strong cusps in the central region which predict increasing dark matter density as one approaches the GC, $\rho \propto 1/r^\gamma$, are obviously more promising. Among these the Navarro-Frenk-White (NFW) requires γ being 1.0. The AMS potential for the DM detection in the channels with γ in final state has been performed in the minimal supergravity scenario mSUGRA[51].

A *wild scan* in the mSUGRA parameter space has been obtained by simulating three thousand models in the $0.025 \lesssim \Omega_\chi h^2 \lesssim 0.3$ region. The framework is fully

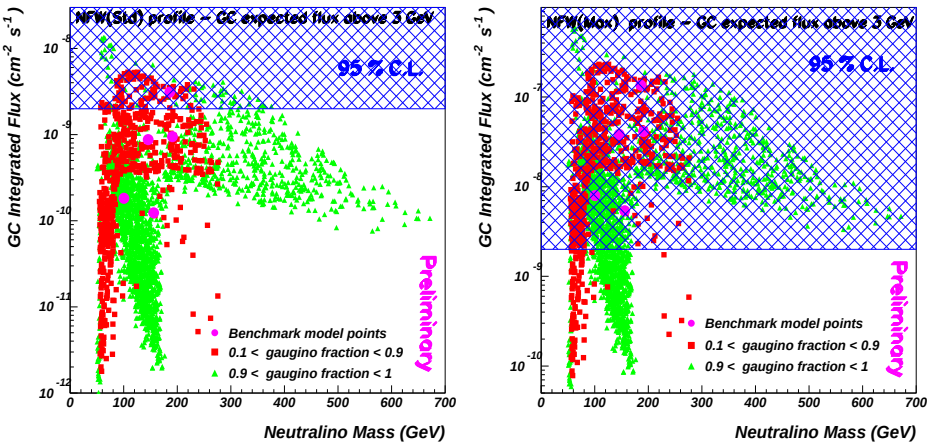

Fig. 11. The integrated γ flux from GC as a function of m_χ for mSUGRA, large m_0 scan as expected for 2 NFW DM halo profiles.

specified by the five parameters: m_0, $M_{1/2}$, A_0, tanβ, sgn(μ). Here m_0, $M_{1/2}$ and A_0 are the universal scalar mass, gaugino mass, and trilinear scalar coupling. They are assumed to arise through supersymmetry breaking in a hidden sector at GUT scale. The conditions of the performed simulations are detailed elsewhere[51]. Some SUSY benchmark models[52], proposed to provide a common way of comparing the SUSY discovery potential of the future accelerators such as LHC or Linear Colliders, have been also examined. Values of the expected number of photons in AMS-02 in 3-year exposure are obtained for different parameterizations of the Galactic Center (GC) dark matter halo. In particular in Fig.11, the mSUGRA scan of the γ flux as a function of the m_χ is shown for two NFW parameterizations: the standard one $NFW(std)$, and one with more dense halo $NFW(max)$, as suggested in Ref. 53. Details of the Monte Carlo simulations are in Ref. 51. The 95% CL was obtained by 3σ fluctuation of the diffuse gamma background spectrum as measured by EGRET. With 3 GeV energy threshold, AMS will reach the sensitivity of $(2.0 \pm 0.2)10^{-9} cm^{-2} s^{-1}$ in 3 years exposure.

6. Conclusions

The AMS spectrometer is a high-energy physics experiment performed in space probing the fundamental aspects of astrophysics and particle physics. Its particle identification capabilities over a wide energy range and the large data sample collected during a 3–year exposure will provide the benchmark data to validate current models for galactic cosmic ray propagation and to reveal the nature of the high-energy γ-ray sky before the advent of the most powerful dedicated gamma telescope, GLAST. By its rigidity range and acceptance, AMS on the ISS will provide the best sensitivity to the $\overline{He}$ and anti-nuclei searches in cosmic rays. Within a class of astrophysical and particle physics models, AMS will open new exclusion/discovery domain in the dark matter searches through the four possible complementary channels: e^+, $\overline{p}$, $\overline{D}$, γ.

Acknowledgments

I sincerely dedicate this letter to all colleagues of the AMS collaboration.

References

1. R. Battiston, astro-ph/0208108 (2002)
2. M. Aguilar et al., Ph. Rep. 366/6, 331 (2002)
3. J. Alcaraz et al., Ph. Lett. B 461, 387 (1999)
4. R. Battiston, Int. J. Mod. Ph. A 17, 1817 (2002)
5. E. Fiandrini et al. J. Geophys. Res. 107, A6 (2002)
6. P. Zuccon et al., Astrop. Phys. in press (2003)
7. T.K. Gaisser et al., Proc. 27th ICRC, 1643 (2001)
8. B. Blau, Nucl. Phys. B (Proc. Suppl.) 113, 125 (2002)
9. R. Battiston, Nucl. Instr. Meth. (Proc. Suppl.) B44, 274 (1995)

10. J. Alcaraz et al., Il Nuovo Cimento, 112 A 11, 1325 (2000)
11. W.J. Burger, Nucl. Phys. B (Proc. Suppl.) 113, 139 (2002)
12. G. Batignani et al., Nucl. Instr. Meth., A277, 147 (1989)
13. M. Acciari et al., Nucl. Instr. Meth., A289, 351 (1990)
14. D. Casadei et al., Nucl. Phys. B (Proc. Suppl.) 113, 133 (2002)
15. T. Siedenburg et al., Nucl. Phys. B (Proc. Suppl.) 113, 154 (2002)
16. J. Casaus, Nucl. Phys. B (Proc. Suppl.) 113, 147 (2002)
17. F. Cadoux et al., Nucl. Phys. B (Proc. Suppl.) 113, 159 (2002)
18. M. Capel et al., Proc. 28th ICRC (2003)
19. M.J. Ryan et al., Phys. Rev. Lett. 28, 985 (1972)
20. J. Buckley et al., ApJ 429, 736 (1994)
21. M. Honda et al., Phys. Rev. 52, 4985 (1995)
22. A.W. Strong, I. Moskalenko, ApJ 509, 212 (1998); Adv. Spa. Res. 27, 717 (2001)
23. G. Lamanna, Proc. 27th ICRC, 1614 (2001);
24. R. Dwyer, P. Meyer, ApJ 322, 981 (1987); J.J. Engelmann et al., A&Ap 233, 96 (1990); K.E. Krombel et al., ApJ 328, 940 (1988); S.P. Swordy et al., ApJ 349, 625 (1990)
25. J.J. Beatty et al., ApJ 413, 268 (1993); A.J. Davis et al., Proc. 24th ICRC 2, 622 (1995); E.S. Seo et al., Proc. 25th ICRC 3, 373 (1997)
26. A.J. Davis et al., Proc. 24th ICRC 2, 622 (1995)
27. W.R. Binns et al., Proc. 26th ICRC 3, 9 (1999) J.J. Connell, ApJ 501, L59 (1998); G.A. de Nolfo et al., Proc. 27th ICRC 5, 1659 (2001); T. Hams et al., Proc. 27th ICRC 5, 1655 (2001); A. Lukasiak et al., Proc. 26th ICRC 3, 41 (1999); M.E. Wiedenbeck, Proc. 19th ICRC 2, 84 (1985)
28. S.P. Ahlen et al., ApJ 534, 757 (2000)
29. J. Casaus, Int. J. Mod. Ph. A 17, 1603 (2002)
30. B. Bertucci, Int. J. Mod. Ph. A 17, 1613 (2002)
31. V. Choutko, G. Lamanna, A. Malinin, Int. J. Mod. Ph. A 17,1817 (2002).
32. R. Battiston et al., Astr. Phys., 13, 51 (2000)
33. G. Lamanna, Nucl. Phys. B (Proc. Suppl.) 113, 177 (2002)
34. G. Lamanna, ICHEP Conf. Proc. 119 (2002)
35. J.K. Daugherty et al., ApJ 458, 278 (1996); R.W. Romani, ApJ 470, 469 (1996)
36. R.C. Hartman, ApJ 385, L1 (1992);
37. F.W. Stecker, M.H. Salamon, ApJ 464, 600 (1996)
38. F.W. Stecker, O.C. de Jager, M.H. Salamon, ApJ 390, L49 (1992)
39. B.L. Dingus et al., Proc. 4th Huntsville GRB Symp., AIP ConfProc, 428, 349 (1998)
40. Y. Galaktionov, Rep. Prog. Phys. 65, 1243 (2002) and references therein
41. M. Cristinziani, Nucl. Phys. B (Proc. Suppl.) 113, 195 (2002)
42. I. Moskalenko, A.W. Strong, ApJ 493, 694 (1998);
43. E.A. Baltz, J. Edsjo, K. Freese, P. Gondolo, Phys. Rev. D65 (2002)
44. P. Maestro, Ph.D. Thesis, University of Siena, AMS-Note 2003-01-01 (2003)
45. L. Bergstrom, J. Edsjo, P. Ullio, Astrop. Jour. 526, 215 (1999)
46. P. Ullio, astro-ph/9904086 (1999)
47. http://ida1.physik.uni-siegen.de/pbarprat.html
48. V. Choutko, Nucl. Phys. B (Proc. Suppl.) 113, 170 (2002)
49. L. Bergstrom et al., ApJ Lett. 534, L177 (2000) and references therein
50. F. Donato, N. Fornengo, P. Salati, Phys. Review D, 62 (2000)
51. A. Jacholkowska, G. Lamanna, E. Nuss, M. Sapinski AMS-Note 2003-05-01 (2003)
52. A. Falvard et al. astro-ph/0210184 (2002)
53. L. Bergstrom et al., astro-ph/9712318 (1997)

Frascati Physics Series Vol. VVV (2007) pp.1-9
Science with the New Generation of High Energy Experiments
Frascati, 18-20 June, 2007

OBSERVATIONS OF VERY HIGH ENERGY GAMMA-RAY GALACTIC SOURCES WITH H.E.S.S.

Giovanni Lamanna[a]
for the H.E.S.S. collaboration

[a] *LAPP - Laboratoire d'Annecy-le-Vieux de Physique des Particules IN2P3/CNRS, 9 Chemin de Bellevue, 74941 Annecy-le-Vieux, France*

Abstract

The H.E.S.S array of imaging Cerenkov telescopes has discovered a number of previously unknown gamma-ray sources at very high energy (VHE) and has provided exciting results from the Galactic plane survey. In this communication a selected sample of highlights are presented.

1 The H.E.S.S. telescope system

The H.E.S.S. array, a system of four large (13 m diameter) imaging atmospheric Cerenkov telescopes, is operated since December 2003 by an international collaboration of about 100 physicists. Located in the Khomas highland of Namibia, the H.E.S.S. system covers a 5^o field of view, with a sensitivity

which allows to detect sources with a flux of 1% of the Crab Nebula in 25 h of observation and an energy threshold between 100 and 700 GeV increasing with the observation zenith angle. The four telescopes provide multiple images of gamma-ray induced air showers in the Cerenkov light emitted by the shower particles, enabling the stereoscopic reconstruction of the shower geometry and the shower energy. The estimated energy resolution is 15% and 0.1^o is the angular resolution for individual gamma-ray corresponding to $1'$ location position of a VHE gamma-ray source. A personal selection of the highlights from H.E.S.S. is imposed by the lack of space: most recent published results from the galactic plane survey and dedicated source observations together with a summary on the studies of shell-type supernova remnants and pulsar wind nebulae will be the main topics of this letter.

2 The H.E.S.S. galactic plane survey

The Galactic plane survey was conducted in the summer of 2004 covering the region of -30^o to 30^o galactic longitude and -2.5^o to 2.5^o in galactic latitude, resulting in 15 new VHE gamma ray sources plus three previously known. Searching for counterparts in radio- and X-ray catalogs they resulted to be related to SNR, a significant fraction to PWNe and at least three "Dark accelerators" without counterpart known. A new observation campaign was conducted during the years 2005-2007 with the scanned region now reaching from -80^o to 60^o galactic longitude. The number of new sources is more than 15 with 6 new "Dark accelerators", others sources incrementing the known classes and some new results. Details on published results on the two campaigns can be found in [1] and [2] respectively.

2.1 HESS J1023-575

The discovery [3] of the source HESS J1023-575 is one of the most relevant highlight of the 2006 data taking: a clue to the investigation on the cosmic-rays origin. The detection of VHE gamma-ray emission associated with the young stellar cluster Westerlund 2 in the HII complex RCW 49 provides evidence that particle acceleration to extreme energies is associated with this region, a luminous massive star formation region already well studied at various wavelengths. The source (Fig. 1) has been observed for a total 14 h of data for a corresponding statistical significance of more than 9 σ and clearly extended beyond the nominal PSF. The differential energy spectrum, extended about two order of magnitude in energy and with a minimum threshold of 380 GeV, can be described by a power law with index 2.53 ± 0.16 and an integral flux of $1.3 \pm 0.3 \times 10^{-11}$ cm^{-2} s^{-1}. A variety of potential emission scenarios are suggested [4] for the interpretation of HESS J1023-575, a new type of astronomical object, profoundly distinguished from other source findings made

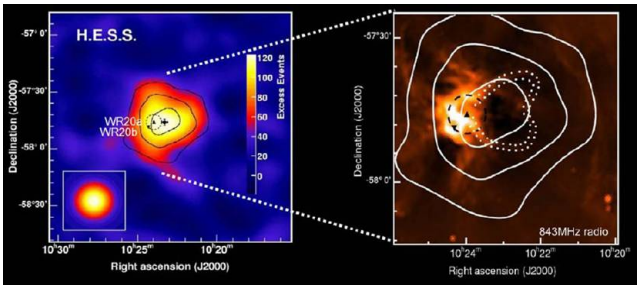

Figure 1: Left: H.E.S.S. gamma-ray sky map of the Westerlund 2 region. The WR stars WR20a and WR20b are marked as filled triangles, while the dashed circle is the extension of the luminous stellar cluster Westerlund2. Right: HESS J1023 5, 7, and 9 σ significance contours overlaid on a radio image.

during Galactic Plane Scan observations. Further investigation with H.E.S.S. will allow to discriminate among alternative interpretations.

3 Study of the shell-type supernova remnants (SNRs)

Two supernova shells already detected as gamma sources by CANGAROO, RX J1713.7-3946 [5] and RX J0852.0-4622 ("Vela Junior") [6](Fig. 2), are now firmly established VHE gamma-ray emitters and morphologically resolved by H.E.S.S.. The energy spectra follow a power law with index of about 2.3, constant across the entire remnants. For both sources, the gamma-ray shell intensity observed with H.E.S.S. is highly correlated with the X-rays one. This correlation would be natural if a common population of primary electrons were responsible for both emission regimes. Assuming that X-rays represents synchrotron radiation and that the gamma rays are generated in Inverse Compton scattering, as it is shown in Fig. 3, simple electronic models assuming an electron injection index of 2.5 and with a local magnetic field of B $\sim$ 10 μG, which accommodates both levels of spectra, fail to consistently fit the multi-wavelength data (e.g.: over shooting the radio flux [8]). In contrast models assuming higher magnetic field and adding gamma-rays from proton-interactions, achieve a good description of wide-band spectra [7]. This interpretation would support the hadronic origin of gamma rays even if a conclusive evidence is still lacking. The currently modest number of shell SNR resolved in VHE has been increased by the recent observation of RCW 86, a supernova remnant with a barrel-shaped shell, visible in X-rays, radio and optical waves. Hints for gamma-ray emission were seen with CANGAROO-II instrument, but no firm detection was claimed. A clear gamma-ray signal with more than 9 σ has

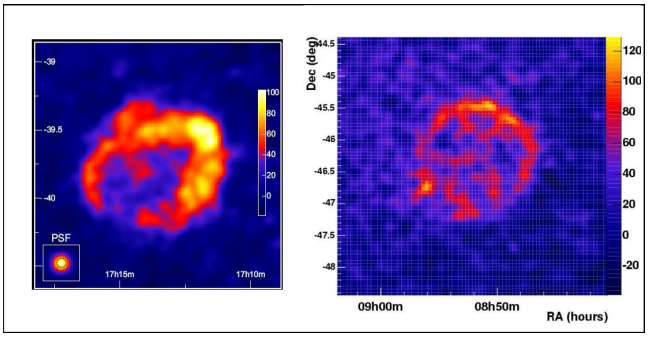

Figure 2: Shell supernova remnants seen in gamma rays by H.E.S.S.: RX J1713.7-3946 (*left*) and RX J0852.0-4622 (*right*).

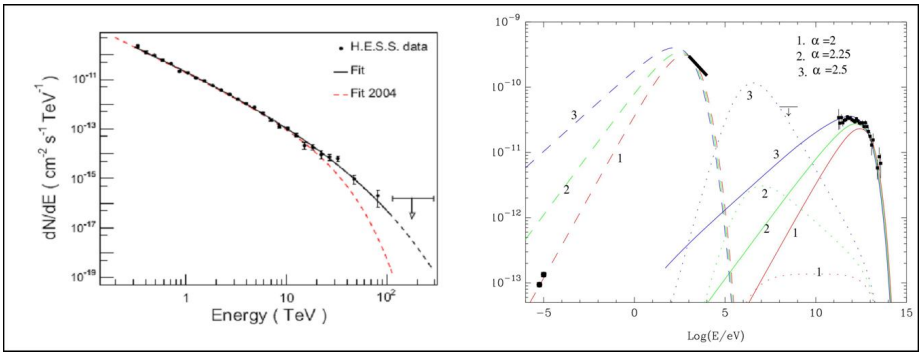

Figure 3: RX J1713.7-3946: energy spectrum (*left*); wide band spectra (together with X-rays, radio data and H.E.S.S. gamma rays measurements) for a magnetic field ~ 10 μG and an electron injection index of 2.0, 2.25 and 2.5 (*right*).

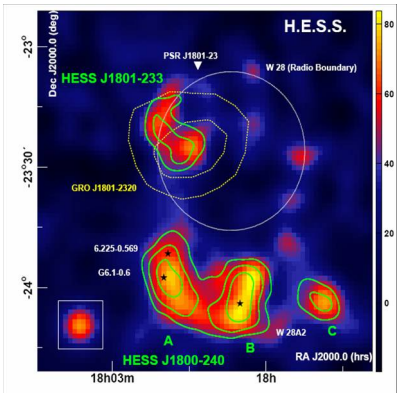

Figure 4: W 28 VHE gamma-rays excess map with 4, 5 and 6σ contour levels for HESS J1801-233 and HESS J1801-240 A, B and C sources.

been detected by H.E.S.S.. A detailed analysis is in progress and preliminary results [9] have shown: a flux 5-10% of the Crab nebula, a 2.3-2.5 spectral index and a shell type morphology.

3.1 HESS J1800-240 and HESS J1801-233

An other composite or mixed-morphology SNR, which is an ideal target for VHE observations, is W 28 (G6.4-0.1). The old-age W 28 SNR is thought to have entered its radiative phase of evolution. The shell-like radio emission peaks at the northern and northeastern boundaries where interaction with molecular cloud is established. The X-ray emission, which overall is well-explained by a thermal model, peaks in the SNR center but has local enhancements in the northeastern SNR/molecular cloud interaction region. On the south boundary several HII regions, including ultra-compact HII region W 28A2 are found. H.E.S.S. observations of W 28 have revealed VHE gamma-ray emission situated at its northeastern (HESS J1801-233) and southern boundaries (HESS J1801-240 with components A, B and C) (Fig. 4) [10]. A multi-wavelength analysis of W 28 has revealed a dense molecular cloud enveloping the southern region, and EGRET MeV/GeV emission centered on HESS J1801-233 and the northeastern interaction region. Overall, these results suggest that old-age SNRs are capable of multi-TeV particle accelerators and candidate hadrons diffusive shock accelerators.

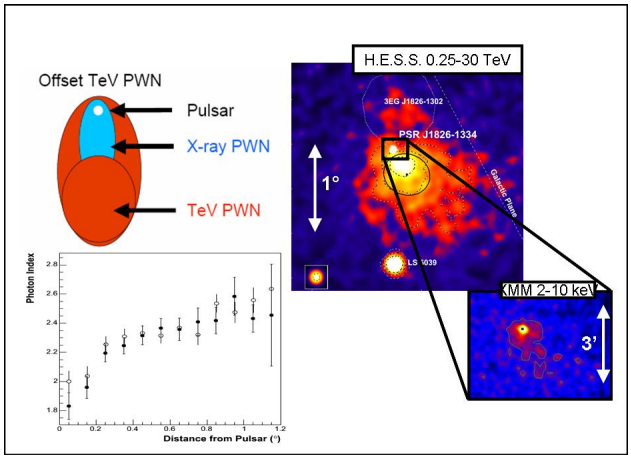

Figure 5: HESS J1825-137, a PWN candidate manifesting an offset from the associated pulsar position, a steepening of the power-law spectral index with increasing distance from the pulsar and a larger extension than in X-ray.

4 Study of the Pulsar Wind Nebulae

Pulsar Wind Nebulae (PWN) are responsible for a significant fraction of the new VHE Galactic sources observed by H.E.S.S.. The purpose of the PWN study is a diagnostic of the spatial and spectral distribution of the high energy electrons responsible of the TeV gamma-ray production dominated by the Inverse Compton scattering off the well-known cosmic microwave background. HESS J1825-137 is a particularly interesting PWN candidate: it is a strong source extended over a fraction of degree [11]. It was detected during the first Galactic plane survey and then further observed. It is located south of the pulsar PSR B1823-13 which exhibits an X-ray nebula trailing extended over $\sim$5' in the direction of the VHE source but then much smaller in size. A natural explanation is that the X-ray generating electrons (via interaction with the nebula magnetic field $\sim$10 μG) have higher energies than those responsible via Inverse Compton scattering for the VHE gamma rays. The higher energy X-ray electrons cool faster and have a shorted range. More importantly, for the first time observations have revealed the energy dependent morphology of the source. This manifests itself as a steepening of the power-law spectral index with increasing distance from the pulsar, as would be expected from the radiative losses of high-energy electrons injected by the pulsar (see Fig. 5).

Among the number of PWNe detected by H.E.S.S. and apart from the almost point-like Crab nebula, extensively studied through different consecutive

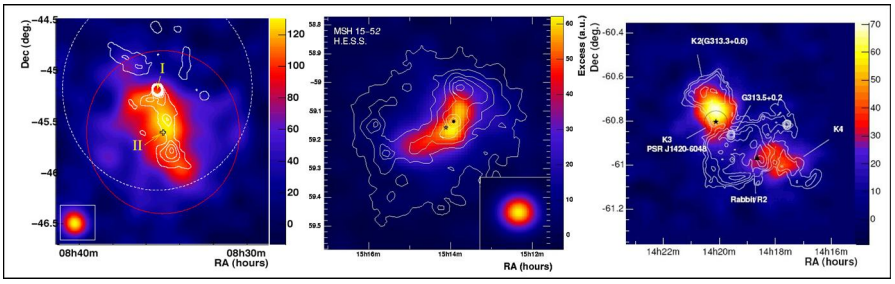

Figure 6: Smoothed gamma-ray excess map (from left to right) from Vela X, MSH 15-52 and the two sources in the Kookaburra region. White contours are X-ray corresponding to count rates contour lines.

observation campaigns [12], Vela X associated with the Vela pulsar (Fig. 6) is likely the most extended one (about a degree south of the pulsar) and significantly old (age ∼11 kyr). The energy spectrum is very hard reaching 50 TeV. The radio, X-rays and VHE gamma-rays emission regions of Vela X are markedly offset from the pulsar position. This may be due to the supernova explosion occurring in an inhomogeneous medium, and the resulting asymmetric reverse shock displacing the PWN in the direction away from the higher density medium. The displacement of the nebulae from the pulsar positions is a surprising constant of almost of extended PWN candidate sources. It is also the case of MSH 15-52, associated with the pulsar PSR B1509-58 inside the G 320.4-1.0 / RCW 89 shell. This elongated and single-sided nebula was revealed by H.E.S.S. as aligned in the same direction of the jet-like high-resolution X-ray Chandra image. More recently, studies of the "Kookaburra" region revealed two new TeV gamma-ray sources, one most likely associated with the pulsar PSR J1420-6048, the other one with the "Rabbit" feature presumably resulting from another pulsar. Both sources have relatively hard spectra index around 2.2, both are extended on the scale of about 10 pc and both are displaced by a similar amount from their pulsars.
Re-observations of the mentioned extended PWNe have been recently accomplished and analysis are in progress to further infer about the spectral and spatial distribution of the energetic electrons within the leptonic interpretation of the VHE emission.

A systematic search for gamma-ray counterparts of known pulsars is addressed by the possibility that all pulsars have associated VHE gamma rays nebulae. Such a research has produced a bunch of new PWN candidates: e.g.: HESS J1718-385 and HESS J1809-193 (Fig. 7) [13]. They show that among pulsars with a spin-down energy flux above 10^{35}ergs/s/kpc^2, a large fraction is

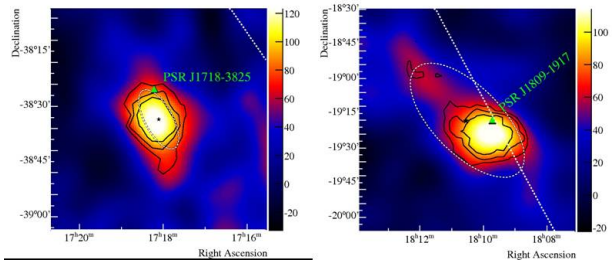

Figure 7: Two new PWNe candidates, HESS J1718-385 and HESS J1809-193, observed during the Galactic sky survey.

visible as gamma-ray emitters, converting about 1% of their spin-down energy into 1-10 TeV gamma rays. This implies that about 10% of pulsar spin-down energy is fed into high-energy electrons. More observations of these sources and corresponding multi-wavelength investigations would provide important progress in the physics of PWNe.

References

[1] F. Aharonian et al, Astrophy. Jour. 777 (2006)

[2] S. Hoppe et al., Proceedings ICRC07 (2007) and references therein.

[3] F. Aharonian et al, Astron. Astrophy. 467, 1075 (2007)

[4] O. Reimer et al., First GLAST Symposium Conference Proceedings (2007)

[5] F. Aharonian et al, Astron. Astrophy. 449, 223 (2006)

[6] F. Aharonian et al, Astrophy. Jour. 661, 236 (2007)

[7] F. Aharonian et al, Science 307, 1938 (2005)

[8] J.S. Lazendic et al, Astrophy. Jour. 602, 271 (2004)

[9] S. Hoppe et al., Proceedings ICRC07 (2007)

[10] F. Aharonian et al, Astron. Astrophy. in press (2007)

[11] F. Aharonian et al, Astron. Astrophy. 460, 365 (2006)

[12] Y. Gallant, In Proc. Barcelona Conf., Astr. and Space Sc. (2006) and references therein.

[13] F. Aharonian et al, Astron. Astrophy. in press (2007)

H.E.S.S. observation of the Vela X nebula

F. Dubois*, B. Glück †, O. C. de Jager‡, Y. Gallant§, J. Hinton¶, B. Khélifi‖, G. Lamanna* and C. Stegmann†
for the H.E.S.S. Collaboration

*Laboratoire d'Annecy-le-Vieux de Physique des Particules,CNRS/IN2P3, 9 Chemin de Bellevue - BP 110 F-74941 Annecy-le-Vieux Cedex, France
†Universität Erlangen-Nürnberg, Physikalisches Institut, Erwin-Rommel-Str. 1, D 91058 Erlangen, Germany
‡Unit for Space Physics, North-West University, Potchefstroom 2520, South Africa
§Laboratoire de Physique Théorique et Astroparticules, CNRS/IN2P3, Université Montpellier II, CC 70, Place Eugène Bataillon, F-34095 Montpellier Cedex 5, France
¶School of Physics and Astronomy, University of Leeds, Leeds LS29JT, UK
‖Laboratoire Leprince-Ringuet, Ecole Polytechnique, CNRS/IN2P3, F-91128 Palaiseau, France

***Abstract*. Vela X is one of the nearest Pulsar Wind Nebulae (PWN) and has served as prototype for evolutionary studies. Associated with the pulsar B0833-45, Vela X has been observed at different wavelengths and in particular in and X-ray bands. The H.E.S.S. Cherenkov telescope array has observed Vela X in 2004 and 2005, discovering very high energy gamma-ray emission in this region, centered to the south of the pulsar, and contained within a region of 0.8 degrees radius. Additional observations from 2006 to 2009 allowed further investigation into the Vela X non-thermal emission. In this work the latest results on the Vela X gamma-ray emission are presented in the context of a multiwave-length analysis.**

***Keywords*: VelaX extension gamma**

I. Introduction

The H.E.S.S. array, a system of four large imaging atmospheric Cerenkov telescopes, which is operating since December 2003, has discovered a number of previously unknown gamma-ray sources at very high energy (VHE). A significant fraction of the new VHE Galactic sources observed by H.E.S.S. are Pulsar Wind Nebulae (PWN) ([1],[2]). The purpose of the PWN study is a diagnostic of the spatial and spectral distribution of the high energy electrons responsible of the TeV γ-ray production dominated by the Inverse Compton scattering off the well-known cosmic microwave background. The PWN Vela X is the bright flat spectrum radio component of the Vela SNR which is at a distance of about 290 pc ([3],[4]) and extented over a diameter of 8°. The Vela X region, within 2 degrees of the pulsar PSR B0833-45, has been observed by the H.E.S.S. γ-ray atmospheric Cherenkov detector in 2004 and 2005. A strong signal was seen from an extended region to the south of the pulsar ([5]), but within a smaller integration region of radius 0.8° around the position (α = $08^h35^m00^s$, δ = -45°36'). The VHE gamma excess observed by H.E.S.S., with intrinsic widths of 0.48° and 0.36° along the major and minor axes, coincides with a hard X-ray region. Such an asymmetric emission can be explained by an inhomogeneous medium, with higher density to the North of the pulsar position ([6]). The approximate full size of the Vela X PWN is about 3° in right ascension and 2° in declination. The actual volume of the VHE gamma cocoon emission is only 5% relative to the total volume of Vela X. This implies the need of further investigation all over the radio extension to better define the VHE gamma ray morphology of the Vela region even if we cannot expect an overall much larger flux than that from the cocoon. With such a purpose follow-up H.E.S.S. observations of the Vela X region have been performed in 2006, 2007, 2008 and 2009. The results of large scale emission are reported and discussed in this communication.

II. Observation and analysis methods

The investigation of the VHE size and morphology of the Vela X emission has an intrinsic limit due to the H.E.S.S. telescopes field of view (about 2.5°) which make it difficult to observe such an extended target. As a consequence, most of observation cannot be analyzed using a reflected background estimation: Vela X region is too close from the center of the field of view and no symmetric OFF-source region can be taken simultaneously. Therefore for the background subtraction a set of runs free of γ-ray sources and taken at the same conditions of the telescopes operations, same zenith and azimuth angles as for the pointing of the runs taken ON-Vela X were selected. Unfortunately residual differences between ON and OFF-runs are possible source of systematic uncertainties. Therefore, as a cross check, new observations were performed (since early 2008) with telescopes pointing 1.3° from the center of gravity of the Vela X cocoon as defined in [5], enabling to study emission till 1.2°. The cocoon, according to the first H.E.S.S. observations, was identified as a 0.8°-radius circular region centered at $\alpha = 08^h35^m$, $\delta = 45°36'$; while the investigated extended region corresponds to a ring between 0.8° and 1.2° around the same center. The total live time concerning the Vela X region after data

quality cuts corresponds to about 58 hours taken since 2004 by the H.E.S.S. telescopes array.

Finally the X_{eff} procedure was used for the data analysis ([7]): a multivariate analysis method which allows for a competitive signal-to-background discrimination, important for searches of tiny signals and morphological study of extended sources. This method combines in a single estimator the main discriminating variables of the three reconstruction methods in use in the H.E.S.S. analysis: Hillas ([8]), Model ([9]), 3D-model ([10]). Shower direction and energy of γ events are also reconstructed by a combining procedure which relies on a composed estimator of the three angular and energy reconstructions coming respectively from the three methods in use. For cross-check purpose, independent Hillas analysis was also performed.

III. RESULTS

A. Global analysis

The X_{eff} analysis of the Vela X region was performed both with two options 80 and 200 photoelectrons (p.e.) charge thresholds. In both cases the analysis provides good results in terms of statistical significance and background rejection. The new data reveal gamma-ray emission up to a radius of about 1.2° from the previously defined center position.

TABLE I: Statistical results with X_{eff}. The On region is a circle of radius 1.2°.

p.e. cut	N_{On}	N_{Off}	γ excess	σ	S/B
80	39794	32242	7611	28.4	0.2
200	12212	7036	5156	37.3	0.7

The X_{eff} methods allows to improve the lower energy sensitivity for spectral analysis and the investigation of possible features in the source morphology.

B. The large scale emission

In the outer ring with inner and outer radii of 0.8° and 1.2°, with 80-pe cut in charge and On/Off analysis, significance of the excess is equal to 11σ for 2106 events and reaches 14.6σ for 1341 events at 200-pe cut in charge. Using a reflected method for background subtraction, the best value is 5.1σ. The preliminary spectrum (see Fig. 1) is well fitted by a power law with exponential cutoff, has spectral index equal to $\Gamma = 1.4 \pm 0.2_{stat} \pm 0.3_{sys}$, an energy cut off $13 \pm 5_{stat} \pm 4_{sys}$ TeV. A previous analysis on the cocoon has been done on data from 2004 to 2005, using Hillas method for reconstruction and event selection (see [8]) and On/Off background subtraction. The spectrum was well fitted by a power law function with index $\Gamma = 1.45 \pm 0.09_{stat} \pm 0.2_{sys}$ and an exponential cut off at an energy of $13.8 \pm 2.3_{stat} \pm 4.1_{sys}$ TeV. The new spectral fit for the ring is compatible with the previous one for the cocoon, confirming the fact that emission observed in the ring also comes from Vela X.

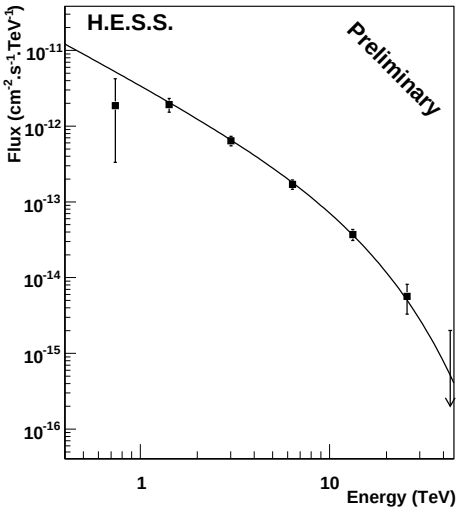

Fig. 1: Spectrum in TeV band of emission from the ring, fitted by a power law function with exponential cut off.

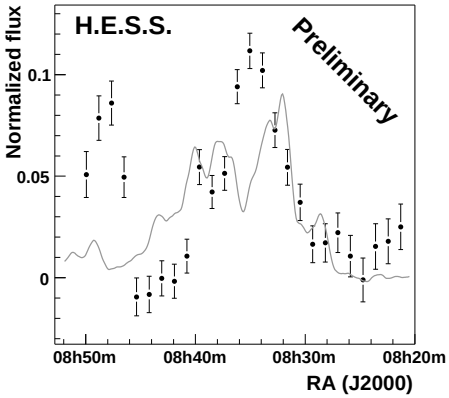

Fig. 2: TeV flux profile in Vela X region along right ascension. The grey line shows the 4.85 GHz radio profile as observed by PMN ([11]), appropriately smoothed for comparison. The peak on the left side of the profile is due to the rim of the supernova remnant RX J0852.0-4622.

C. multiwavelength comparison

A radio map of the Vela X region at 4.85 GHz was obtained in the Parkes-MIT-NRAO Southern Survey ([11]). Fig. 2 shows the radio and TeV profiles of the emission along right ascension. Each TeV flux point is computed by the integration of excess events in boxes of 0.2° width (along the right ascension axis), extending in declination from -46.54° to -44.94°. These plots show that the TeV emission (black dots) extends over essentially the full extent of the radio emission (grey line) of Vela X.

IV. Conclusion

H.E.S.S. observations of the Vela X region since 2004 to 2009 have allowed for a deep investigation of this PWN in the TeV regime. Thanks to the increased observation time, it was possible to detect significant emission in a larger region than the cocoon to 1.2° from the center of gravity. The energy spectrum of photons in such a ring is compatible with the cocoon ones in terms of spectral index and the high energy cut-off, while integrated flux is about a factor 3 less important.

References

[1] Carrigan, S. et al., Proceedings of the 30^{th} ICRC (2007)
[2] Gallant, Y. et al., AIP Conference Proceedings, Volume 983, pp. 195-199 (2008)
[3] Caraveo, P. A., De Luca, A., Mignani, R. P., & Bignami, G. F. 2001, ApJ, 561, 930
[4] Dodson, R., Legge, D., Reynolds, J. E., & McCulloch, P. M. 2003, ApJ, 596, 1137
[5] Aharonian et al., A&A 448 (2006) L43-L47
[6] Blondin, J. M., Chevalier, R. A., & Frierson, D. M., ApJ, 563, 806 (2001)
[7] Dubois, F., Lamanna, G. & Jacholkowska, A. 2009, Astroparticle journal (submitted)
[8] Aharonian et al., A&A 457 (2006) 899-915
[9] de Naurois, M., Proc.Cherenkov 2005, astro-ph/0607247v1 (2005)
[10] Lemoine-Goumard, M., Degrange, B. & Tluczykont, M., Astropart. Phys. 25, 195 (2006)
[11] Condon, J. J., Griffith, M. R. & Wright, A. E., AJ 106, 1095 (1993)